Extreme Ultraviolet Measurements of Thermal and Elastic Dynamics in Nanostructured Media

by

Travis Daniel Frazer

B.S., California Polytechnic State University San Luis Obispo, 2013

M.S., University of Colorado Boulder, 2016

A thesis submitted to the

Faculty of the Graduate School of the

University of Colorado in partial fulfillment

of the requirements for the degree of

Doctor of Philosophy

Department of Physics

2019

This thesis entitled:

Extreme Ultraviolet Measurements of Thermal and Elastic Dynamics in Nanostructured Media

written by Travis Daniel Frazer

has been approved for the Department of Physics

_____

Prof. Margaret M. Murnane

_____

Prof. Henry C. Kapteyn

Date _____

The final copy of this thesis has been examined by the signatories, and we find that both the content and the form meet acceptable presentation standards of scholarly work in the above mentioned discipline.

Frazer, Travis Daniel (Ph.D., Physics)

Extreme Ultraviolet Measurements of Thermal and Elastic Dynamics in Nanostructured Media

Thesis directed by Prof. Margaret M. Murnane and Prof. Henry C. Kapteyn

Nanofabrication today spans from atomic level precision to hierarchically organized structures reaching up to microns. Nanoscale material properties are profoundly different from their bulk counterparts, and when combined with metamaterial approaches, systems can be engineered with properties unavailable in naturally occurring substances. These effects have applications from nanoelectronics, to thermoelectrics, to nanoparticle-based cancer therapies. However, the full capabilities of these materials have not yet been realized due to the difficulty of studying functional nanosystems. In this thesis, I study the properties of nanoscale materials at their intrinsic length and time scales, via the diffraction of extreme ultraviolet (EUV) beams, generated coherently using tabletop high harmonic generation. First, using periodic nanoline gratings, I systematically explore size- and spacing-dependence in the ultrafast cooling of nanoscale heat sources. We find that, though nanoscale heat sources generally cool much slower than the bulk diffusive prediction, they can be brought within a factor of two of the efficient, diffusive prediction simply by bringing them closer together. I then use similar nanoline transducers to study nanoscale acoustic waves, and thus extract the elastic tensor of isotropic, amorphous films, down to 11nm thickness. We find that hydrogenating these films to a critical level of broken bonds causes a divergence towards incompressible behavior, which could also mitigate thickness-dependent changes in the films' mechanical properties. I next demonstrate our technique can measure thermal and elastic dynamics in 3D silicon metalattices, a promising thermoelectric material. To measure even more general samples, I finally extend this EUV nanometrology technique into a non-contact modality. First, I implement an optical transient grating excitation to study micron-scale thermal transport in 2D nanoparticle-molecular arrays. We measure an effective thermal conductivity for the arrays that is three orders of magnitude lower than bulk gold. Second, I participate in EUV transient grating experiments at the FERMI free electron laser to directly excite deep nanoscale thermal and elastic dynamics, and design a similar experiment for tabletop EUV light sources.

Dedication

To my family, to Bianca

To Mr. Koop, to Kat

To those who came before, to those who come behind

To those who aren't here now, to those who are always there

"The mind that is not baffled is not employed."

-Wendell Berry, from "The Real Work"

Acknowledgements

If I have learned one thing over the course of this degree, it's that science is a collaborative effort. I am deeply grateful to so many people over the last six years – I will acknowledge all that I can, but the list will be incomplete. Margaret and Henry, thank you for your years of leadership, guidance, and mentoring, as I came from not even being sure what grad school entailed to finally completing my Ph.D. Kathy, Damiano, and Nico, thank you for teaching me about the lab, grad life, and starting me on a great project. Nico, Josh, and Begoña, thank you for being my team through it all. I'm so grateful that you were not only exceptional to work with, but you were a team that supported balance and health, and I can call you my friends on the other side of all the hard work. Josh and Brendan, I'm confident that you will have amazing theses, and you will continue to do awesome science in B1B19 and beyond. Thank you to the rest of the KM group plus Daisy and Kevin for all your assistance, particularly with our old laser! Thank you to all of our collaborators, particularly the FERMI team for an incredible experience working and learning in Italy. I also thank for their patient instruction Xavier Alvarez, Dan Adams, Alex Maznev, Hossein Honarvar, and Mahmoud Hussein, each of whom has taught me a great deal. Thank you to the Physics and JILA staff, especially Jeanne, Kim, Kyle, Hans, Felix, Terry, J.R., Dave, Mark, Julie, Steven, Jen, Brian, Lois, Lauren, Kim, Agnieszka, Beth, Cindy and all the custodial and administrative staff that keep JILA running. Finally, I thank the friends and family who have supported me throughout my time in Boulder. Emily, Scott, Will, and Adam, thank you for your guidance as I navigated all the changes and trials of grad school. Amy, Adam, Torrey, and Houston, thanks for the food in the desperate final push! Mom and Dad, thank you for always supporting me with calls, visits, prayers and cookies. Bianca, thank you for being my partner closer than anyone else on this journey and for keeping me human, even when it got overwhelming. I'm so grateful we supported each other on the final mile, and I'm glad you'll be there for miles to come.

Contents

Chapter

1 Introduction 1

2 Experimental Methodology 9

2.1 Introduction 9

2.2 Optical Pump – EUV Probe Measurements 12

2.2.1 High Harmonic Generation 15

2.2.2 Diffraction Measurements 17

2.3 Upgrades to the Experiment 23

2.3.1 Optical Transient Grating Setup 24

2.3.2 Synchronized Chopper as a Pump Shutter 30

2.3.3 B-Integral and Chirped Mirrors 39

2.4 Conclusions and Future work 44

3 Nanoscale Thermal Transport 45

3.1 Introduction and Motivation 46

3.2 Experimental Methods 48

3.2.1 Nanoline Grating Design and Excitation 50

3.2.2 Probing and Measurement Sensitivity 54

3.2.3 Finite Element Analysis to Fit the Data 58

3.3 Results and Discussion 59

3.3.1 Collectively Diffusive Model 59

3.3.2 Silicon and Fused Silica Results 60

3.3.3 Comparison to Other Experiment and Theory. 64
3.4 Conclusions and Future Work 68
4 Thin Film Elastic Properties 69
4.1 Introduction and Motivation 69
4.2 Experimental Methods 73
4.2.1 Sample Design 74
4.2.2 Data Processing and Interpretation 77
4.2.3 Fitting and Modeling Elastic Properties 86
4.3 Results and Discussion 90
4.3.1 Hydrogenation-dependent Study 90
4.3.2 Thickness-dependent Study 93
4.4 Conclusions and Future Work 100
5 Extending Dynamic EUV Metrology 102
5.1 Introduction and Motivation 103
5.2 Silicon Metalattices 104
5.3 Optical Transient Gratings 111
5.3.1 Data Processing and Fitting 111
5.3.2 Thermal Transport in Novel Nanosystems 117
5.4 Extreme Ultraviolet Transient Gratings 124
5.4.1 EUV TG with an Optical Probe 127
5.4.2 EUV TG with an EUV Probe 132
5.4.3 EUV TG on a Tabletop 135
5.5 Conclusions and Future Work 143
6 Conclusions and Future Work 144
Bibliography 148
Appendix 160

Tables

Table

2.1 Delay box and chopper settings for specific pulse exposures 39

3.1 Linewidth and period of each nickel grating on silicon, measured by AFM 51

3.2 Linewidth and period of each nickel grating on fused silica, measured by AFM 51

3.3 Pump beam average power, spot size at the sample plane, and average fluence 54

3.4 Parameters used in FEA multiphysics simulations 58

4.1 Hydrogenation-dependent thin films nominal properties 74

4.2 Thickness-dependent thin film nominal properties 75

4.3 Nanoline grating dimensions 76

5.1 Volume fraction of constituent elements in nanoparticle arrays and nanomeshes 119

5.2 Bulk material properties used in eigenfunction calculations 119

5.3 Best fit conductivities for nanoparticle molecular arrays 123

5.4 Example signal strength reductions for non-Bragg probing 137

Figures

Figure

1.1 Colloidal suspensions of gold nanoparticles 2

1.2 Transistor number per chip and clock speeds since 1970 3

1.3 Structural metamaterials with nanoscale effects 5

2.1 Example of pump probe measurements 10

2.2 Block diagram of the experimental apparatus 12

2.3 Nanograting and optical transient grating excitations 14

2.4 High harmonic generation 16

2.5 Dynamic diffraction measurements 19

2.6 Experimentally measured diffraction signals 22

2.7 The modular optical TG setup 25

2.8 New vacuum chamber for TG and nanograting measurements 28

2.9 Optical chopper as a beam shutter 31

2.10 Timing schematic of the experiment 32

2.11 Comparator circuit with voltage dividers 34

2.12 Diagram of the analog to TTL converter circuit 35

2.13 The one-shot K parameter 36

2.14 Function of the analog to TTL converter circuit 37

2.15 Chirped mirrors and vacuum redesign to reduce B integral 43

3.1 The EUV nanometrology laser setup 49
3.2 Diagram of the pump-probe technique 50
3.3 SEM images of the fused silica sample 52
3.4 Dynamically changing diffraction signals for 20nm linewidth gratings on silicon 53
3.5 Measurement sensitivity to nanostructure and substrate temperatures 56
3.6 Measurement sensitivity to the substrate coefficient of thermal expansion 57
3.7 Best fit effective thermal boundary resistivity for nanolines on silicon and fused silica 61
3.8 Comparison to previous measurements on silicon 62
3.9 Results for the constant 1500nm period series of gratings 63
3.10 MD temperature profiles compared to the diffusive prediction 67
4.1 Low-k dielectrics for metal interconnects 70
4.2 Thin film sample design and characterization 76
4.3 EUV diffraction measurement of thin film acoustic waves 77
4.4 SAW confinement for the thickness-dependent study 79
4.5 The matrix pencil method for frequency extraction 80
4.6 11nm Film (#155) fLAW and carbon deposition 81
4.7 fLAWs for films 148 and 145 84
4.8 fLAWs for film 503 85
4.9 Measuring the two independent elastic constants with acoustic waves 87
4.10 FEA calculations of thermoelastic dynamics 89
4.11 Young’s modulus and Poisson’s ratio for the hydrogenation-dependent study 92
4.12 Film 145 (44nm thick) elastic constants 94
4.13 Film 155 (11nm thick) elastic constants 94
4.14 Elastic properties of varying-thickness SiOC:H films 95
4.15 TEM measurements of film 503 – double deposited 5nm SiC:H films 97
4.16 HAADF and EDS measurements of film 503 98

4.17 Elastic characterizations of SiC:H films 335 and 503 99

5.1 Fabrication of silicon metalattices from silica templates 105

5.2 Measurements of 30nm gratings on a 30nm metalattice 106

5.3 Measured signals on larger gratings for the two 30nm metalattices 107

5.4 Comparing diffraction from a 100nm linewidth, 400nm period grating 108

5.5 Surface acoustic wave dispersion in silicon metalattices 109

5.6 MD calculations of thermal transport in porous silicon metalattices 110

5.7 Geometry for eigenfunction expansion calculations 112

5.8 Graphical intersection method for the determination of eigenvalues 114

5.9 Nanoparticle molecular hybrid arrays 117

5.10 Example of nanomesh geometry and diffraction 118

5.11 Optical microscope images of burned-in TG patterns 121

5.12 Identification of sample burning and subsequent calculation of TG period 122

5.13 Best fits for the nanoparticle molecular arrays 124

5.14 Pulse front tilt and the 4f optical TG setup 126

5.15 The mini-TIMER setup for optically-probed EUV TG 127

5.16 Optically probed EUV TG signal on single crystal diamond 130

5.17 Optically probed EUV TG signal on BK7 glass 131

5.18 Optically probed EUV TG signal on $Bi_4Ge_3O_{12}$ 131

5.19 Schematic of the TIMER experiment with EUV-probed EUV TG 133

5.20 EUV TG signal on a Si_3N_4 membrane 134

5.21 EUV TG signal on a Si membrane 134

5.22 Design for initial demonstration of EUV TG at JILA 135

5.23 Thin and thick grating diffraction conditions 137

5.24 Calculated TG patterns and diffraction for single- and multi-frequency beams 139

5.25 Schematic of four-mirror design for all-EUV TG at JILA 142

Chapter 1

Introduction

"We're going to see things no one has ever seen before." In the classic science fiction film, *Fantastic Voyage*, the character Cora Peterson delivers this line before being shrunken to a sub-micron size to explore inside the human body and remove a blood clot. While shrinking humans is completely fictional, modern medicine is closer to a *Fantastic Voyage* than you might think – nanoparticles can be used to treat tumors, precisely deliver drugs, and kill bacteria [1, 2]. Unlike in the movie, however, these nanoparticles don't behave like "miniaturized submarines". When confined to the nanoscale, material properties drastically change from those expected at the macroscale. This presents both opportunity and challenge to nanotechnology in general, where fabrication is now controlled one atomic layer at a time.

As an example of the opportunity given by nanoscale changes in materials, consider gold. When it is scaled down into particles only a few nanometers across and suspended in water, gold loses its familiar metallic sheen and instead looks bright red. As the nanoparticle diameter is increased, the solution's color changes from red to purple, as shown in Fig. 1.1. These optical effects come from surface plasmon resonances, where specific optical wavelengths resonantly excite charge oscillations in each nanoparticle [3, 4]. By increasing only the nanoparticle diameter, the resonant wavelength correspondingly increases, leaving a blue-shifted spectrum of scattered, non-absorbed light. This size-dependence introduces a new degree of freedom to materials engineering – using nanoscale effects to produce useful materials properties not present in bulk samples. Indeed, the use of gold nanoparticles extends all the way back to ancient Rome, where artisans used colloidal nanoparticles to produce impressive glasses that appear green when viewed from the outside, but red when illuminated from within [5].

Figure 1.1: Colloidal suspensions of gold nanoparticles. As the nanoparticle diameter is increased from 5nm to 100nm, the scattered light from the suspension changes from red to purple. This is because the surface plasmon resonant wavelength increases with increasing nanoparticle size. Thus, for the smallest nanoparticles, blue wavelengths are absorbed from white light, while for the largest nanoparticles, red wavelengths are absorbed from white light. Image from nanoComposix.

As an example of the challenges presented by nanoscale materials, however, you need look no further than your computer. All of modern computing relies on complex patterned materials at the deep nanoscale, with the critical dimensions of the latest generation of transistors now reaching below 10nm. Accounting for changes in material properties at these scales is critically important for the successful production and operation of devices. Indeed, materials innovation is what is now needed for the continued scaling of computing power.

The first materials challenge for the semiconductor industry is how to manage heat. When current runs through wires, they heat up, and computer chips are essentially a densely packed nest of current-carrying wires. To keep the heat at tolerable levels, the industry has not been able to increase clock speeds since 2004 [6], as shown in Fig. 1.2. To continue scaling computing power, they have instead had to parallelize processors, all running at the same, heat-limited clock speed. The heat management problem is exacerbated by the fact that thermal transport at the nanoscale is much slower than we would predict from macroscopic behavior [7].

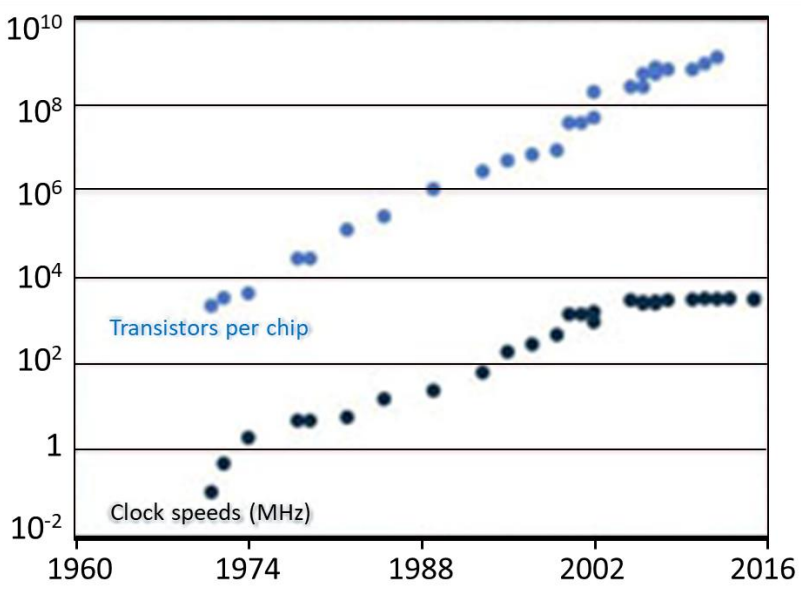

Figure 1.2: Transistor number per chip and clock speeds since 1970. The number of transistors per chip (blue points) has doubled every two years since the 1970s – an observation and prediction known as Moore's Law. The clock speed of processors (black points), however, has stagnated since 2004. This capping of clock speeds is required to limit the thermal load to manageable levels. Figure adapted from [6].

At the macroscale, heat flow is governed by Fourier's law of heat conduction, where the heat flux, q, is proportional to the temperature gradient, ∇T, according to the material's thermal conductivity, κ:

$$\vec{q} = -\kappa \nabla T.$$

This diffusive behavior assumes heat transfer is occurring over large enough distances for the heat carriers to repeatedly scatter and form a smooth thermal gradient. At the nanoscale, however, this assumption breaks down. For semiconductors, the main heat carriers are phonons (quanta of lattice vibrations), which can travel hundreds of nanometers, up to microns without scattering [8-11]. This means that some of the phonons carrying heat away from nanoscale hot spots travel ballistically, and deposit their heat non-locally, in stark contrast to diffusion. Simply applying Fourier's law to nanoscale systems dramatically over-predicts the rate of heat transfer, when the heat flux is in reality limited by the ballistic velocity of phonons. Since transistors and other circuit elements essentially serve as nanoscale hot spots on top of a semiconductor, this quasiballistic thermal transport is certainly at play in the large thermal load faced by modern electronics.

One further materials challenge relevant to the semiconductor industry is nanoscale mechanical properties. Between the metallic, current-carrying interconnects on a chip, a dielectric material is required that is both low dielectric constant, and sufficiently mechanically robust to produce a functional device. However, it is difficult to achieve a low dielectric constant material, which increases both the device's efficiency and its switching speed, without sacrificing its mechanical properties, which can lead to device failure [12]. Moreover, the elastic properties of materials can change at the nanoscale, due to the large fraction of atoms at free surfaces or at interfaces [13, 14]. To get around challenges at the nanoscale, the semiconductor industry has often had to resort to trial-and-error, modifying the fabrication recipe until a successful combination is found. How much better would it be, however, if we could design materials up front with the desired properties?

One powerful materials-by-design approach is to fabricate metamaterials, where some form of periodic structuring gives rise to novel properties not attainable by homogenous, bulk materials [15, 16]. Combined with nanoscale effects, metamaterials are an exciting avenue to solving difficult technological problems, particularly by engineering new thermal and elastic properties. As one example, the Greer group at Cal Tech produces structural metamaterials by engineering nano-truss structures out of metallic glass tubes [17]. As shown in Fig. 1.3, by reducing the wall thicknesses of the tubes to the deep nanoscale, the metamaterial undergoes a brittle-to-deformable transition. Thus, this stiff yet ultralight truss structure has tunable mechanical properties by taking advantage of nanoscale size effects. As a second example, the Hussein group at CU Boulder has developed the concept of nanophononic metamaterials, where forests of nanopillars are placed on the surface of a thin film [18]. The local resonances of these pillars hybridize with the phonons in the film to slow their group velocity and reduce the rate at which they can carry heat. Thus, through only surface engineering, this metamaterial can reduce the thermal conductivity of the underlying film, without impacting its electrical conductivity. This is a promising route towards producing an efficient thermoelectric material.

Thermoelectric materials produce a voltage when a thermal gradient is placed across them, according to the Seebeck effect. Using this effect, the field of thermoelectrics seeks to recover the energy

lost as waste heat in industrial, transportation, and power generation contexts (over 60% of the energy produced [19]). However, the barrier to recovering the vast amounts of waste heat into useable energy is that most materials are very inefficient at this process. The efficiency of a thermoelectric material is largely determined by its nondimensional figure of merit, ZT. ZT must be greater than three for a material to be commercially viable on a large scale. ZT is defined by

$$ZT = \left(\frac{S^2\sigma}{\kappa}\right)T,$$

where S is the Seebeck coefficient, σ is the electrical conductivity, and κ is the thermal conductivity. This means that the ideal thermoelectric material would have very low thermal conductivity, but very high electrical conductivity, which a nanophononic metamaterial may be able to achieve.

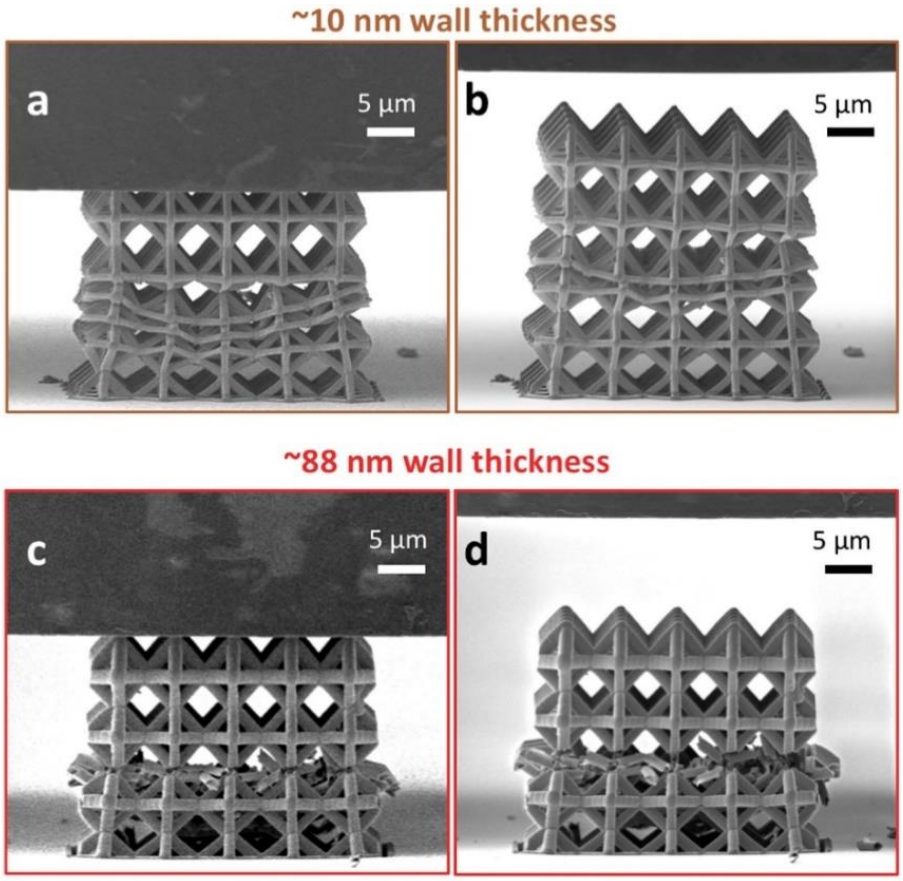

Figure 1.3: Structural metamaterials with nanoscale effects. These truss structures are fabricated out of hollow nanotubes of metallic glass (Zr-Ni-Al). When the tubes have 10nm wall thickness, they exhibit more ductile compression (a), and partially elastically recover to their initial shape when the stress is removed (b). When the wall thickness is increased to 88nm, however, the structures exhibit brittle fracture upon compression (c), and cannot recover their shape (d). Figure from [17].

Given the fundamental and technological importance of nanoscale materials, with applications ranging from integrated circuits and thermoelectrics, to metamaterials and nano-medicine, there is a great need for more research. In many cases, we are still developing theories to connect first principles rigor to real experimental geometries, and computational approaches are forced to balance sufficient complexity with feasibility as every atom in an extended nanosystem cannot yet be simultaneously modeled. To increase understanding of nanomaterials and benchmark these theories and computations, the Kapteyn-Murnane group uses coherent, nanometer-wavelength beams to directly probe functional nanosystems.

For my thesis, I have used tabletop extreme ultraviolet (EUV) sources to study the ultrafast thermal and elastic dynamics of nanostructured materials. By using ultrafast pulses, this technique accesses phonon transport on its natural timescales (sub-picosecond to several nanoseconds), enabling repeatable, non-destructive measurements, unlike that shown in Fig. 1.3. Moreover, the use of coherent EUV beams enables the direct, non-contact probing of nanostructures well below the diffraction limit of visible light (hundreds of nanometers). To further advance EUV metrology to general samples and in-situ environments, I have devoted a substantial portion of my thesis to the development of fully non-contact methods based on the transient grating technique, where two coherent beams are interfered to produce periodic excitations in a sample. The culmination of this effort is the interference of two EUV beams to directly excite dynamics in the deep nanoscale. This has been demonstrated at the FERMI free electron laser and is currently under construction at JILA.

In Chapter 2, I present details on the experimental approach I took to perform nanoscale thermal and elastic measurements. After an overview of the entire experiment, I explain in more detail high harmonic generation and diffraction-based measurements, which are unique distinguishing factors of the technique. I then comprehensively present the major upgrades to the experimental apparatus that were made during my thesis.

In Chapter 3, I present measurements of nanoscale thermal transport in silicon and fused silica. For silicon, we observe quasiballistic reduction in heat flow away from laser-heated nanostructures into the silicon substrate. Once these structures are brought closer together, within the scattering distance of

phonons, thermal transport recovers back towards the faster, diffusive prediction. These results confirm our surprising prediction made in [20] that closely spaced nanostructures can cool faster than widely spaced ones, when period dependence in thermal transport counteracts quasiballistic effects. By independently tuning nanostructure size and spacing, this work maps the transition between isolated quasiballistic and collectively diffusive thermal transport. For fused silica, no deviation from diffusive transport is observed as a function of nanostructure size or spacing. This is expected as phonons in this amorphous material are scattered at lengths smaller than those accessed experimentally. This sample serves as an important control study, showing that our results are not dominated by effects coming from the nanostructures alone, independent of thermal transport in the substrate material. This chapter is based on our publication by Frazer, et al. [21]. At the end of the chapter, I also briefly discuss theoretical efforts currently underway to explain the fundamental mechanisms behind our observations. These efforts are in preparation for publication by Beardo, et al., and Honarvar, et al.

In Chapter 4, I present acoustic measurements of ultrathin film elastic properties. Using the same nanostructure transducers as in Chapter 3, we are able to launch nanoscale acoustic waves whose velocities depend on the elastic properties of the sample materials. By measuring these wave velocities, we first characterize the full elastic tensor of a series of low-dielectric-constant films relevant to the semiconductor industry. These films are hydrogenated to lower their dielectric constant, but beyond a critical level, this hydrogenation causes a transition towards incompressible behavior. This section of the chapter is based on our publication by Hernandez-Charpak, et al. [22]. Second, we use this method to explore thickness-dependence in the elastic properties of two separate series of dielectric films, down to 5nm thickness. We observe no thickness dependence in the series of SiOC:H films, but we do see evidence of thickness-dependent softening in the series of SiC:H films. This section of the chapter is currently in preparation for publication by Frazer, et al.

In Chapter 5, I present efforts to extend the technique used in Chapters 3 and 4 to more general samples. First, we use the same nanostructure transducers to study the thermal and elastic properties of silicon metalattices − 3D periodic inverse opal materials with hierarchical structuring from single

nanometers up to microns. This work is being prepared for publication by Abad, et al., and Knobloch, et al. Next, I present measurements of micron-scale thermal transport using EUV-probed, optically-generated transient gratings. Using this approach, we successfully characterize the thermal conductivity of hybrid nanoparticle-molecular arrays. This work is in preparation by Frazer, et al., for publication. Finally, I present the work to date using EUV transient gratings to excite thermal and acoustic dynamics. In collaboration with the FERMI free electron laser, we demonstrated optically-probed, EUV-generated transient gratings for the thermal and elastic characterization of materials, as reported in [23]. Our work with FERMI later contributed to the first demonstration of all-EUV transient grating measurements in the deep nanoscale, as reported in [24]. I close the chapter with a discussion of the current state of the effort to demonstrate all-EUV transient gratings on a tabletop at JILA.

Chapter 6 closes this dissertation with a summary of its major results, and a brief description of the next steps expected in the near future. The Appendix gives further details on the COMSOL modeling performed to analyze our thermal and acoustic measurements, as well as more details on the thermal data fitting procedure.

Chapter 2

Experimental Methodology

In this chapter, I will describe the details of the experimental apparatus used for the tabletop measurements presented in this dissertation. Our lab first demonstrated these types of measurements in 2004 with an apparatus very similar to the one I use [25]. While the basic principles of the approach have not changed during the last 15 years, some significant additions and improvements have been made to the apparatus over the course of my PhD. After a brief description of the experimental methodology, I will focus the bulk of this chapter on the three primary new additions. These additions are 1) rebuilding our optical transient grating capability, 2) implementing a synchronized optical chopper in the excitation beam, and 3) taking steps to mitigate nonlinear effects during the propagation of our high-intensity laser beam.

2.1 Introduction

To measure ultrafast dynamics, we use a pump-probe approach. In pump-probe experiments, some form of "pump" is used to initiate dynamics in a sample. After a controlled delay, some "probe" is used to measure the state of the system at precisely that time. Provided the excited dynamics are repeatable, this process may be repeated for a whole series of delay times, at a temporal resolution down to the pump duration. The repeated measurements at various delays may then be ordered into a single temporal signal or effective slow-motion movie of the sample dynamics. As an approachable example, consider the study of dripping water shown in Fig. 2.1. For this experiment, the repeatable dynamics are water drops forming at the base of a glass capillary tube, stretching out a liquid bridge, and finally releasing to fall. The probe is a precisely timed 15μs flash of light, which exposes photographic film. By adjusting the timing of the flash

from drop to drop, the authors photograph each step in the water dripping process, and use the full time series of images to study the fluid mechanics involved in water dripping [26].

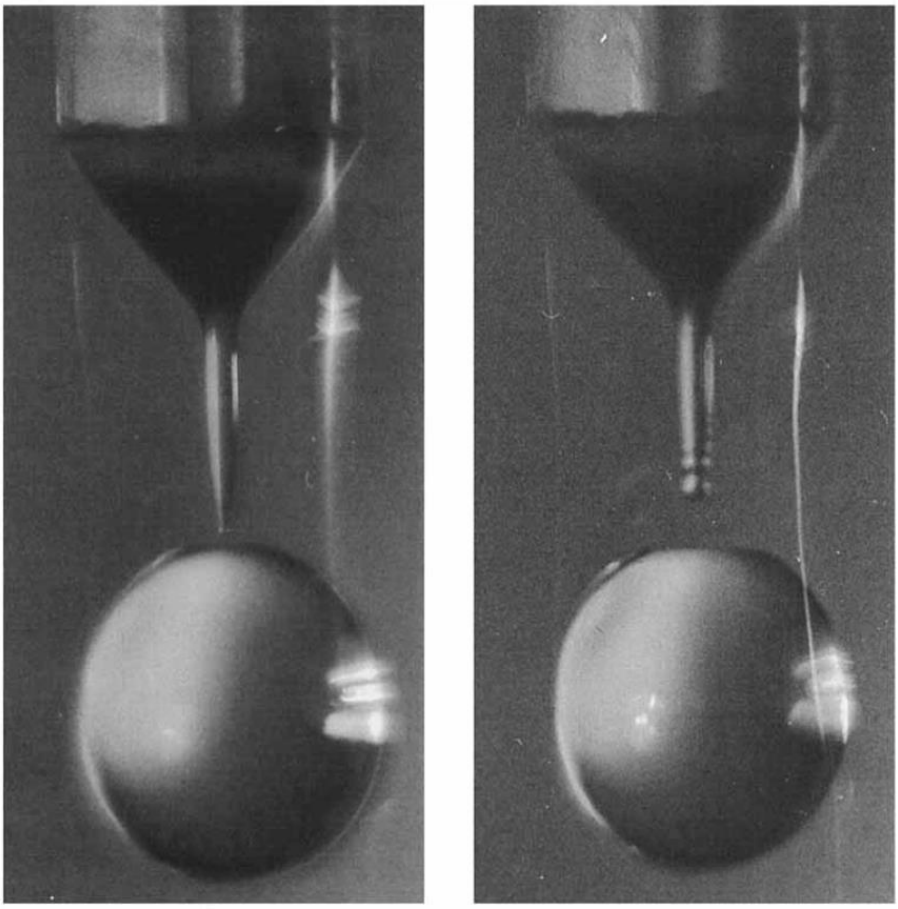

Figure 2.1: Example of pump probe measurements. In general, high temporal resolution pump-probe measurements carefully delay repeated "snapshots" of the system, measured by a probe, with respect to the repeated initiation of dynamics, launched by the pump. In this case, the repeatedly "pumped" dynamics are regularly spaced water drips from a capillary tube. The probe is a 15μs camera flash, which exposes photographic film. By slightly delaying the flash from one drop to the next, the researchers resolve each step of the dripping process, such as the initial release of the water bridge connecting the drop to the water still in the tube (left), and the subsequent retraction of the water bridge back into the tube (right). Figure taken from [26].

For the work presented in this dissertation, I study the repeatable thermal and elastic dynamics of nanoscale materials. The natural timescales for such dynamics at nanometer dimensions range from sub-picosecond to several nanoseconds. Thus, to use a pump-probe technique to study these dynamics, I require a pump duration well below the fastest dynamics analyzed (~0.5ps in the present work). This is available in the form of ultrafast mode-locked lasers, which are an expertise of the Kapteyn-Murnane group. In

particular, I use a near-infrared (IR) laser with pulse durations of 30fs to launch dynamics in the sample. To probe these dynamics directly at the nanoscale, a nanoscale wavelength ultrafast laser would be ideal. Thankfully, this is also an expertise of the Kapteyn-Murnane group in the form of coherent EUV beams generated by high harmonic generation (HHG). Using these coherent EUV beams, we extend established optical metrology techniques into the nanoscale.

Our experiment grows out of the tradition of optical techniques that measure thermal and elastic material properties [27]. It takes elements from transient thermal gratings [28, 29], picosecond ultrasonics [30], and surface acoustic wave (SAW) spectrometry [31]. Similar to transient gratings (TG), we excite specific acoustic wavelengths and thermal transport distances. Similar to picosecond ultrasonics, we measure longitudinal acoustic pulses that reflect from buried interfaces. Similar to SAW spectrometry, we measure a spectrum of SAWs, and characterize their dispersion in the sample material. We differ from each of these optical measurements, however, in our use of a coherent EUV probe.

By using our EUV probe, we have made several advancements and discoveries beyond traditional optical probes. Beyond micron-scale TG, we have observed a previously-unpredicted period-dependence in nanoscale thermal transport, where closely-spaced non-diffusive heat sources can cool down faster than widely spaced ones [20]. Building from laser picosecond ultrasonics, we have measured thin film mechanical properties down to monolayer sensitivity, and we have also observed thickness dependence in bilayer elastic properties [32]. Extending SAW spectrometry to nanoscale SAW wavelengths, we have measured the full elastic properties of films down to 11nm thickness and observed a deviation towards incompressible behavior in highly-hydrogenated films [22]. All of this has been achieved in a single measurement platform, using an EUV probe to measure optically-excited dynamics from nanoscale metallic gratings.

In this chapter, I present the experimental details of our measurements. I first give a broad overview of the experimental apparatus, followed by more detailed descriptions of HHG and diffraction-based measurements. I then present in-depth discussion of the three primary additions to the experimental apparatus made during my PhD. First, I describe the optical TG setup I implemented to generate micron-

scale dynamics without a grating transducer. Next, I describe the optical chopper added to the pump beam of our experiment, which allows for short exposure times and rapid alternation between pumped and unpumped measurements. Finally, I describe steps taken to reduce the B-integral along our optical path, a measure of nonlinear effects that can cause laser mode degradation and instabilities.

2.2 Optical Pump – EUV Probe Measurements

All of the tabletop experiments described in Chapters 3-5 are performed using the same basic optical pump – EUV probe technique. In this technique, a sample absorbs energy from an incident optical laser pulse, launching thermal and acoustic dynamics at its surface. After a controlled temporal delay, an EUV probe pulse encodes the dynamic changes to the sample surface as a change in diffraction efficiency. The dynamically changing diffraction is then analyzed to extract both the thermal and acoustic contributions to the surface deformation. Using appropriate modeling, we then determine the thermal and elastic properties of the sample. With this general approach in mind, I now describe the experimental apparatus shown in Fig. 2.2.

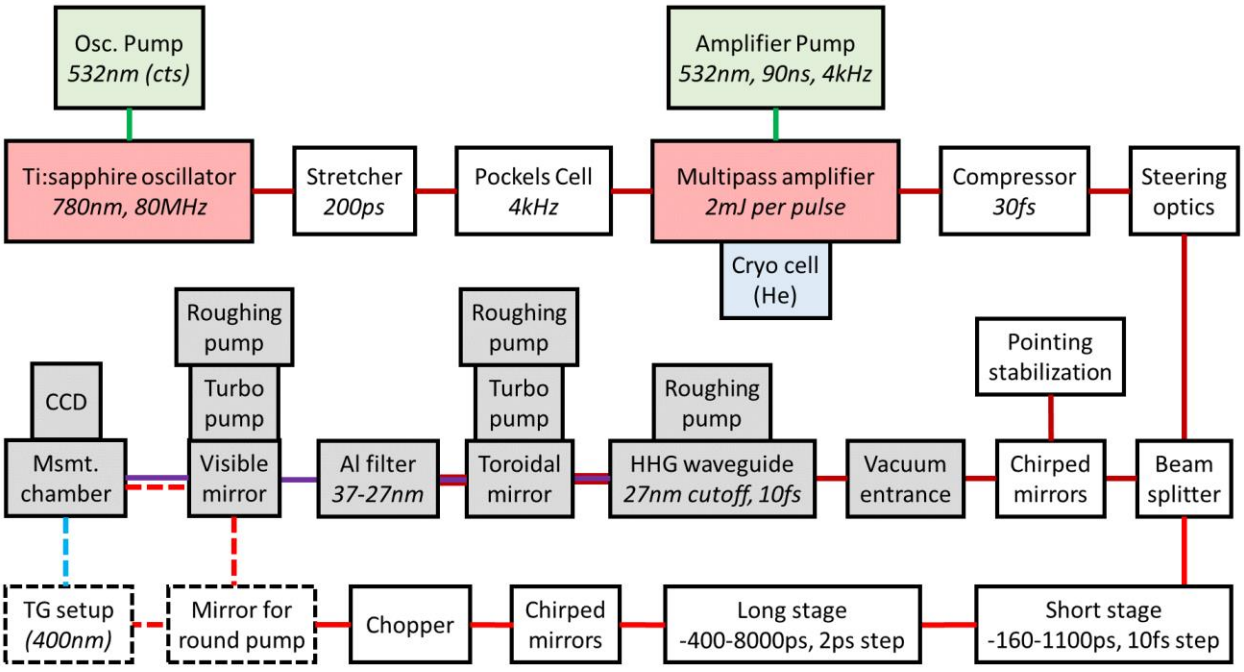

Figure 2.2: Block diagram of the experimental apparatus. The laser properties at each stage are labeled in italics. The lines between each block represent the laser wavelength there, while the block colors mark subsystems: pump lasers in green, IR sources in red, vacuum system in grey, and cryo system in blue.

Each experiment begins with a Ti:sapphire oscillator. In the oscillator, Kerr lens mode-locking produces an ultrafast pulse train at 80MHz repetition rate, with 780nm central wavelength and 50nm bandwidth. This process is pumped by a 532nm continuous wave laser. After being coupled out of the oscillator, the pulse train enters a chirped pulse amplification system.

The first step in chirped pulse amplification is to stretch the ultrafast pulses out to ~200ps width using a grating-based stretcher. These pulses then pass through a Pockels cell, which down-samples the pulse train to a 4kHz repetition rate. The pulses are next amplified by multiple passes through a second, helium-cooled Ti:sapphire crystal that is pumped by a 532nm wavelength, 90ns pulse width Q-switched laser. This amplifies each pulse to 2mJ of pulse energy. The amplified pulses then pass through a grating-based compressor, which compresses the pulse length close to its 30fs limit. The pulses are not fully compressed until later in the setup to avoid nonlinear effects during propagation, as detailed in Sec. 2.3.3.

Having completed chirped pulse amplification, the pulse train is then steered to a beam splitter that divides the beam with most of the energy going towards the probe line, and part of the energy going towards the pump line. In the pump line, the optical path length is controlled by both a short, high-resolution mechanical delay stage, and a long, low-resolution mechanical delay stage. The optical path length difference between the pump and the probe lines sets the delay between pump and probe pulses at the sample. The pump pulses next reflect six times off of chirped mirrors that finish compressing the pulse width down to 30fs. The pump pulses are then periodically blocked and unblocked by a chopper that is synchronized to the laser system. This provides a constant alternation between pumped and unpumped measurements of the sample. After the chopper, the pump may either be routed directly to excite a nanostructured sample, or it may be passed through a transient grating setup, to produce periodic interference fringes that excite the sample. These two pumping schemes are shown in Fig. 2.3. The pump is assumed to excite the sample identically at each path length (delay time) chosen. This means it is critical that the pump beam be collimated through the delay stages so the spot size does not change at the sample as a function of optical path length. The changing pump intensity would create a systematic error as a function of delay time.

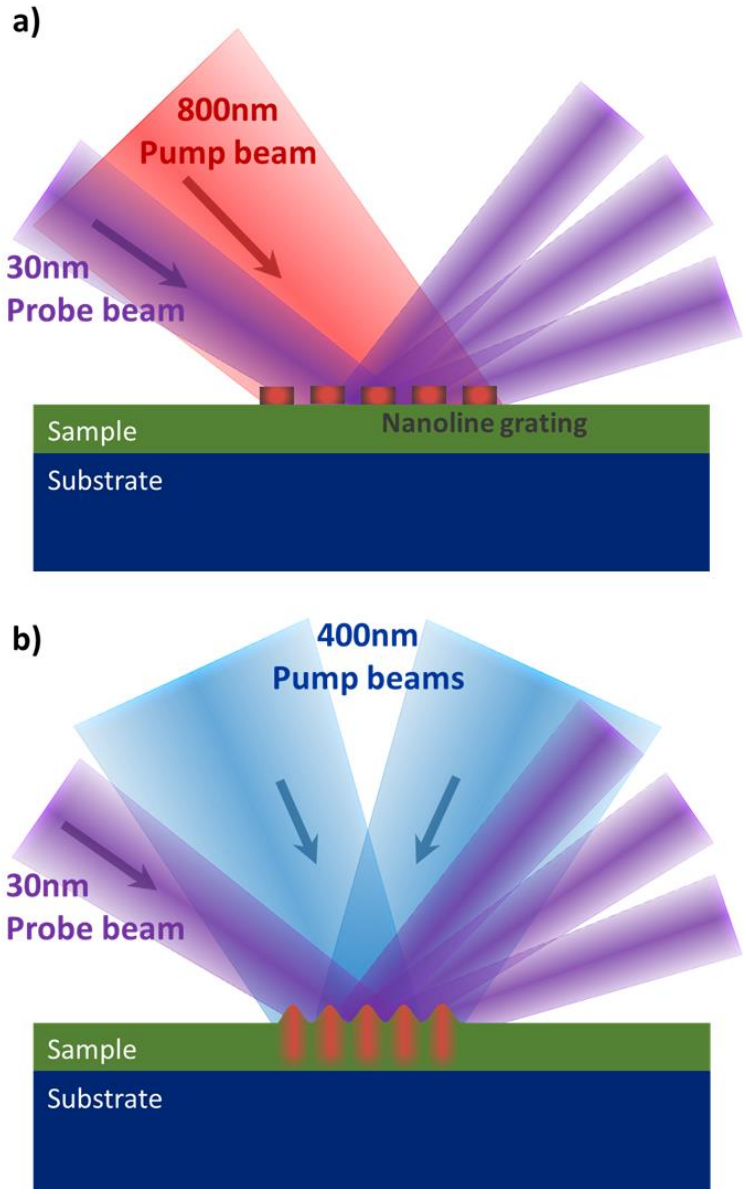

Figure 2.3: Nanograting and optical transient grating excitations. a) For most of our samples, gratings of periodic nanolines are used to transduce thermal and acoustic dynamics, upon optical excitation. b) More recently, we have added an optical transient grating capability. Here, we interfere two pump beams to directly sinusoidally excite an absorbing sample at the micron scale. In both (a) and (b), we probe the surface deformation by diffracting a coherent EUV probe from the sample, into a camera.

For the probe line, the first step is to fully compress the pulses to 30fs, again using chirped mirrors. Part of the weak leak-through from these mirrors is collected and used as feedback for an active beam pointing stabilization system. After compression, the probe pulses enter a vacuum system before performing HHG. This is necessary because EUV photons are strongly absorbed in air. The intense near-IR probe

pulses drive high harmonics in an argon-filled, 150μm inner diameter waveguide. The generated harmonics extend up to about a 27nm cutoff wavelength and lie under a 10fs envelope. Next, the harmonic pulses and driving laser reflect together from a toroidal mirror that focuses the diverging beam toward the sample. Two 200nm thick aluminum filters then remove the residual driving laser and the harmonics longer than about 37nm wavelength. This leaves a comb of about 5 harmonics, from the 21^{st} to the 29^{th}, with the 25^{th} being dominant, impinging on the sample. The EUV probe beam diffracts in a reflection geometry from the optically pumped sample, either from periodic nanostructure transducers, or from periodic interference fringes of the pump light. A charge coupled device (CCD) camera collects the diffracted beams with an additional two 200nm thick aluminum filters that prevent pump light from reaching the camera.

These two processes of high harmonic generation and dynamic diffraction are what differentiate our technique from optical techniques, such as Brillouin light scattering or time domain thermoreflectance. I will describe each of our unique processes in more detail in the following two sections.

2.2.1 High Harmonic Generation

The field of high harmonic generation (HHG) is at this point both well established and constantly growing [33, 34]. I will limit the discussion here to summarizing what is important to our thermal and acoustic experiments [35, 36]. The basics of HHG include two processes – the single-atom yield of EUV photons, and the macroscopic phase matching of multiple atoms' emissions to obtain a coherent beam.

The single-atom picture of HHG may be most simply understood in the three-step model, shown in Fig. 2.4(a) [37, 38]. In this semiclassical model, we first consider an electron bound in the Coulomb potential of its parent atom. We then place this atom in a high intensity laser beam. Provided the intensity is high enough, the oscillating electric field of the laser is comparable to the Coulomb potential of the atom, and it depresses one side upon linear superposition. This allows the electron to tunnel ionize from its parent atom (step 1). The electron is then accelerated in the laser field, gaining extra momentum (step 2). As the laser field oscillates, it next reverses and begins to accelerate the electron back towards its parent ion. There is some probability then that the electron will recombine with the ion, emitting its excess energy in the form

of an EUV photon (step 3). Thus, every half-cycle of the driving laser, there is a burst of EUV photons emitted from the irradiated atoms, as shown in Fig. 2.4(c).

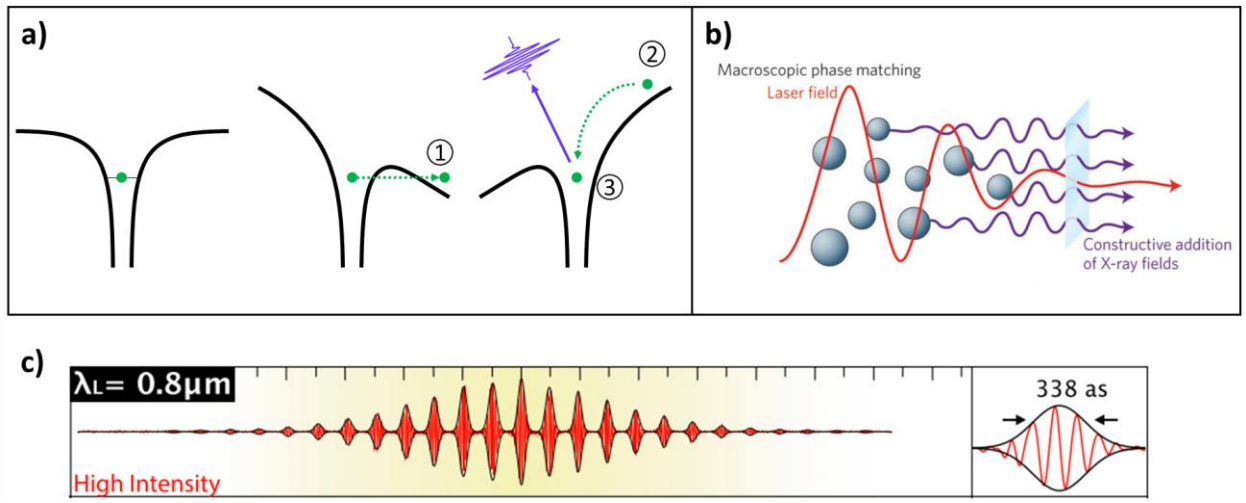

Figure 2.4: High harmonic generation. a) The three-step model for HHG. For an electron in its ground state in the Coulomb potential (left), the electric field of a sufficiently intense laser will distort the potential enough for the electron to tunnel ionize (1). The electron then accelerates in the field (2) and returns to its parent ion when the oscillating electric field reverses. The electron then recombines (3) and emits its excess energy as an EUV photon. b) Phase matching yields a macroscopic, coherent beam. This is achieved by tuning the gas pressure to match the velocities of the driving IR laser and the EUV beam being generated. c) EUV photons are emitted in attosecond bursts every half cycle of the driving laser. These bursts lie under a ~10fs envelope, defined by the phase matching window. Panel (b) is from [34], and panel (c) is from [39].

The next step is to phase match the photons emitted from each atom to obtain a macroscopic, coherent EUV beam, as shown in Fig. 2.4(b) [36]. If the phase is uncontrolled, each EUV photon will in general be out of phase, resulting in destructive interference and negligible output beam intensity. To avoid this, the phase velocities of both the HHG and driving laser must be matched in the HHG medium. The phase velocity of the EUV will remain largely unaffected, as the EUV index of refraction remains very close to 1 for all materials. For the driving laser, however, the phase velocity is reduced by neutral atoms, but it is increased by the plasma of ionized atoms and the waveguide. Thus, by tuning the pressure of gas in the waveguide, the atom, plasma, and waveguide contributions to the driving laser phase velocity can be balanced at a critical ionization percentage to match the EUV phase velocity. For our case of generating high harmonics in argon with a 780nm driver, we obtain an EUV beam up to the 29^{th} harmonic with about 1nJ of pulse energy.

Though the energy of our EUV pulses is relatively low, when the coherent beam is focused, there is enough intensity to cause some experimental challenges. The short-wavelength EUV photons have sufficient energy to break apart long hydrocarbon chains. No matter how good a vacuum system is, it is impossible to completely avoid hydrocarbon contamination. Thus, at the sample and at any other location the EUV beam is focused to a sufficient intensity, a large number of carbon radicals will be generated, which then deposit on the sample as an amorphous, hydrogenated carbon film [40]. As this process is relatively slow, measurements may be made before a significant carbon layer is developed, but in general carbon deposition must be considered for any experiment involving EUV.

Using an HHG probe has many distinct benefits for our measurements. First, with 30nm wavelength and 10fs pulse duration, HHG is ideally suited to measure the ultrafast repeatable dynamics of nanoscale systems. Second, because the EUV probe is generated from the same near-IR laser as the pump, there is intrinsic timing stability in our pump-probe measurements. Also, by using EUV photon energies that are away from core electron resonances in our sample materials, our probe is largely insensitive to the electron temperature. Rather, we measure the surface deformation of the lattice, down to picometer-scale sensitivity, without hot electron effects dominating the signal at early times [41].

2.2.2 Diffraction Measurements

Diffraction can be thought of as the interference of light coming from two different points on an object, with locally varying amplitude or phase. For example, in the familiar double slit experiment, rays from each of the two slits have different relative phases at the image plane, yielding the classic interference fringes. In the far field, under the Born approximation, the diffracted light at the image plane is simply a Fourier transform of the light at the exit surface of the object. This means that Fourier intuition may be applied to diffraction, e.g. more closely spaced slits produce more widely spaced interference fringes. For our modeling, we improve the accuracy of the approximation by adding Fresnel phases ($e^{ix_{i,o}^2\pi/\lambda z}$ in 1D, for wavelength, λ, propagating a distance, z) at both the object (x_o) and image (x_i) planes, but it is still based on a Fourier transform.

For the majority of our measurements, we diffract our probe from nickel nanoline gratings fabricated on the surface of our flat sample by collaborators. Because these nanolines form a 1D diffraction grating, I will only discuss 1D diffraction here. This process is, however, generalizable to 2D and 3D diffraction in principle, and we have previously measured 2D diffractive objects [42]. We use nickel for the nanoline material because of its good absorption of IR light and large coefficient of thermal expansion; however, other metals may also be used. The height of the nanolines is ~10nm, which is thin enough for the nanolines to be uniformly heated by the pump laser, but thick enough to maximize our diffraction signal. To maximize signal, both the static diffraction, and the change in diffraction (slope as a function of grating height) must be large. This is because our approach measures small, dynamic changes to the grating height, as described below.

The gratings diffract the EUV beam by periodically modulating both its amplitude (differing reflectivity from the substrate) and phase (differing path lengths for EUV rays reflected from the top of the nanolines and EUV rays reflected from the sample surface). As each grating consists of a square wave with a particular period and duty cycle, its diffraction pattern (Fourier transform) consists of a discrete series of diffracted orders, as well as the directly reflected beam, or DC peak. Because there are up to 5 harmonic wavelengths present in our EUV beam, each diffracted order consists of multiple peaks, as longer wavelengths diffract to wider angles, for a given diffracted order. Next, we launch thermal and acoustic dynamics in the sample by preferential absorption of IR pump light in the metallic nanolines.

Upon ultrafast laser pumping, the metallic nanolines impulsively thermally expand within 3-10ps, launching acoustic waves in the substrate down to a temporal period roughly equal to twice the thermal expansion time. Both the thermal expansion and the acoustic waves change the amplitude of the phase grating by changing the nanoline height and/or the substrate surface profile, as illustrated in Fig. 2.5(a). This changes the diffraction efficiency of the grating, which I'm defining here to be the ratio of power in the diffracted orders versus that in the DC beam. For example, if the phase difference between uniformly expanded gratings and the substrate is exactly 2π (path length difference of λ), then there will be no diffraction from the phase grating. There is in general a small change in the amplitude grating, as thermal

expansion slightly changes the material density and thus its reflectivity, but our signal is dominated by the change in the phase grating coming from changes in the surface profile [41].

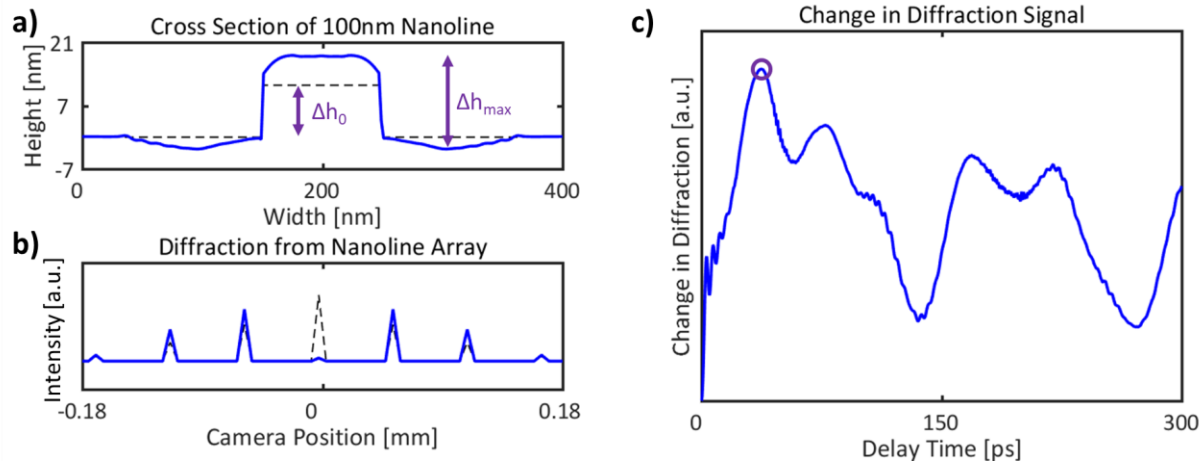

Figure 2.5: Dynamic diffraction measurements. This is a COMSOL simulation of a 100nm linewidth, 400nm period grating on fused silica. a) Viewed in cross section, we see both the thermal expansion of the nanoline and acoustic waves in the line and substrate change the surface profile (solid versus dotted lines). Relative changes in nanoline-substrate heights (purple arrows) change the amplitude of the phase grating. b) Changing the phase grating amplitude changes the diffraction efficiency compared to the unpumped pattern (dotted line). c) By subtracting the change in the DC peak from the changes in diffracted orders, we get a temporal signal showing thermal and acoustic dynamics. The purple circle marks the point of maximal expansion, corresponding to panels (a) and (b). Changes are amplified for clarity, 50x in (a) and 25x in (b). More details on COMSOL simulations are given in Chapters 3, 4, and the Appendix.

The experimental signal is the relative change in diffraction efficiency upon laser pumping. As thermal expansion and acoustic waves change the amplitude of the phase grating, the relative intensities of the DC beam and the diffracted orders change with the diffraction efficiency, as shown in Fig. 2.5(b). To conserve energy, all of the intensity that is gained in the diffracted orders must be taken from the DC beam, assuming no change in absorption or transmission of the EUV probe. This means that dynamic changes in the DC intensity encode all the information from each diffracted order, with an opposite sign. Analyzing the DC beam thus allows us to measure dynamics down to the diffraction limit of our probe, even though we have poor numerical aperture (NA) with our camera. Changes in the diffracted orders' intensities, on the other hand, each contain partial information about the dynamics of the system. In the case of surface acoustic waves, where the spectrum of SAWs launched is the same as the spectrum of spatial frequencies that define the grating's diffraction, each diffracted order contains the frequency of each respective SAW.

To build a change in diffraction efficiency signal, we first take the difference between pumped and unpumped diffraction patterns and normalize by the integrated unpumped diffraction pattern. This normalization is performed at every delay time to reduce the influence of probe intensity fluctuations on our measurement. Next, we subtract the normalized difference in the DC peak from that of the diffracted peaks. In this way, we obtain twice the signal of the DC peak alone. This final value for the change in diffraction efficiency as a function of delay time is the signal shown in Fig. 2.5(c). Note that we currently subtract an offset from this temporal signal so that the pre-time zero (the time when dynamics begin) points average to zero. We should also subtract the dark-current baseline counts on the camera from our raw diffraction patterns, as this pedestal only reduces the amplitude of our signal. This has not yet been implemented, however. To reduce the noise in our final signal, we follow a specific experimental routine that I describe now in more detail.

Our signal begins with CCD-recorded diffraction patterns, fully vertically binned on-chip to produce a single count value for each of our 1024 pixels (chip width). These diffraction patterns alternate between pumped and unpumped diffraction (via manual blocking of the pump beam) with each camera exposure. The camera integrates over some number of pulses, depending on the selected exposure time. At a given pump-probe delay time (stage position), we further average over several repeated exposures of both pumped and unpumped diffraction. After recording average diffraction patterns at each delay time, we repeat the entire process to obtain at least three "loops" across the full experimental time window. These loops are averaged together to obtain a final "scan" of both pumped and unpumped diffraction patterns as a function of delay time. By averaging over both exposures and loops, we reduce the influence of fluctuations and drift in our probe intensity on both short and long timescales. Note that each loop is currently saved as a combination of each preceding loop. To "unwrap" a loop to contain only the diffraction measured during that loop, use the following formula:

$$D_{unwrapped} = n_{current} D_{current} - n_{previous} D_{previous},$$

where D is the pixel by time matrix of a scan's diffraction patterns, and n is the loop number. This process is done separately for the pumped and unpumped measurements. In the future, it might be possible to

normalize each pair of pumped and unpumped diffraction patterns to the unpumped total intensity, for each pair of exposures in the set of averages. This would allow us to remove the influence of fluctuations on the scale of twice the exposure time (generally tens of milliseconds), which is faster than we currently do.

Finally, I will now discuss the dynamics present in our experimentally measured traces, as shown in Fig. 2.6. First, there are the desired, repeatable dynamics illustrated in Fig. 2.6(a)-(c). At timescales from 10ps to 8ns, depending on grating linewidth and period, we observe the oscillations of the multiple excited SAWs, which change the relative heights of both the nanolines and the substrate in between lines. These oscillations are superimposed on a multiexponential thermal decay, where the expanded height of the nanolines relaxes back towards the unpumped profile as heat is transferred into the substrate. At sub-100ps timescales, depending on sample thickness and mechanical properties, we can observe discrete bumps in the signal. These bumps are echoes of longitudinal acoustic waves that are launched downward by the impulsive nanoline expansion and reflected back to the surface by any buried interfaces, e.g. the interface between an ultrathin film sample and its substrate. At sub-10ps timescales, we can observe the longitudinal acoustic resonance of the nanoline itself, as it rings briefly upon impulsive expansion. The shortest timescale material response we have observed is a low-amplitude ultrafast peak at ~130fs (observed in the 30nm metalattice discussed in Chapter 5 and thin film #148 discussed in Chapter 4). Though our signal is largely insensitive to electron dynamics, I believe with sufficient signal to noise ratio (as obtained for these measurements) we can distinguish a small hot electron signal. The other potential explanation for a material response this fast would be magnetic dynamics, as the nanolines are made of nickel. Because the ultrafast peak is very small, we have not tried to analyze it further, thus far. I discuss the analysis of the other decays and oscillations in the signal for thermal and elastic properties in Chapters 3 and 4, respectively.

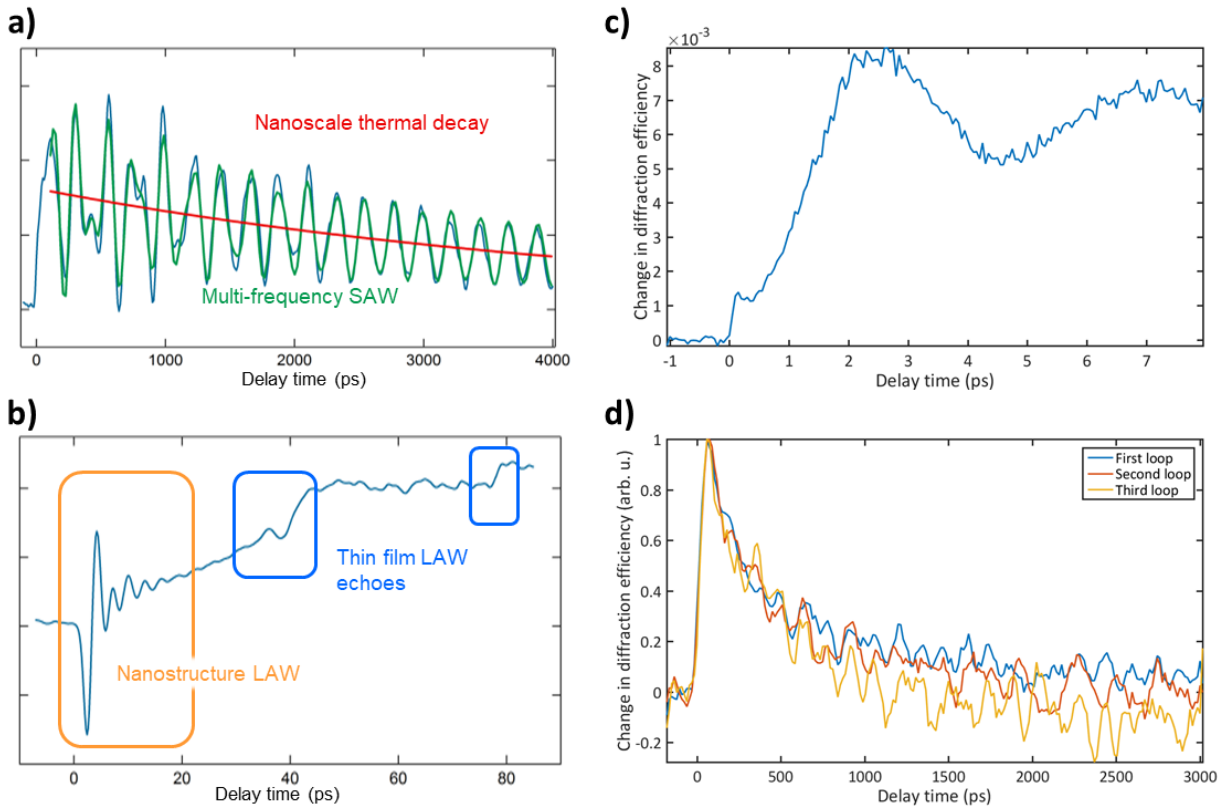

Figure 2.6: Experimentally measured diffraction signals. a) At long timescales, we observe the multifrequency SAWs launched by the gratings, and their slow thermal decay as heat is transferred into the substrate. We also observe the decay of the acoustic wave amplitude as SAWs are scattered in the sample. b) At shorter timescales, we observe the longitudinal acoustic resonance of the nanolines themselves, and the echo of longitudinal acoustic pulses reflected from buried interfaces. c) At ~130fs after the start of thermal expansion, we observe a low-amplitude peak, which I attribute to hot electrons. d) When there is sample damage occurring during a measurement, one good indication is the normalized loops of a scan not exhibiting identical dynamics, as shown here. Panels (a) and (b) are from [22]. Panel (c) is from a 100nm linewidth, 400nm period grating on a 30nm silicon metalattice. Panel (d) is from a 200nm linewidth, 800nm period grating on sapphire.

In addition to the repeatable dynamics that reveal intrinsic sample properties, we also analyze our measured signals for non-repeatable dynamics that indicate sample damage. For the most obvious check, we monitor the static diffraction pattern while we are taking data. If we observe the DC peak steadily grow while the diffracted orders shrink over the course of a scan (as a function of real time, not delay stage position), this indicates we are ablating our metallic nanolines with our pump beam, constantly reducing their height and burning the sample. If we observe both the DC and diffracted peaks either grow or shrink together, this does not necessarily indicate sample damage, and it is more likely a result of drifting probe intensity or carbon deposition. The next check is to compare the signal in each loop of a scan, normalized

to its maximum. If the dynamics are not the same from loop to loop, as shown in Fig. 2.6(d), this can indicate sample damage. For the measurements shown in Fig. 2.6(d), the gratings were later confirmed via atomic force microscopy to have been ablated to a lower height. Note that normalization is required as a mere loss of signal amplitude does not necessarily indicate sample damage. Degrading probe stability or carbon deposition can each reduce signal amplitude over the course of a scan. Additionally, if the signal is low enough that many loops must be averaged to see signal in the scan, then the loop-to-loop comparison would not be a good test for sample damage. A more rigorous test is to compare the unpumped diffraction patterns from the beginning and end (in real time) of a scan. This is done extensively for the optical TG data described in Chapter 5, where the appearance of TG diffracted orders in the unpumped diffraction indicates the TG pattern has been burned into the sample. Finally, we also check for signatures of pulse accumulation during our measurements.

Our analysis assumes all dynamics have fully relaxed before the next pump pulse arrives, which is generally a good assumption for few-kHz repetition rates. However for some systems, such as suspended membranes, the sample might not be fully cooled before the next pump pulse arrives. In this case, the system reaches an elevated temperature steady-state background once the pump pulses have been accumulating for long enough in real time. To check for this behavior, we manually block the pump beam with a card, and observe the diffraction pattern and signal upon unblocking the pump beam before time zero. If the pre-time zero diffraction or signal change, this indicates there is pulse accumulation as there are still dynamics occurring before the next pump pulse arrives.

2.3 Upgrades to the Experiment

Now that I have described the experimental methodology in some detail, I will describe the main additions to the apparatus made in the last five years. I will first describe the optical TG setup, followed by the implementation of an optical chopper in the pump beam, and lastly the mitigation of nonlinear effects during IR beam transport.

2.3.1 Optical Transient Grating Setup

Transient gratings are an elegant approach to the study of material dynamics. By interfering two single-wavelength beams at a defined crossing angle, this method produces pure sinusoidal excitations in a completely non-contact modality [29]. The single-frequency excitation greatly simplifies the interpretation and analysis of both thermal and acoustic signals, and the avoidance of transducer fabrication allows a greater variety of samples to be studied, including liquids.

By simple geometric consideration of the wavevectors of the two pump beams and the resulting transient grating, one may derive the transient grating period, Λ, as a function of the pump wavelength, λ, and the half crossing angle, θ, as

$$\Lambda = \frac{\lambda}{2 \sin \theta}.$$

It is clear that the smallest TG period possible is half the pump wavelength. However, this requires counter-propagating pump beams, which is generally impractical for exciting real materials. Thus, most optical TG periods are confined to the micron scale in practice, with the limit being around 500nm [43]. While these optical TG periods do not reach the deep nanoscale accessible by EUV probes, we have implemented an optical TG setup to (a) enable the measurement of systems where transducer fabrication is prohibitive, and to (b) serve as a stepping stone to all-EUV TG using HHG beams.

Our optical TG setup is similar to that of Ref. [44], and it was first demonstrated in 2006 in our lab using an HHG probe [45]. The 2006 setup was dismantled, however, so I have reimplemented it as a modular pumping setup on our existing EUV nanometrology apparatus. In the optical TG setup, our 780nm pump beam is first up-converted to 390nm by second harmonic generation (SHG) in a beta barium borate (BBO) crystal. The second harmonic beam is preferentially reflected by two dielectric mirrors and then passes through a transmission phase mask, optimized to send most of the beam intensity into the +1 and -1 diffracted orders. Several phase masks are etched into the same transmissive optic, with a series of corresponding TG periods: 2, 2.5, 3.2, 4, 5, 7, 9, 13, 20, 30, 40, 60, 90, and 130μm. This allows for rapid changing of TG periods by translation of the phase mask optic from one mask to the next. However, due to

spherical aberration in subsequent lenses, changing phase masks will slightly change the position of the overlap plane (the required sample position).

We next collect the beams with a 4f imaging system of two 12.5cm focal length (f), 2” diameter lenses, where the phase mask−first lens separation is 1f, the inter-lens separation is 2f, and the second lens−sample separation is 1f. This geometry images the phase mask period onto the sample, with a pulse front tilt to optimize maximal interference fringes [44]. Note that ideal TG excitation requires only two beams to be crossed at the sample, but the phase mask does not ideally produce only the ±1 diffracted orders. Thus, we use spatial filters to block all beams reflected and transmitted from the phase mask, except for the two desired diffracted orders. This also blocks any residual 780nm light not filtered by the two dielectric mirrors. See Fig. 2.7 for a schematic of the optical TG setup.

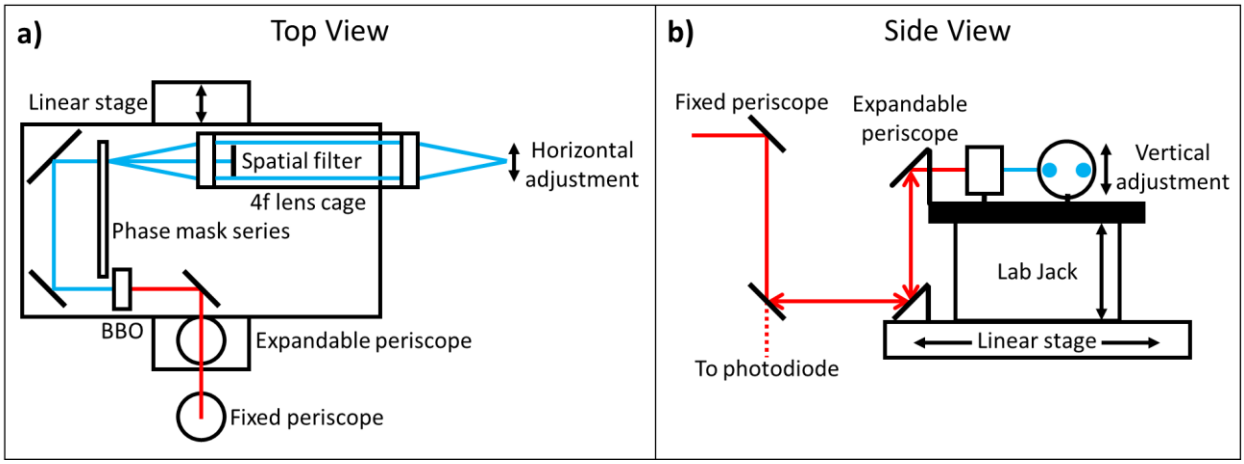

Figure 2.7: The modular optical TG setup. a) Top view of the setup. By adjusting the linear stage beneath the TG breadboard, the horizontal position of the TG pump spot on the sample is adjusted. b) Side view of the setup. By adjusting the lab jack beneath the TG breadboard, the vertical position of the TG pump spot on the sample is adjusted. Note that the linear stage adjusts the path length between the two periscopes, and the lab jack adjusts the path length in an expandable periscope.

As shown in Fig. 2.7, the setup is slightly more complicated than just the 4f imaging system used historically. This is because we must spatially overlap the pump and probe beams at the sample, but the EUV optics are not adjustable to tune the probe position. Instead, we must adjust the TG pump position to overlap it with the probe. To do this, we move the entire setup described above on a breadboard with horizontal and vertical adjustment via manual stages. Adjusting these manual stages slightly changes the

total path length of the pump, relative to the probe, but this may be corrected using the delay stages earlier in the pump line. To ensure the alignment of the setup is not disrupted upon adjustment of the stages beneath the TG breadboard, the horizontal and vertical beam path segments that change length (marked in Fig. 2.7(b) by arrows) must be aligned to the stage axes. Use the following procedure to ensure this alignment.

First, place a target in the position of the bottom mirror of the expandable periscope. Move the horizontal linear stage to either end of its travel. If the pump beam changes position on the target, adjust the two fixed periscope mirrors until the beam no longer moves on the target, and it is aligned to the linear stage axis. Next, replace the mirror in the bottom of the expandable periscope and place a target after the expandable periscope, on the TG breadboard. Move the vertical lab jack through its travel range and check if the beam moves on the target. If it does, adjust the bottom periscope mirror to align the beam to the lab jack axis. Note that single mirror alignment will set the beam pointing, but not its position. Provided the initial placement of the mirrors is close enough to the ideal, differences in beam position may be corrected by the subsequent mirrors. It is also important to check the beam polarization when adjusting periscope alignment. If a periscope is not aligned linearly, it will rotate the pump beam polarization. Because both periscopes are present in the pump line whether using nanograting or TG excitation approaches, polarization variation from the periscopes can reduce the nanograting pumping efficiency. Ideal absorption occurs when pump polarization is aligned to the grating line direction. Polarization rotation may be simply checked using a reference polarizer on the TG breadboard and corrected using the half waveplate earlier in the pump line.

After aligning the periscopes and expandable beam path segments, the rest of the TG setup must be aligned. The focus of the pump beam, set by a ±1m lens pair earlier in the pump line, should be set at the BBO crystal for maximum conversion efficiency. The BBO tip, tilt, and rotation must also be adjusted to optimize phase matching. Note that pushing the focus of the beam too far from the optical chopper described in the next section will reduce the number of pulses that can be cleanly passed per exposure as the beam will be too large at the chopper position. The two dielectric mirrors after the BBO are next used to align the beam to the 4f lens system.

The 4f lens system is mounted in an optical cage. To align the beam to it, we first remove the phase mask and first 4f lens, and block the beam from entering the measurement chamber. We place an empty lens mount in the lens's place to maintain stability of the optical cage. Using the two dielectric mirrors and a 2" cage target, we align the beam to the cage axis. We then reinsert the lens at the previously-marked position for 4f geometry on the cage and replace the phase mask in its mount. To check that the phase mask is placed at the proper 4f condition, we use the cage target to verify the ±1 diffracted orders are parallel to one another between the two lenses. To correct the diffracted orders getting closer together (farther apart) as they propagate between the lenses, we move the phase mask slightly closer to (further from) the first lens. Finally, the sample must be placed in the TG overlap plane. Provided the initial placement of the TG breadboard and optical cage is as close as possible to the measurement chamber, the distances should already be close to correct, and the final adjustment of the sample may be done by the long in-vacuum sample stage, which should be set roughly in line with the optical cage axis.

As a part of the optical TG build, I also designed a new measurement chamber in collaboration with JILA machinists, who fabricated the final chamber. Computer-aided design (CAD) drawings of the chamber are shown in Fig. 2.8(a-b). The chamber is shaped like a rectangle with one clipped corner, which houses a square sapphire window that admits the TG beams, visible in Fig. 2.8(d). This design allows the optical cage outside the chamber to approach as close to the sample as possible, without intersecting with the CCD camera placed in the TG measurement position, shown in Fig. 2.8(d). The three vacuum flanges on the chamber shown in Fig. 2.8(a) are currently used for the two electrical feedthroughs needed by the in-vacuum sample stages, and a dual-range vacuum gauge. The larger flange is placed in line with the beam-entrance flange to enable transmission experiments by mounting the CCD camera on this flange. This has not been attempted yet. Also note that the cathode of the vacuum gauge is known to sputter in argon-containing environments. Over the years of use, we have observed discoloration of the chamber near the gauge, and loss of gauge accuracy, which likely indicate the residual argon from HHG is sputtering the cathode.

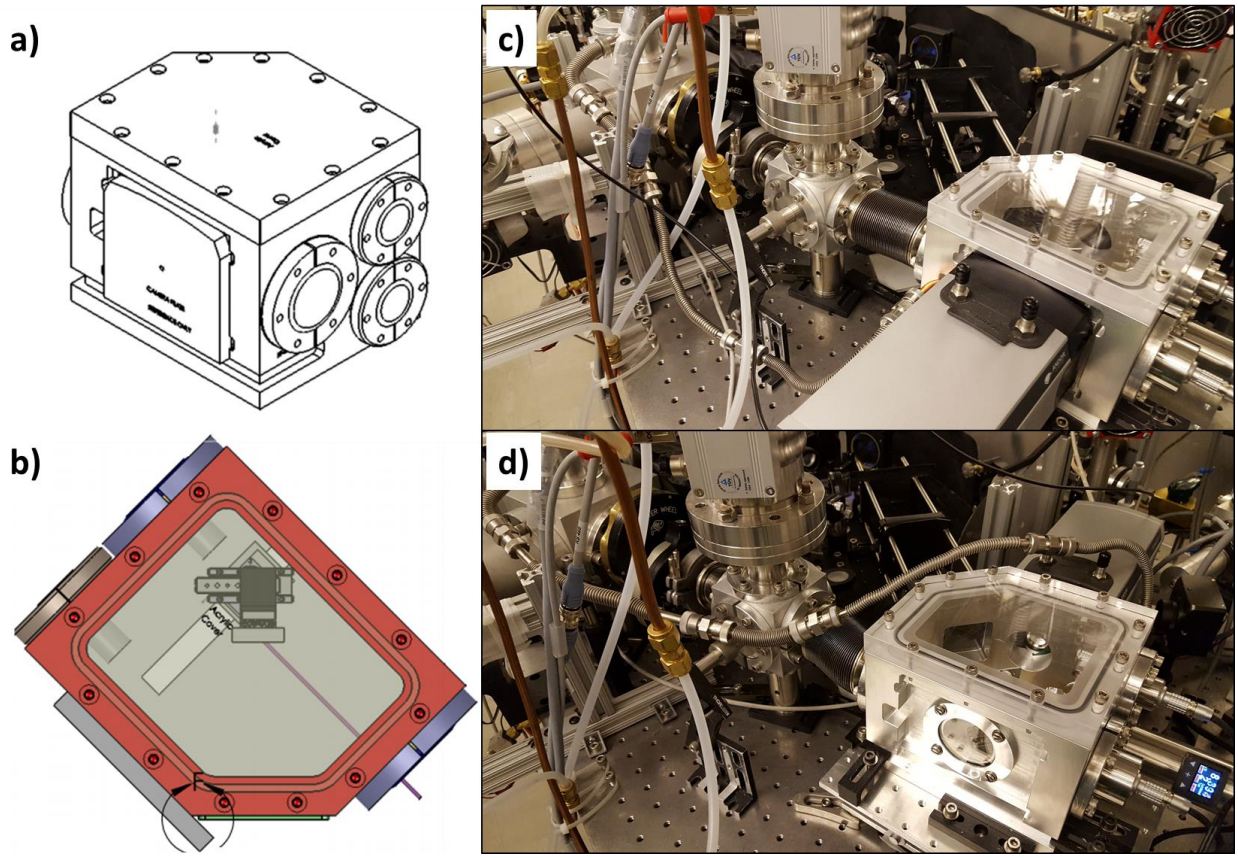

Figure 2.8: New vacuum chamber for TG and nanograting measurements. a) CAD drawing of the chamber showing the vacuum flanges on the back, and the inset pocket in the wall that decreases camera-sample distances when measuring nanogratings. The groove along the bottom of the chamber is used to clamp it in position. b) Top view of the chamber, showing the in-vacuum stages. The circle marks how close the camera filters (grey rectangle) come to the TG window (green rectangle). c) Camera and chamber positions for nanograting measurements. d) Camera and chamber positions for TG measurements. Note the chamber is clamped to a platform that rests on two manual stages used to adjust the chamber position.

Also visible in Fig. 2.8(b) is a CAD drawing of the in-vacuum sample stages purchased as a part of the optical TG build. This stage assembly has encoded xy-translation to move the measurement position to different sample locations, with nanoscale precision. It also has un-encoded stages for sample rotation (rotation axis points out of the page in Fig. 2.8(b)) and long-distance translation. When performing TG measurements, this long stage should be rotated from the position shown in Fig. 2.8(b) to be perpendicular to the TG entrance window. This allows for easy placement of the sample surface at the TG interference plane. The rotation and long-translation stages are further used when switching between TG measurements and nanograting measurements, which only require uniform, round beam pumping.

To switch between round beam (RB) and TG pumping, the system was made to be relatively modular. Starting from the TG pumping configuration, shown in Fig. 2.8(d), vent the vacuum system and flip the CCD and its filters from the far side of the chamber to the near side of the chamber, as shown in Fig. 2.8(c). Remove the middle segment of the string of thin bellows connected to the CCD filters. The extra length is not needed with the camera in the RB position. Remove the block holding the chamber platform in place and adjust the linear stage beneath it, parallel to the camera axis, to the furthest pencil mark. This will place the incident probe beam as close to the near side of the chamber as possible. This, combined with the camera inset in the chamber wall, increases the numerical aperture (NA) of the RB pumping configuration, which is important for measuring nanoscale gratings, rather than micron-scale TG. Reposition the in-vacuum sample stage assembly from its position along the optical cage axis to instead be parallel to the camera axis. Place the long stage on the row of bolt holes that places the sample holder in line with the center of the CCD window. Rotate the rotation stage 90° so that the probe reflection from the sample will go towards the new camera position. The long stage may now be used to adjust the sample-camera distance, and it should be set such that the probe beam strikes the center of the sample. Note that the full range of the sample's x-stage may not be accessible without striking the chamber wall, when the sample is very close to the camera. Striking the wall should be avoided, so care must be used when adjusting the x-stage.

Next align the pump and probe lines for RB pumping. Start with aligning a weak IR beam through the probe line, into the chamber. The linear stage beneath the chamber platform that is aligned along the probe line may be adjusted to ensure the focus of the toroidal mirror lands at the sample plane. This probe line reference beam will be important for aligning the RB pump line. To align the RB pump, begin by removing the first mirror on the TG breadboard (just before the BBO) and the optical cage so that the beam can freely exit the expandable periscope and travel across the breadboard. Make sure to mark the cage and mirror positions for easy replacement when switching back to TG pumping. Next place a 2" silver mirror on the optical table just past the TG setup. Using the silver mirror's position and pointing, adjust the pump beam to enter the in-vacuum mirror chamber (connected by large bellows to the measurement chamber,

shown in Fig. 2.8(c)) and propagate nearly co-linearly with the probe, crossing at the sample plane. Do not adjust the top mirror of the expandable periscope as this will make it more difficult to switch back to TG pumping. To switch from RB pumping back to TG pumping, exactly reverse the process described above, and follow the TG alignment procedure instead of the RB alignment procedure just described. Note that the periscopes should not have to be realigned every time.

2.3.2 Synchronized Chopper as a Pump Shutter

To perform our pump-probe technique, we require a series of pump-on and pump-off measurements at each delay time. This means that the pump beam must be periodically blocked to measure the un-pumped sample profile via EUV diffraction. In the past, we have done this using a mechanical shutter, set to certain exposure and cycle times. When the shutter wore out, however, we took the opportunity to upgrade it to an optical chopper. A chopper consists of a wheel, as shown in Fig. 2.9, rotating at a set frequency and with a set number of slots. As the slots rotate past the laser beam, they imprint their specific frequency on the beam by repeatedly blocking and unblocking it. This is the same result as a simple mechanical shutter, but the optical chopper has distinct advantages. First, its frequency may be locked to the repetition rate of the laser, enabling the selection of a specific numbers of pulses, repeatably, in each diffraction measurement. Second, the rotating wheel of the chopper is able to close across the beam faster than a mechanical shutter. This enables "clean chopping" where the beam is blocked between laser pulses such that the first pulse is fully passed, and the next pulse fully blocked. In principle, our chopper can go down to single pulse exposures. The upper and lower bounds on selecting exposure lengths for a given wheel are the maximum physical rotation frequency of the wheel (106.5Hz), and when jitter and the loss of clean chopping become too significant at slow wheel speeds, respectively.

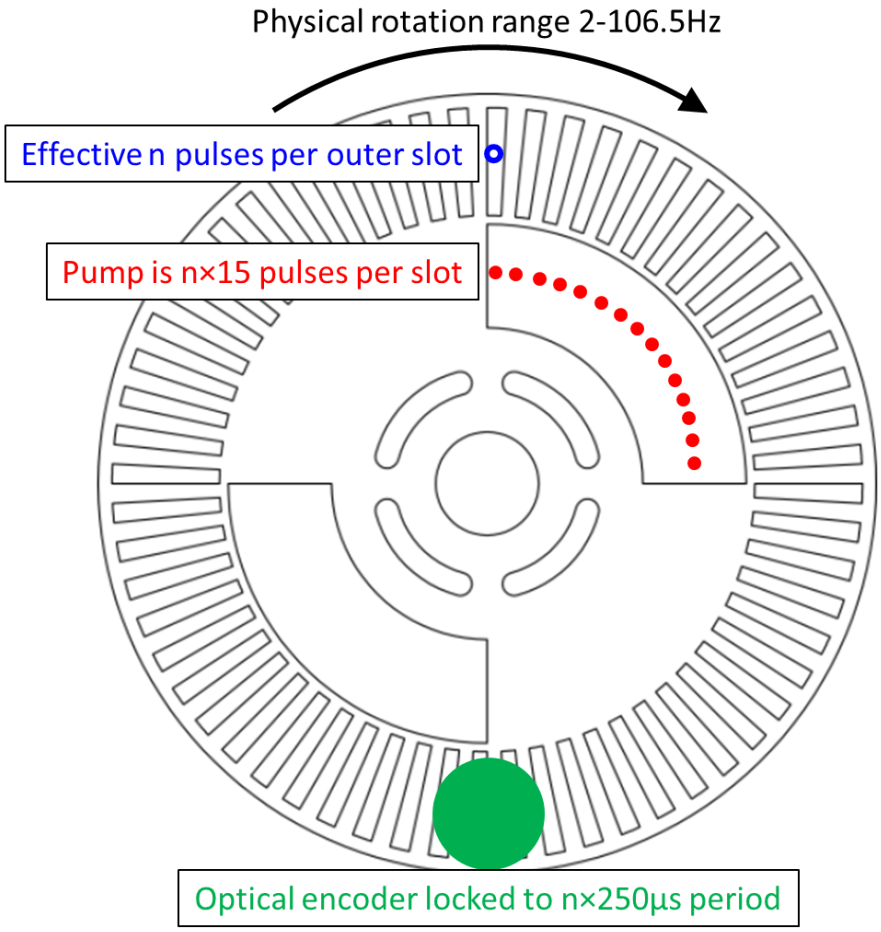

Figure 2.9: Optical chopper as a beam shutter. As the chopper wheel rotates at a given physical frequency, it locks to a frequency set by the outer number of slots, but it chops the beam at a frequency determined by the inner number of slots. We have a variety of chopper wheels, but the most commonly used one is shown here: 60 outer slots and 2 inner slots. When synchronizing the chopper to the 4kHz laser repetition rate, the outer frequency may be locked to multiples of the 250µs pulse period. This then produces multiples of 15 pulse exposures in the inner slots, for this wheel. The number of pulses per exposure may be further adjusted using the harmonic/subharmonic function of the chopper controller.

We synchronize the chopper to the laser repetition rate using the reference trigger output signal from the amplifier controller (one pulse every 250µs). We pass the reference trigger signal through a DG 535 digital delay/pulse generator, or delay box, which allows multiples of 250µs pulse periods to then be sent as a trigger signal to the chopper. To select the pulse period, we set the falling edge of the delay box's output pulse to the desired multiple of 250µs and the rising edge to be 1.5µs earlier. Note that the chopper must be set to trigger on the falling edge for this to work properly. This input signal to the chopper sets its

fundamental frequency, though more chopping frequencies are obtained using the harmonic and subharmonic functions of the chopper controller.

Once the chopper frequency is set, the camera must be synchronized to it such that the camera exposures line up precisely with when the pump beam is unblocked or blocked, as the case may be. The relative timings of pump, probe, chopper, and camera exposure are shown schematically in Fig. 2.10. To start the camera exposure exactly when pump pulses are unblocked, we trigger the camera from the pump beam after the chopper. We collect the low-power leak-though from the bottom mirror of the fixed periscope in the TG setup (see Fig. 2.7) on a photodiode for this purpose. The analog pulses from the photodiode cannot directly trigger the camera, however. The 4ns response of the photodiode is too fast for the camera, which requires a transistor–transistor logic (TTL) trigger. Thus, I have built an analog to TTL converter circuit to go between the photodiode and the camera.

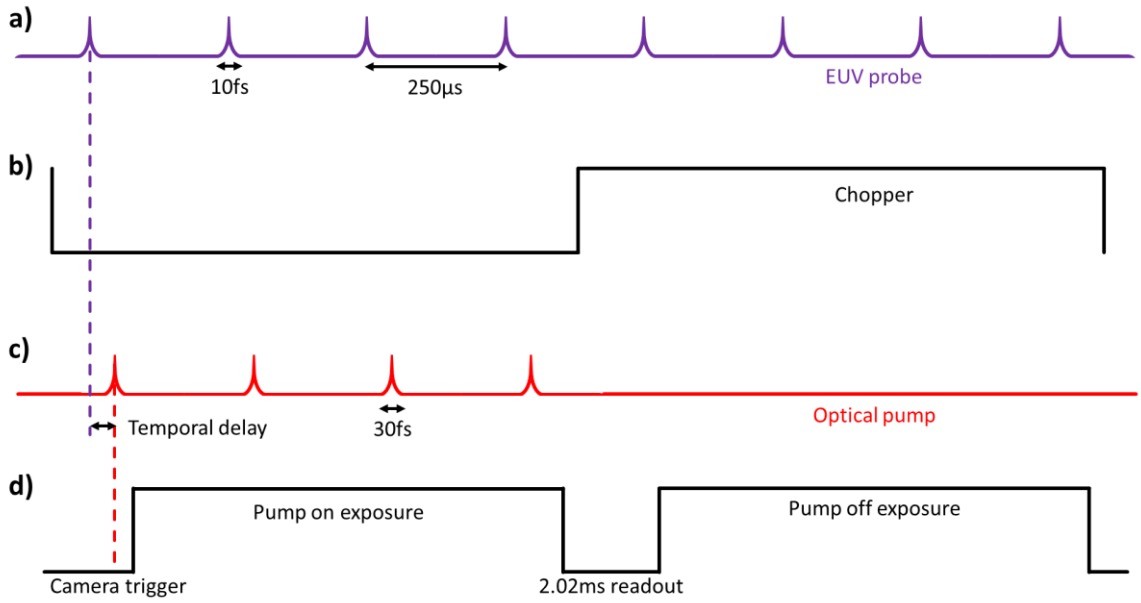

Figure 2.10: Timing schematic of the experiment. The chopper periodically blocks the pump beam, which is temporally delayed from the probe beam, according to the mechanical stage position. The camera records the probe pulses when the pump beam is both blocked and unblocked to obtain unpumped and pumped diffraction patterns, respectively, at each delay time. The length of each segment in the schematic is not quantitative, as several pulses are skipped during the 2.02ms camera readout, and an unknown number of pulses are skipped between the triggering of the camera and the beginning of the camera exposure.

First, we must prepare the photodiode's pulses for the circuit using analog means. A 35MHz low pass filter stretches the pulse to 20ns, and a combination of up to two Mini-Circuits ZFL-1000LN+

amplifiers and up to two 10dB attenuators produce a signal amplitude >400mV going into the converter circuit. It is important to choose a combination of circuit elements that avoids clipping the pulse amplitude in the amplifiers. This relatively amplifies the noise around the main pulse. If these specifications cannot be obtained, or the signal is jumpy, it is likely that the photodiode position needs to be adjusted to properly catch the leak-through beam. Once we have a good analog signal, we send it to the converter circuit.

The first part of the converter circuit is a comparator that cleans up the signal and converts each analog pulse into a digital pulse of similar width. The comparator design is shown in Fig. 2.11(a). I AC-couple the input signal to the comparator, biased up to 1V, to avoid negative voltages that are incompatible with the comparator chip. To AC-couple a signal, send it through a capacitor to a voltage divider that sets the DC offset. The time constant of this RC circuit must be much longer than the pulse width, but much shorter than the pulse period, which is achieved by setting the time constant equal to 1μs. Because we have a very low duty cycle signal (10ns pulses every 250μs), the baseline voltage of the AC coupled signal will be only slightly below the DC offset voltage, as shown in Fig. 2.11(b). The comparator outputs a digital high voltage only when the input signal is larger than a reference voltage. Using a second voltage divider, I set the reference voltage to 1.4V. This way, an 800mV amplitude pulse from the amplified photodiode signal will be captured at FWHM. Note that the comparator chip used cannot exceed 3V input voltage. This sets the upper limit for the input signal amplitude at 2V, though clipping occurs in the amplifiers at ~1.5V, before this limit is reached.

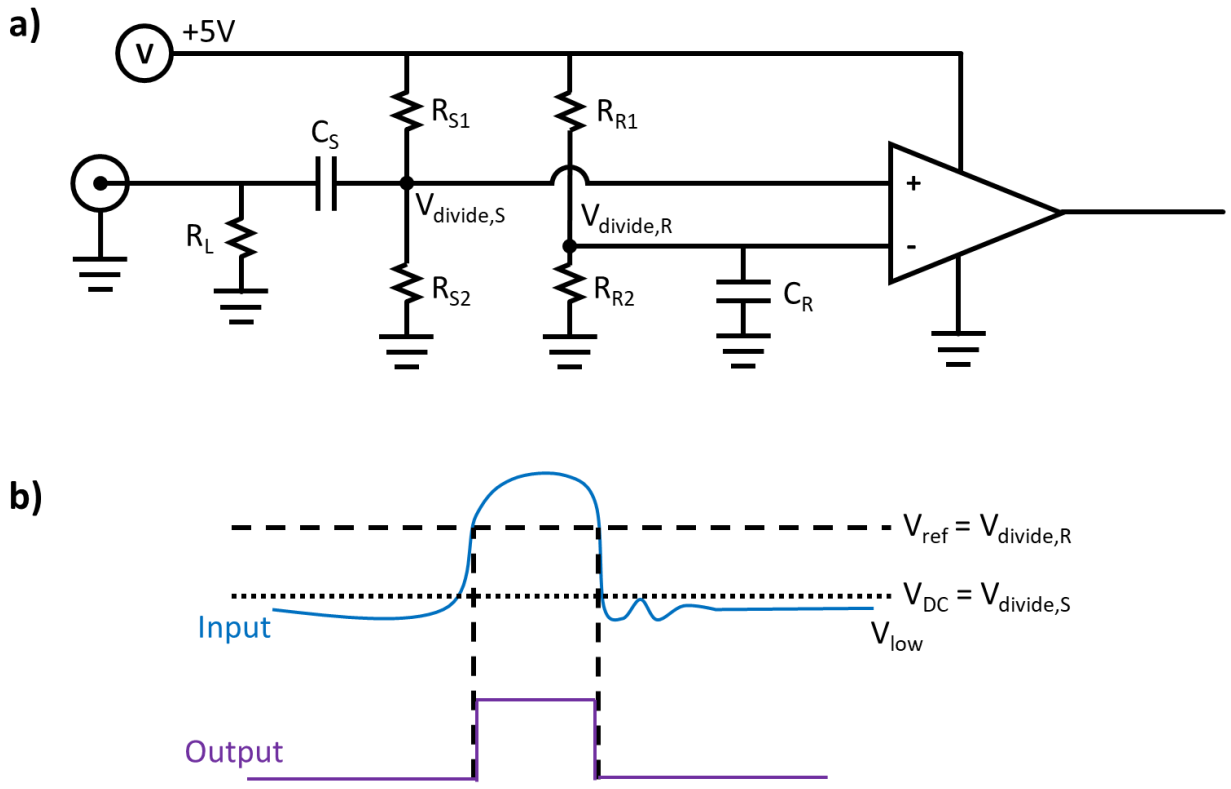

Figure 2.11: Comparator circuit with voltage dividers. a) Circuit diagram. The signal is input through a grounded BNC, and a small load resistor impedance matches the circuit to 50Ω. The signal is AC-coupled through C_S with a DC offset voltage, $V_{divide,S}$, determined by the R_S voltage divider. The reference voltage, $V_{divide,R}$, for the comparator is set by the R_R voltage divider. b) When the input of the amplified, stretched photodiode signal is greater than the reference voltage, the comparator outputs a steady digital high voltage. By AC-coupling the input signal, its average is exactly at the DC offset voltage, V_{DC}. This means the baseline voltage between pulses, V_{low}, is slightly lower than V_{DC}.

The comparator chip has a bias current, which must be taken into account to precisely set the resistor values for the input and reference voltage dividers. To do this, I use the principle of superposition, where the voltage at the node of interest is the sum of the voltage from the voltage divider in isolation and the voltage from the comparator's bias current in isolation. Together, I derive the following equations for the voltage divider resistor values, where *i* denotes either the signal (*S*) or the reference (*R*) comparator inputs, V_{supply}=5V, $V_{divide,S}$ and $V_{divide,R}$ are at the labeled nodes in Fig. 2.11(a), V_{bias}=1mV, and I_{bias}=3.5μA:

$$R_{i,1} = \frac{V_{supply}}{V_{divide,i}} \frac{V_{bias}}{I_{bias}},$$

$$R_{i,2} = \frac{V_{supply}}{V_{supply} - V_{divide,i}} \frac{V_{bias}}{I_{bias}}.$$

The capacitors are then determined by the following equation, with the condition that the RC time constants are $\tau_S = 1\mu s$, and $\tau_R = 1ms$:

$$C_i = \tau_i \frac{R_{i,1} + R_{i,2}}{R_{i,1}R_{i,2}}.$$

Lastly, a load resistor must be added to the input, so the signal is impedance matched at 50Ω. This reduces reflections that can cause significant problems in ultrafast electronics. The load resistor is determined by the condition $R_L // R_{p,s}$, where $R_{p,s} = R_{s1} // R_{s2}$. Thus,

$$R_L = \frac{(50\Omega)R_{S1}R_{S2}}{R_{S1}R_{S2} - (50\Omega)(R_{S1} + S_{S2})}.$$

The available resistors and capacitors that most closely match the ideal calculated values are shown in Fig. 2.12, the schematic of the full analog to TTL converter circuit.

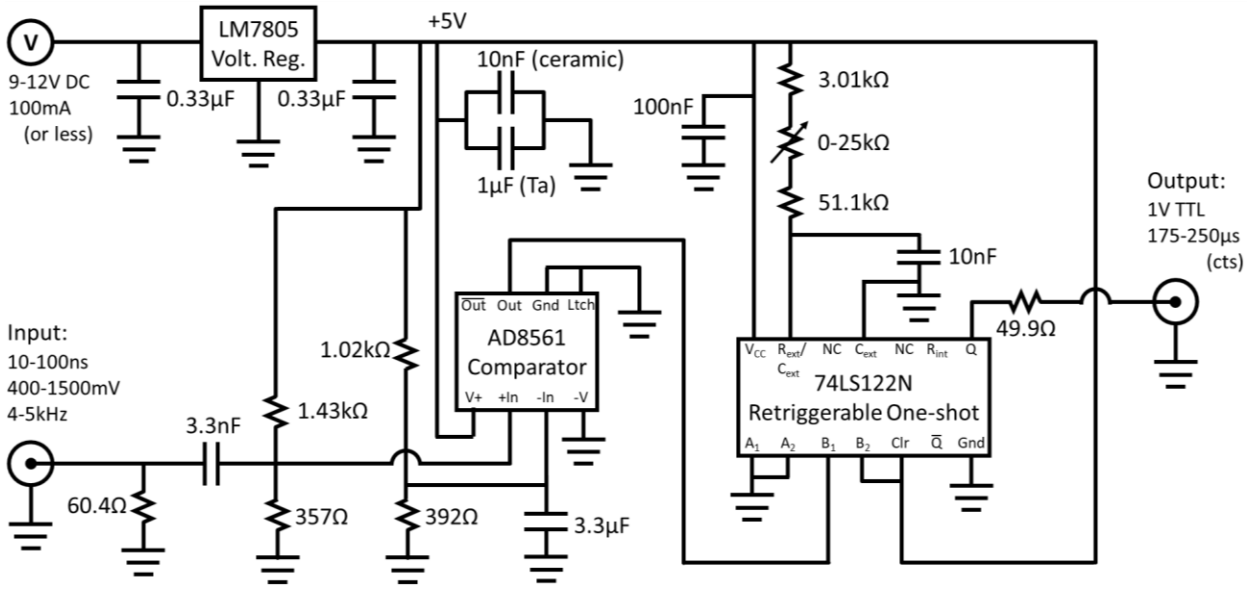

Figure 2.12: Diagram of the analog to TTL converter circuit. The voltage input first goes through a voltage regulator to smooth out any power fluctuations and reduce the supply voltage to 5V. The capacitors on each chip's supply voltage line further smooths the power supply to each integrated circuit (IC). The BNC input and output are directly grounded to the metal box holding circuit, which is also the circuit's ground. The comparator portion of the circuit is identical to the diagram in Fig. 2.11(a), though the explicit resistor and capacitor values used are shown here.

The digital pulse from the comparator is then sent to a 74LS122N retriggerable one-shot, as shown in Fig. 2.12. The one-shot produces a TTL pulse of a specified length, when triggered by an input signal pulse. The length of this pulse, t_W is set by

$$t_w = KR_{ext}C_{ext},$$

where R_{ext} and C_{ext} are set by external resistors and capacitors, and K varies with C_{ext} as shown in Fig. 2.13. This one-shot is also retriggerable, which means if it receives another input pulse before the full width of the output pulse has passed, it will retrigger to maintain a high voltage output. Thus, by tuning $t_W > 250\mu s$, the one-shot will output high (1V) as long as laser pulses are passing through the chopper and hitting the photodiode, as shown in Fig. 2.14. This defines the exposure window of the camera while the pump is unblocked. The one-shot's output TTL pulse, with 50Ω termination added, may then be used directly to trigger the camera. Note the output pulse was originally tunable from 175-250μs, but I had to add resistance to R_{ext} after a few months of operation to obtain pulse widths >250μs. This could have been caused by deviations in V_{CC}, V_{RC}, temperature, or C_{ext}, all of which change K. Alternatively, I recently discovered the potentiometer that sets R_{ext} had been degrading, which could have been changing the attainable range of t_W. I have now repaired the potentiometer, so the attainable pulse widths may now be 211-308μs, as nominally calculated from the resistor and capacitor values in Fig.2.12 and K=0.39. In this case, the converter circuit can no longer resolve individual pulses at 5kHz.

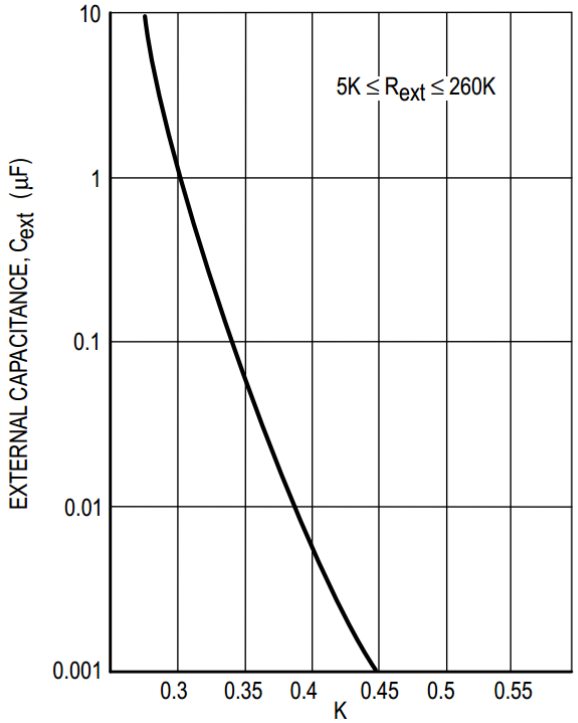

Figure 2.13: The one-shot *K* parameter. For the range of R_{ext} we use, K depends on the (constant) value of C_{ext} as shown. Note K also varies with temperature, V_{CC} and V_{RC}. See the IC's datasheet for more details.

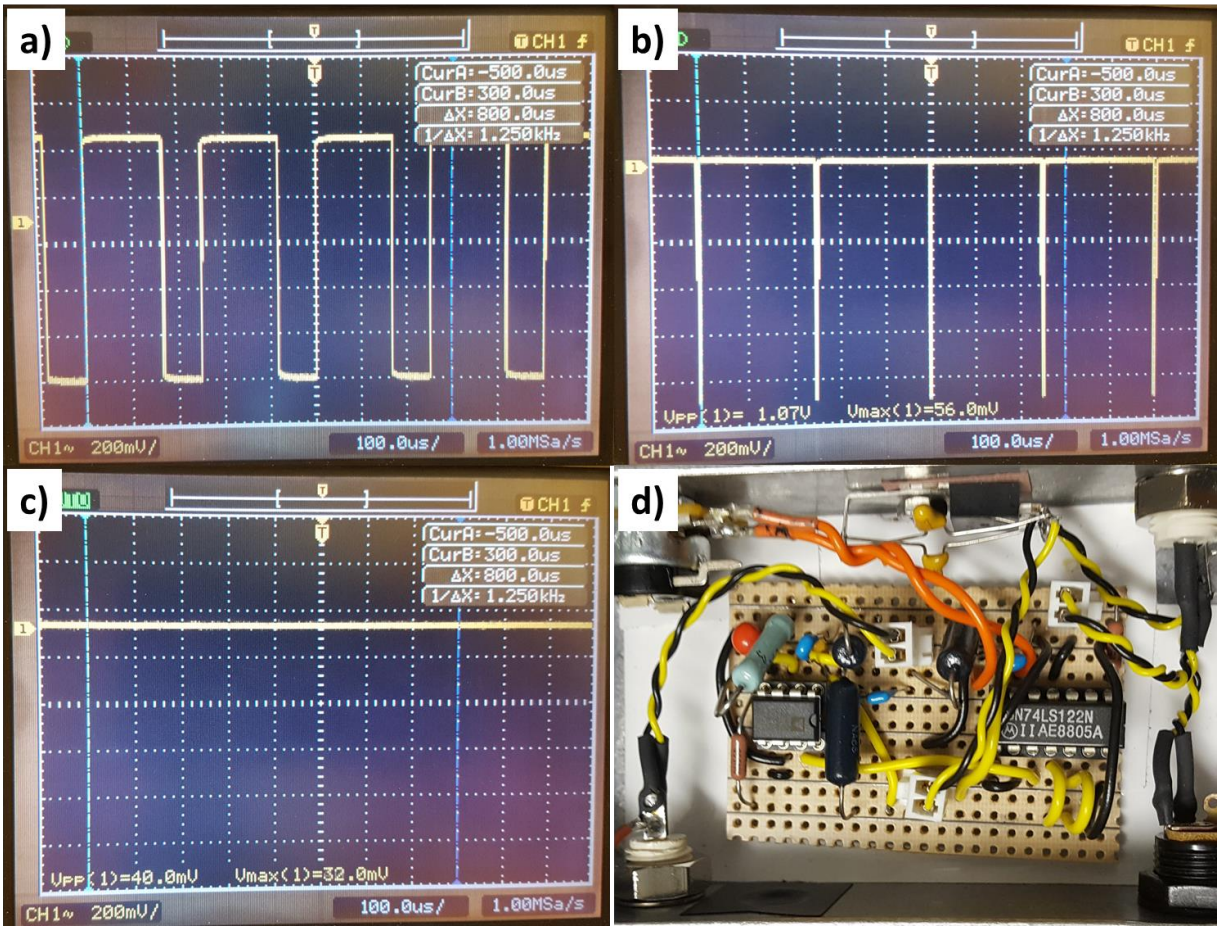

Figure 2.14: Function of the analog to TTL converter circuit. Panels (a)-(c) show an oscilloscope reading of the circuit's output while tuning R_{ext}. When t_W is below 250μs (a), each pulse of the pump laser produces a TTL signal pulse. As t_W is increased, the gap between pulses shrinks (b), until t_W>250μs and a continuous high voltage is output until the pump laser is blocked (c). (d) Picture of the completed circuit. Note the cables are twisted, the wire lengths are kept short, and the input and output BNC's are separated. These steps are important when working with ultrafast electronics. The BNC/filter/amplifier chain connecting the photodiode to the circuit (not shown) should also be kept as short as possible to avoid picking up spurious frequencies from other lab equipment. Also note C_{ext} is a surface mount capacitor on the underside of the breadboard, and so it is not visible here.

Finally, now that the camera has a trigger synchronized to the pump laser, we must set the camera exposure. To set the camera exposure, we use a kinetic series of at least two exposures, since the camera is triggered when the pump beam passes through the chopper apertures (pump on), but both pump on and pump off exposures are needed. Use the following equation to set the kinetic series cycle time and set the camera exposure time to be 2.02ms shorter to allow for the minimum camera readout time:

$$t_{cycle} = \frac{1}{2f_{outer}\frac{S_{inner}}{S_{outer}}}.$$

Here, f_{outer} is the exact frequency of the outer row of slots, as read out from the chopper controller, S_{inner} is the number of slots on the inner portion of the wheel (where the pump beam is), and S_{outer} is the number of slots on the outer portion of the wheel (where the chopper's optical encoder is). In practice, doing a kinetic series of up to 50 leaves fewer skipped chopper cycles while waiting for the next trigger pulse to arrive.

Use Table 2.1 to get a specific number of pulses through the chopper. To check for clean chopping, use an oscilloscope to read the output from the analog to TTL converter circuit. If the pulse is not of a constant, expected width, then clipping of the pulses is occurring. To get a specific number of pulses on the camera, however, more work is needed. There is a finite time for the camera to begin exposing, once it receives a trigger, and this skips some pulses. This delay time needs to be better characterized and controlled before the system can be operated at a precise number of pulse exposures.

Pulses:	**1**	**2**	**3**	**4**	**5**	**6**	**7**	**8**	**9**
Delay box µs	250	500	750	1000	1250	1500	250	2000	2250
Delay box kHz	4	2	4/3	1	0.8	2/3	4	0.5	4/9
7/5 harmonic	-	-	-	7/10	7/10	7/10	1/10	7/10	7/10
42/30 harmonic	7/10	7/10	7/10	-	-	-	-	-	-
Pulses:	**10**	**11**	**12**	**13**	**14**	**15**	**16**	**18**	**20**
Delay box µs	250	250	250	250	250	250	500	500	500
Delay box kHz	4	4	4	4	4	4	2	2	2
60/2 harmonic	3/2	15/11	5/4	15/13	15/14	1	15/8	15/9	3/2
Pulses:	**21**	**22**	**24**	**25**	**26**	**27**	**28**	**30**	**33**
Delay box µs	500	500	500	500	500	500	500	500	500
Delay box kHz	2	2	2	2	2	2	2	2	2
60/2 harmonic	10/7	15/11	15/12	6/5	15/13	10/9	15/14	1	10/11
Pulses:	**35**	**36**	**39**	**40**	**42**	**45**	**48**	**50**	**52**
Delay box µs	750	750	750	750	750	750	1000	1000	1000
Delay box kHz	4/3	4/3	4/3	4/3	4/3	4/3	1	1	1
60/2 harmonic	9/7	15/12	15/13	9/8	15/14	1	15/12	6/5	15/13
Pulses:	**54**	**55**	**56**	**60**	**65**	**66**	**70**	**72**	**75**
Delay box µs	1000	1000	1000	1000	1000	1000	1000	1500	1250
Delay box kHz	1	1	1	1	1	1	1	2/3	0.8
60/2 harmonic	10/9	12/11	15/14	1	12/13	10/11	6/7	15/12	1
Pulses:	**78**	**80**	**84**	**90**	**100**	**105**	**120***	**135***	**150***
Delay box µs	1500	1500	1500	1500	1500	1750	2000	2250	2500
Delay box kHz	2/3	2/3	2/3	2/3	2/3	4/7	1/2	4/9	2/5
60/2 harmonic	15/13	9/8	15/14	1	9/10	1	1	1	1

Table 2.1: Delay box and chopper settings for specific pulse exposures. The delay box is set to a multiple of the 250µs period trigger from the laser amplifier. Using the specified wheel (S_{outer}/S_{inner}) and harmonic/subharmonic setting of the chopper controller, a specific number of pulses is passed by the chopper. The asterisk means the wheel spins too slowly at these exposure times to cleanly chop the beam.

2.3.3 B-Integral and Chirped Mirrors

I will now present the steps taken to mitigate nonlinear effects during transport of our intense IR beam. Specifically, we reduce the value *B*, which is a measurement of the nonlinear phase accumulated over distance. *B* is in general an integral, but as an estimate of the maximum nonlinear phase accumulated, we calculate the *B* integral at the peak of our laser pulse, with a constant intensity along the full optical path. This reduces to

$$B = k_0 n_2 I L, \tag{1}$$

where k_0 is the wavevector of the laser, L is the propagation distance, and n_2 is the nonlinear component of the refractive index from the Kerr effect ($n = n_0 + n_2 I$). The peak intensity of the Gaussian laser pulse is given by

$$I = 4\sqrt{\frac{ln(2)}{\pi}}\frac{E}{\tau(\pi r^2)}, \quad (2)$$

where τ is the full width at half maximum (FWHM) pulse duration, E is the pulse energy, and r is the beam radius. Because B varies with intensity, the nonlinear phase accumulated varies across the width of the beam. This can apply a quadratic phase to the beam and cause self-focusing, or it can cause more general mode distortion.

To check if there is significant B integral for a given optical setup, there are a few tests that may be performed. First, by un-seeding the amplifier by removing the oscillator input, the IR beam is changed from high intensity, ultrafast pulses to low intensity, longer pulses of amplified spontaneous emission (ASE). If the focal plane of a short focal length lens changes when unseeding the beam, this indicates the high intensity beam accumulates nonlinear phase as it propagates. The next check is to direct a low intensity portion of the fully seeded beam into a spectrometer. If there is a fluctuating peak on the short-wavelength end of the spectrum, this indicates there is self phase modulation during propagation. Lastly, the predicted B value may be calculated using Eqn. 1 for every segment of the beam path, and every transmissive optic the beam passes through. Performing this calculation for our experiment, I estimate a maximum B of 6 for the combined optical path up to the beam splitter plus the probe line. The pump line has much lower intensity, and will only have a lower B integral. As B measures phase, this value is large on the scale of pi, indicating nonlinear phase is a problem. Ideally, B should be well below 1.

Considering Eqns. 1-2, the B integral can be reduced by reducing any of the values k_0, n_2, I, or L. Assuming the beam path is already as short as possible, L is fixed. For most of the beam path, k_0 is also fixed, though waiting until the final moment possible to do second harmonic generation helps to reduce B as nonlinear phase generally accumulates faster for the shorter wavelength beam. This primarily leaves n_2

and *I* as the experimentally adjustable parameters for *B* integral reduction. To reduce n_2, some materials are better than others. For example, CaF_2 glass has a lower n_2 than other optical glasses, so the easy first step to reducing *B* in our setup is to replace the silica lens focusing the probe into the HHG fiber with a CaF_2 lens. In the extreme case, n_2 may be further reduced by doing all high intensity beam transport in vacuum (n_2=0). This is cumbersome, however, and not a practical solution for our setup, where multiple alignments and adjustments must be performed on the optics regularly. This leaves reducing *I* as the primary method for reducing the *B* integral.

To reduce *I*, we cannot reduce the pulse energy, *E*, as large pulse energies are needed to perform HHG. Instead, we ensure that τ is as large as possible where nonlinear phase accumulation is occurring. We do this by leaving the pulse not quite fully compressed out of the amplifier, for the majority of beam propagation. We then fully compress the probe just before entering vacuum using chirped mirrors. The pump is compressed before entering the chopper due to space constraints and the necessity of having a compressed pulse to perform SHG in the TG setup. As the pump is lower intensity than the probe, this should be tolerable. There is a separate pair of identical chirped mirrors in both the pump and probe lines.

Chirped mirrors are multilayer mirrors designed to have a negative group delay dispersion (GDD). They compress the pulse by reflecting each wavelength in the optical pulse at a different depth in the multilayer stack. In this way, each wavelength has a different optical path length, and these differences can be carefully designed to align the phases of each component wavelength, fully compressing the pulse. Mathematically, a pulse is stretched by a positive GDD according to the equation

$$\tau = \tau_0 \sqrt{1 + \left(4ln(2)\frac{D_2}{\tau_0^2}\right)^2}, \tag{3}$$

where τ_0 is the fully compressed pulse duration (again in FWHM), and D_2 is the GDD. Using Eqn. 3, we then calculate how many bounces from our $D_2 = -450fs^2$ chirped mirrors would be needed to compress a pulse of a desired stretched length. Using six bounces, we fully compress a stretched pulse of 300fs duration.

Propagating this longer pulse until the chirped mirrors reduces the *B* integral coming from our 8m of propagation in air from 1.9 to 0.2.

To fit six bounces on a pair of 2" chirped mirrors in both the pump and probe lines, we use compact mirror geometries, as shown in Fig. 2.15(a-b). In the pump line, the beam is picked off before entering the chopper and directed to the pair of chirped mirrors. After 3 bounces between the two mirrors, the beam is caught on a dielectric mirror that is tilted slightly horizontally off from retro-reflecting. This directs the beam back through the three bounces between the chirped mirrors, for a total of six, and leaves the beam horizontally displaced enough from the input beam to be picked off with an additional mirror. This final mirror then directs the beam through the chopper, and onward toward the rest of the experiment. For the probe, the design is somewhat simpler. The beam bounces back and forth between the two chirped mirrors, three times on each. One slight complication is that these multi-bounce mirrors must be used to align the HHG fiber line, as they are the final mirrors before entering vacuum. I have found it is easiest to use the chirped mirror closest to the fiber to align to the first iris (before the fiber position), and the chirped mirror furthest from the fiber to align to the second iris (after the fiber position).

Lastly, we utilize a larger beam radius, *r*, to get the final reductions in *B*. It is impractical for us to expand the beam size everywhere after the amplifier using a telescope, though this could be done in more extreme cases. Instead, we increase the beam size at its most critical position by moving the vacuum entrance window closer to the HHG focusing lens, as shown in Fig. 2.15(c). This position is critical because the beam is fully compressed, and n_2 for any solid material is much higher than it is for air. By moving the entrance window as close as possible to the lens, the beam radius is close to its largest value, and this change alone reduces our *B* integral by 2. Using a thinner entrance window would further reduce the *B* integral by an additional 0.4, but we have not implemented this at the present time.

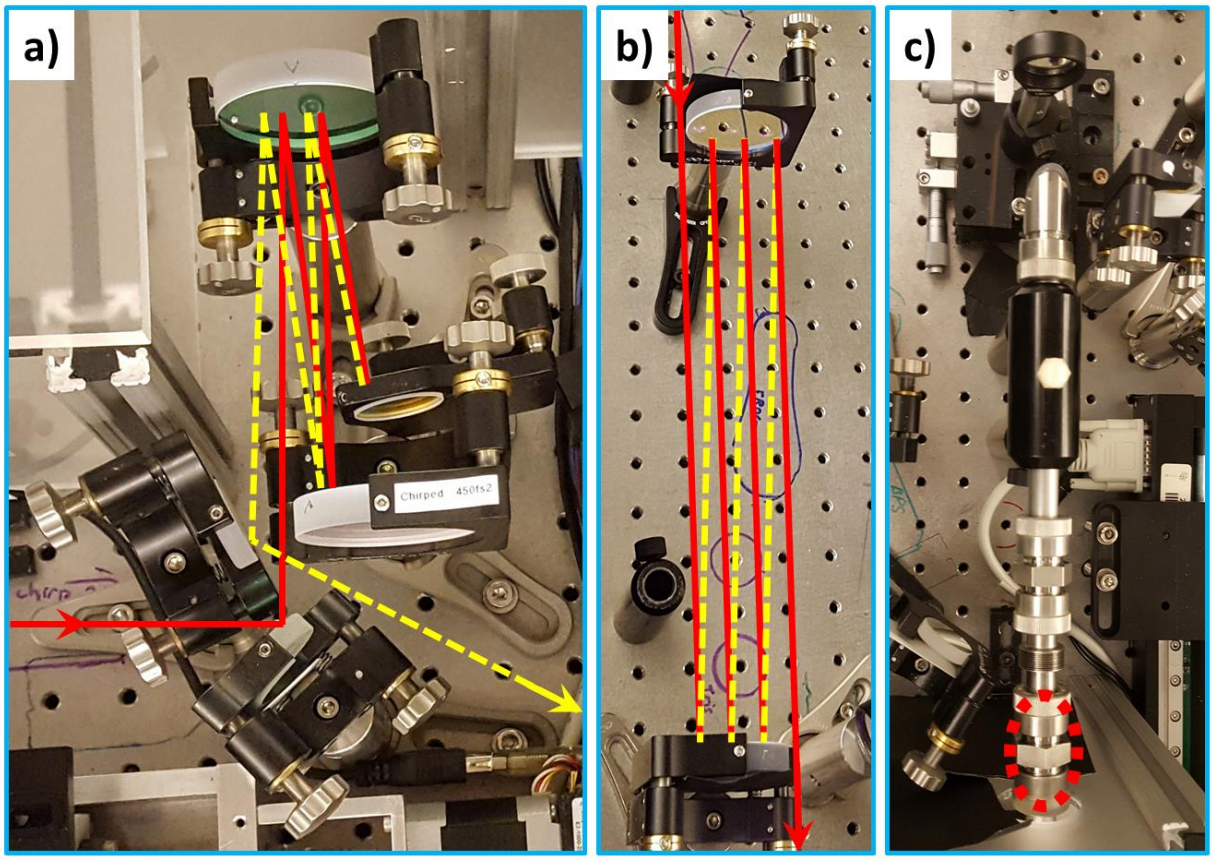

Figure 2.15: Chirped mirrors and vacuum redesign to reduce B integral. a) In the pump line, the beam is diverted to the chirped mirrors before entering the optical chopper. A nearly retro-reflecting dielectric mirror sends the beam back along an output path (yellow dotted lines) nearly retracing its input path (red lines). b) In the probe line, the beam is bounced back and forth 6 times between the chirped mirrors. Path segments alternate between red and dotted yellow lines, for clarity. c) The entrance window to the vacuum system was originally at the position marked by a dotted red oval. It was extended to be closer to the HHG focusing lens so that the beam passing through the glass would have a larger radius, and lower intensity.

With all of the above changes in place, I calculate a *B* integral reduced to 1.15 from the initial 6. To try to reduce it further would take more significant changes to our experimental apparatus. We have, however, addressed the most significant issues, such as reducing the nonlinear phase accumulation during propagation in air. Phase differences across the beam, even if small, can build to significant issues over long propagation distances, such as ours. Thus, it is important to have low B in air, which starts directly after the compressor and continues until entering vacuum. Conversely, the unavoidably high B in the final lens and entrance window can be more tolerable because the propagation after them is shorter. That said, the lens and vacuum entrance window are now the limiting factor in further reducing *B*, together contributing ~0.8 to the total *B* integral.

2.4 Conclusions and Future Work

In this chapter I have explained the most important aspects of our experimental methodology. I have primarily focused on the details necessary for understanding Chapters 3-5, where the setup is used to characterize the thermal and elastic properties of nanoscale materials. I have also taken a large portion of this chapter to describe the significant upgrades made to the experimental apparatus during my PhD.

In particular, I have described the modular optical TG setup implemented in the pump line, along with how to switch between TG and uniform round beam pumping configurations. I have also described the optical chopper, along with a camera triggering circuit used to rapidly obtain pump-probe measurements. Finally, I described the steps taken to reduce nonlinear phase accumulation by our high intensity IR beam, most significantly by using chirped mirrors to compress the probe and pump pulses as close to when they enter vacuum as possible.

In the near future, more upgrades to the experiment are planned. We are expecting a new amplifier pump laser, and we have the components for an optical isolator to avoid back-lasing into our oscillator. We are also expecting a direct blue-diode-pumped oscillator, and a higher repetition rate amplifier system. A higher repetition rate will give better statistics for an enhanced signal-to-noise ratio, though the experiment will then be more likely to suffer from pulse accumulation in low thermal conductivity samples. We are also in the process of upgrading our beam pointing stabilization system to automate some of our alignment procedure. We could also consider reducing the change in pump beam spot size with delay stage position by collimating the beam to a larger size before it enters the stages. For an ideal Gaussian laser beam, larger beam waists produce longer Rayleigh ranges, and the beam radius stays approximately constant for longer.

This experimental apparatus is a valuable tool for nanoscale metrology, and it should continue to provide useful measurements well into the future. One of the most significant capabilities of our technique is the direct probing of non-diffusive thermal transport in nanostructured systems. This research is the topic of Chapter 3.

Chapter 3

Nanoscale Thermal Transport

Nanoscale thermal transport is becoming ever more technologically important with the development of next generation nanoelectronics, nano-mediated thermal therapies, and high efficiency thermoelectric devices. However, direct experimental measurements of nondiffusive heat flow in nanoscale systems are challenging, and first principle models of real geometries are not yet computationally feasible. In recent work, we used ultrafast pulses of short wavelength light to uncover a new regime of nanoscale thermal transport that occurs when the width and separation of heat sources are comparable to the mean free paths of the dominant heat carrying phonons in the substrate. In this chapter, I now systematically compare thermal transport from gratings of metallic nanolines with different periodicities, on both silicon and fused silica substrates, to map the entire nanoscale thermal transport landscape – from closely spaced through increasingly isolated to fully isolated heat transfer regimes. By monitoring the surface profile dynamics with sub-angstrom sensitivity, we directly measure thermal transport from the nanolines into the substrate. This allows us to quantify for the first time how the nanoline separation significantly impacts thermal transport into the substrate, making it possible to reach efficiencies that are within a factor of 2 of the diffusive (i.e. thin film) limit. We also show that partially-isolated nanolines perform significantly worse, because cooling occurs in a regime that is intermediate between close-packed and fully isolated heat sources. This work thus confirms the surprising prediction that closely spaced nanoscale heat sources can cool more quickly than when far apart. These results are important for benchmarking new theories that go beyond the Fourier model of heat diffusion, and for informed design of nanoengineered systems.

3.1 Introduction and Motivation

Advancing technology through nanoengineering often requires an understanding of how nanoscale thermal transport differs from its bulk counterpart. In modern electronics, characteristic dimensions are already below 10nm – thus, thermal load management is already facing challenges imposed by nanoscale thermal transport. In medicine, nanoparticle-mediated thermal therapies are being developed to treat cancer and tumors with localized heating of those cells [1, 46]. Additionally, nanostructuring is a promising avenue to engineer novel materials for efficient thermoelectric devices, either through enhanced scattering [47, 48] or through phononic metamaterial effects [18, 49, 50]. For these and many other applications, informed design must take into account that nanoscale thermal transport can be significantly slower than bulk model predictions.

Fourier's law of heat conduction, which accurately describes thermal transport in bulk materials, relies on the fundamental assumption that the distances being considered are much larger than the average mean free path (MFP) of heat carriers in the system, therefore establishing a smooth thermal gradient that drives transport in a material. As a result, when the relevant length scale of thermal transport is on the order of the MFP of the heat carriers, Fourier's law is no longer accurate because it dramatically overpredicts the heat transfer rate [7]. In this regime, some of the heat carriers travel ballistically from the heat source and deposit their energy non-locally, producing non-diffusive (quasiballistic) thermal transport. Since the dominant heat carriers for dielectric and semiconducting materials are phonons, which can have MFPs from nanometers up to several microns in materials such as silicon at room temperature [11, 20, 51, 52], quasiballistic effects are observable in nanostructured systems, even at dimensions up to microns [10].

Observations of quasiballistic thermal transport have been made in several experimental geometries, including 1D transport using transient grating experiments, ballistic transport through a thin slab of material whose thickness is shorter than the heat carrier's MFP, and also by measuring the transport away from nanoscale heat sources [8-10, 51, 53]. In this last category, effectively isolated heat sources were initially used to study thermal transport as a function of heat source size. As the size of the heat source was

decreased, a monotonic deviation from the Fourier prediction was observed, due to the onset of quasiballistic transport. More recently, the study of nanoscale heat sources that are not isolated has revealed that not only the size of, but the spacing between, heat sources impacts the nature of thermal transport [20, 54-56]. In past work, we made the first observation of a new collectively diffusive regime, where the thermal transport away from nanoscale hot spots can return towards the diffusive prediction when their spacing is reduced below the dominant heat carrying phonon MFPs of the substrate [20]. This previously unobserved phenomenon has promising technological applications. We also developed a predictive, period- and linewidth-dependent theory for the effective resistivity, which predicted that the period, or line spacing, mattered. However, in our initial work, we did not independently vary both the heat source size and spacing, or explore the transition between isolated and close-packed regimes, motivating the need for more systematic studies to benchmark advanced models and theories.

Here, I present a systematic study that independently controls the nanoscale heat source size and spacing with laser heated nanolines fabricated on silicon and fused silica substrates. This allows us to definitively validate our surprising prediction that nanoscale heat sources whose separation is comparable to the phonon mean free paths of the substrate should cool faster than identical heat sources that are spaced much farther apart [20]. Using an effective Fourier model, we quantify the enhancement of nanoscale thermal transport by engineering the heat source spacing: for example, for a constant 20nm-width nanoline, the isolated heat source model [9] predicts an effective thermal boundary resistivity, r_{eff}, of 52nKm^2/W, nanolines spaced by 400nm have a measured r_{eff} of 9.2nKm^2/W, nanolines spaced by 80nm have a measured r_{eff} of 3.7nKm^2/W, while the diffusive prediction for a uniform film is 2.45nKm^2/W. Thus, the closely-packed nanolines exhibit thermal transport very close to diffusive, and varying their spacing makes it possible to significantly tune their transport properties. We also explore the transition from collective, close-packed transport to isolated, quasiballistic transport, which represents a broad parameter space that is important for optimized thermal design and for the development of full, first principles models. Finally, we perform the same series of measurements on nanolines fabricated on a fused silica glass substrate, which exhibit no changes in transport as a function of either heat source size or period. This behavior is expected:

the phonon mean free paths in fused silica are small compared to our experimental geometries, and thus heat transfer from these nanolines should be well described using a diffusive model. This measurement serves as a control to confirm that plasmonic or other effects in the nanolines do not influence our measurement. I also briefly discuss how these new results compare to past results using different measurement techniques, and describe potential theories for the underlying transport mechanisms.

3.2 Experimental Methods

We measure nanoscale thermal transport in silicon and fused silica using extreme ultraviolet (EUV) nanometrology, as described in Chapter 2. For this study, the silicon and fused silica substrates are patterned with periodic gratings of nickel nanolines via e-beam lithography. Using an ultrafast femtosecond laser pulse, we impulsively excite these nanostructures, which serve as transducers for the thermal dynamics we measure. The excited thermal and acoustic dynamics deform the nanostructures and substrates, whose composite surface is then measured very sensitively using coherent EUV beams generated by the high harmonic generation (HHG) process. All measurements presented here are obtained at room temperature and high vacuum. See Fig. 3.1 for a diagram of the laser setup used in these measurements and Fig. 3.2 for a diagram of our pump-probe technique.

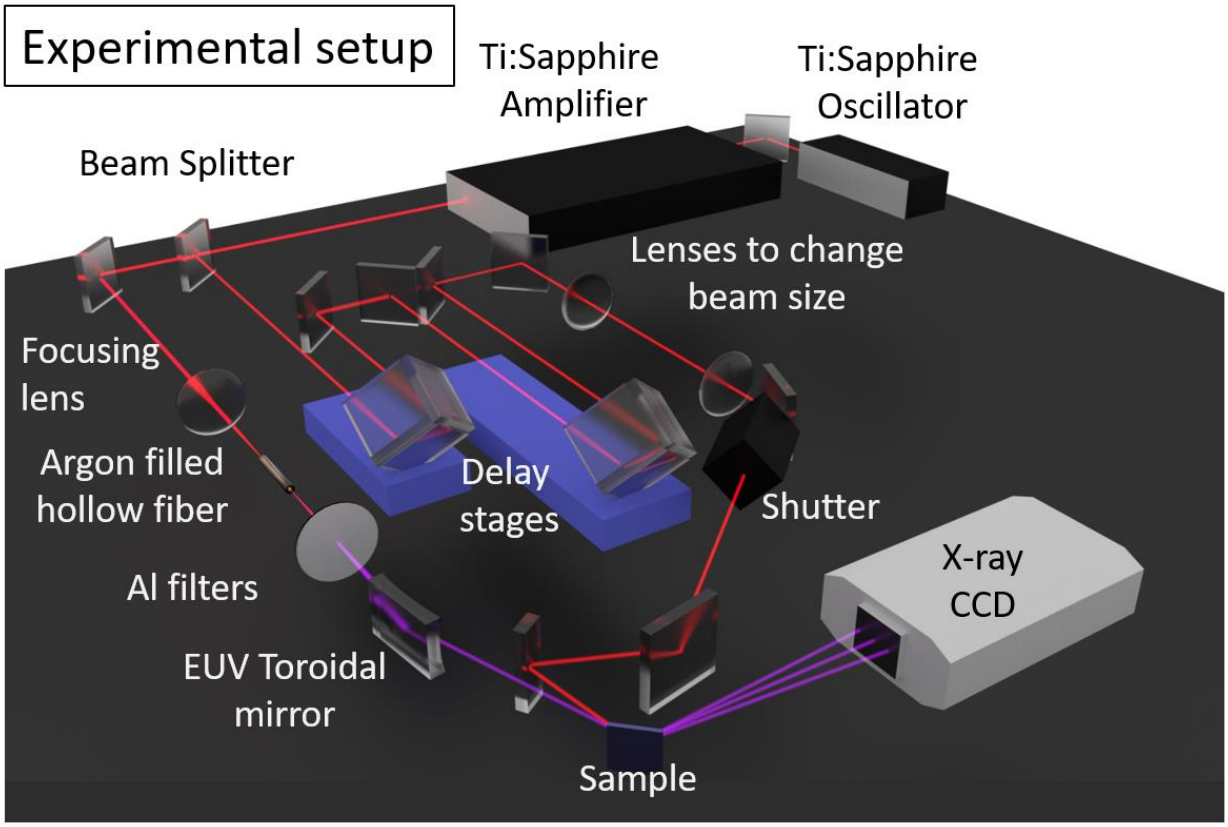

Figure 3.1: The EUV nanometrology laser setup. From the same amplified, ultrafast laser source, we pump and probe the nanostructured samples. The pump remains in the near-IR wavelength region, while the probe is converted to the extreme ultraviolet region via high harmonic generation in an argon-filled hollow waveguide. Pump-probe delay is controlled by a translation stage in the pump beam path, and a shutter blocks and unblocks the pump beam to provide an unexcited reference measurement at each pump-probe delay. The probe beam is focused onto the sample with a glancing incidence toroidal mirror, and the beam diffracted from the sample is collected on a CCD camera.

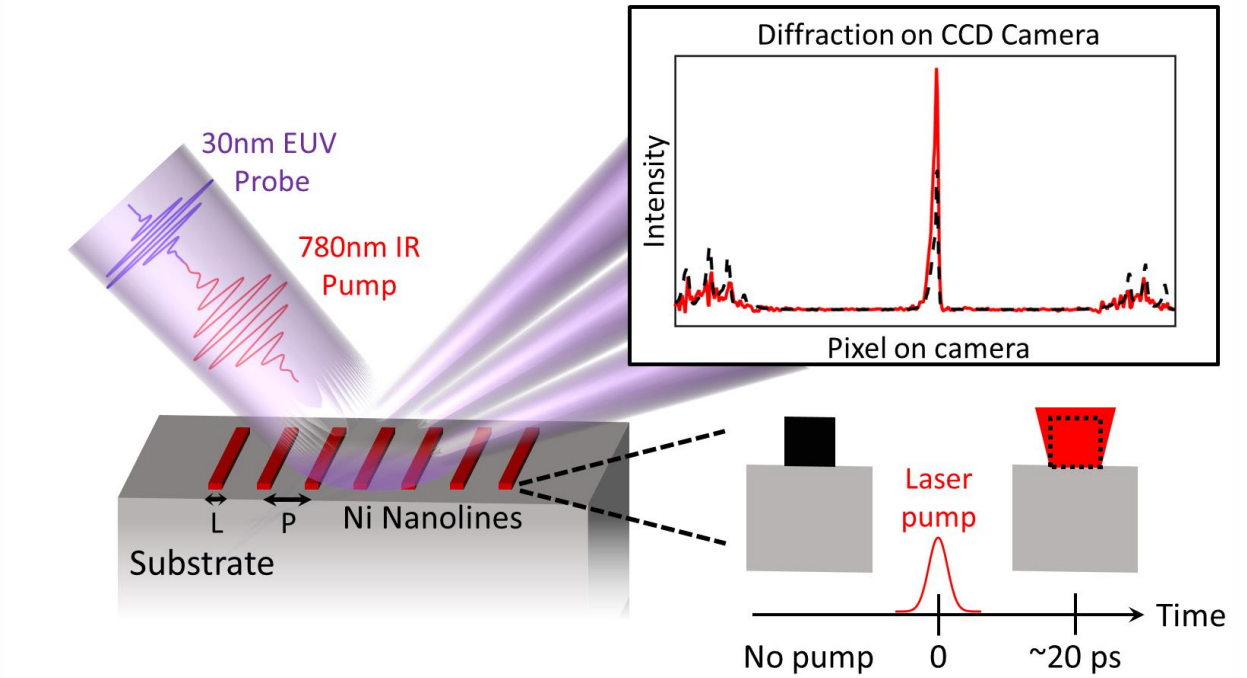

Figure 3.2: Diagram of the pump-probe technique. Gratings of nickel nanolines of linewidth L and period P are fabricated on silicon and fused silica substrates. An ultrafast IR laser pulse heats the nanolines and they impulsively thermally expand (shown in lower right). An ultrafast EUV pulse then probes the sample as a function of time delay by measuring diffracted light using a CCD camera. The diffraction efficiency for a thermally excited sample (red in inset) changes compared to an unperturbed sample (black dotted line in inset). This change in diffraction efficiency captures the thermal and elastic dynamics that are deforming the sample surface. Note the change in the diffraction pattern shown is magnified 150x for illustration purposes.

3.2.1 Nanoline Grating Design and Excitation

To explore the various nanoscale thermal transport regimes, we choose grating linewidths and spacings that span from much smaller, to comparable, to greater than the average MFP, which is ≈ 300nm in silicon [20, 57]. Therefore, we compare constant 25% duty cycle gratings to constant period (varying duty cycle) gratings with linewidths ranging from 20nm to 1000nm. For the smallest linewidths (20nm to 100nm), the constant period was chosen to be 400nm so that collective effects would still be present, but the reducing linewidth would probe the transition from the collectively diffusive regime to the isolated quasiballistic heat source regime. Similarly, for linewidths from 100nm to 300nm, the constant period is 1500nm, where collective effects should be much weaker. A complete list of grating L and P characterized by AFM is given in Tables 3.1 and 3.2. Example SEM images are given in Fig. 3.3.

Nominal L/P (nm)	L from AFM (nm)	P from AFM (nm)	Duty Cycle
1000/4000	970 ± 30	4110 ± 40	23.5%
300/1500	300 ± 20	1580 ± 20	19%
300/1200	260 ± 10	1240± 10	21%
200/1500	190 ± 20	1570 ± 20	12%
200/800	188 ± 9	842 ± 9	22%
100/1500	99 ± 8	1520 ± 10	6.5%
100/400	86 ± 5	412 ± 5	21%
50/400	41 ± 7	411 ± 5	10%
50/200	41 ± 2	205 ± 2	20%
30/400	25 ± 1	411 ± 5	6%
30/120	23 ± 2	121 ± 1	19%
20/400	20 ± 4	411 ± 5	5%
20/80	19 ± 1	82 ± 1	23%

Table 3.1: Linewidth and period of each nickel grating on silicon, measured by AFM. Note that the duty cycles for the gratings marked in grey are systematically lower than the nominal value of 25%, but still consistent, averaging 21.4±1.5%. The two sets of constant period gratings, marked in white, vary by no more than 2% from a constant period, though the linewidths can differ from the corresponding constant duty cycle gratings by up to 13% for the large sizes, and 8% for the small sizes. The nanoline heights are 11±1nm. AFM data was analyzed using WSxM [58]. Uncertainty is calculated by standard deviation of measurements and AFM image pixel size.

Nominal L/P (nm)	L from AFM (nm)	P from AFM (nm)	Duty Cycle
1000/4000	940 ± 40	3930 ± 40	24%
300/1500	280 ± 10	1500 ± 10	19%
300/1200	280 ± 20	1200 ± 10	23%
200/1500	188 ± 9	1500 ± 10	12.5%
200/800	190 ± 10	804 ± 8	23.5%
100/1500	90 ± 10	1510 ± 10	6%
100/400	96 ± 6	405 ± 4	24%
50/400	45 ± 4	407 ± 4	11%
50/200	43 ± 3	204 ± 2	21%
30/400	25 ± 2	406 ± 4	6%
30/120	24 ± 2	123 ± 1	19.5%
20/400	19 ± 4	406 ± 4	4.7%
20/80	15 ± 4	83 ± 1	18%

Table 3.2: Linewidth and period of each nickel grating on fused silica, measured by AFM. The nominally constant duty cycle gratings are highlighted in grey. For this series of gratings, the duty cycle systematically decreases for the sub-100nm linewidth gratings, but as we observe no trend in the effective resistivity for these gratings, this is not significant to our results. The series of constant period gratings, marked in white, show excellent consistency in period, and the linewidths compare well to the constant duty cycle gratings for all but the 20nm linewidth. The nanoline heights are 11.2±0.5nm. AFM data was analyzed using WSxM [58]. Uncertainty is calculated by standard deviation of measurements and AFM image pixel size.

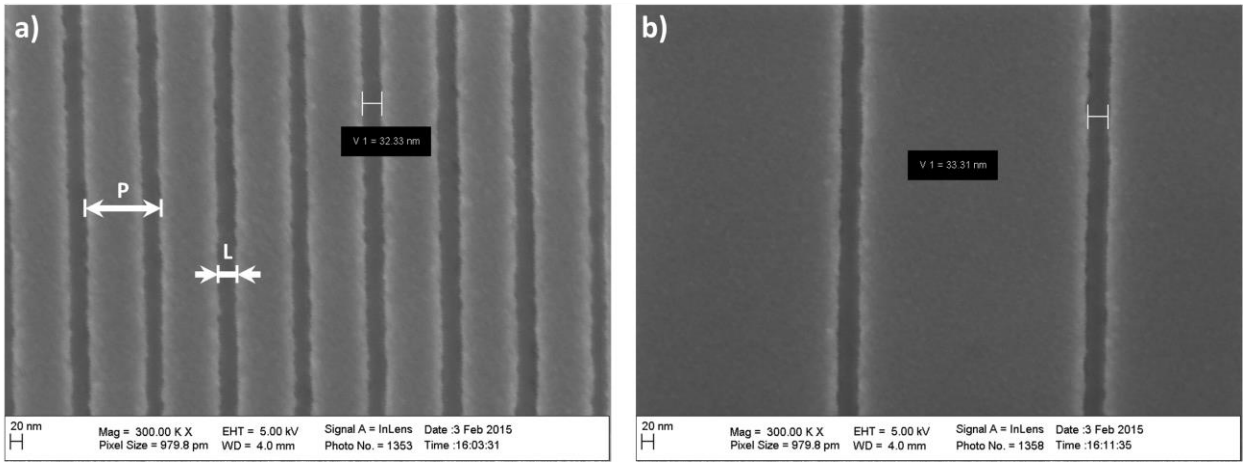

Figure 3.3: SEM images of the fused silica sample. a) A grating with 30nm linewidth (L) nanolines and 120nm period (P). b) A grating with 30nm linewidth and 400nm period. Note the measurements made by SEM are slightly larger than the values measured by AFM. Only AFM values for linewidth and period are tabulated above because a comprehensive set of measurements by SEM was unavailable. The slight systematic offset between the two characterizations does not change our trends or conclusions.

By comparing the measured thermal transport from each of these gratings, we directly probe the effect of heat source spacing on nanoscale thermal transport. The constant period set of gratings produces increasingly isolated heat sources as the linewidth is decreased, whereas the constant duty cycle set of gratings brings the heat sources closer together as the linewidth is decreased. Each grating covers an area of 150μm^2 and each nanoline is 11nm tall on average.

We excite the nanolines using an ultrafast infrared laser pulse with a central wavelength of 780nm, with a 25fs pulse duration, and at a 4kHz repetition rate. The nickel gratings preferentially absorb the laser light, with no significant heat deposition in the substrate underneath: fused silica is transparent to this wavelength, while silicon has a >8μm penetration depth. The nanolines are thinner than the optical penetration depth of Ni, ensuring uniform heating. After impulsive heating, the nanolines thermally expand within ~20ps, launching acoustic waves that are visible in our raw data, as shown in Fig. 3.4. (In Chapter 4, these acoustic waves were used to characterize the elastic properties of ultrathin films.) After expanding, the Ni nanolines relax back to their unperturbed surface profile, as heat is transferred into the substrate on few nanosecond time scales. The maximum experimental time window is 8ns, as determined by a mechanical delay stage in the pump line.

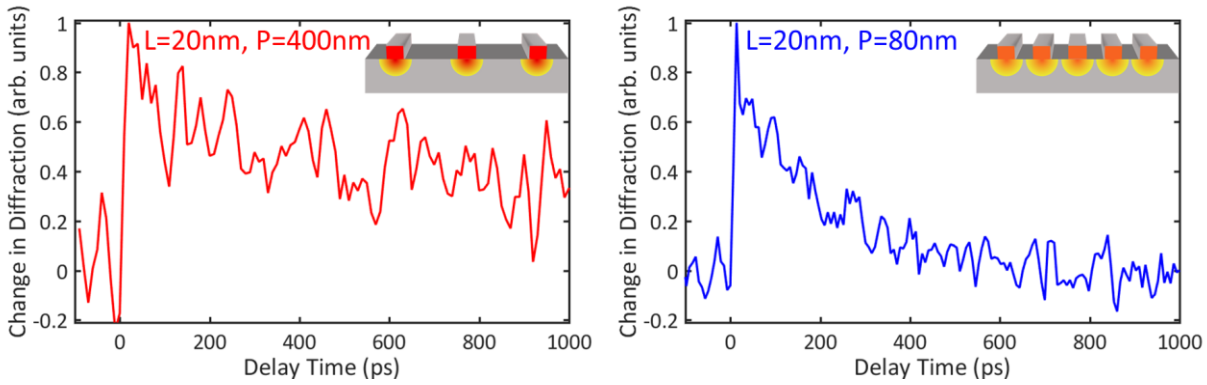

Figure 3.4: Dynamically changing diffraction signals for 20nm linewidth gratings on silicon. The raw data directly show that closely spaced nanolines cool faster. Multifrequency acoustic oscillations in the substrate visibly modulate the slow thermal decay of the signal. Left: 20nm nanolines at a 400nm period do not fully cool, even after 1ns. Right: 20nm nanolines at an 80nm period have almost completely cooled within 1ns.

Note that we assume the measured system response is linear with pump power. We check this by normalizing experimental signals from the same grating at several different laser pump fluences and confirming that the dynamics are the same. We confirmed this for all the gratings at all the pump fluences listed in Table 3.3. We also assume there is uniform pumping of the grating over the probed region. For this study, the pump beam diameter is 320μm on average, and the probe spot size is ~50μm radius, so we should meet this condition and be mostly insensitive to transport along the length of the nanolines.

Power (mW)	Pump diameter (μm)	Fluence (mJ/cm^2)
45	-	-
35	-	-
35		
31	300	11.0
30	340	8.3
38	-	-
40	-	-
50	-	-
50	-	-
50	350	13.0
47	-	-
47	-	-
47	-	-
47	-	-
60	400	12.0
60	400	12.0
60	-	-
60	-	-
65	-	-
60	300	21.2
110	360x390	24.9
135	-	-
150	-	-
175	-	-
125	400x436	22.8
190	440x500	27.4

Table 3.3: Pump beam average power, spot size at the sample plane, and average fluence. Note that the spot size was not recorded every day during the experiment. When the beam was oblong, an average radius was used to estimate the fluence. The averages of pump power, spot size, and fluence over the course of the experiment are 70.8mW, 323μm, and 17.0mJ/cm^2, respectively. Note that for all the data presented, at all the fluences listed, there was no discrepancy between change in diffraction efficiency signals after normalization. This indicates our observations are linear with pump fluence.

3.2.2 Probing and Measurement Sensitivity

We use coherent EUV beams to directly measure changes in the nanosystem surface profile. We generate the EUV beams at a central wavelength of 29nm through high harmonic generation [36]. This is an extreme nonlinear quantum process that up-converts IR light into the EUV region by focusing the laser pulse into an argon-filled waveguide. Since we use the same Ti:sapphire laser for both the excitation pulse and also to generate the probe EUV pulse, the timing stability between our excitation and probe pulses is in the sub-femtosecond range. In addition, EUV wavelengths are far from any electronic resonances in the nanosystem, so that the EUV reflectivity is largely insensitive to the electron temperature [41]. Thus, our

technique predominantly probes lattice expansion and surface deformation, even for very short times after excitation (few picoseconds).

The diffracted EUV beam probes the dynamically changing sample surface, and is collected on a CCD camera, as shown in Fig. 3.2. The diffraction efficiency, i.e. the relative power in the direct beam and diffracted orders, is a function of the height difference between the tops of the nanolines and the substrate. Thus, by monitoring the change in diffraction efficiency as a function of excitation-probe delay time, we measure the thermal and elastic dynamics in both the nanolines and substrate, with picometer scale sensitivity (see Fig. 3.4 for an example) [41].

Our measured signal closely follows the lattice temperature of an average nanoline; this differs from the temperature difference measured by the transient thermal grating (TTG) technique [29]. This distinction is important to keep in mind, as TTG signal is lost once the peak-valley temperature difference is lost, even if the average temperature of the sample is above the pre-excitation value. Thus, for shorter period gratings, there is a shorter distance to transfer heat, and the signal should decay faster as the peak-valley temperature difference washes out. This effect mimics our observed period dependence, but it is different in origin.

By using a separate metallic grating as our heat source, we measure the thermal expansion of the nanolines for any temperature above the pre-excitation value, even in the case that the top layer of the substrate has thermalized. Additionally, our heating geometry generates inherently two-dimensional thermal transport in the substrate – one dimension cross plane and one dimension in plane. Because the metal nanolines are uniformly pumped and thermalize internally in the first few picoseconds after laser excitation, our signal tracks this 2D thermal transport away from the resulting heat sources at the substrate surface. Traditional TTG measurements only measure the 1D thermal transport in-plane.

To confirm that a 1D TTG interpretation of our signal (peak-valley temperature difference washing out, as shown in Fig. 3.5(c)) with diffusive thermal transport does not explain our diffraction measurements, we perform finite element analysis (FEA) calculations of the thermal transport from the L=20nm, P=80nm and L=20nm, P=400nm gratings on silicon with identical thermal boundary resistivities. We compare the

diffraction signal for each simulation to both the peak-valley temperature difference in the substrate and the temperature in the center of the nanostructure. As shown in Fig. 3.5(a,b), the diffraction signal nearly identically follows the temperature of the nanostructure, not the temperature difference in the substrate.

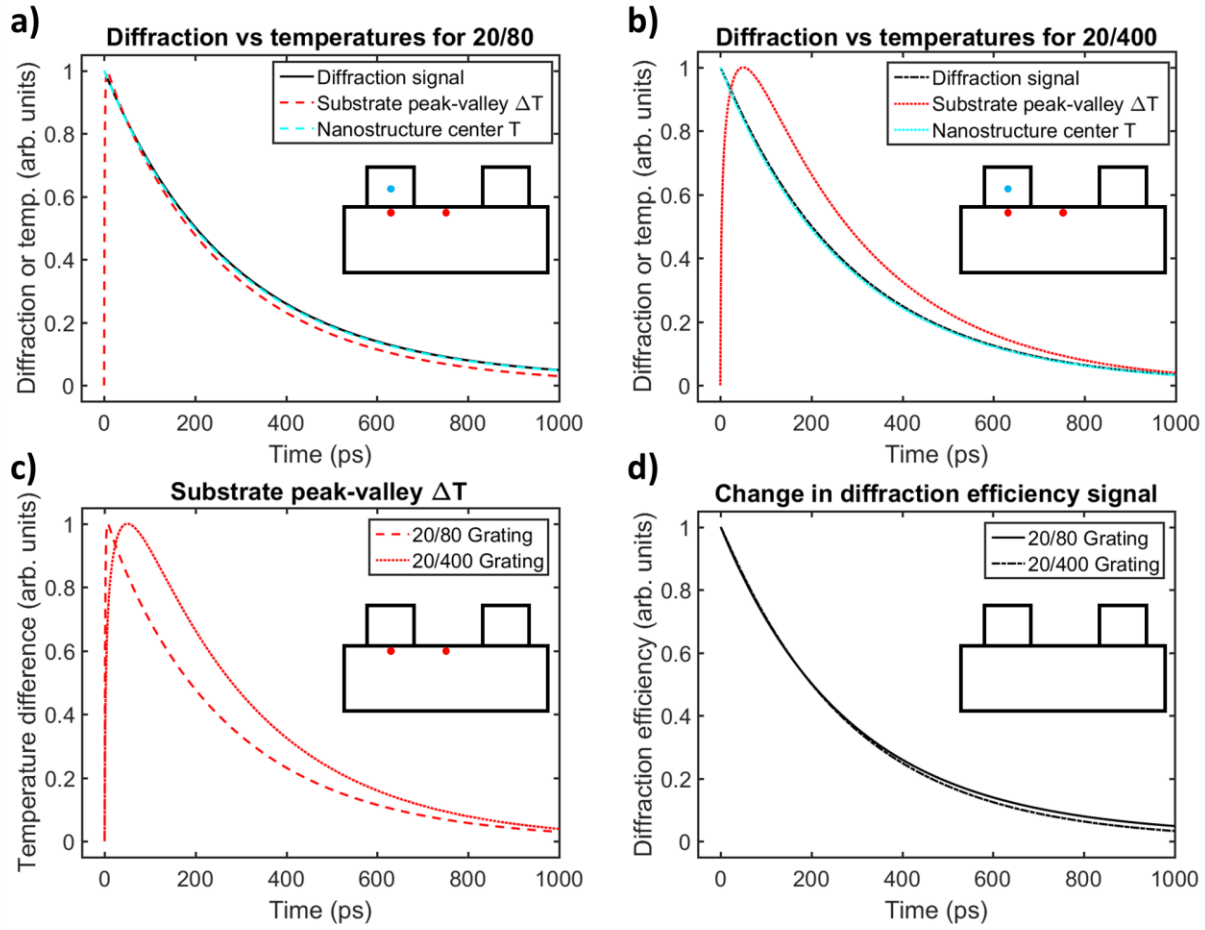

Figure 3.5: Measurement sensitivity to nanostructure and substrate temperatures. Simulations of the two L=20nm gratings on silicon are shown, both with r=5nKm^2/W. I compare the change in diffraction efficiency signal to the temperature at different points in the sample. Black lines are change in diffraction efficiency signals; cyan lines are the temperatures at the nanostructure centers; red lines are the peak-valley temperature differences in the substrate between the two red points shown schematically. a) For the 80nm period grating, the change in diffraction efficiency signal nearly identically tracks the temperature of the center of the nickel nanostructure but does not follow as closely the peak-valley temperature difference in the substrate. b) For the 400nm period grating, the change in diffraction efficiency signal again follows the temperature of the center of the nanostructure. c) The peak-valley temperature difference in the substrate goes to zero faster for the 80nm period grating as there is a shorter distance to transfer the heat, compared to the 400nm period grating. This temperature difference is similar to what is of interest to 1D TTG, but does not match our diffraction signal, as shown in (a) and (b). d) When both gratings have the same effective resistivity, the change in diffraction efficiency signal for the 80nm period grating (solid line) is slightly slower to decay than the 400nm period grating (dash-dot line). Thus, a period dependence of the thermal transport is required to model our experimental results.

We further checked the sensitivity of our measurement to the temperature difference in the substrate washing out by enhancing the substrate coefficient of thermal expansion (CTE) in the FEA calculations. As shown in Fig. 3.6, for the L=20nm gratings, substrate CTE values up to ten times nominal do not change our diffraction signal, confirming diffraction is indeed predominantly sensitive to the nanostructure expansion at small sizes.

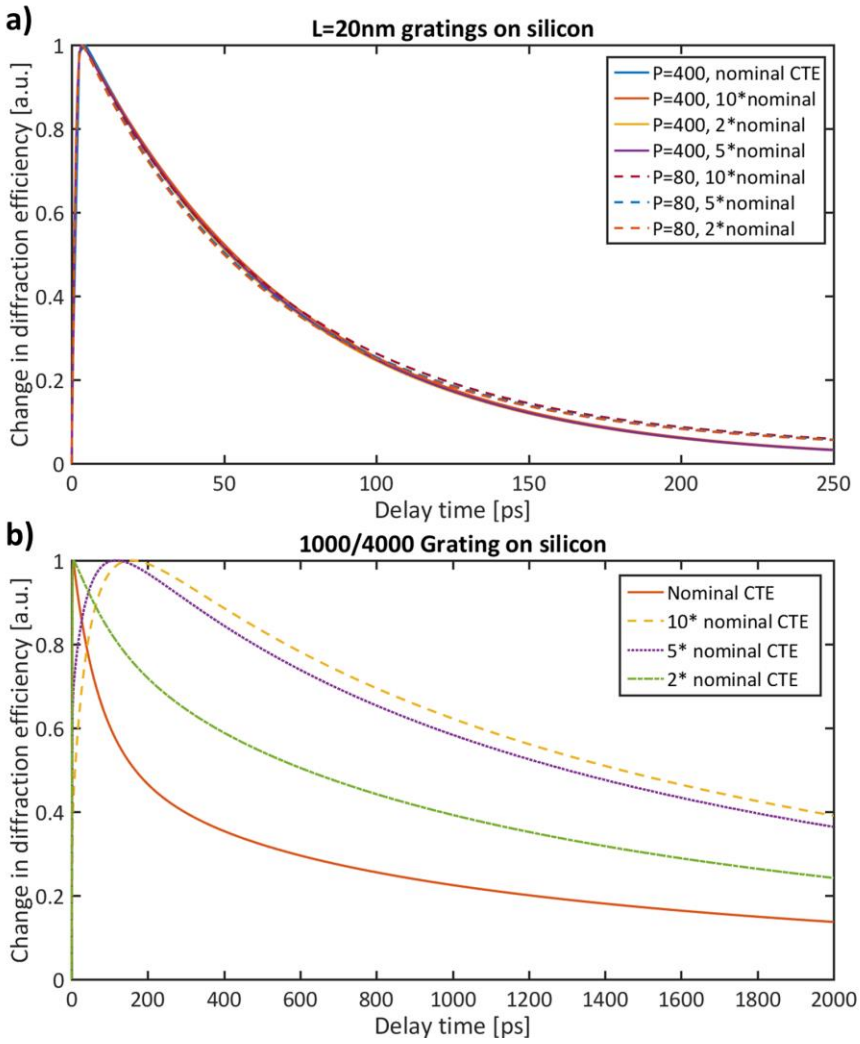

Figure 3.6: Measurement sensitivity to the substrate coefficient of thermal expansion. FEA calculations shown are performed in the quasistatic approximation, at a constant thermal boundary resistivity, with a uniform excitation. A two-temperature model is used to couple the electrons and phonons in the nanostructure, which provides the rapid thermal expansion at the earliest delay times [59]. a) For the 20nm linewidth gratings, whether 80nm or 400nm period, changes to the substrate coefficient of thermal expansion up to ten times the nominal value do not significantly affect the diffraction signal. b) For large grating sizes, where there is a large volume of substrate between nanostructures, we observe more dependence of the signal on substrate CTE. This cannot, however, explain the period dependence of thermal transport we observe, as the period dependence only manifests for small gratings, where the sensitivity to substrate CTE is minimal, as shown.

3.2.3 Finite Element Analysis to Fit the Data

We analyze the change in EUV diffraction efficiency signal by fitting with an effective Fourier model, implemented in the FEA software, COMSOL [60]. See the appendix for more details. FEA calculations use literature values for the nickel, silicon and fused silica properties, as listed in Table 3.4. The thermal boundary resistivity at the nickel-substrate interface is taken as the effective fitting parameter. We simulate the thermal expansion and cooling of the nanolines for a variety of effective resistivities, and then calculate the diffraction of a Gaussian EUV beam from the dynamically changing surface using Fresnel propagation. The resulting calculated change in diffraction efficiency signal is then fit to the experimental signal to determine which effective resistivity best fits our experimental data. This effective resistivity contains both the intrinsic thermal boundary resistivity between the nanolines and the substrate, as well as an effective correction that is larger for greater deviations from diffusive thermal transport near the nanolines. The intrinsic thermal boundary resistivity should be constant across all gratings, independent of size and spacing, as all gratings on a given substrate were fabricated simultaneously. Therefore, trends in the best fit effective resistivity as a function of experimental geometry are due to the measured thermal transport's deviation from the diffusive prediction.

Material Properties	Nickel	Silicon	Fused silica
c_p at 300K (J/kgK)	456.8 [20]	710.0 [61]	830.2 [9]
k_{bulk} (W/mK)	90.9 [62]	149.0 [62]	1.19 [63]
Poisson's Ratio	0.31 [64]	0.27 [64]	0.17 [65]
Young's Modulus (GPa)	200 [66]	131 [67]	72 [65]
α, linear coefficient of thermal expansion (10^{-6}/K)	12.77 [68]	3 [69]	0.54 [65]
ρ, density (kg/m^3)	8910 [62]	2330 [62]	2650 [70]

Table 3.4: Parameters used in FEA multiphysics simulations.

3.3 Results and Discussion

Using the approaches described above to obtain and analyze our data, we characterize nanoscale thermal transport in silicon and fused silica. To fit and interpret the effective resistivity parameter obtained from COMSOL, we use the suppression function approach from [20].

3.3.1 Collectively Diffusive Model

Here, I summarize the suppression function approach used to fit our measured trends, as described in detail in [20]. The collectively diffusive model relates each grating geometry to all the phonon modes' contributions to the thermal transport, according to the suppression function formalism [57, 71]. The different MFP phonon modes' contributions to the total thermal conductivity are suppressed depending on the linewidth and reintroduced depending on the period of the grating. The suppression function is defined as

$$S(L,P,\Lambda) = tanh\left(\frac{L}{2\Lambda}\right) + \left[1 - tanh\left(\frac{P}{2\Lambda}\right)\right], \quad (1)$$

where Λ is the MFP of a given phonon mode. Applying this suppression function to the bulk differential thermal conductivity spectrum of the substrate, $k(\Lambda_i)$, we obtain an effective nanoscale conductivity for each grating geometry,

$$K_{nano} = \sum_i k(\Lambda_i) \cdot S(L,P,\Lambda_i), \quad (2)$$

where the sum is over each MFP mode, Λ_i. The model for the collectively diffusive effective resistivity is then defined by

$$r_{eff} = d * ln\left(\frac{P}{L}\right)\left(\frac{1}{K_{nano}} - \frac{1}{K_{bulk}}\right) + r_{tbr}, \quad (3)$$

where r_{tbr} is the intrinsic thermal boundary resistivity, K_{bulk} is the bulk thermal conductivity of silicon, and d can be interpreted as the depth into the substrate where transport is affected by the nanoscale geometry.

We additionally compare our results to the isolated quasiballistic heat source model for 1D gratings, as presented in [9, 20], where no collective effects take place. The predictions of this model represent an

upper limit to the transition region between collectively diffusive and isolated quasiballistic transport, which our measurements explore. The isolated quasiballistic model gives an effective resistivity of

$$r_{isolated} = \frac{4\Lambda_{gray} d}{3K_{bulk}(L/2)ln(P/L)} + r_{tbr}, \quad (4)$$

where Λ_{gray} is the gray MFP approximation for the substrate (single, average MFP). Note that this model does not take the fully ballistic limit into consideration, so it may not be valid at extremely small grating sizes. It is presented here as a reference limiting case, using a previously-derived model.

3.3.2 Silicon and Fused Silica Results

First, we compare a series of gratings with constant period with another series of gratings with 25% duty cycle, both on a silicon substrate. For the 25% duty cycle gratings, as the linewidth is decreased from 1000nm to 20nm, the effective resistivity first increases due to the quasiballistic deviation from diffusive transport, then decreases due to collective effects, as shown in Fig. 3.7(a) (blue points). At the smallest sizes, the effective resistivity approaches the diffusive, uniform heat source limit, where there is only the intrinsic thermal boundary resistivity, which has no effective correction due to nanoscale effects (black dashed line, Fig. 3.7(a)). The reduction in effective resistivity occurs when the period becomes comparable to the dominant heat carrying phonon MFPs in silicon at room temperature (≈300nm). These findings are in good agreement with our previous work, as illustrated in Fig. 3.8.

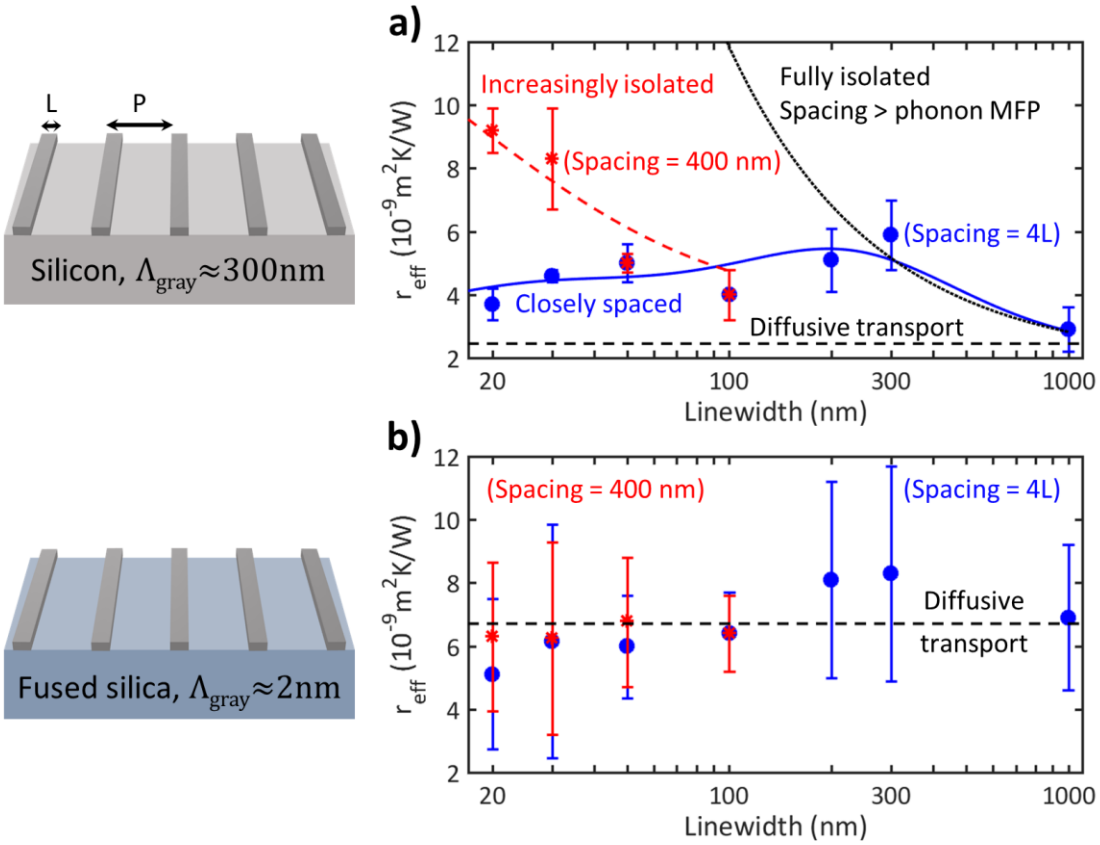

Figure 3.7: Best fit effective thermal boundary resistivity for nanolines on silicon and fused silica. a) For silicon (gray MFP≈300nm [20, 57]), as the linewidth is reduced below 50nm, the effective resistivity of the constant 25% duty cycle gratings (blue points) decreases, which is a return towards the diffusive prediction (thin film case, black dashed line). In contrast, the constant 400nm period gratings' resistivities increase as the linewidth is reduced (red points), mapping the transition from dominant collective effects towards isolated quasiballistic thermal transport (isolated prediction, black dotted line). The blue solid line is the 25% duty cycle collectively diffusive prediction from [20], whereas the red dashed line is a fit with the same model to the new data. b) For fused silica, the resistivities of constant duty cycle (blue points) and 400nm period (red points) gratings all agree within error bars. This indicates that there is no non-diffusive transport that depends on experimental geometry for this short phonon MFP material (~2nm [9]), and that there are no dominant systematic errors coming from the grating geometry independent of the sample substrate material. The dotted line is the average of all grating resistivities on fused silica (6.7nKm^2/W). Error bars in (a) and (b) are calculated by the standard deviation of best fit values from multiple measurements.

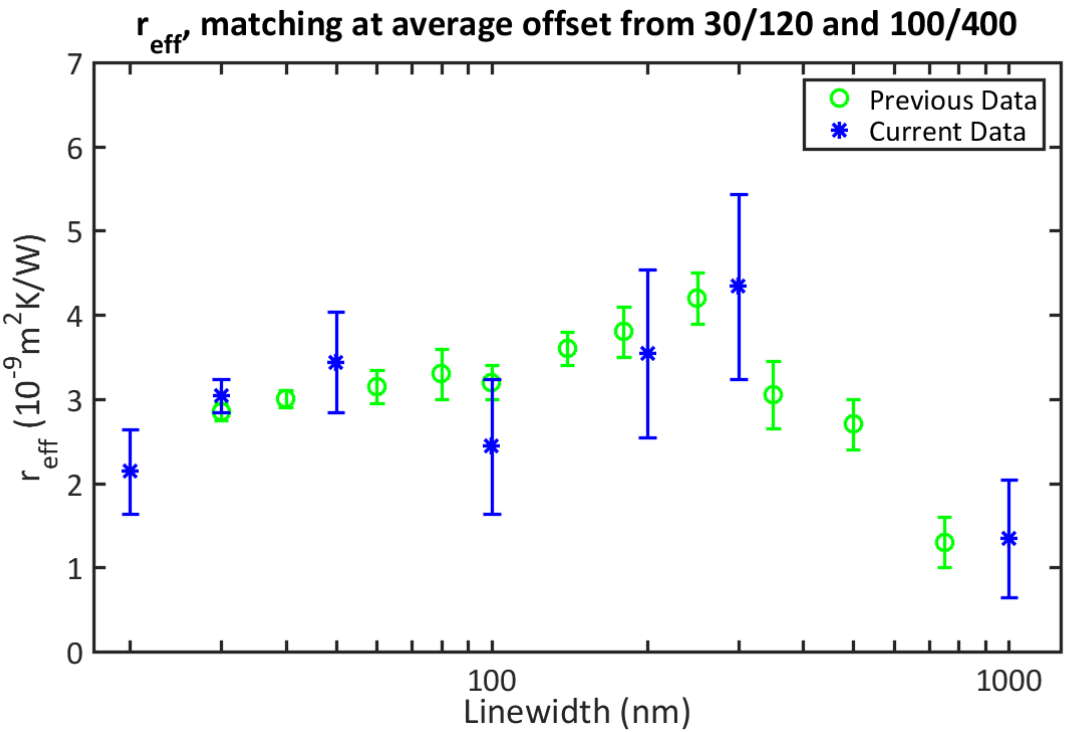

Figure 3.8: Comparison to previous measurements on silicon. The data of Hoogeboom-Pot, et al. [20] are shown in green and the present data are shown in blue. The two samples were fabricated from two different silicon wafers at two different times, so we expect a constant offset between the two data sets coming from different intrinsic thermal boundary resistivities, which are determined by fabrication conditions. To compare trends in the two data sets in this plot, we subtracted a constant 1.56m^{2}nK/W from all points in the current data set. This constant offset was calculated as the average difference between previous and current resistivities, weighted by the current study's uncertainty, of the 30nm and 100nm gratings, which are the only identical geometries between the two data sets. We observe good agreement between the previous and current studies. This same experimental offset was added to the collectively diffusive model fit, intrinsic r_{tbr} fit, and isolated quasiballistic model fit from the previous study to plot them with the new data in Fig. 3.7(a).

As the grating period is increased for a fixed nanoline width, we would expect that thermal transport will become less efficient, if the models developed in [20] are valid. Fig. 3.7(a) plots the effective resistivity (red data points) as the period is increased from the collectively diffusive regime (blue data points). These values are seen to increase significantly when the period is increased, confirming model predictions. Considering now the trend in the red data points alone, the grating linewidth is reduced from 100nm to 20nm at a constant 400nm period. Thus, the heat sources become increasingly isolated and the increasing effective resistivity maps the transition from collectively diffusive toward isolated quasiballistic transport. To successfully fit the 400nm period data, we use the collectively diffusive model described by Equations 1-3, applied to all the new data. As shown by the red dashed line in Fig. 3.7(a), this predictive model

provides good fits, even in the intermediate regime, where heat sources are neither isolated nor closely spaced.

These measurements on silicon represent the direct observation that the more closely spaced heat sources cool more quickly for sufficiently small periods at early times. At larger periods and linewidths, we do not observe this effect within our uncertainty, as shown in Fig. 3.9(a). Our observed trends for different periods over the full range from 20nm to 300nm linewidth gratings with the full effective Fourier analysis have not been previously reported and reveal that bringing heat sources closer together can bring the thermal transport within a factor of 2 of the diffusive prediction, even for heat source sizes far below the dominant heat carrying phonon MFPs. We further conclude that this effect is only dominant when grating periods are below the substrate MFPs, which is further supported by our control study on fused silica. We note that our best fit effective resistivities in the present work are close to the resistivity calculated from the corresponding thermal boundary conductance measured by time-domain thermoreflectance (TDTR): 5.1±0.3nKm^2/W, converted from [72]. Some difference is expected due to differences in sample fabrication and the effective correction we add to the intrinsic thermal boundary resistivity to capture non-diffusive effects in the substrate.

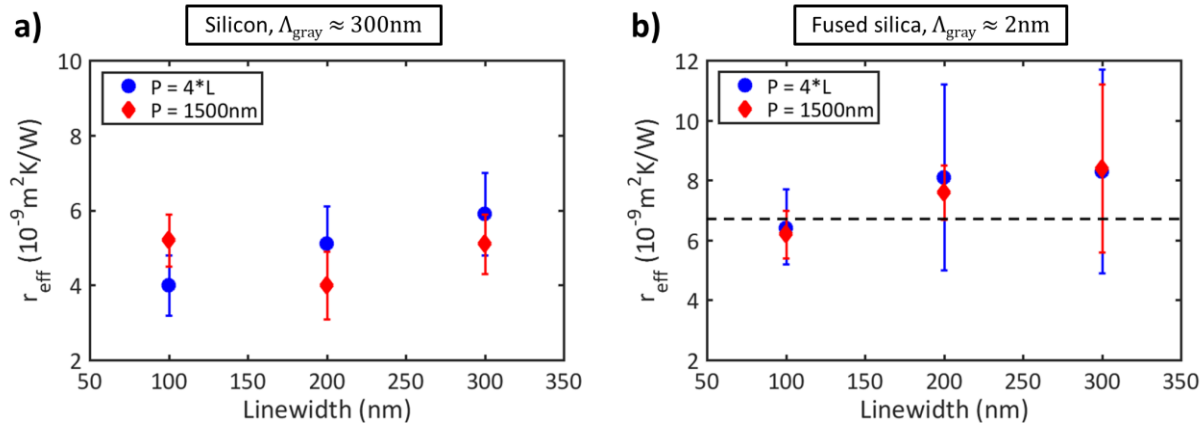

Figure 3.9: Results for the constant 1500nm period series of gratings. I compare constant period gratings (red diamonds) to constant 25% duty cycle gratings (blue points) at large linewidths. a) For silicon, we observe no period dependence in effective resistivity within error bars. This lack of period dependence is likely because these grating periods are still large compared to the mean free paths of the dominant heat carrying phonons in silicon at room temperature (≈300nm), and because the percent change in periods for large linewidths is not as great as in the small linewidth case, where period dependence was observed. b) For fused silica, the 1500nm period gratings agree with both the 25% duty cycle gratings, and the average of resistivities fit for all grating geometries on fused silica (dotted line). This indicates there is no deviation from the diffusive prediction, as expected for this short MFP (~2nm) material.

Next, we perform the same series of measurements on nanolines fabricated on a fused silica glass substrate, where the phonon mean free paths (≈ 2nm) are small compared to our experimental geometries, and therefore no deviation from diffusive transport would be expected. The phonon mean free paths of fused silica can be estimated as only a few nanometers at room temperature [9], and non-propagating modes (diffusons) that contribute to the thermal conductivity should not be affected by our geometries [53, 73]. Thus, these data serve as a control to confirm that plasmonic or other effects in the nanolines do not influence our Si measurements. Indeed, as shown in Fig. 3.7(b), the effective resistivity that best fits our data is constant, within error bars, for all linewidths and periodicities. It should be noted that the error bars for the fused silica data, calculated from the standard deviation of multiple measurements, are larger than in the silicon case due to two factors. First, experimental noise was larger, and second, our fitting has decreased sensitivity for low conductivity samples where the thermal transport into the substrate is dominated by substrate conductivity rather than thermal boundary resistivity. The thermal boundary resistivities we fit for fused silica are consistent within error bars with previous measurements using this technique, with only a small offset we attribute to differences in the glass substrates and sample fabrication conditions [9].

3.3.3 Comparison to Other Experiments and Theory

Some care must be taken when comparing the results of the current study to TDTR measurements reported in the past on nanostructured systems [54-56]. We note that this comparison can be beneficial for an improved understanding of the physics that is present in all three cases. Zeng, et al., use periodic nanoline transducers, like we do, but with a constant sub-wavelength gap to avoid directly optically exciting their substrates of interest. This results in a decreasing duty cycle with decreasing heat source size, so their measured monotonic deviation from the diffusive prediction is not necessarily inconsistent with our results. Indeed, their analysis shows that higher duty cycle gratings have higher effective conductivities, which agrees with our direct observations.

Oyake, et al., and Hu, et al., both also measure fused silica substrates, but both use different approaches compared to us to obtain nanoscale heat sources. Oyake, et al. use aperiodic gold nanoislands formed by annealing a gold film on their substrate of interest. While the authors' results are generally consistent with the other TDTR experiments, they observe suppressed thermal transport in fused silica as a function of heat source size. This is inconsistent with both our results on fused silica, and those of Hu, et al., where no size-dependence is observed down to 30nm. I tentatively attribute this difference to our different transducer designs, though the effects of periodicity versus aperiodicity are beyond the scope of the present work. Hu, et al., use a hybrid transducer to generate nanoscale 2D heat sources at a constant 50% duty cycle without directly optically exciting their substrates of interest. Their measurements of fused silica agree with ours – no non-diffusive transport is observed. The authors also show results for 2D (nanocube) gratings of constant period but decreasing linewidth on silicon, and they observe a similar monotonic deviation from the bulk Fourier prediction as we observe for that case.

All three TDTR measurements differ from our results, however, in that they never observe a return towards the diffusive prediction at constant duty cycle, when the heat source period is comparable to the dominant substrate phonon mean free paths. The reason for this difference might come from the different experimental temporal frequencies, as suggested by recent work by Hua and Minnich [74].

In their work, Hua and Minnich cast the Boltzmann transport equation (BTE) for phonons into the spatial frequency domain, under the relaxation time approximation, and apply it to nanoscale grating transducer geometries. They find that, due to the interplay of cross-plane and in-plane quasiballistic effects, thermal transport can indeed deviate from, and then return to, the diffusive prediction at constant duty cycle, but this will happen at smaller grating sizes for higher temporal frequencies of heating. For our EUV nanometrology measurements, we use a laser amplifier system to generate high harmonics at a few kilohertz repetition rate. In contrast, the TDTR measurements use laser oscillators with a repetition rate of ≈80MHz, modulated in the megahertz range as well. This difference might explain the difference between the EUV nanometrology and the TDTR measurements. Note that the authors also predict a greater deviation from diffusive transport for smaller duty cycle gratings, which is consistent with both our work and Zeng's.

Other theoretical approaches are in development that are very promising for explaining the fundamental mechanism behind our observed return towards the diffusive prediction. First, hydrodynamic and super-diffusive views of the BTE show lower temperatures near nanoscale heat sources than the temperature predicted by effective Fourier models [75-77]. This indicates these models capture physics excluded by effective Fourier approaches. The hydrodynamic formulation is particularly useful, as it provides a physical intuition for how quasiballistic effects appear as a vorticity of the heat flux, and it captures sufficient complexity to be fully predictive of our data, down to L=300nm, using only first principles inputs [78]. However, the present form of this model has been shown to not hold for constrictions smaller than twice the hydrodynamic length (176nm for silicon at room temperature) [79]. This could be the cause of the model's loss of predictive power when the experimental measurements return towards diffusive behavior at the smallest sizes. We are collaborating with the Alvarez group from Universitat Autònoma de Barcelona to see if modifications to the level of approximation currently in the hydrodynamic approach can explain our experimental findings.

Finally, it has been predicted that coherent effects such as local resonance can modify the thermal transport in nanostructured systems, even at room temperature [18, 50]. According to lattice dynamics and molecular dynamics (MD) calculations, nanostructures can behave as local resonators that hybridize with phonon branches in the substrate to create a lower group velocity, and thus slower thermal transport. This is a metamaterial effect which occurs at room temperature and tens of nanometer dimensions. In contrast, holey-membrane-based phononic crystals rely on phonon coherence effects that require low temperatures or few nanometer dimensions to have hole periods comparable to the phonon wavelength [80, 81]. Thus, local resonance effects could be more plausible in our experiment, though the strongest effects are expected for nanostructures with much higher aspect ratio than those used in our experiment [50]. Currently, the mechanism behind the collectively diffusive regime is unclear, but we are pursuing MD simulations of our geometries in order to understand the mechanics governing our observations at an atomistic level.

In collaboration with the Hussein group at CU Boulder, we have performed non-equilibrium MD simulations of heated silicon nanolines on a silicon substrate. This avoids the ambiguities related to heat

transfer across dissimilar material interfaces and focuses instead on effects related to periodic heating and nanostructuring. As shown in Fig. 3.10(b), the temperature profiles obtained by MD exhibit the same effect predicted by hydrodynamic and superdiffusive models, where the temperature near the nanostructure is lower than that predicted by diffusion. Significantly, as we reduce the nanostructure size at constant 50% duty cycle, we observe the temperature profile first deviate from the diffusive prediction and then return towards diffusive behavior, as calculated by FEA (Fig. 3.10(a)). This agrees with our experimental findings of the collectively diffusive regime, and we are now further analyzing the MD data to determine what the mechanism is for the return towards diffusive behavior for the smallest grating linewidths and periods.

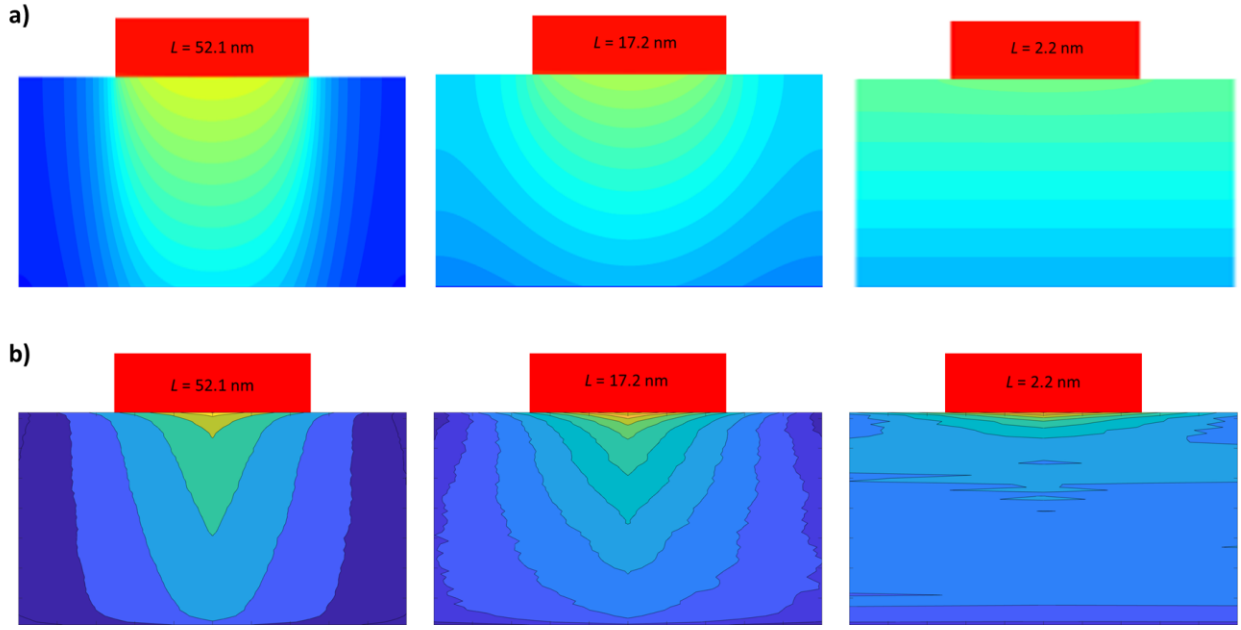

Figure 3.10: MD temperature profiles compared to the diffusive prediction. a) Using FEA, we calculate the temperature field in a silicon substrate beneath three different nanoline widths, assuming diffusive transport. b) Using MD, we calculate the local temperature for bins of atoms in the substrate, using the same geometries as FEA. Note that the pointed temperature contours in the middle of the simulation cells are artifacts from using only three bins in the in-plane direction, but this does not change our conclusions. Comparing (a) and (b), we observe the largest linewidth results agree well. However, for the middle linewidth, MD shows the substrate surface furthest from the nanoline is cooler than the diffusive result. This leads to a "lightbulb" temperature field in the substrate not obtained using FEA. At the smallest linewidth, this effect is reduced in MD, and the temperature field bears more similarity to the diffusive prediction by FEA. The duty cycle of all gratings shown is 50%. Simulations courtesy of Hossein Honarvar in (b), and Joshua Knobloch in (a).

3.4 Conclusions and Future Work

We use ultrafast, coherent EUV beams to measure the thermal transport away from periodic gratings of laser heated nickel nanolines with varying linewidth and spacing on both single-crystal silicon and amorphous fused silica substrates. We observe quasiballistic transport that deviates from the diffusive prediction for nanolines on silicon and model this behavior with a higher effective thermal boundary resistivity between the nanolines and the substrate. We observe that quasiballistically suppressed thermal transport returns towards the diffusive prediction when the nanoline spacing is comparable to the dominant phonon mean free paths in the substrate. This period dependence confirms our previous prediction that closely spaced heat sources can initially cool faster than widely spaced ones and is now quantified to be a significant effect in silicon, bringing the thermal transport within a factor of 2 of the diffusive, uniform heat source limit. Measurements on a fused silica substrate displayed no quasiballistic behavior down to heat source sizes of 20nm. Our observations are in general agreement with other experimental and theoretical works. More work is needed to describe the fundamental physics behind these collective effects, and we are pursuing first principles models to determine the fundamental mechanisms underlying these behaviors.

In the near future, we expect to have a comprehensive explanation of our experimentally observed phenomena, using a combination of hydrodynamic thermal transport models and MD simulations. We will also perform new measurements of nanoscale thermal transport at sizes that reach fully into the ballistic regime, where no phonon modes behave diffusively. In this regime, we can expect thermal decay times comparable to the lifetime of phonon modes. Here, it may be useful to consider the coherent oscillation of phonons, which is the subject of the next chapter. Chapter 4 presents our work using coherent acoustic waves to characterize the elastic properties of nanoscale materials.

Chapter 4

Thin Film Elastic Properties

Thin films from micron to nanometer to single atomic layer thicknesses present a rich field of study, both for practical applications and fundamental materials science. Thin films are an enabling technology for items we use daily, such as scratch-resistant eyeglasses or protective linings in soda cans. Extending to the nanoscale, patterned ultrathin films form the basis of all modern integrated circuits. From a fundamental perspective, ultrathin films are a class of nanomaterials, which can exhibit significantly different properties from bulk materials due to their nanoscale thicknesses. There is much work still to be done in exploring how different materials change once made ultrathin, where surfaces and interfaces become a significant fraction of the material volume. One change that takes place at the nanoscale, which is also very difficult to measure experimentally, is deviations in the elastic properties that govern the mechanical performance of ultrathin films.

In this chapter, I will describe our work characterizing the elastic properties of ultrathin films down to 5nm thickness. I will first survey the main areas of interest for these films (semiconductor applications and fundamental thickness-dependent changes) and then describe our experimental approach to characterize the full elastic tensor of these films. I will then present results on a series of films with varying hydrogenation levels, and a series of films with varying thicknesses.

4.1 Introduction and Motivation

The number of transistors on a chip has doubled every two years for decades, an observation known as Moore's Law. To continue increasing computing power at this rate, the semiconductor industry needs materials innovation beyond simply making systems smaller. One significant challenge that requires new

materials to solve comes from scaling down the metal interconnect structures that electrically connect the different layers throughout an integrated circuit. Each pair of closely spaced metal wires in the interconnect and routing structure, shown in Fig. 4.1(a), can be thought of as a parallel-plate capacitor, as illustrated in Fig. 4.1(b). In essence, the metal interconnects and routing form an unintentional network of resistor-capacitor (RC) circuits. This decreases the efficiency of the device as power is lost to parasitic capacitance [82]. It also limits the switching speed of the device once the characteristic relaxation time for RC circuits ($\tau = RC$) approaches the transistor speed [12]. This problem becomes substantial as device dimensions are scaled down, because shrinking the wires increases their resistance, and bringing them closer together increases their capacitance. To overcome the challenges of parasitic capacitance and RC time delay, there is a great need for new low dielectric constant (k) materials to serve as the interlayer dielectric and reduce the overall capacitance of the interconnect structure.

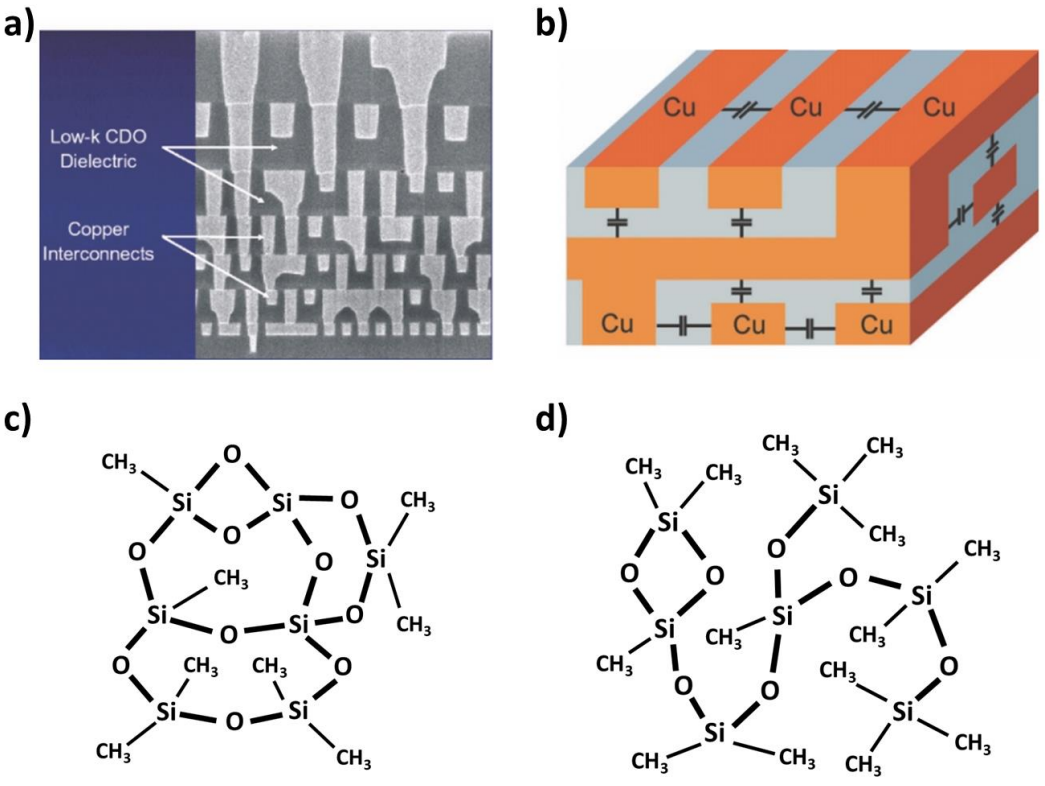

Figure 4.1: Low-k dielectrics for metal interconnects. a) Cross section of metal interconnect structure at the 90nm node. b) Schematic of the resulting RC circuits. c) Schematic of SiO_2 with few terminal groups added, and the rigid network emphasized in bold. d) Schematic of SiO_2 with many added terminal groups and a less interconnected network. a) and b) from [12], c) and d) modeled after [83].

To lower the dielectric constant of materials, one approach is to fabricate materials with fewer polar bonds. In practice, this has meant either introducing terminal CH_3 groups into the amorphous SiO_2 historically used as the interlayer dielectric (shown in Fig. 4.1(c)) or using less polar materials like SiC. Additional hydrogenation for Si-H bonds further reduces the dielectric constant. Note the other main approach to engineering new low-*k* materials is to introduce porosity or air gaps. While all the results in this chapter are for non-porous films, I will show measurements of porous silicon in Chapter 5.

The main challenge in these routes to lowering *k* is that hydrogenation and porosity also change the elastic properties of these materials, which in the extreme can lead to mechanical failures of the device, such as delamination of layers. Hydrogenation terminates bonds and lowers the network connectivity of the overall material, as illustrated in Fig. 4.1(d). Once a critical level of network connectivity is reached, the material loses its rigidity, and several material properties, including Young's modulus, Poisson's ratio, thermal conductivity, and electrical resistivity behave fundamentally differently [22, 82, 84]. Thus, it is very important to have reliable measurements of low-*k* films' elastic properties to feed forward and inform the design of integrated circuit architectures.

The other consideration for the elastic properties of ultrathin films, beyond their chemical composition, is the presence of changes that come from nanoscale dimensions alone. The fundamental mechanisms of thickness dependence in elastic properties are generally related to the high proportion of atoms at the surface of the material, as opposed to in the bulk volume. However, the final effect on elastic properties varies from system to system and can make the film either softer or stiffer than the bulk prediction [13, 85]. Additionally, high residual strain in thin films [86], fabrication-dependent changes like grains and islands in thin film deposition [87, 88], or density gradients and interlayer mixing [89, 90], can all lead to different elastic properties from bulk. In the present work, however, I focus on elastic property deviations coming fundamentally from surface effects.

Atoms at the surface of a material generally have a lower coordination number, or number of nearest neighbors, than do atoms in the bulk. This can be imagined by cutting through an infinite atomic lattice to form an outer surface, leaving dangling bonds on the surface atoms, reducing their number of

nearest neighbors. In reality, these dangling bond defects will be passivated, for instance by H, but such terminal groups will still reduce the average coordination number of the surface [84, 91]. Note that surfaces can be made that are not undercoordinated, even down to a monolayer of material, depending on how the film is grown [92]. Indeed, defect-free sheets of graphene have been shown to reach the intrinsic strength of the carbon bonds – the highest strength achievable for that material [93]. For most materials, however, this will not be the case.

When surface atoms are under-coordinated, this can make the surface softer or stiffer due to two competing effects. Surfaces soften due to bond loss and under-coordination, making them less rigid [85]. This mechanism is conceptually similar to how terminal groups in the bulk of low-*k* films reduce network connectivity and soften the entire film. Softening in thin films has been experimentally observed in systems such as TiN films (along with increasing strain) [94], in nanoscale Si cantilevers and films [95, 96], and in amorphous polymer films [97]. Surfaces can also stiffen, however, as the electrons redistribute for the under-coordinated surface atoms. This can lead to charging or contraction of the remaining bonds, which stiffens the surface [83, 98]. Stiffening has been observed in Au films [99], Pt films [86], and Fe films [100]. In the latter case, Pt films were also measured, and the two films softened with decreasing thickness first, then stiffened for the smallest sizes. Also, the measured strain in Pt and Fe films trended in opposite directions. In addition to single films, there have been many observations of softening in multilayers [14], though in this case interface effects can be dominant over surface effects. Our group has previously measured Ni/Ta bilayers and observed evidence of simultaneous softening of Ni and stiffening of Ta [32]. The work I present here, however, focuses on single films, aiming to isolate surface effects.

It should be noted that surface effects can also mediate large plastic (permanent) deformations to nanoscale materials. This can be related to the surface atomic coordination and exhibits a strong size-dependence. Taking advantage of this effect enables the destructive testing of thickness dependent elastic properties [97, 101]. For the work I present here, however, we require only elastic deformations that are non-destructive to characterize thin film elastic properties.

Thickness-dependence in elastic properties can be modeled using continuum approaches considering surface and bulk energies [96, 102, 103]. These approaches naturally account for surface stress and predict the strongest deviations in elastic properties usually for only 1-2nm films. One notable exception is [96], where the authors derive a strain-dependent critical thickness at which surface energy equals bulk energy. According to their calculations and nanoindentation measurements, this thickness can be tens of nanometers in silicon, though in general sub-micron nanoindentation measurements need careful analysis as it is difficult to avoid substrate influence [104, 105]. Molecular dynamics and statics approaches are also very valuable in modeling nanoscale elastic properties as they explicitly incorporate atomic coordination effects, and long-range non-bonding effects [83, 85, 106]. Particularly in [85], the authors use molecular statics to show only the outermost atomic layer is softened due to under-coordination, but this can cause softening of nanowires up to 20nm in diameter.

Considering the industrial and fundamental interest in nanoscale film elastic properties as a function of chemical composition and thickness, I now present measurements of the elastic properties of three series of amorphous low-*k* ultrathin films. The first is a series of SiC:H films with varying levels of hydrogenation and thicknesses above 50nm, where we observe divergence towards incompressible behavior once a critical number of bonds are terminated. The second series is a trio of SiOC:H films with identical chemical composition, and a range of thicknesses down to 11nm. We observe no deviations in the elastic properties of these films. The final series is a pair of SiC:H films with nominally identical composition and thicknesses of 50nm and 5nm, where we observe significant softening for the thinner film.

4.2 Experimental Methods

In Chapter 2, I outlined the general procedure for our EUV diffraction experiments. I now present the details of how we analyze the measured data to extract thin film elastic properties. The approach we use is similar to picosecond ultrasonics with a structured transducer and SAW spectroscopy, which have both been used previously to characterize thin film systems [94, 107-109]. However, our technique extends to thinner, device-relevant film scales, enabled by the nanoscale sensitivity of our EUV probe, and by accurate

finite element analysis of our systems [22, 32, 42]. In the following section, I will describe in detail how I extend our established technique to thinner films, with special emphasis on the aspects of the analysis that require the most expert input to correctly identify acoustic dynamics.

4.2.1 Sample Design

All the samples characterized in this chapter are amorphous, dielectric ultrathin films deposited on silicon (100) by Intel. The films consist of either SiC:H or SiOC:H and are assumed to be isotropic. The films are fabricated by plasma enhanced chemical vapor deposition from diluted silane precursors, according to [82, 110, 111]. Nanoindentation and Rutherford backscattering (RBS) characterizations are performed by Intel on thicker films of nominally the same material, while X-ray reflectivity (XRR) measurements are performed on the ultrathin films to obtain their thicknesses and densities. Results are summarized in Table 4.1 for the hydrogenation-dependent study and in Table 4.2 for the thickness-dependent study. The only inputs required a-priori for our analysis are thickness and density, but nanoindentation and RBS provide a nominal Young's modulus value to compare to and reveal the films' compositions and network connectivities, respectively. Also note that these films strain the silicon substrate, which can be used to tune the Si electron mobility, as in [112]. Studying this is beyond the scope of this work, but the acoustic waves are highly sensitive to strain, so it must be included in our fitting.

Film name	Thickness (nm)	Young's (GPa)	Density (g/cm^3)	Network Connectivity
63	65.8	4.7	1.3	2.02
7	103.2	13.05	1.9	2.39
5	131.6	12.87	1.8	2.43
75	95.3	33.12	1.8	2.56
65	97.9	62.08	1.9	2.62
9	103.3	153	2.2	3.06
49	83.6	175	2.7	3.2

Table 4.1: Hydrogenation-dependent thin films nominal properties. From [22]. Thicknesses and densities are measured by X-ray reflectivity (XRR). Young's modulus is measured for thicker films of the same material with nanoindentation. Network connectivity is calculated from Rutherford backscattering (RBS) measurements of elemental composition.

Film name	**145**	**148**	**155**	**335**	**503**
Film material	$SiO_{1.2}C_{0.3}$:H	$SiO_{1.2}C_{0.3}$:H	$SiO_{1.2}C_{0.3}$:H	SiC:H	SiC:H
Thickness (nm)	43.75	18.73	10.9	50	5
Density (g/cm^3)	1.5±0.1	1.5±0.1	1.5±0.1	2.5±0.1	2.5±0.1
Young's (GPa)	19±2	19±2	19±2	210±10	210±10
Hardness (GPa)	3.0±0.5	3.0±0.5	3.0±0.5	26.1±1.5	26.1±1.5
Stress (MPa)	50	50	50	6±1	6±1
k	3.3±0.1	3.3±0.1	3.3±0.1	7.2±0.2	7.2±0.2
RBS %Si	20.27	20.27	20.27	37.1	37.1
RBS %O	34.03	34.03	34.03	0.3	0.3
RBS %C	15.50	15.50	15.50	36.3	36.3
RBS %H	30.20	30.20	30.20	26.3	26.3
Network Connectivity	2.4	2.4	2.4	3.2	3.2

Table 4.2: Thickness-dependent thin film nominal properties. The listed properties are measured via XRR, RBS, and nanoindentation on thicker films of nominally the same material. The thicknesses listed for films 335 and 503 are the nominal deposited thicknesses. See Section 4.3.2 for complete TEM measurements of these samples. SiOC:H data are from [110], with further information provided by Intel, and SiC:H data are from [82] and [111].

Once the films are deposited by Intel, our collaborators at Lawrence Berkeley National Lab (LBNL) fabricate a set of nanoline gratings on top to serve as our transducers. The nanolines are fabricated by e-beam lithography and lift-off. As described in Chapter 2, we use nickel as the transducer material as it has good absorption of our 780nm wavelength pump laser and good thermal expansion to launch acoustic dynamics. The core-electron absorption edges of nickel are also well away from the 43eV photon energy of our probe beam, giving us minimal sensitivity to hot electrons, allowing us to observe acoustic dynamics down to few picosecond timescales. The nanolines are deposited to be ~12nm tall on average, to give strong diffraction and change in diffraction signal. The duty cycle (nanoline width divided by nanoline period) is maintained at 33% for all gratings. Each grating covers an area of 150μm^2, and is spatially separated by 200μm from the next nearest neighbor. Table 4.3 lists all of the grating linewidths, periods, and heights, as characterized by atomic force microscopy (AFM). Fig. 4.2 shows a schematic of a general thin film sample, as well as representative AFM and scanning electron microscopy (SEM) characterizations of these samples.

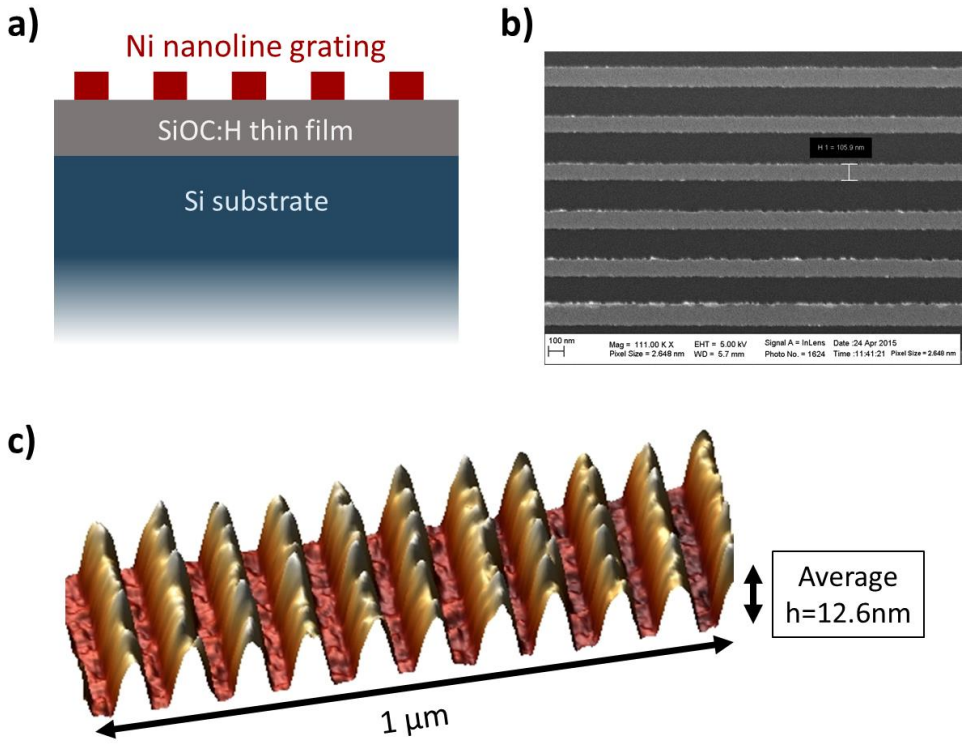

Figure 4.2: Thin film sample design and characterization. a) Schematic cross-section of the thin films samples. b) SEM image of a 100nm linewidth grating on film 145. Scale bar is 100nm. c) AFM height map of a 30nm linewidth grating on film 145. Average height is the average for that grating.

Film name	**145**	**148**	**155**	**335**	**503**
500(nm)/1500 (nm)	490/1540	510/1540	500/1510	540/1530	480/1520
350(nm)/1050 (nm)	350/1080	360/1080	360/1060	390/1060	330/1070
200(nm)/600 (nm)	240/610	210/620	220/610	230/610	170/610
100(nm)/300 (nm)	90/310	100/310	110/310	130/300	80/300
50(nm)/150 (nm)	40/160	40/150	50/150	80/150	40/150
30(nm)/90 (nm)	24/91	22/94	36/94	47/97	24/91
20(nm)/60 (nm)	19/61	20/62	24/62	-	26/62
15(nm)/45 (nm)	15/40	13/40	-	-	18/42
Average height (nm)	12.8	11.7	11.1	14.8	11.0

Table 4.3: Nanoline grating dimensions. All measurements made by AFM, with data processing in WSXM [58]. Values are stated as "linewidth/period" and organized by nominal sizes in the left-most column. The average height for all gratings on each film is listed in the final row. Note not every grating size was fabricated on every film, and the gratings on film 335 were fabricated by a different researcher than the others, and at an earlier date.

4.2.2 Data Processing and Interpretation

As described in chapter 2, the nanoline transducers simultaneously launch surface acoustic waves in the film and substrate (SAWs), longitudinal acoustic waves in the film (fLAWs), and longitudinal acoustic waves in the gratings' nanolines themselves (gLAWs). Each of these waves is sensitive to a different elastic property, and all are measured via EUV diffraction. Measuring the velocities of SAWs and fLAWs is sufficient to extract the two independent elastic constants of isotropic thin films. The gLAW velocity, on the other hand, accesses one elastic constant of the metal nanoline. Though not a complete characterization of the nanoline's elastic properties, measurements of these waves still provide important information about the mechanical properties of nanoscale materials, as shown in [32]. The gLAW frequency is also highly sensitive to the nanostructure's environment, providing information about the relative acoustic impedances between the nanoline and the film (open vs closed pipe modes) and about the presence of any additional mass on top of the nanoline (like a quartz microbalance). Generally, SAWs occur on long timescales (ns), while fLAWs and gLAWs occur on shorter timescales (ps), providing a natural separation for easy identification of the different waves. This is illustrated in Fig. 4.3.

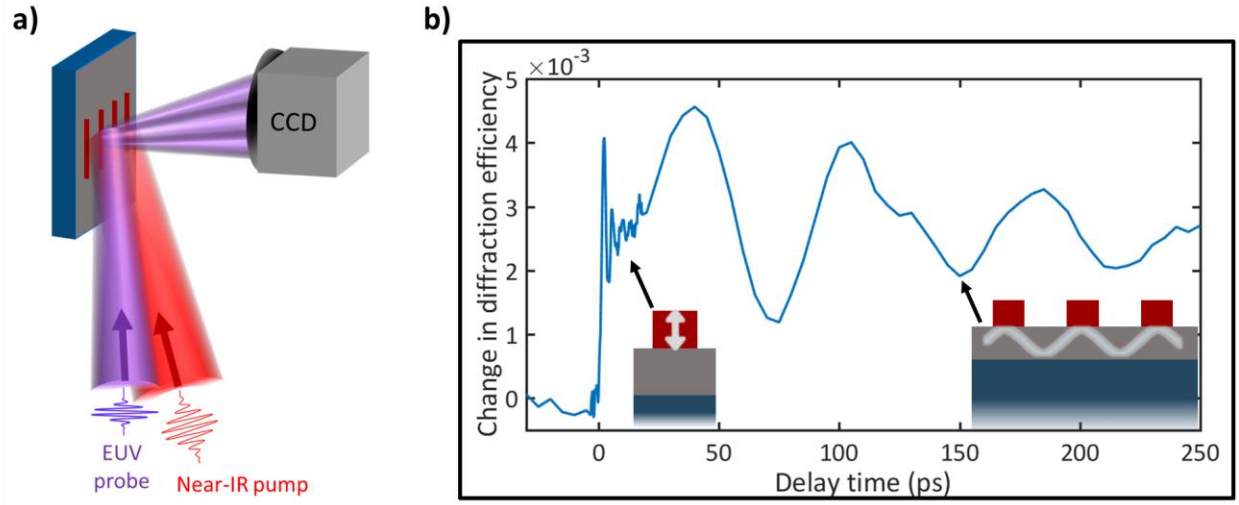

Figure 4.3: EUV diffraction measurement of thin film acoustic waves. a) Schematic of the EUV diffraction measurement. A near infrared (IR) pump pulse launches acoustic waves by impulsively heating nanoline gratings. After a controlled delay time, an EUV probe pulse diffracts from the surface into a CCD camera, recording changes to the sample surface profile. b) The change in diffraction efficiency (as a fraction of the integrated counts on the camera) shows a gLAW at early times, and a SAW at longer times. Insets show the waves that produce the two signals. Note this is a composite trace of two back-to-back scans on film 145 (100nm linewidth) with different time steps. No normalization was needed for alignment.

The SAW velocity in the film is the first of two pieces of information needed to characterize the film's elastic properties. From the temporal change in diffraction signal, e.g. that in Fig. 4.3(b), we extract the SAW frequency via chirp-Z transform. This is a generalization of the discrete Fourier transform that provides finer interpolation in the window around the SAW frequency [32, 113]. The wavelength of the SAW is defined by the nanoline grating period, which can then simply be multiplied by the SAW frequency to obtain the SAW velocity. The penetration depth of SAWs is confined to the surface by a fraction of the SAW wavelength. Because the SAW wavelength is defined by the grating period, we can tune SAW penetration from large depths (large gratings) primarily sensitive to substrate elastic properties, to very short depths (small gratings) that are fully confined within ultrathin films. We use this to independently characterize the substrate (e.g. slight shifts due do the film straining the substrate) and film elastic properties. An example of SAW velocity changing with confinement to softer films on stiffer substrates is shown in Fig. 4.4. Using an EUV probe is critical to this approach to characterizing ultrathin films. We have diffracted our 29nm wavelength probe from 45nm period gratings (far below the diffraction limit of visible probes), which confines SAWs to ~15nm thick films, and provides high sensitivity to even thinner films. Note, to extract the films' elastic properties, we must also account for the influence of the nanolines, which suppress the "unloaded" SAW frequency. This is discussed in the next section.

It is worth noting that all the analysis in this chapter uses only the fundamental SAW that is launched by each grating, though higher orders are simultaneously excited. The gratings that launch the waves can be approximated as a 33% duty cycle square wave, which is composed of a characteristic Fourier series of sine waves. This is the series of SAWs that are launched when the gratings uniformly impulsively expand. Because the Fourier series of each grating is also what defines the diffraction of our EUV probe (which spatial frequencies are present), the first, second, third, etc. SAW mode frequencies can be seen most clearly in the dynamic changes to the first, second, third, etc. diffracted orders. All of these SAWs lie on the same branch in the material's dispersion; the higher order SAWs simply correspond to higher wavevectors, and shorter penetration depths. It is possible that the weak presence of frequencies higher than the fundamental SAW frequency in the first diffracted order correspond to points on different branches in

the material's dispersion (different frequencies with the same wavevector), as in [114]. This is worth investigating, but it is beyond the current scope of this work.

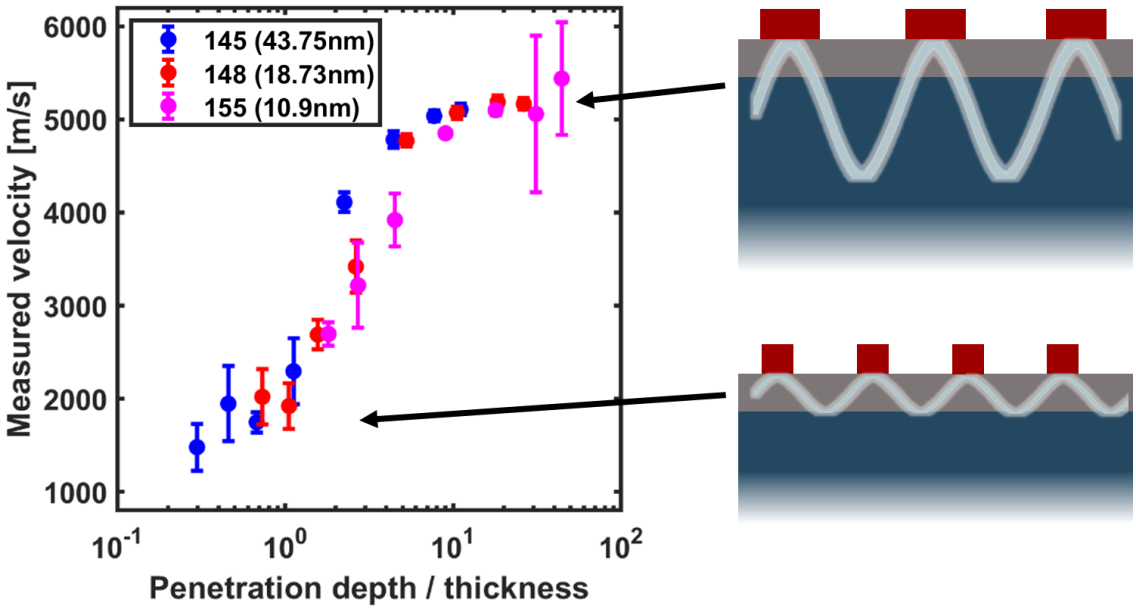

Figure 4.4: SAW confinement for the thickness-dependent study. Large penetration depths compared to film thicknesses (greater than 10x), converge to the SAW velocity of Si. For penetration depths less than or equal to the film thicknesses, the SAW velocity converges to that of the dielectric thin film.

At shorter times than SAWs, we measure a gLAW, which is each nanoline's vertical breathing mode, excited by its rapid thermal expansion. The gLAW generally decays within the first few tens of ps, completing only a few periods of oscillation before it drops below the experimental noise. This rapid decay of the oscillation makes a Fourier transform ill-suited to extract the gLAW frequency. Instead, we use the matrix pencil method (MPM), which performs a singular value decomposition on the data, then projects the singular values onto the family of complex exponentials [32]. The so-called scree plot, pictured in Fig. 4.5(a), shows how the singular values are naturally separated by this algorithm into single nodes that correspond to purely decaying exponentials, pairs of nodes that correspond to decaying oscillations, and a noise tail that embodies the rest of the data. The single and paired nodes can then be separately plotted and analyzed to isolate the frequencies present in the data. Fig. 4.5(b) gives an example of how the extracted exponents lie in the complex plane to give exponential decays (only real component) and decaying oscillations (pair of points with identical real components and opposite complex components).

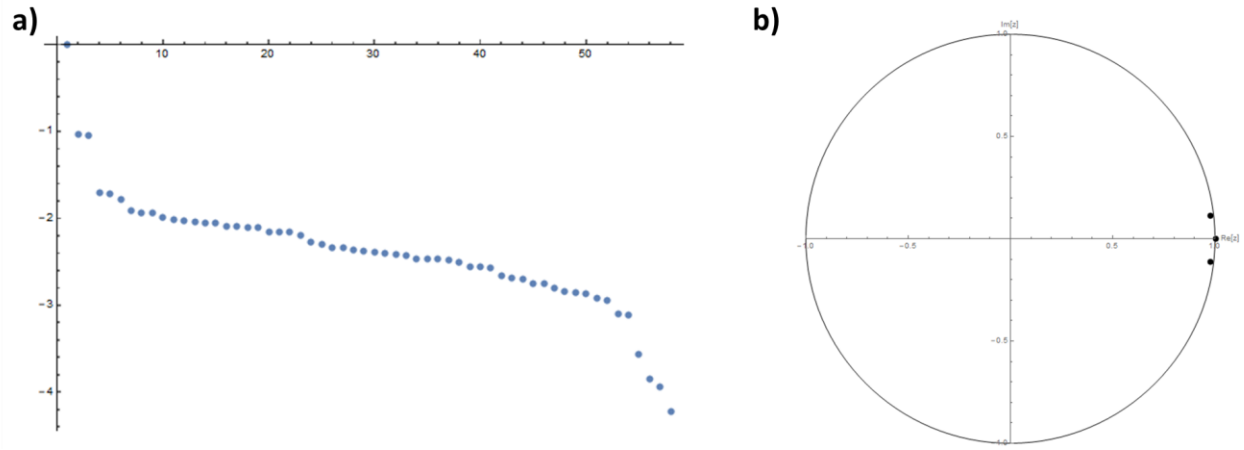

Figure 4.5: The matrix pencil method for frequency extraction. a) The algorithm performs singular value decomposition on the data and projects the singular values onto the family of complex exponentials. The scree plot, shown here, displays a single node that corresponds to a purely decaying exponential, a pair of nodes that correspond to a decaying oscillation, and a tail of closely-spaced nodes that embody the rest of the features in the data. b) Taking the first three nodes and plotting the values of their exponents in the complex plane, we can see that indeed the single point has only a real component, producing a pure decay, while the pair of points have equal real components and opposite complex components, producing a decaying oscillation. The waveform generated by these three nodes is compared to the data in Fig. 4.7(a).

The initial expansion of the gratings, in addition to launching gLAWs, generates a longitudinal pulse in the film – the fLAW mentioned above. The fLAW pulse reflects from the film-substrate interface with an amplitude and phase determined by the acoustic impedance mismatch between the two materials. When the fLAW returns to the surface, it causes a change in EUV diffraction efficiency. In general, the gLAW launches a pulse train of fLAWs into the film, though usually only the strongest, first pulse is observed above experimental noise. The round-trip time for the echo's arrival, combined with the known film thickness, gives the longitudinal velocity of the film. This is the second piece of information, along with the SAW velocity, that is needed to fully characterize the elastic properties of the film. Because the fLAWs do not have a well-defined frequency, they must be identified by eye rather than extracted by methods such as a Fourier transform. Due to the high level of expert input in their identification, the process used to analyze fLAWs must be carefully documented. It is especially important in the thickness-dependent study, where the films are thin enough that the fLAWs are not well separated in pump-probe delay time from the gLAWs. That is, the fLAW arrives before the gLAW has fully decayed.

To correctly identify fLAWs for thinner films, both fLAWs and gLAWs must be analyzed together. This is most evident for the 11nm thick film 155, where the first fLAW echo returns within the first gLAW oscillation. The ideal way to unambiguously distinguish the two waves experimentally would be to have a mechanism to tune the frequency of one, but not the other. Thankfully, the carbon deposition caused by the EUV probe does this automatically. Amorphous, hydrogenated carbon is deposited on the whole irradiated sample surface due to the high energy photons in our EUV probe beam breaking down residual hydrocarbons in our vacuum chamber [40]. The longer a given grating has been irradiated during measurement, the more carbon will have been deposited on the top surface of that grating. The presence of carbon on top of the nanolines lowers their gLAW frequency, whereas the fLAW return time remains unaffected, being dictated by subsurface interfaces. Thus, by observing which features shift with each repeated measurement, and which stay at the same pump-probe delay time, we unambiguously identify the fLAWs for this thin film, as shown in Fig 4.6(a). Furthermore, I use the shifting gLAW frequency to estimate how thick the deposited carbon layer is, which is confirmed by AFM, as in Fig. 4.6(b).

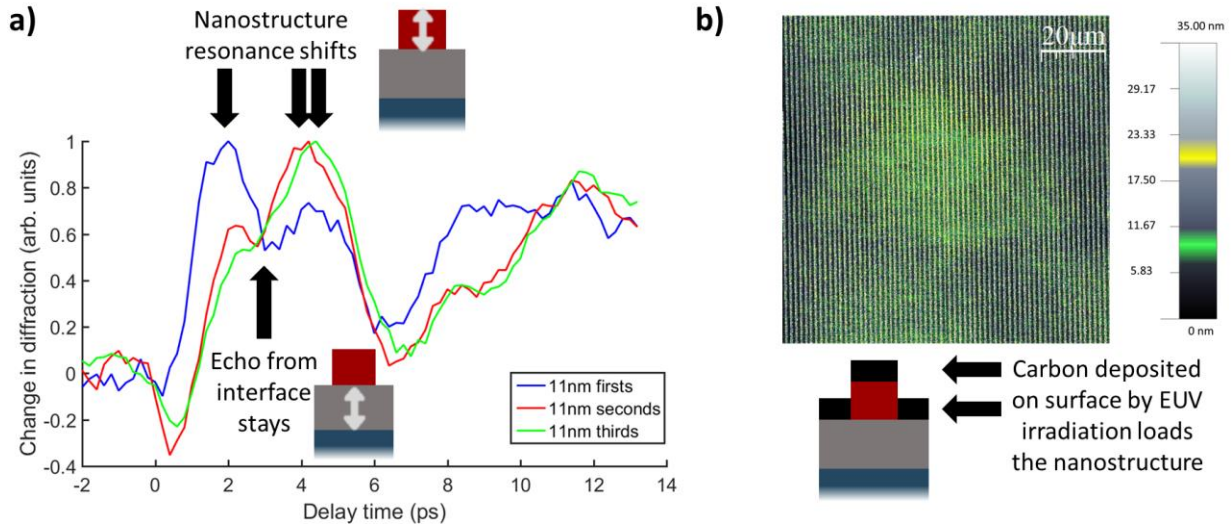

Figure 4.6: 11nm Film (#155) fLAW and carbon deposition. a) As carbon is deposited on top of the nanolines, the gLAW frequency lowers, while the fLAW return time from the film-substrate interface remains unaffected. Traces shown are averages of the first short time-window scan taken on each large linewidth grating on this film, then the second short scan on each grating, then the third. This approach did not carefully control exposure time, but simply ensured each average trace had more carbon deposition than the last. b) Large area AFM scan of 19m film (148), 500nm linewidth. Carbon on top of the nanolines is highlighted in yellow, while that on the substrate is highlighted in green. A horizontal lineout through the highest deposited area shows 7.4±0.5nm and 7±1nm of carbon on the substrate and nanolines respectively. Note film 155 was not available for AFM due to subsequent sample damage, but film 148 is representative.

To estimate the carbon deposition from the shifting gLAW frequency, I use the transfer matrix approach, following [32, 115, 116]. This approach is very precise, but the results are only approximate because exposures were not carefully controlled during the experiment – various long time-window scans were taken between the short time-window scans that were averaged together. To solve for the thickness of the carbon layer, I first define the acoustic transfer matrix for the vertical displacement of a wave traveling through the carbon and nickel layers from the transfer matrices of each material individually, considering that the displacement and stress must be continuous,

$$T = \begin{pmatrix} \cos\left(\frac{\omega d_{Ni}}{V_{Ni}}\right) & (\omega\rho_{Ni}V_{Ni})^{-1}\sin\left(\frac{\omega d_{Ni}}{V_{Ni}}\right) \\ -\omega\rho_{Ni}V_{Ni}\sin\left(\frac{\omega d_{Ni}}{V_{Ni}}\right) & \cos\left(\frac{\omega d_{Ni}}{V_{Ni}}\right) \end{pmatrix}\begin{pmatrix} \cos\left(\frac{\omega d_{C}}{V_{C}}\right) & (\omega\rho_{C}V_{C})^{-1}\sin\left(\frac{\omega d_{C}}{V_{C}}\right) \\ -\omega\rho_{C}V_{C}\sin\left(\frac{\omega d_{C}}{V_{C}}\right) & \cos\left(\frac{\omega d_{C}}{V_{C}}\right) \end{pmatrix}.$$

Here, ω is the angular frequency of the acoustic wave, $d_{Ni(C)}$ is the thickness of the nickel (carbon) layer, $V_{Ni(C)}$ is the longitudinal acoustic wave velocity of nickel (carbon), and $\rho_{Ni(C)}$ is the density of nickel (carbon). Carrying out the matrix multiplication gives

$$T = \begin{pmatrix} \cos(\xi_{Ni})\cos(\xi_{C}) - \eta\sin(\xi_{Ni})\sin(\xi_{C}) & {\phi_{C}}^{-1}\cos(\xi_{Ni})\sin(\xi_{C}) + {\phi_{Ni}}^{-1}\sin(\xi_{Ni})\cos(\xi_{C}) \\ -\phi_{Ni}\sin(\xi_{Ni})\cos(\xi_{C}) - \phi_{C}\cos(\xi_{Ni})\sin(\xi_{C}) & -\eta^{-1}\sin(\xi_{Ni})\sin(\xi_{C}) + \cos(\xi_{Ni})\cos(\xi_{C}) \end{pmatrix},$$

where $\xi_{Ni(C)} \equiv \omega d_{Ni(C)}/V_{Ni(C)}$, $\phi_{Ni(C)} \equiv \omega\rho_{Ni(C)}V_{Ni(C)}$ and $\eta = \rho_{C}V_{C}/\rho_{Ni}V_{Ni}$ have been introduced for brevity. Assuming there is zero stress at the free surface (the carbon-vacuum interface), I now solve for the eigenvector of T that corresponds to our mode

$$T\begin{pmatrix} u \\ 0 \end{pmatrix} = \lambda\begin{pmatrix} u \\ 0 \end{pmatrix},$$

where u is the displacement and λ is the eigenvalue. Substituting in the expression for T gives the equation

$$(-\phi_{Ni}\sin(\xi_{Ni})\cos(\xi_{C}) - \phi_{C}\cos(\xi_{Ni})\sin(\xi_{C}))u = 0,$$

or simplifying and substituting the material properties back in explicitly,

$$\frac{\rho_{C}V_{C}}{\rho_{Ni}V_{Ni}}\tan\left(\frac{\omega d_{C}}{V_{C}}\right) = -\tan\left(\frac{\omega d_{Ni}}{V_{Ni}}\right).$$

This final formula is then solved for the carbon layer thickness at each experimentally measured ω by graphical intersection as a function of d_{C}. The values of ρ_{C} and V_{C} are taken from [117], where the authors characterize the density and longitudinal acoustic velocity of a variety of amorphous, hydrogenated

carbon films. According to [40], the films deposited by EUV exposure should be soft, so I use the values of the lower velocity films in [117], ρ_C = 0.97 – 1.24g/cm^3 and V_C = 3025 – 4198m/s. I further account for the possibility that the nickel velocity is lowered to 5000m/s from its bulk value of 5630m/s, while its density remains nominal, according to [32]. With this range of inputs, I calculate that 0.7 – 1.1nm of carbon is deposited between the first and second gLAW measurements, and only 0.1nm of additional carbon is deposited between the second and third gLAW measurements. Because there was EUV exposure during long time-window measurements before the first short time-window measurement, I calculate 5.1 – 7.2nm of carbon was already present on the nanolines at the start of the first short time-window scan. These results are consistent with AFM measurements of 7±1nm of carbon deposition on the nanolines, as shown in Fig. 4.6(b). Note that further EUV exposure occurred between the third gLAW measurement and the AFM measurement, indicating that the AFM measurement is likely an overprediction of the carbon present during the measurements shown, and the lower limit of the carbon velocity is likely more accurate. In future work, it would be interesting to use this approach to precisely determine the carbon deposition rate as a function of exposure time. In the present study, however, exposure time was not precisely controlled as the main goal was distinguishing the gLAW and fLAW for film 155.

To identify the fLAWs for films 148 and 145, their gLAWs must once again be taken into account. For film 148, the fLAW was particularly weak and difficult to identify. The best method I found was to use MPM to fit the gLAW and look for bumps where the full data trace deviates from the pure gLAW oscillation. This also shows up as a wider bump in the residual error between the MPM fit and the full data trace, as shown in Fig. 4.7(a). For film 145, the fLAW was much stronger, and even showed evidence of a pulse train of echoes, launched by the strong gLAW, as shown in Fig. 4.3(b). Because the film has a lower acoustic impedance than both the nickel nanolines and the silicon substrate, we expect the pulse train that returns to the surface to be 180° out of phase with the gLAW that launched it. This is why the dip is "downward". For film 145, I thus identify the location of the fLAW by "missing peaks" in the gLAW oscillation, where the fLAW has destructively interfered with it. This effect is shown in Fig 4.7(b) along with reference sinusoids as guides to the eye. At the location of the third peak of the gLAW in this

measurement, we instead observe a slight dip and then rise in the signal 180° out of phase with the gLAW oscillation. This indicates that the fLAW returns to the surface at almost exactly the same time as the third gLAW peak, cancelling it out. Similar features are consistently repeated in other measurements of gratings on this film, with both first and second fLAW echoes at the appropriate delay times.

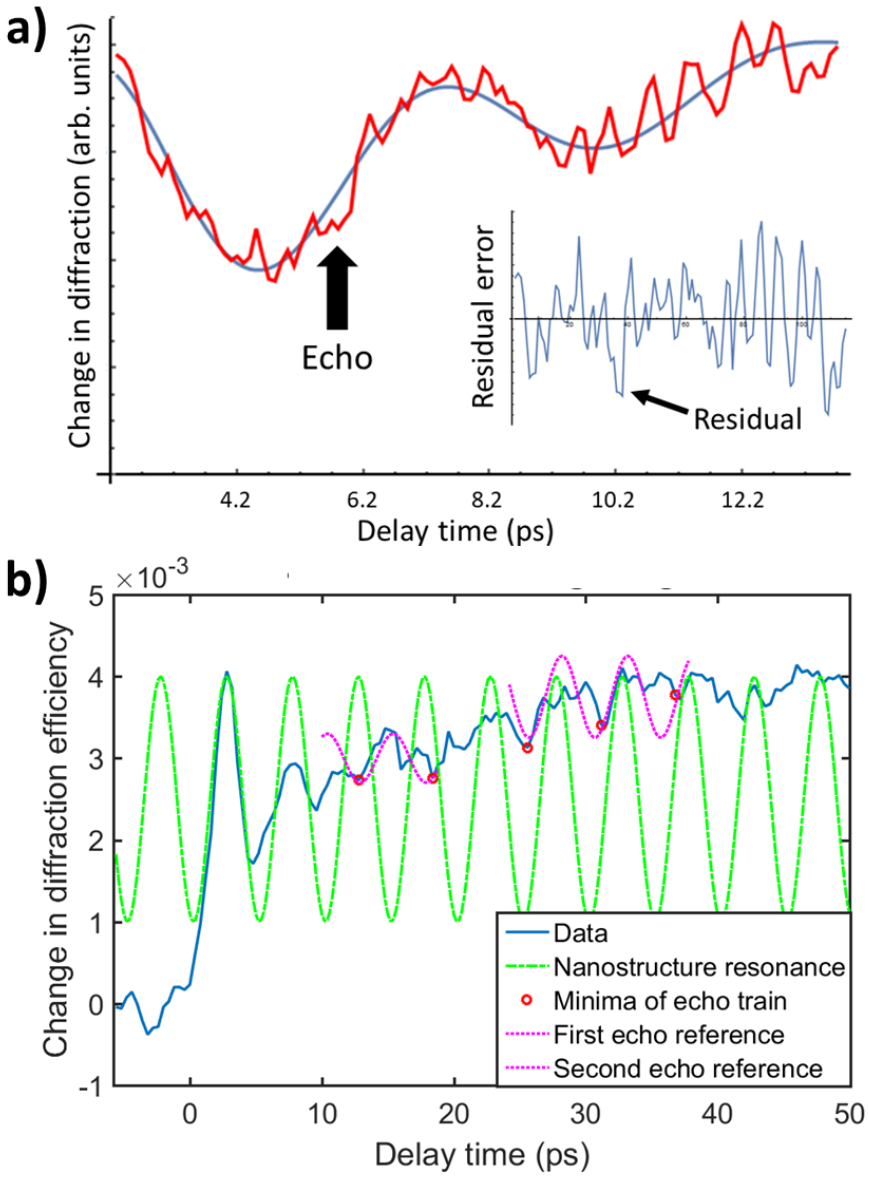

Figure 4.7: fLAWs for films 148 and 145. a) Using MPM, we identify the exponential rise of the initial thermal expansion, and the pure decaying oscillation of the gLAW for film 148 (scree plot and complex exponents shown in Fig. 4.5). Comparing the full data trace (many grating measurements averaged together) to the curve fit by MPM, we observe an fLAW dip at approximately 6ps. Inset: the residual error between the two curves shows a slightly broader feature, corresponding to this dip. b) Comparing to reference sinusoids for film 145, we can see that the third peak of the gLAW is missing, due to destructive interference with the fLAW. A second fLAW pulse train is visible at twice the return time of the first fLAW.

Finally, the fLAWs for films 503 and 335 are relatively easy to identify. Film 503 is so thin, that the fLAW arrives before the first full oscillation of the gLAW, allowing for clear identification. Fig. 4.8 shows that the fLAW arrives on a sub-picosecond timescale. Note that this fLAW return time is still well after the weak electronic peak sometimes visible in our signal at ~100fs, as discussed in Chapter 2. Thus, the off-resonance condition of our EUV probe, with minimal sensitivity to electron temperature, is critical to characterizing such ultrathin films. Film 335 is thick enough that the fLAW is well separated from the gLAW and may be readily identified.

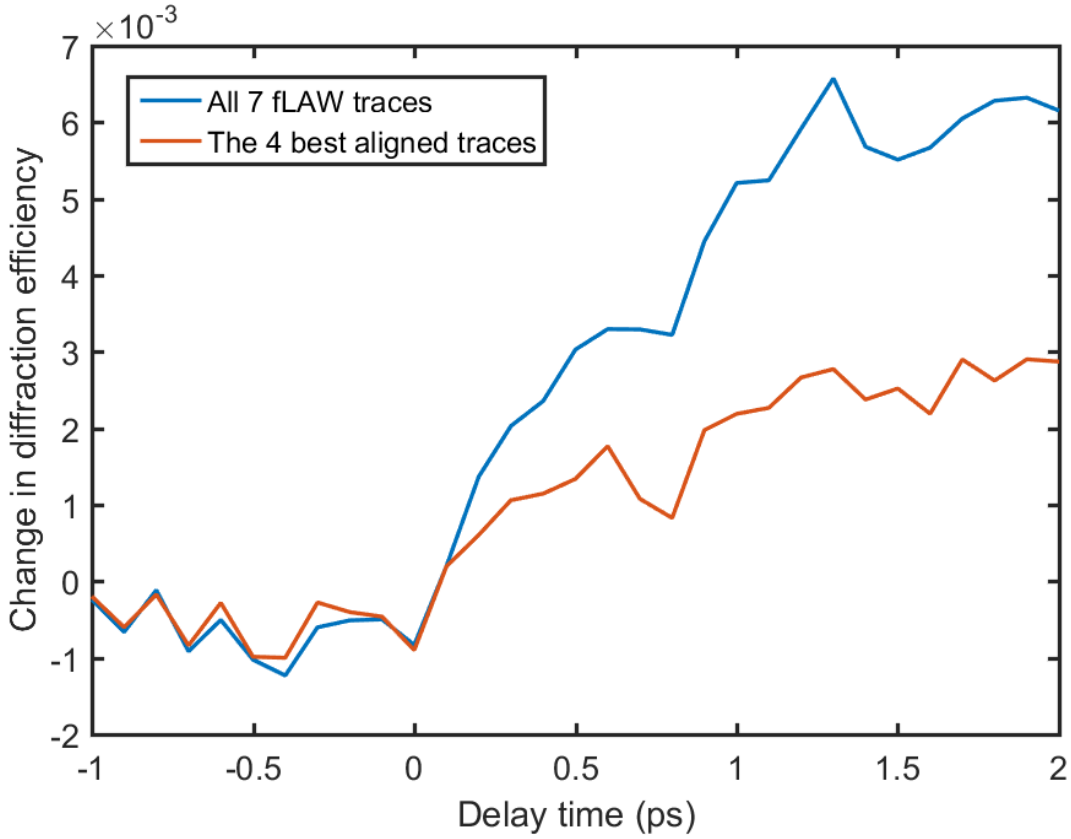

Figure 4.8: fLAWs for film 503. For this 5nm thick film, the fLAW return time is shorter than the period of the gLAW, meaning that the dip in the signal is clearly identifiable in the initial rise of the signal. Two average traces are shown, which include measurements of the largest linewidth gratings on this film, where the fLAW signal is strongest. The blue trace exhibits a dip at 0.7ps and 1.4ps for the first and second fLAW, respectively, while the orange trace includes only the traces that align the best in time, showing the first fLAW most clearly. This sub-picosecond feature is not present on thicker films, indicating it is indeed the fLAW for this 5nm film. Note that this feature is well after the time of the weak electronic signal discussed in Chapter 2. Indeed, in these traces we see no evidence of electronic sensitivity. Change in diffraction efficiency for each trace going into the average is expressed as a fraction of the total integrated intensity on the camera.

4.2.3 Fitting and Modeling Elastic Properties

The complete elastic properties of a material are expressed in a rank 4 tensor known as the elasticity tensor [118, 119]. This is a generalization of Hook's law, which states the force on a spring is proportional to its extension. Similarly, the stress in a material is proportional to its strain, with the proportionality constants organized in the elasticity tensor. Written mathematically,

$$T_{ij} = c_{ijkl}\, S_{kl},$$

where T_{ij} is the stress in the *i* direction on the *j*-oriented surface, c_{ijkl} is the *ijkl* component of the elasticity tensor, and S_{kl} is the strain in the *k* direction of the *l*-oriented surface. To give a concrete example, consider compressing a spring placed on the *x*-axis. The force on the spring in the *x*-direction is proportional to the displacement in the *x*-direction at a ratio of c_{xxxx}.

Though there are 81 components to the elasticity tensor, only two of them are important for the current study. It can be shown that, for any material, at most 21 of the tensor components are independent elastic constants. For the case of an isotropic material, further simplifications show that only two of the elastic constants are independent; all the others are either 0 or simple expressions of these two constants. The two constants will be denoted here as c_{11} (equal to c_{xxxx}=c_{yyyy}=c_{zzzz}) and c_{44} (equal to c_{ijij}).

In experimental and engineering contexts, it is more common to express the elastic properties of isotropic materials in terms of Young's modulus, E, and Poisson's ratio, ν. These constants are more intuitive, as Young's modulus reflects how much pressure needs to be applied to a material for a given on-axis displacement, while Poisson's ratio is the ratio of how much a material displaces to the sides relative to its on-axis displacement. Schematics of this are shown in Fig. 4.9(b). Note that Poisson's ratio must be between 0 (fully compressible material) and 0.5 (fully incompressible material), excluding auxetic materials that have negative Poisson's ratio. Young's modulus and Poisson's ratio are related to c_{11} and c_{44} by

$$E = c_{44}\left(\frac{3c_{11} - 4c_{44}}{c_{11} - c_{44}}\right) \tag{1}$$

$$\nu = \frac{c_{11} - 2c_{44}}{2(c_{11} - c_{44})} \tag{2}$$

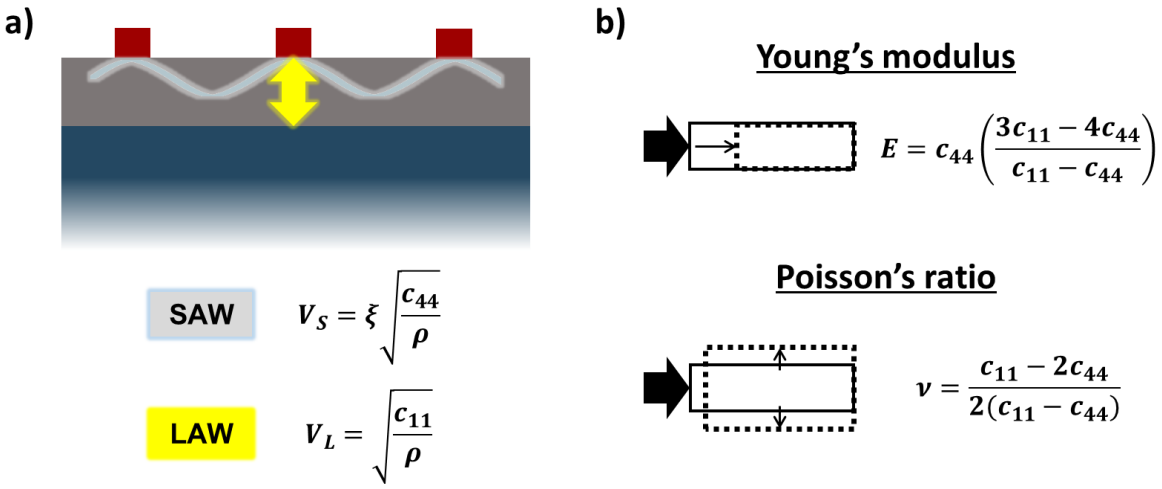

Figure 4.9: Measuring the two independent elastic constants with acoustic waves. a) The SAW and LAW velocities in the film are related to c_{44} and c_{11}, respectively. b) Young's modulus and Poisson's ratio are functions of c_{11} and c_{44}. Young's modulus relates an applied pressure to the materials on-axis deformation. Poisson's ratio is the ratio of transverse deformation to on-axis deformation, for a given applied pressure.

Two independent measurements are needed to extract the two independent elastic constants. Longitudinal and surface acoustic waves confined to the film very naturally provide these measurements. The film's LAW velocity, calculated from the known film thickness and the measured fLAW return time, is related to c_{11} by

$$V_L = \sqrt{\frac{c_{11}}{\rho}}, \tag{3}$$

where ρ is the film's known density. The film's SAW velocity, calculated from the grating period and the measured SAW frequency, is related to c_{44} by

$$V_S = \xi\sqrt{\frac{c_{44}}{\rho}}, \tag{4}$$

where ξ is the ratio between a surface acoustic wave and a pure transverse acoustic wave. While ξ may be calculated [120], this expression is only true for an un-loaded surface, and our case with nanolines on top of the film is actually more complicated. To extract the film's c_{44} elastic constant, and thereby calculate Young's modulus and Poisson's ratio, we must account for how the nanolines change the SAWs we measure.

The presence of nanoline gratings on top of the films makes the surface into a hypersonic surface phononic crystal, which can be modeled using finite element analysis (FEA) [64, 121]. For our FEA calculations, the geometry of a single nanoline period is implemented in COMSOL Multiphysics with periodic boundary conditions and a mesh of discrete calculation points, such as that shown in Fig. 4.10(a) [60]. The temperature and displacement are then calculated at each mesh point as a function of time, according to the thermoelastic differential equations and method described in [22]. See Appendix for more details. This approach captures all the continuum mechanics properties of this system, including the surface acoustic wave's confinement to the surface, how its energy is scattered into the bulk substrate by the gratings, and how the mass of the nanolines lowers the frequency of the SAW. By diffracting a Gaussian beam from the FEA calculated surface displacement using Fresnel propagation, we can produce a calculated change in diffraction efficiency signal, which compares very well with our experimentally measured change in diffraction efficiency signal (see Fig. 4.10(b)). While this is a good indication that the approach is valid, in practice the full physics calculations are computationally expensive, and we use a faster approach than simulating a full transient signal and fitting it to our experimental signal.

To obtain the best fit elastic properties of the films, we use a combination of full physics calculations of the dynamic displacement field and eigenfrequency analysis of the static structure, all performed in COMSOL. First, we perform eigenfrequency analysis on the un-deformed nanoline-film-substrate structure to identify all the modes it supports. Next, we apply a transient heat source to the nanoline, and the full physics displacement field is calculated only until the time when the nanoline has reached maximum thermal expansion. This captures the amplitude and content of the initial excitation of the acoustic waves we measure. Finally, the displacement field at maximum expansion is projected onto the set of eigenmodes for the structure to identify which long-lived acoustic waves are excited and measured in our experiment. The elastic properties of the system are varied until the calculated frequencies match the experimentally observed frequencies. This method is executed for each experimental geometry we measure.

First, large linewidth gratings are used to fit the silicon substrate's elastic properties and account for strain and wafer-to-wafer variation. Because these waves penetrate deep into the substrate and are only

minimally sensitive to the thin film, we perform FEA using the approximate thin film properties estimated from the confined SAW velocity that hasn't yet been corrected for the presence of the smaller linewidth gratings (Eqn. 4). Next, we use the corrected substrate properties and fit the thin film Young's modulus by matching the measured frequency on a small linewidth grating that confines the SAW to the film. Together with c_{11} calculated from the film LAW velocity, this value gives the true elastic properties of the film. We additionally calculate the frequencies for each intermediate grating, using these extracted elastic constants, which verifies our results as they exhibit good agreement with experiment. The intermediate grating sizes could be used in future work to characterize sub-surface layers in a multilayer system.

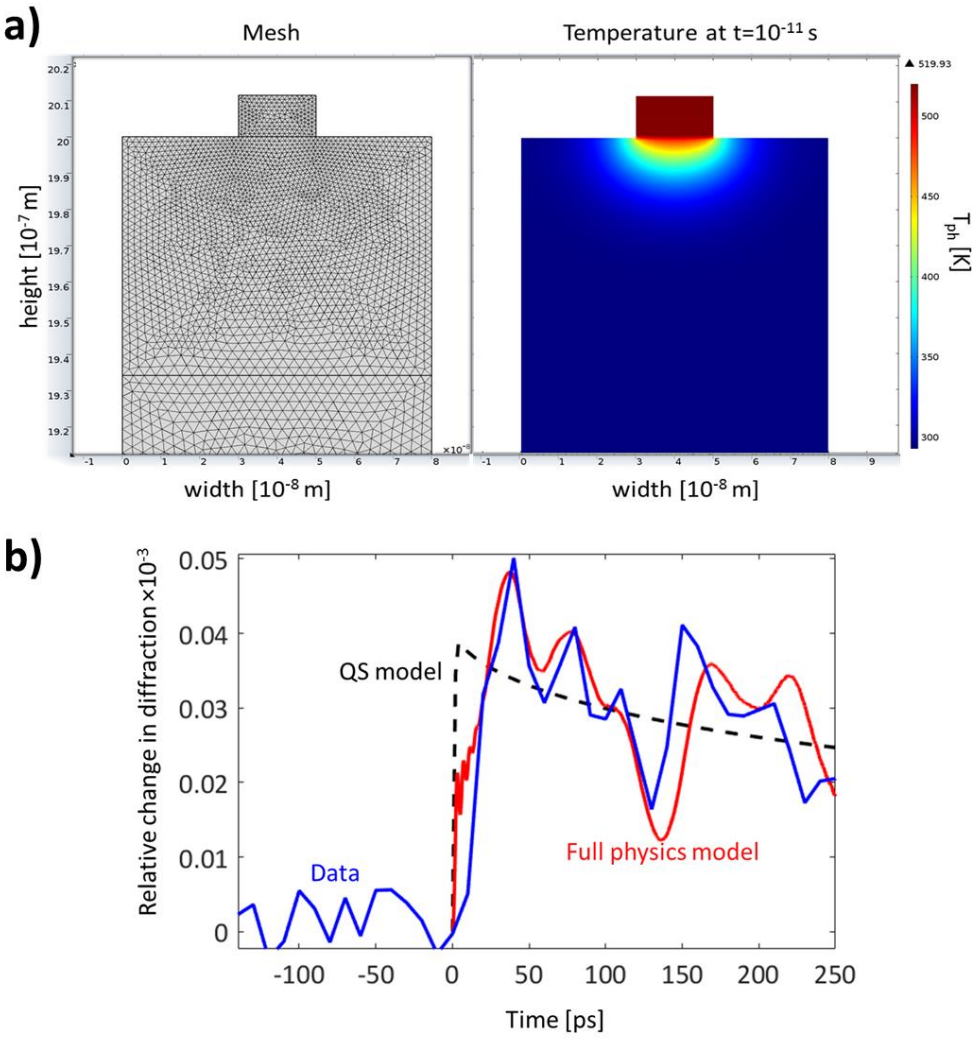

Figure 4.10: FEA calculations of thermoelastic dynamics. a) FEA calculations of the temperature (right) and displacement at a mesh of discrete points (left). b) The calculated diffraction from the dynamically deforming surface in the FEA model agrees well with the experimentally measured diffraction signal.

Finally, we calculate the uncertainty on our best fit thin film elastic properties. To do this, we must propagate the experimental uncertainties in film density, film thickness, fLAW return time, and SAW frequency through our analysis procedure. Due to the numerical approaches used, there is no analytic equation for error propagation in our analysis. Instead, we set the inputs to the FEA calculations at the extreme ends of their error bars that produce the lowest calculated SAW frequency. We then increase the film's Young's modulus until the calculated frequency matches the upper end of the experimental SAW frequency error bar. We repeat this process with the inputs that give a high calculated SAW frequency and tune Young's modulus to match the lower end of the experimental SAW frequency. In this way, our error bars capture the maximal deviations possible, and are rather conservative as it is unlikely that all properties would be at the limits of their ranges simultaneously. More details are provided in [22].

4.3 Results and Discussion

I now present the full elastic characterization of SiC:H and SiOC:H ultrathin films using the approach described above. The SiC:H films have varying levels of hydrogenation to reduce their dielectric constant, and we observe critical behavior in Poisson's ratio when enough bonds in the network are broken. The SiOC:H films are all made from the same material, at the critical level of broken bonds, but they vary in thickness from 50nm down to 11nm. We observe no thickness-dependent changes in the elastic properties of these films. In comparison with this set of films, we characterize two additional SiC:H films at 50nm and 5nm thicknesses, which have much more interconnected networks with fewer broken bonds than the SiOC:H film series. We do see evidence of thickness-dependent softening for this pair of films.

4.3.1 Hydrogenation-dependent Study

To understand the results of the hydrogenation-dependent study, we must first formalize our discussion of bond termination to soften a material. This is best achieved in the Phillips-Thorpe framework of topological constraint theory, originally developed to describe bulk glasses [122, 123]. In this framework, a material is flexible if there are fewer constraints on each atom than the three degrees of freedom they have to move. Similarly, a material is rigid if each atom has more than three constraints on its motion. Since the

constraints on each atom come from the network of bonds in a material, we can relate the average number of atomic constraints, n, to the average coordination number of the atoms in the material, $\langle r \rangle$. For example, consider an atom with two nearest neighbors, $\langle r \rangle = 2$. These neighboring bonds constrain one degree of freedom of this atom, giving $n = 1$ for the bond constraint. Additionally, since a material has fixed bond angles, one more degree of freedom is constrained for the central atom, $n = 1$ for the angle constraint. As we increase the coordination number of the central atom, each new bond defines two new angles, thus angular constraints for $\langle r \rangle = 3$ gives $n = 3$, $\langle r \rangle = 4$ gives $n = 5$, and so on. Taking the bond and angle constraints together, we define the general formula

$$n = \frac{\langle r \rangle}{2} + (2\langle r \rangle - 3). \tag{5}$$

The critical transition from a flexible material to a rigid material occurs when the number of atomic constraints exactly balances the number of degrees of freedom, $n = 3$. Substituting this into Eqn. 5, we obtain the critical value $\langle r \rangle_c = 2.4$, known as the rigidity percolation threshold. Once the average coordination number of the atoms is 2.4, rigid structures percolate throughout the material, creating an interconnected network. With this in mind, the average atomic coordination number, $\langle r \rangle$, is also referred to as the network connectivity of a material.

The network connectivity of a material is calculated from the coordination numbers of each atomic species comprising it, r_i. If the mole fractions of each element, x_i, in the material is known, for instance measured by RBS, then the network connectivity is calculated by

$$\langle r \rangle = \sum_i x_i r_i. \tag{6}$$

For the SiC:H films in this study, $r_{Si} = 4$, $r_C = 4$, and $r_H = 1$. Thus, by increasing the hydrogenation of the films, we reduce their network connectivity, as calculated by Eqn. 6 and the mole fractions measured by RBS. As shown in Table 4.1, the seven films characterized in this study span network connectivity values from 2.02 – 3.2, crossing the rigidity percolation threshold.

As shown in Fig. 4.11, we extract the Young's modulus and Poisson's ratio of the full series of SiC:H films. For those films with network connectivity above the rigidity percolation threshold, the elastic

constants behave nominally. The Young's modulus of the thin films matches nanoindentation measurements on thicker films of the same material, and it scales with network connectivity according to the trend observed in [82]. Similarly, Poisson's ratio stays at about 0.2, the nominal value for this material. Below the rigidity percolation threshold, however, Poisson's ratio diverges towards 0.5, that of a fully incompressible material, like rubber. Due to the difficulty in measuring Poisson's ratio for ultrathin films, it is usually assumed to be constant. Our results show that this assumption is not valid once a film drops below the rigidity percolation threshold. This divergence coincides with a number of other discontinuities in material properties across the rigidity percolation threshold, as shown in [82]. Note that MD simulations in the similar material, SiOC:H, did predict that adding hydrogen terminal groups for a lower network connectivity would make the Poisson's ratio increase [84]. However, the change they predict is smaller than that which we measure in SiC:H, making these measurements an important insight for designing robust nanosystems with this material.

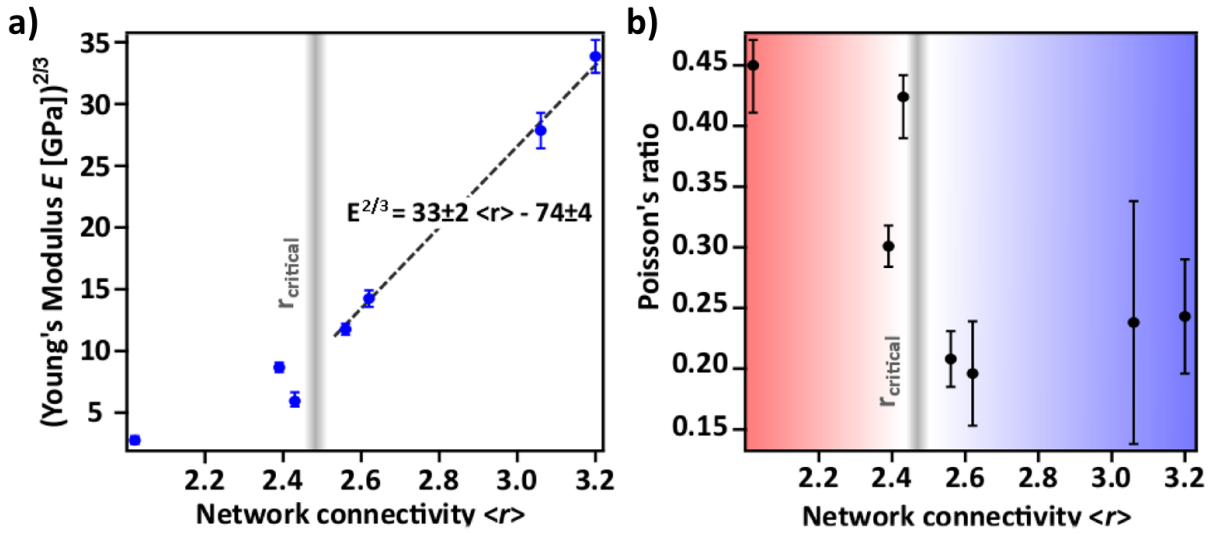

Figure 4.11: Young's modulus and Poisson's ratio for the hydrogenation-dependent study. a) The Young's modulus for all seven films follows the trend with $\langle r \rangle$ predicted in [82] for network connectivity above the rigidity percolation threshold. Below the threshold, our measured values still agree well with nanoindentation measurements on thicker films [82]. b) The Poisson's ratio diverges from its assumed-constant value for films with $\langle r \rangle$ below the rigidity percolation threshold. This rapid change towards incompressible behavior coincides with other material property changes at the threshold [82], and it is an important property of these materials to consider when engineering nanosystems with thin films like those measured. Figure from [22].

4.3.2 Thickness-dependent Study

To study thickness-dependent elastic properties, we first characterize a set of three SiOC:H films with thicknesses of 44nm, 19nm, and 11nm. As shown in Table 4.2, these films all have $\langle r \rangle = 2.4$ (note that $r_O = 2$). To best represent the results, it is worth considering again the calculation process described in Section 4.2.3. The experimentally measured quantities are SAW frequency and fLAW return time, which both have associated uncertainties from the standard deviation of multiple measurements. We calculate c_{11} from the fLAW, and fit Young's modulus using FEA. While these two quantities contain all the information about the film's elastic tensor, they are an odd pair to report. Using Eqn. 1 – 2, we instead convert the results into either c_{11} and c_{44}, to report the independent components of the elastic tensor, or we convert to Young's modulus and Poisson's ratio, to report the most commonly used elastic constants. As shown in Fig. 4.12, all of these transformations are well behaved for the thicker film. Note, however, that the properties of these films place their elastic constants close to a physical boundary in $c_{11} - c_{44}$ space, at $c_{11} = 2c_{44}$ (Fig. 4.12(c), red region). Considering Eqn. 2, this boundary comes from the requirement that Poisson's ratio be positive, as these materials are assumed to be non-auxetic. There is an additional boundary at $c_{11} = 4/3\, c_{44}$, from the requirement that Young's modulus be greater than zero (Eqn. 1), but this lies within the red region shown in Fig. 4.12(c) and does not need to be shown. The $c_{11} = 2c_{44}$ boundary can then be back-propagated into c_{11} – Young's modulus space, and finally to SAW frequency – fLAW echo space (Fig. 4.12(b) and Fig. 4.12(a), respectively). This boundary complicates our results when the film thickness is reduced.

The thinner films have larger experimental uncertainties, which cross the back-propagated boundary, as shown in Fig. 4.13(a). Note even a small uncertainty in return time is significant because the films are so thin. Crossing the boundary does not mean that the materials are auxetic, but rather the unrelated experimental uncertainties, such as the fLAW pulse width, can make the calculated value cross the boundary that this material's constants are naturally close to. Once the $c_{11} = 2c_{44}$ boundary is crossed, the lower bound on Poisson's ratio is pulled down to 0 (Fig. 4.13(d)). Due to these transformations, the error bars are more symmetric in $c_{11} - c_{44}$ space, though Young's modulus and Poisson's ratio are generally preferred.

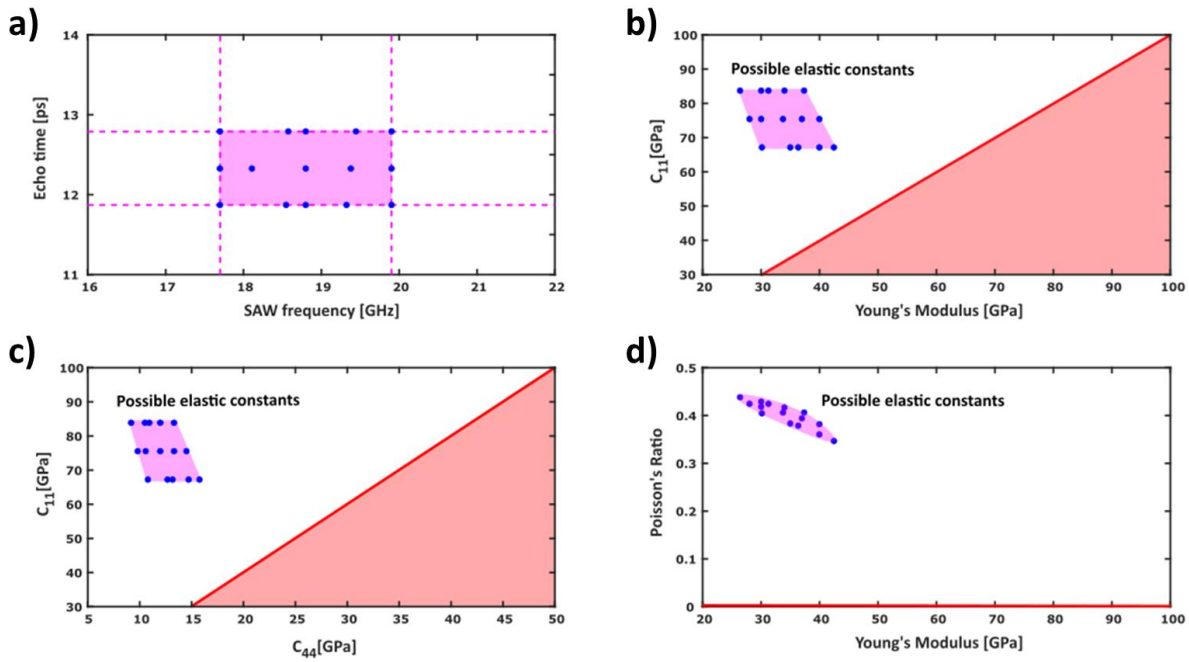

Figure 4.12: Film 145 (44nm thick) elastic constants. a) Measured fLAW echo return time and SAW frequency. The central blue dot tracks the calculations performed at the measured values. The other blue dots are calculations sampling the rest of the region within experimental uncertainty (dashed pink lines). Calculations are then carried forward into b) c_{11}–Young's modulus space, c) c_{11}–c_{44} space, and d) Poisson's ratio–Young's modulus space. The red boundary is defined by $c_{11} > 2c_{44}$ for non-auxetic materials, and it is then back-propagated into other spaces.

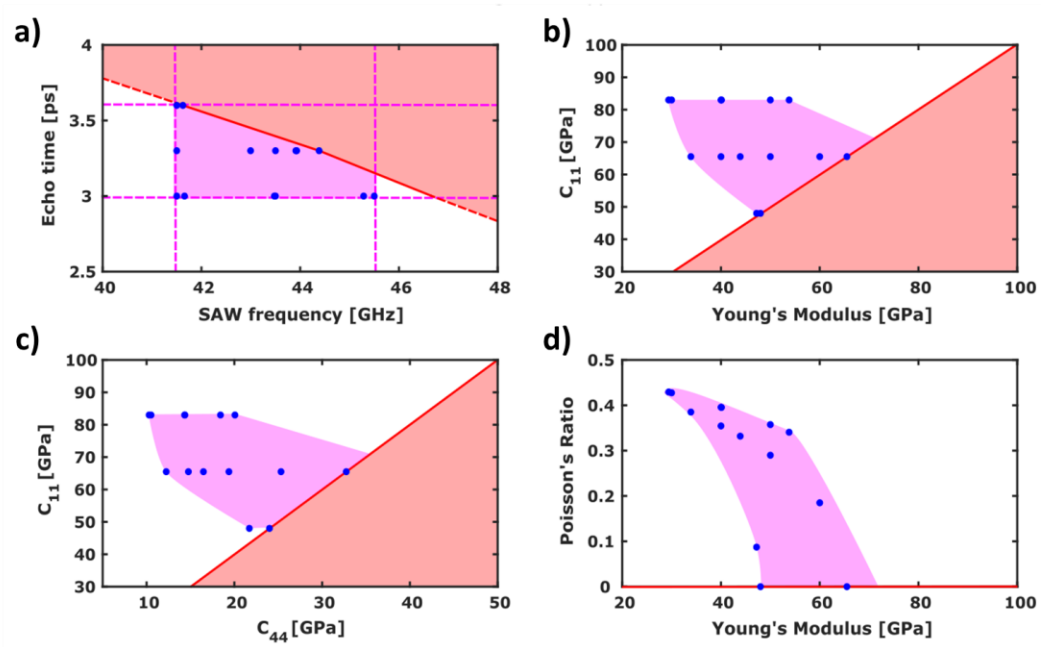

Figure 4.13: Film 155 (11nm thick) elastic constants. The same process is carried out here as for Film 145, shown in Fig. 4.12. The points and lines shown have the same meanings as above. Note how crossing the $c_{11} = 2c_{44}$ boundary in (c) brings the lower bound on Poisson's ratio to 0 in (d). The same plot windows are used in (b), (c), and (d) here as are used in Fig. 4.12. Note Film 148 behaves similarly to Film 155.

Following the process described above, we extract the elastic properties of all three SiOC:H films, presented in both c_{11}–c_{44} space and Young's modulus – Poisson's ratio space in Fig. 4.14. We observe no evidence of thickness-dependence as all three films' elastic constants overlap within uncertainty. This agrees with the lack of thickness-dependence (aside from differences in fabrication) for measurements of porous films in [124]. Note, however, that the films in our study are not porous.

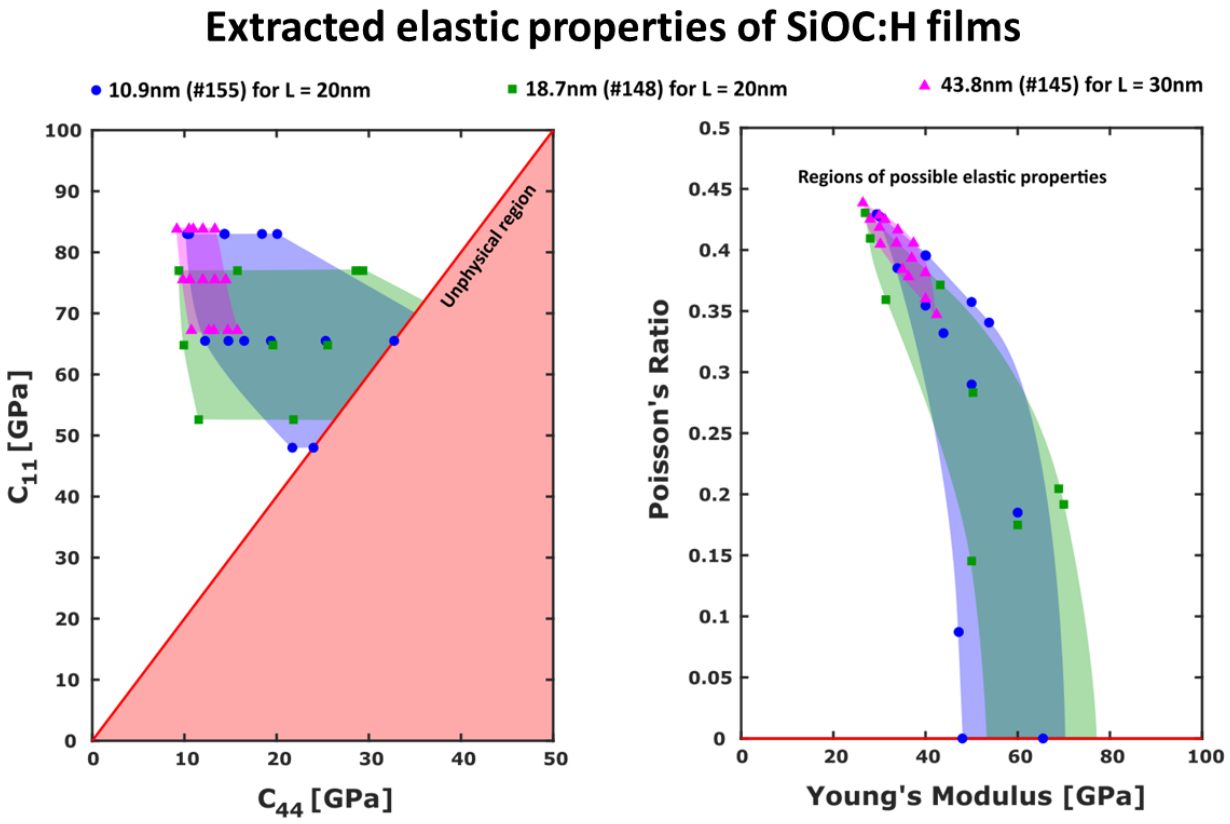

Figure 4.14: Elastic properties of varying-thickness SiOC:H films. Results are reported as c_{11} and c_{44} on the left, and as Young's modulus and Poisson's ratio on the right. The range of possible elastic constants is consistent between films, within experimental uncertainty, indicating a lack of thickness-dependence. Note that these films lie close to the $c_{11} = 2c_{44}$ boundary (red line) separating conventional materials from auxetic materials (negative Poisson's ratio). Calculations spanning to the limits of experimental uncertainty (solid points) cross this boundary for the thinner two films, pulling the lower bound on Poisson's ratio to 0. The 11nm film (blue) is fit using its 20nm linewidth grating, the 19nm film (green) is fit using its 20nm linewidth grating, and the 44nm film (pink) is fit using its 30nm linewidth grating. Shaded regions represent the full range of the elastic constants within uncertainty, approximated from the calculated points.

Considering the body of work showing thickness-dependent elastic properties in other materials, it is worth asking why there is no thickness dependence for these SiOC:H films. While it is possible that 11nm is simply not thin enough to see thickness-dependent changes, depending on what model prediction is

correct, these films are also at the rigidity percolation threshold, which we showed above significantly affects the behavior of a material. With this in mind, we hypothesize that the reduced network connectivity in the bulk of the film, caused by hydrogenation, reduces the impact of under-coordinated atoms at the surface. In other words, there is only a minimal difference for these films between the average coordination numbers of the surface and the bulk, producing only minimal surface effects. For most materials, there would be a much larger difference between bulk and surface coordination numbers, in general. In [125], the authors develop a simple effective coordination number model based on the differences between surface and bulk coordination numbers in nanocrystals, and they successfully predict size-dependent properties including the surface energies of nanodroplets. They show that this model agrees with the bond contraction model mentioned above [98]. With this in mind, the best test of our hypothesis is to study an additional set of varying-thickness films with much more interconnected networks in their bulk.

While we do not currently have a set of SiOC:H films at higher network connectivity, we do have a pair of SiC:H films that have network connectivity well above the rigidity percolation threshold. As these two films have nominal thicknesses of 5nm and 50nm, they are a good initial test of our hypothesis. However, these films (numbers 503 and 335, see Table 4.2) were accidentally double deposited during fabrication. This means the process of ammonia plasma treatment to improve film adhesion followed by SiC:H film deposition was performed twice on the silicon substrates. This makes for a stack of two films on top of the native oxide of the wafer, separated by a nitrogen-containing layer from the plasma treatment. We need very precise characterization of these layers to correctly model the system and extract elastic constants from our measurements, especially for a film only 5nm in thickness. For this reason, we performed cross-sectional transmission electron microscopy (TEM) on a section of film in the center of one of our 500nm linewidth gratings. Representative images are shown in Fig. 4.15, along with the measured thicknesses of each layer in the stack. In addition to the film thicknesses, we observe a difference in contrast between the two nominally identical films in the stack. To explore this further, we also performed energy-dispersive x-ray spectroscopy (EDS) with the electron beam for high resolution elemental composition.

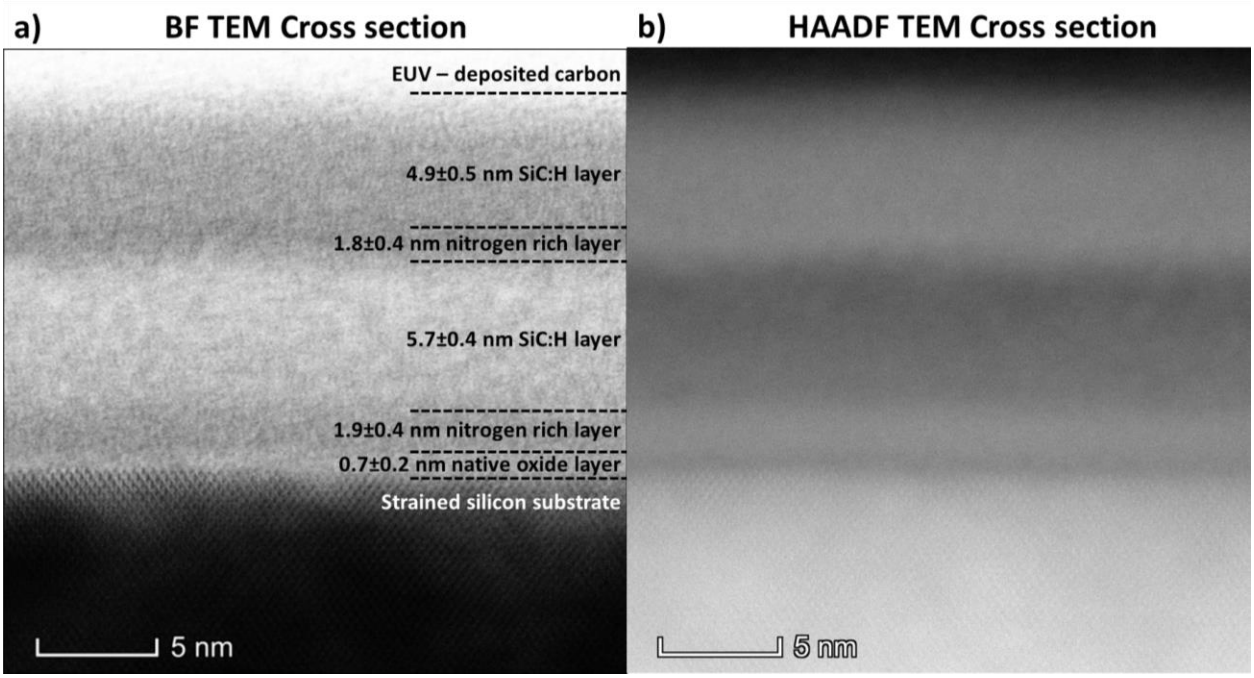

Figure 4.15: TEM measurements of film 503 – double deposited 5nm SiC:H films. This image was taken of the full stack of films in a region between two 500nm nickel nanolines. The bright field (BF) image (a) exhibits the best contrast between the two SiC:H films and the nitrogen-rich layers coming from the plasma treatment in the deposition process. The high angle annular dark field (HAADF) image (b) exhibits better contrast between the top SiC:H film and the EUV-deposited carbon coating the surface of the sample. Thicknesses and uncertainties listed are the averages and standard deviations, respectively, of several measurements spanning the width of the image taking both the widest and narrowest extents of the gradients between different layers. In this way, the uncertainty reflects both the diffusiveness of the boundaries and the variation across the imaged region. Note that (b) was used to help identify the top surface of the upper SiC:H film in the measurements of (a).

We performed EDS measurements to determine the elemental composition of film 503 beyond its nominal values. Results are shown in Fig. 4.16(b). Referencing Table 4.2, the nominal fractions of Si and C should be roughly equal in the film, but EDS shows roughly seven times more Si than C. This could indicate a fabrication-dependent change in the film, though it should be noted EDS cannot detect hydrogen, which is a significant fraction of this material, and it is difficult to detect C, N, and O. Aside from the non-nominal relative concentrations of Si and C, EDS shows that there are only few-percent differences between the compositions of the top and bottom films. This could indicate that the difference in HAADF contrast comes from different amounts of hydrogen in the two films. It has been observed that plasma treatments can remove terminal CH_3 groups and soften SiOC:H films [126]. However, for SiC:H films similar to ours, N_2 plasma treatments did not significantly change the Young's modulus of multilayers down to 1nm layer

thickness [111]. It is thus reasonable to approximate the top and bottom films as having identical elastic properties for preliminary calculations. Note that the EDS spatial map indicates a surface oxide layer on the top film with a similar thickness as the N-rich layers. This could be the cause of the poor contrast between the top film and the EUV-deposited C in Fig. 4.15(a). We are currently performing TEM and EDS on film 335 to confirm its layer thicknesses and verify its composition matches that of 503.

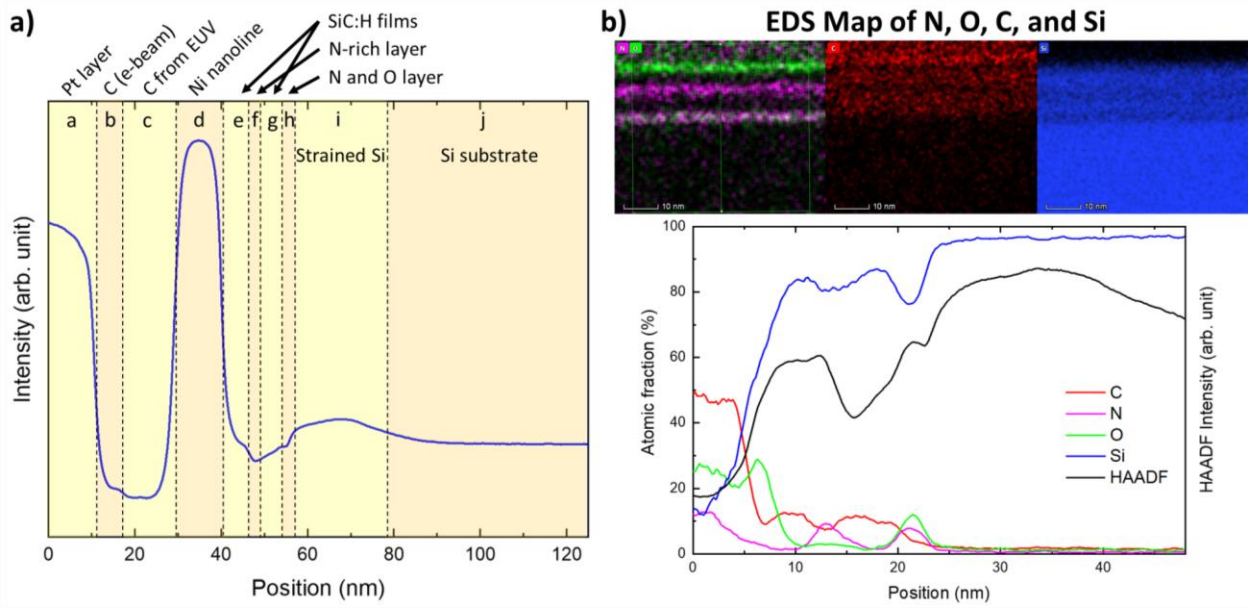

Figure 4.16: HAADF and EDS measurements of film 503. a) Integrated HAADF intensity as a function of depth for a region topped by a 500nm nickel nanoline. Note that the carbon deposited by the e-beam and that deposited by EUV is resolvable by HAADF contrast. The large amount of deposited carbon (12nm) is due to the fact that we used this sample for calibration measurements (additional EUV exposure) between the completion of its elastic characterization, and the cross-sectional TEM measurement. This measurement shows the strain in the silicon substrate that we account for when fitting the acoustic waves of large linewidth gratings b) EDS measurement of Si, O, N, and C for a region with no nickel nanoline, both spatially resolved (top) and integrated (bottom). Though the bottom SiC:H film shows only slightly more Si and less C than the top film, its HAADF contrast is significantly different. Note that EDS did not resolve the N-rich and native oxide layers resolvable by TEM in Fig. 4.15.

With these more detailed measurements of the films, we can now report preliminary elastic characterizations of films 503 and 335. First, the fLAW reflects from the N-rich interface between the two SiC:H films, in both cases. This means the c_{11} we calculate is that of the top film. As shown in Fig. 4.17(a), c_{11} stays constant between the 5nm and 50nm films. This calculation used Eqn. 3, the nominal film density, the top film thickness measured by TEM for film 503, and for film 335 I used half of the XRR measurement of the full stack thickness (95nm). Second however, the SAW dispersion exhibits a strong thickness-

dependence, as shown in Fig. 4.17(b). For the thicker film 335, the SAW fully confined to the top film has a velocity of 4600±200m/s. For the thinner film 503, the most confined SAW (15nm linewidth grating) has a velocity of 2400±200m/s. This indicates a significant softening of the 5nm film, compared to the 50nm film. FEA calculations for precise determination of the two films' elastic constants are ongoing to account for the surface oxide, potential differences between the top and bottom films in each stack, and whether the isotropic assumption is less valid than using a transversely isotropic elastic tensor.

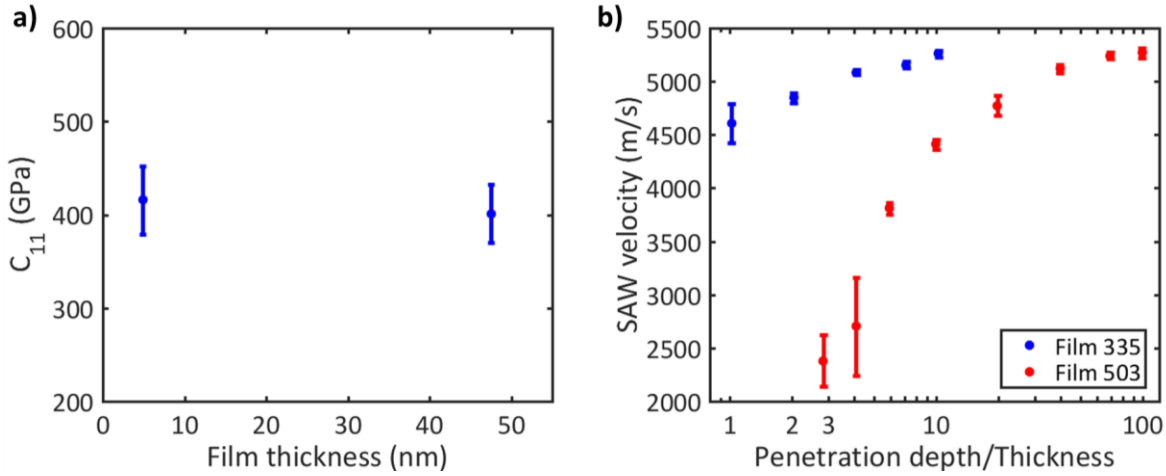

Figure 4.17: Elastic characterizations of SiC:H films 335 and 503. a) The calculated c_{11} for both the 5nm (503) and 50nm (335) film is nearly identical. This elastic constant is calculated from the measured fLAW, which reflects from the N-rich interface between the two SiC:H films in the double-deposited stack. Thus, the reported c_{11} is that of the top SiC:H film, even if the two films in the stack are different. b) The SAW dispersions for the two films indicate a significant softening in the 5nm film. Even when confined to three times the film thickness, the SAW velocity in 503 is already significantly lower than that of the SAW fully confined to the top film in 335. FEA calculations are being performed to extract the films' elastic constants from these measurements.

The observed differences between the two thicknesses of films could indicate that high network connectivity SiC:H exhibits thickness dependence while low connectivity SiOC:H does not. This would support our hypothesis that the more interconnected bulk of the film is more affected by the under-coordinated atoms at the surface. However, we cannot yet conclude that this hypothesis is correct. We still need to verify that films 335 and 503 have the same composition as one another to confirm that the differences in their elastic constants come from thickness dependence. We additionally cannot rule out that the existence of thickness dependence in the SiC:H pair but not in the SiOC:H series is due to some other material difference, or simply because the SiC:H pair includes an even thinner film than the SiOC:H series.

Future work systematically studying both film thickness and network connectivity will clarify these questions.

The measurements of SiC:H films at 50nm and 5nm thicknesses show the importance of having access to nanoscale SAWs with high surface confinement by using an EUV probe. Deviations in elastic properties between these two films is only observable in the SAW dispersion, and not in c_{11}, which can be measured by visible picosecond ultrasonics. This makes our EUV nanometrology technique an important addition to Brillouin light scattering (BLS) for the full elastic characterization of ultrathin films. BLS has been used to characterize films down to 2.2nm thickness, though this measurement had to assume a Poisson's ratio between 0-0.5 to obtain fits [89, 90]. Moving forward, both techniques will be valuable for ultrathin film characterization.

4.4 Conclusions and Future Work

In this chapter, I have presented measurements of the elastic properties of low dielectric constant ultrathin films. These films are directly applicable to improving the efficiency and speed of integrated circuits, but they are also a great platform to explore both materials engineering and fundamental thickness-dependence coming from surface effects. I first presented measurements of SiC:H films with varying levels of hydrogenation, which lowered their network connectivities below the rigidity percolation threshold. At this point, Poisson's ratio diverged towards incompressible behavior, which contradicts the constant-value assumption frequently used when characterizing such thin films. I then presented measurements of two sets of films with varying thickness, one set of SiOC:H films, and one set of SiC:H films. The SiOC:H set of films exhibited no thickness-dependent changes in elastic properties down to 11nm thickness. The SiC:H pair of films showed no change in c_{11} for 50nm and 5nm thicknesses, but their SAW velocities did show a significant softening of the thinner film, indicating thickness-dependent changes to c_{44}.

In future work, we will confirm the thickness dependence of the SiC:H films and conduct a more systematic study of thickness dependent changes to elastic properties for different material compositions. We will further use intermediate grating sizes to individually characterize the elastic properties of a series

of buried layers in a multilayer system. We will also continue to develop dynamic coherent diffractive imaging, which measures local thermal and elastic dynamics by reconstructing full field images of nanostructured systems [127]. In parallel to this effort to obtain local information, we have continued to develop our established technique, which measures average information from periodic samples. To characterize still more complicated nanosystems with this technique, we must extend it beyond what has been described in Chapters 3 and 4. In Chapter 5, I will show the different ways we are extending our technique to characterize more novel nanosytems.

Chapter 5

Extending Dynamic EUV Metrology

In the previous two chapters, I have explored the fundamental thermal and elastic behavior of materials either at a semi-infinite surface, or with one dimension of nanoscale confinement as ultrathin films. There are, however, many exciting materials systems that have two and three dimensions of nanoscale confinement, with complex geometries and engineered structure. These nanoengineered and self-assembled materials have unprecedented thermal and elastic properties, with promising applications in waste heat recovery, advanced electronics, ultralight materials, and more. For many of these materials systems, the fabrication of grating transducers is either impossible, or could fundamentally change the physics at play.

In this chapter, I present efforts to extend from our established, grating-based approach, to measure more general materials systems. First, I present nanoscale thermal and acoustic measurements of 3D silicon metalattices using grating transducers, as described previously. This represents the most complex sample characterized to date using our grating-based approach. Second, I present measurements of long-range thermal transport in novel nanosystems where grating fabrication is impossible. These samples are instead excited using visible transient gratings (TG), and still probed by a coherent EUV beam. Finally, I present measurements of nanoscale thermal and elastic dynamics launched without the need for transducers by using an EUV transient grating. These measurements were made using both a visible and EUV probe while collaborating at the free electron laser, FERMI, in Italy. I further present the work to date in implementing EUV TG on a tabletop using HHG at JILA.

5.1 Introduction and Motivation

Metamaterials can achieve naturally-unattainable material properties, resulting from their hierarchical structuring. Examples range from photonic crystals [128] to phononic bandgap materials [49] to structural metamaterials that are ultralight yet stiff [129]. For most of these applications, periodic structuring must be done at the nanoscale, yet have a well-defined periodicity over orders of magnitude larger length scales. One solution to this nanofabrication challenge is to use self-assembly, for instance by forming colloidal crystals of nanoparticles.

Colloidal crystals are a powerful and versatile platform for materials engineering. Nanoparticles can be organized into a variety of extended crystal structures, and they can optionally be functionalized with ligands before assembly [130]. The nanoparticle cores can range from inert to plasmonic to magnetic materials, and the ligands coating them can range from relatively short conductive molecules to long polymer chains optimized for specific applications [131, 132]. Colloidal crystals have already been demonstrated to perform a number of functions, including ultrathin membrane filtration [133], chemical and biological sensing [134], economic hypersonic phononic crystal fabrication [135], and molecular electronics and switching [136]. Furthermore, 2D and 3D colloidal crystals of nanospheres can be used as scaffolds or templates for the fabrication of complex nanostructured materials [137, 138]. Both metals and semiconductors can be infiltrated into the interstitial spaces between spheres, resulting in novel material properties coming from both the material's confinement to nanoscale "meta-atoms" and their extended periodic ordering into "metalattices" [139, 140].

In this chapter, I present a series of works that extend our established thermal and elastic metrology technique to colloidal-crystal-based systems, with potential for measurement of other more general samples. I first present thermal and acoustic characterizations of 3D silicon metalattices using our grating-based technique. I then present transducer-free measurements based on transient grating (TG) excitations. Measurements are obtained on 2D ligand-coated gold nanoparticle arrays and on 2D gold nanomeshes fabricated from a nanosphere template. Finally, I present work at the FERMI free electron laser and at JILA

to implement an EUV transient grating. EUV TG represents a significant advance in materials characterization, as it directly excites deep nanoscale and ultrafast dynamics without the need for nanofabrication of metallic transducers. This enables the measurement of a much wider variety of samples, as well as other applications such as super resolution imaging and magnetic characterization via nanoscale spin gratings.

5.2 Silicon Metalattices

First, I test the limits of our established nanograting-based approach by characterizing complex, three dimensional materials systems. Specifically, I characterize 3D, hierarchical nanosystems known as metalattices, fabricated by the Badding group at Penn State University. I measure both the acoustic and thermal properties of three different silicon metalattices, using the same technique as described in Chapters 3 and 4. These metalattices have periodic structure on scales from the single nanometer to several microns, making them interesting for a variety of applications, from thermoelectrics to ultralight materials.

The structure of a metalattice is best described by considering its fabrication process. First, silica nanospheres are assembled into a colloidal crystal with hexagonal close-packed order from monolayer thickness up to micron thickness [138]. This colloidal crystal serves as a template for the metalattice, as shown in Fig. 5.1(a). Next, the interstitial space between nanospheres is infiltrated with the metalattice material. This material can be metallic, such as Ni, Pd, or Pt, or it can be semiconducting, such as Ge, or Si. We measure Si metalattices, as shown in Fig. 5.1(b). Next, the silica spheres may be selectively etched out, leaving only the highly-porous metalattice material, as shown in Fig. 5.1(c). In this case, confined volumes of silicon called “meta-atoms” are connected by thin necks, or “meta-bonds”, that are only a few nanometers wide. Finally, the metalattice may then be re-infiltrated to produce a less porous system, with stronger interactions between meta-atoms. This is shown in Fig. 5.1(d).

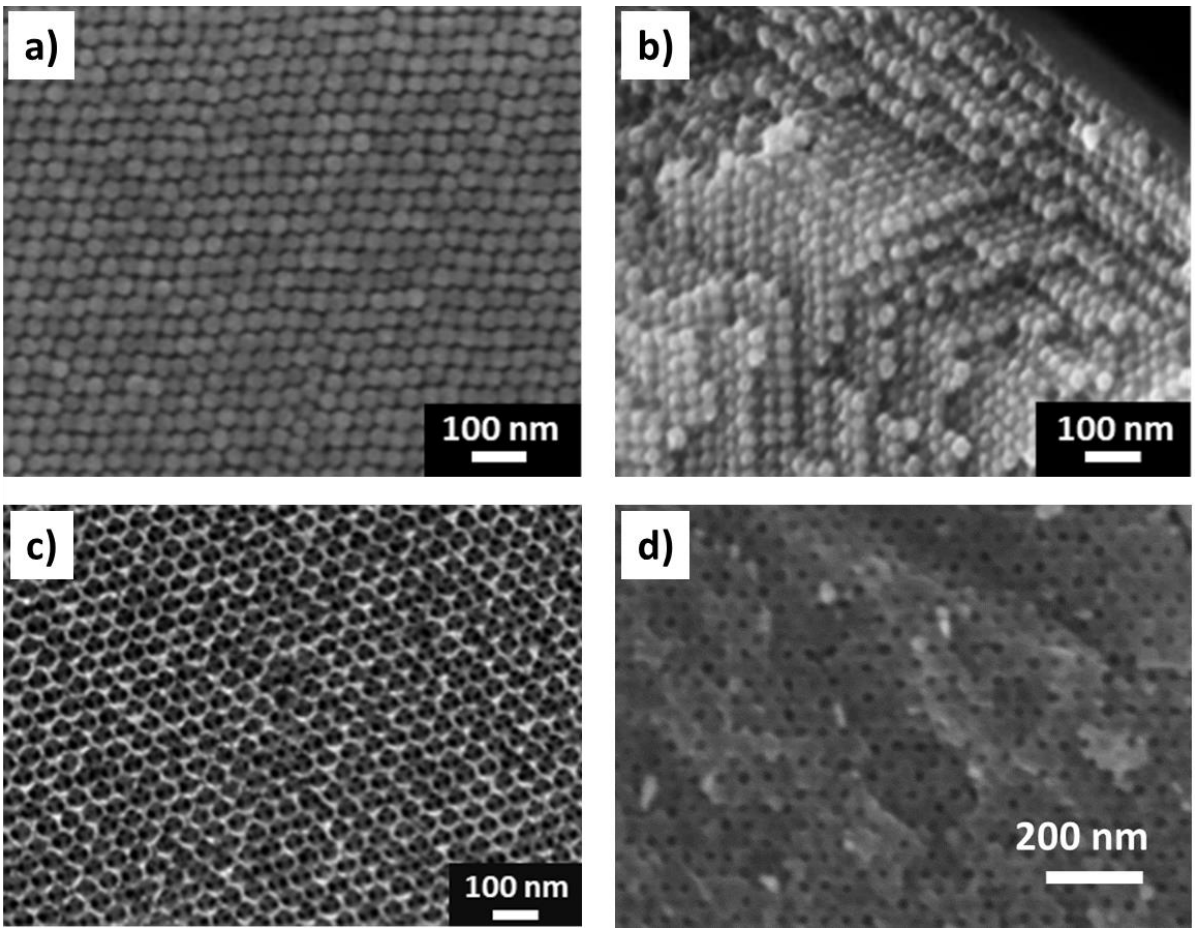

Figure 5.1: Fabrication of silicon metalattices from silica templates. a) A colloidal crystal of silica (SiO_2) nanospheres (30nm diameter pictured) is first assembled. b) Silicon is then infiltrated into the interstitial regions between nanopheres. Two of the metalattices we measure (at 30nm diameter and 14nm diameter templates) are at this stage of fabrication. c) The silica spheres may then be selectively etched away, leaving a highly porous silicon metalattice. d) The metalattice may then be re-infiltrated with silicon to reach a lower porosity. One of the metalattices we measure (starting from a 30nm template) is at this stage of fabrication. SEM images courtesy of John Badding.

Previous work on thermal transport in porous 3D metalattices shows many interesting phenomena. Measurements of silicon metalattices at 100s of nanometer periods show evidence of coherent phonon scattering at grain boundaries and very low thermal conductivity [141]. Copper metalattices at similar scales exhibit quasiballistic electron transport, due to increased scattering at surfaces [142]. Molecular dynamics (MD) calculations of few-nanometer silicon metalattices show up to a 10,000-fold reduction in thermal conductivity compared to bulk, due to phonon localization [143]. Our work focuses on silicon metalattices obtained from 14nm – 30nm nanosphere templates. These systems are an order of magnitude smaller than experimental works to date, and come closer to the small scales investigated by MD.

For our measurements, we characterize three different silicon metalattices fabricated on top of silicon substrates. Two of the metalattices have the silica spheres remaining inside. One starts from a 14nm diameter nanosphere template, and the other starts from a 30nm diameter nanosphere template. The third metalattice is porous, where the 30nm template has been etched out, and the metalattice re-infiltrated to a lower porosity. After fabricating these three silicon metalattices, collaborators at Penn State place nickel nanogratings on top as transducers for our experiments. The gratings range from 1000nm linewidth down to 30nm linewidth, and periods range from 4000nm to 120nm, respectively. As shown in Fig. 5.2(a), the e-beam lithographically deposited nanolines conform to the surface of the metalattice. Even for 30nm grating lines at a period of 400nm, we are successfully able to diffract our EUV probe and measure transient change in diffraction signal (Fig. 5.2(b-d)).

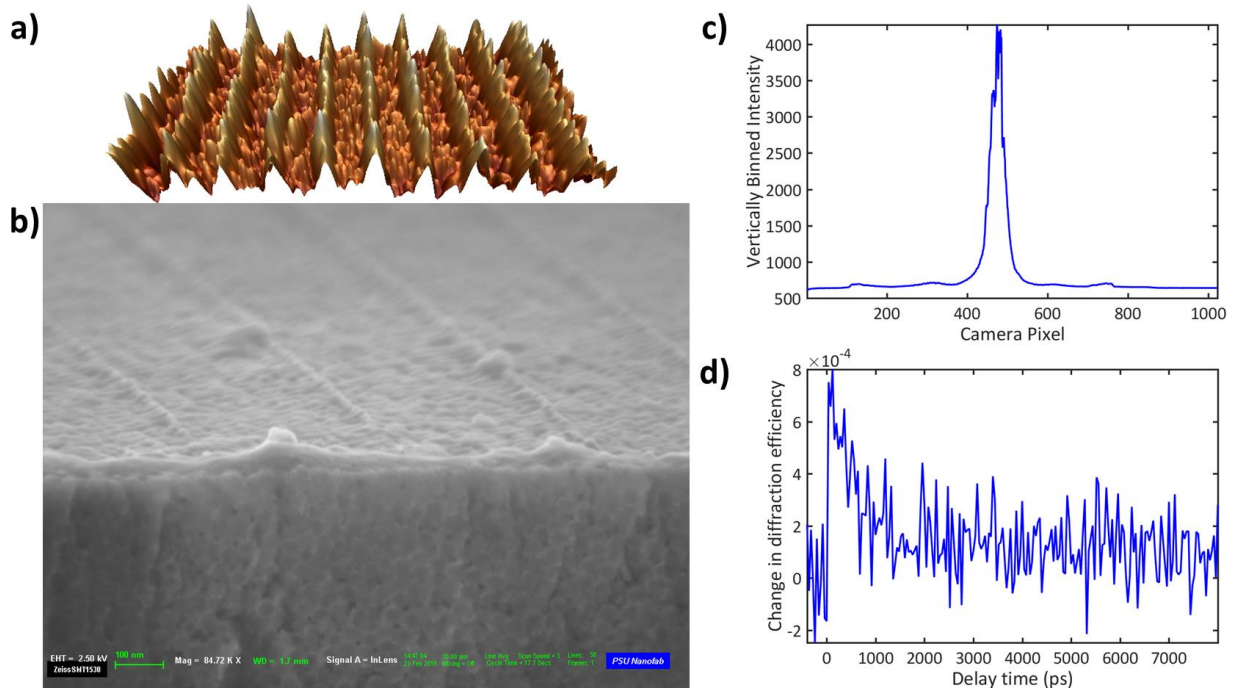

Figure 5.2: Measurements of 30nm gratings on a 30nm metalattice. a) AFM height map of a 30nm linewidth, 120nm period nickel grating deposited on a silicon metalattice with the 30nm silica sphere template remaining inside. b) Cross-section SEM of a 30nm linewidth, 400nm period nickel grating deposited on the same metalattice. Note the silica spheres are visible in the cross section of the metalattice layer (~800nm thickness). c) Vertically binned EUV diffraction pattern obtained from the grating in (b). Note the low diffracted orders at approximate pixel numbers 100, 300, 600, and 750. The second order diffracted beams are partially clipped by a filter before the CCD. d) Change in diffraction signal as a fraction of integrated intensity on the camera is visible above noise for this grating (b) and diffraction pattern (c). SEM image courtesy of Nabila Nova.

For larger grating sizes, namely 50nm linewidth to 1000nm linewidth, the signal is quite strong. As shown in Fig. 5.3(a), the diffraction efficiency changes by up to 1.5% of the total integrated intensity of the probe on the camera. This is stronger than the signals we have previously measured by about an order of magnitude. One possible explanation for the signal strength comes from the broadened diffraction of our EUV probe due to the highly uneven surface of the metalattice, demonstrated in Fig. 5.4. By having a more diffuse beam on the camera, we are less likely to saturate pixels in our CCD. Though we ensure the fully vertically binned image recorded by our camera does not saturate, it is possible that some of the individual pixels of the CCD do in general saturate before being summed. Thus, because the diffracted beams from the metalattice are more diffuse, the individual CCD pixels do not saturate, leading to an enhanced signal.

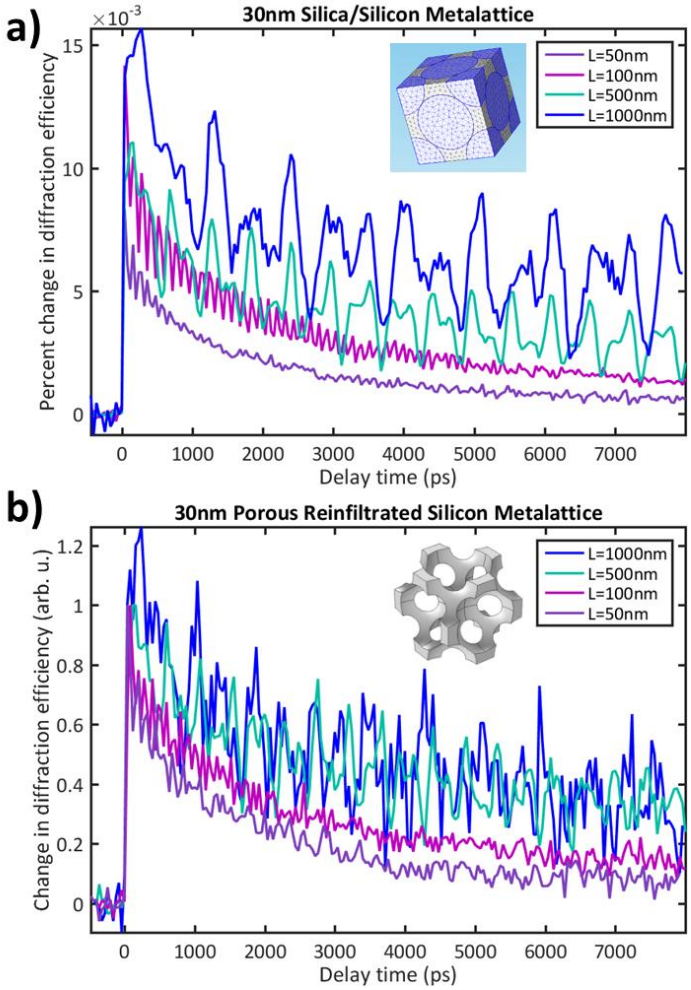

Figure 5.3: Measured signals on larger gratings for the two 30nm metalattices. a) The diffraction signal is shown as a fraction of total intensity on the camera, without further scaling. b) Signals are arbitrarily normalized to separate the signals for clarity. Insets: silica spheres remain inside (a) but are removed in (b). Actual sample porosity in (b) is lower than that shown for illustrative purposes in the inset.

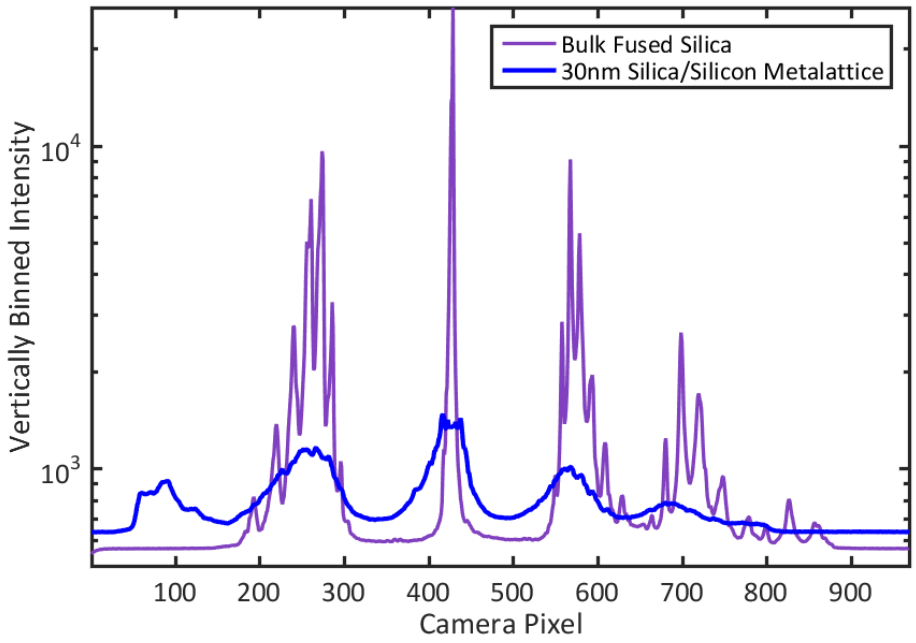

Figure 5.4: Comparing diffraction from a 100nm linewidth, 400nm period grating. The vertically binned diffraction pattern for the metalattice sample (blue line) is much broader than the diffraction pattern for a flat fused silica substrate (purple line). Note that the vertical axis is on a log scale. The vertical offset between the two diffraction images comes from differences in IR pump intensity, camera exposure time, and the number of camera exposures averaged together. The two images were also collected at slightly different angles, and different camera-sample distances, producing the slight differences in diffracted order spacing, and where the CCD filter edge cuts off the diffraction pattern. I have manually shifted the metalattice image horizontally to align the DC beam, for clarity.

To analyze the measured signals from each grating, we first consider the acoustic waves that are clearly visible in each trace. As seen in Fig. 5.3, multiple surface acoustic wave (SAW) frequencies are present, which define the range of the SAW dispersion we can access. As described in Chapter 4, SAWs are confined to the surface by about $1/\pi$ of their wavelength. Thus, as shorter wavelength SAWs are measured, the SAW velocity changes from that of the silicon substrate, to that of the metalattice layer. For the smallest gratings, the mass loading effect of the nanolines becomes dominant, and begins to suppress the SAW velocity below the metalattice's intrinsic value. This is shown in Fig. 5.5. The SAW velocities of the middle grating sizes agree well with finite element analysis (FEA) calculations for an ideal FCC silica/silicon structure. This indicates that the elastic properties of these metalattices follow continuum mechanics, even for surface acoustic waves down to a wavelength of 4 nanospheres, and penetration depths of ~1.5 layers. The measurements on the re-infiltrated metalattice also validate our technique on a porous

material. We can launch and probe SAWs, even with large pores of vacuum throughout the material. Note that all the frequencies we excite with our transducers are below the predicted phononic bandgap for these periodic structures.

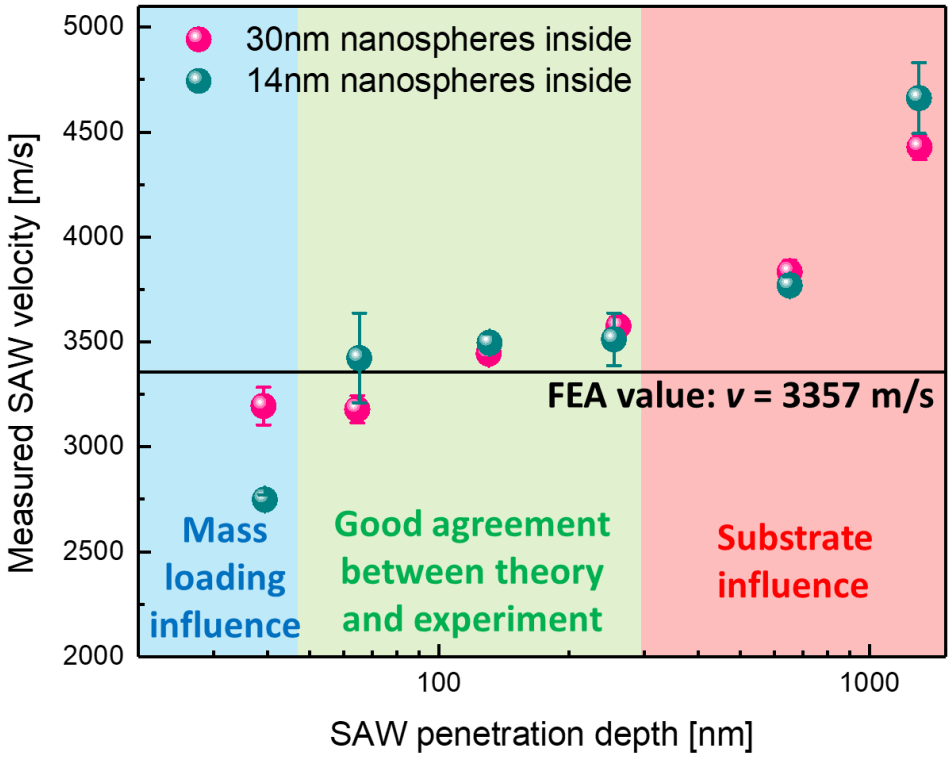

Figure 5.5: Surface acoustic wave dispersion in silicon metalattices. At large penetration depths, the SAW velocity approaches that of the silicon substrate. At intermediate penetrations, results agree with the FEA prediction. At the smallest penetration depths, mass loading from the transducer nanolines becomes a dominant effect, depressing the SAW frequency and lowering the SAW velocity. SAW penetration depth is the SAW wavelength (defined by the grating period) divided by pi. The SAW velocity is calculated from the measured SAW frequency and the grating period. Each point corresponds to the fundamental SAW launched by each grating on the 30nm template metalattice (red points) and the 14nm template metalattice (green points). Note that both metalattices have the same porosity, and so are predicted to have the same SAW velocity.

Though the elastic properties of these metalattices can be designed using continuum mechanics assumptions, their thermal properties are very non-classical. As shown in Fig. 5.3, nanolines on these metalattices have a much slower thermal decay than that observed on bulk silicon, as shown in Chapter 3. The fitting of our data with an effective Fourier model is still underway, as we need an independent measurement of the porosity of the re-infiltrated sample. However, the slow decays in the raw data already support molecular dynamics (MD) calculations by Ismaila Dabo at Penn State. In these calculations, our

collaborators show an enhanced scattering factor beyond what continuum mechanics would predict for porous metalattices made from smaller templates (few nanometer spheres). This leads to a greatly reduced thermal conductivity, as shown in Fig. 5.6. The Dabo group is currently pursuing non-equilibrium MD simulations of a nanoline-on-metalattice system analogous to ours to inform the interpretation and fitting of our experimentally observed thermal decays.

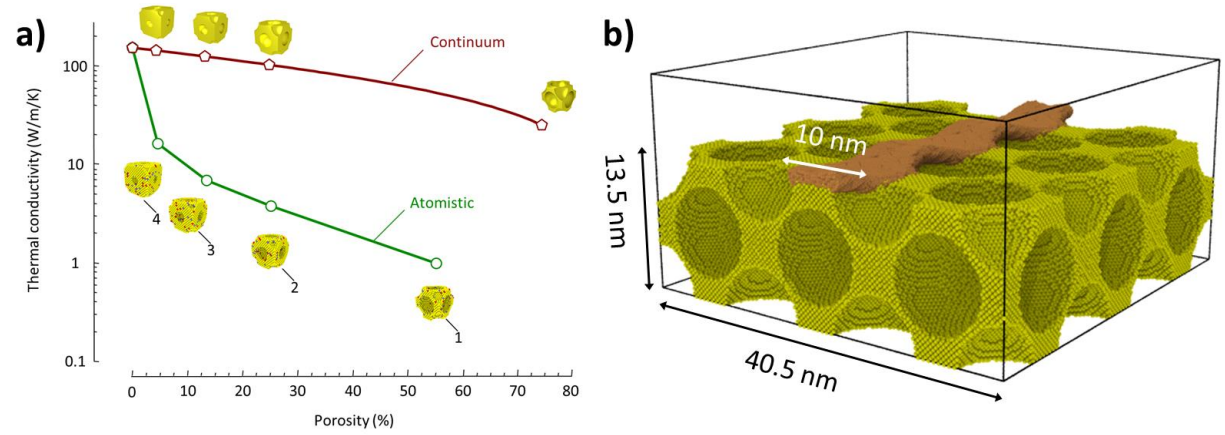

Figure 5.6: MD calculations of thermal transport in porous silicon metalattices. a) Equilibrium MD calculations of varying porosity metalattices (largest pore size is 2.2nm) show a reduced thermal conductivity compared to FEA predictions. Our collaborators attribute this to an enhanced scattering factor not captured in continuum mechanics b) Work is currently underway to understand the mechanisms behind our thermal transport measurements in these systems, using nonequilibrium MD with transient heating. Note the nanoline is made of copper in this simulation, rather than nickel, due to constraints on the inter-atomic potentials available to build MD models. Courtesy of Ismaila Dabo.

The measurement of complex hierarchical structures by our EUV nanometrology technique shows that it is not limited to bulk and thin film systems. However, to extend to more general materials systems, and to in-situ environments where nanograting fabrication is impossible, the technique must be broadened to a fully non-contact, truly non-destructive modality. Moreover, relying on nanoline transducers both limits the smallest excitations that we can produce, and the presence of the nanolines themselves can affect the system being measured. To overcome all of these challenges, I have pursued integrating transient grating excitations with our established EUV nanometrology technique.

5.3 Optical Transient Gratings

As a first step towards fully non-contact measurements, I have implemented a visible transient grating pump to launch dynamics at the micron scale, as described in Chapter 2. While this setup currently only reaches down to 2μm TG periods, it is sufficient for characterizing the effective thermal conductivity of novel materials systems. While an EUV probe is not necessary at these large TG periods, by using one we avoid the hot electron signal at early times that is measured by visible probes. The shorter wavelength of our EUV probe also has higher sensitivity to small displacements than a visible probe. This visible TG setup broadens our capabilities to more general samples, and serves as an important stepping stone to EUV TG, where direct, non-contact excitation of nanoscale dynamics is possible. Additionally, the simplicity of TG excitation permits analytical and semi-analytical solutions to the diffusion equation and/or the thermoelastic equation, depending on the system being studied. Thus, I first derive a fitting procedure for our measured signal from TG excitations that avoids the need for computationally intensive FEA modeling.

5.3.1 Data Processing and Fitting

A standard and successful method for fitting TG signals is to use the Fourier transform approach, as in [144]. However, when I implemented this method to fit our signals, I found it was not a good approach for our data. The samples we have measured to date with TG excitations have very low thermal conductivity, and they do not fully relax within the time window we can probe. Note, however, that the sample does fully relax before the next pump pulse arrives. Because our time window is short compared to the thermal dynamics we measure, we must calculate too large of a vector in frequency space to fit it. To have enough points in our time window to fit the experimental data, the calculated signal must have a sufficiently large maximum frequency. However, to properly sample the calculated signal in the frequency domain, it must also have a sufficiently short frequency step. These two requirements together define a calculated data set in the frequency domain that is cumbersome to try to calculate and Fourier transform back into the time domain. Thus, I followed a different approach to calculate theoretical signals to fit to our experimental data.

To accommodate our relatively short time window for these low conductivity samples, I follow the eigenfunction expansion method of Ju, et al. [145]. I modify the derivation the authors present to be for a single layer on a thick substrate and to explicitly introduce a thermal boundary resistivity at the interface. The calculation geometry is shown in Fig. 5.7, where the index i=1 corresponds to the film, and i=2 corresponds to the substrate.

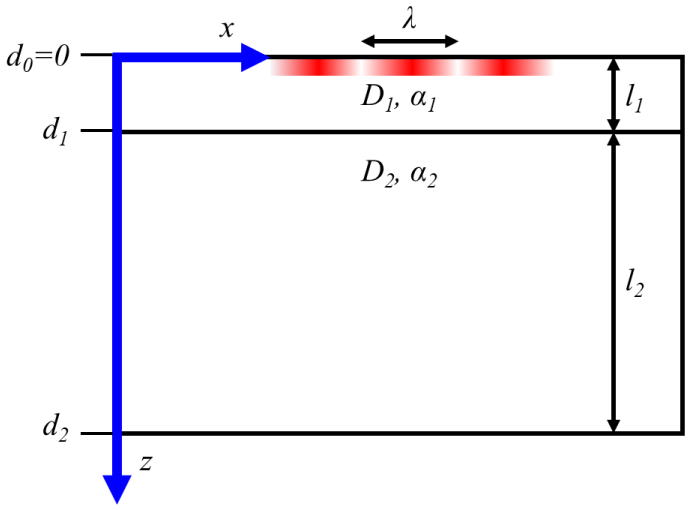

Figure 5.7: Geometry for eigenfunction expansion calculations. Note that the positive z-axis is defined as going down into the depth of the film-substrate system. The film is l_1 thick, while the substrate is l_2 thick. The thermal diffusivity, D_i, and optical absorption coefficient, α_i, are different for the film and substrate materials, in general. The transient grating period is λ. Relevant points on the z-axis are labeled with the definitions $d_0 = 0$, $d_1 = l_1$, and $d_2 = l_1 + l_2$.

The derivation begins with the 2D thermal diffusivity equation,

$$\frac{\partial}{\partial t}T_i(x,z,t) - D_i \Delta T_i(x,z,t) = Q_i(x,z,t), \quad \text{for} \;\; d_{i-1} \le z \le d_i, \tag{1}$$

where D_i is the thermal diffusivity of the film or substrate. I take the heat source, Q_i, to be

$$Q_i(x,z,t) = I_0 \left[1 + \cos(px)\right] E_i(z)\delta(t), \quad \text{with} \;\; p \equiv \frac{2\pi}{\lambda}, \tag{2}$$

where I_0 is the fluence of the incident pump beam (J/m^2), and λ is the period of the transient grating. Note that the instantaneous excitation at $t = 0$ is a reasonable approximation in this case. The ultrafast laser pulse heats the electrons on the order of femtoseconds, which in turn thermalize with the lattice in a few picoseconds. This is essentially instantaneous excitation for thermal decays of several nanoseconds.

Mathematically, this means the heat source serves as an initial condition on the temperature field. The quantity E_i is given by

$$E_1(z) = \frac{\alpha_1}{\rho_1 c_{p1}} e^{-\alpha_1 z}, \quad \text{and} \quad E_2(z) = \frac{\alpha_2}{\rho_2 c_{p2}} e^{-\alpha_2 (z-d_1) - \alpha_1 l_1}, \tag{3}$$

where α is the optical absorption coefficient (1/m), ρ is the density, and c_p is the specific heat capacity [146]. Using separation of variables and eigenfunction expansion in the z-direction, the solution is

$$T_i(x,z,t) = Z_i(z) g(t) \left[1 + e^{-p^2 D_i t} \cos(px)\right], \quad \text{with} \;\; g(t) = e^{-\varepsilon t}, \tag{4}$$

$$Z_i(z) = A_i \cos\left[\xi_i (z - d_{i-1})\right] + B_i \sin\left[\xi_i (z - d_{i-1})\right], \quad \text{with} \;\; \xi_i = \sqrt{\frac{\varepsilon}{D_i}}, \tag{5}$$

where ε is the eigenvalue. To solve for the four A and B coefficients, as well as the eigenvalues, I apply boundary conditions in the z-direction. The top and bottom surfaces are adiabatic (heat flux is zero):

$$-\kappa_1 \left.\frac{\partial T_1}{\partial z}\right|_{z=0} = 0, \quad \text{and} \quad -\kappa_2 \left.\frac{\partial T_2}{\partial z}\right|_{z=d_2} = 0, \tag{6}$$

where κ is the thermal conductivity. At the interface, the heat flux must be continuous, but the temperature has a discontinuity according to the thermal boundary resistivity, R,

$$-\kappa_1 \left.\frac{\partial T_1}{\partial z}\right|_{z=d_1} = -\kappa_2 \left.\frac{\partial T_2}{\partial z}\right|_{z=d_1}, \tag{7}$$

$$T_1\big|_{z=d_1} - T_2\big|_{z=d_1} = R\left(-\kappa_1 \left.\frac{\partial T_1}{\partial z}\right|_{z=d_1}\right). \tag{8}$$

Noting that $d_2 - d_1 = l_2$ and $d_1 - d_0 = l_1$, I apply the boundary conditions to obtain the four equations

$$B_1 = 0 \tag{9}$$

$$A_2 \sin(\xi_2 l_2) - B_2 \cos(\xi_2 l_2) = 0 \tag{10}$$

$$\kappa_1 \xi_1 A_1 \sin(\xi_1 l_1) + \kappa_2 \xi_2 B_2 = 0 \tag{11}$$

$$\left(\cos(\xi_1 l_1) - R\kappa_1 \xi_1 \sin(\xi_1 l_1)\right) A_1 - A_2 = 0 \tag{12}$$

Eqn. 9 immediately determines B_1. The other coefficients and the eigenvalues are obtained by expressing the remaining equations in matrix form,

$$\begin{bmatrix} \cos(\xi_1 l_1) - R\kappa_1\xi_1 \sin(\xi_1 l_1) & -1 & 0 \\ \kappa_1\xi_1 \sin(\xi_1 l_1) & 0 & \kappa_2\xi_2 \\ 0 & \sin(\xi_2 l_2) & -\cos(\xi_2 l_2) \end{bmatrix} \begin{bmatrix} A_1 \\ A_2 \\ B_2 \end{bmatrix} = 0. \quad (13)$$

By setting the determinant of this matrix equal to zero, I obtain the transcendental equation

$$R\kappa_1\kappa_2\sqrt{\frac{\varepsilon^2}{D_1 D_2}} \sin\left(\sqrt{\frac{\varepsilon}{D_1}} l_1\right) \sin\left(\sqrt{\frac{\varepsilon}{D_2}} l_2\right) = \kappa_2\sqrt{\frac{\varepsilon}{D_2}} \cos\left(\sqrt{\frac{\varepsilon}{D_1}} l_1\right) \sin\left(\sqrt{\frac{\varepsilon}{D_2}} l_2\right) + \kappa_1\sqrt{\frac{\varepsilon}{D_1}} \sin\left(\sqrt{\frac{\varepsilon}{D_1}} l_1\right) \cos\left(\sqrt{\frac{\varepsilon}{D_2}} l_2\right), \quad (14)$$

which can be solved by graphical intersection for the infinite series of eigenvalues, ε_j. To numerically search for each intersection between the left- and right-hand sides of Eqn. 14, it is convenient to partition the ε axis into intervals containing one intersection each. This condition should be met by searching over the intervals of ε defined by the zeros of the left-hand side. This is shown in Fig. 5.8.

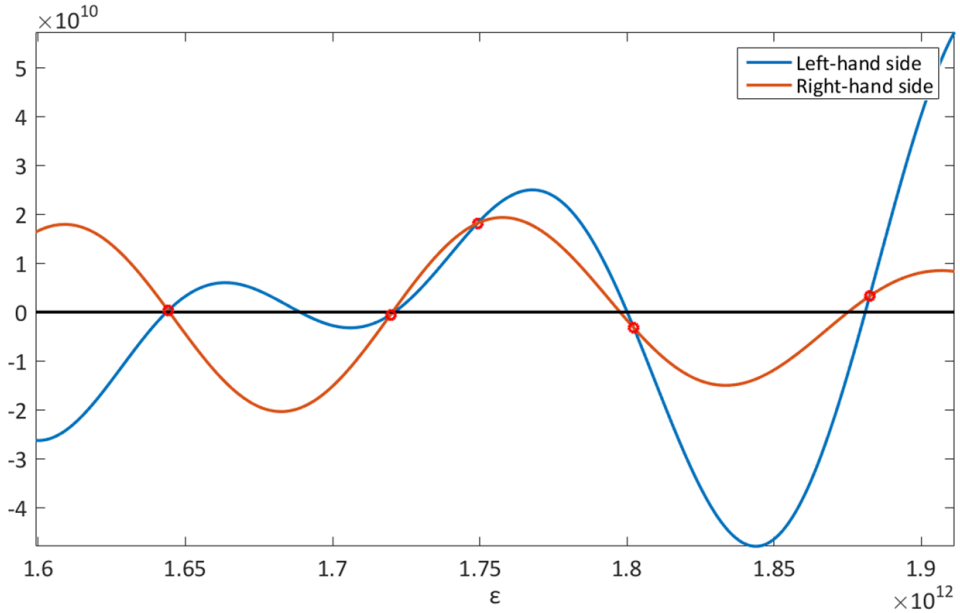

Figure 5.8: Graphical intersection method for the determination of eigenvalues. The left- and right-hand sides of Eqn. 14 are plotted as a function of ε (blue and orange, respectively). Each intersection point, marked with a red circle, defines an eigenvalue, ε_j. This plot shows the 49th – 53rd eigenvalues for a gold film on BK7 glass. Note there is exactly one intersection per interval between zeros of the left-hand side.

To determine the remaining coefficients, explicitly solve the system of equations in terms of A_1:

$$0 = [\kappa_2\xi_2 \cos(\xi_1 l_1)\sin(\xi_2 l_2) + \kappa_1\xi_1 \sin(\xi_1 l_1)\cos(\xi_2 l_2) - R\kappa_1\kappa_2\xi_1\xi_2 \sin(\xi_1 l_1)\sin(\xi_2 l_2)]\, A_1 \quad (15)$$

$$A_2 = [\cos(\xi_1 l_1) - R\kappa_1\xi_1 \sin(\xi_1 l_1)]\, A_1 \quad (16)$$

$$B_2 = -\frac{k_1\xi_1}{k_2\xi_2} \sin(\xi_1 l_1) A_1 \quad (17)$$

The bracketed expression in Eqn. 15 is exactly zero at each eigenvalue, according to Eqn. 14. Thus, A_1 is a free parameter for each ε_j. Plugging back into Eqn. 5, we obtain expressions for $Z(z)$ in the film and substrate,

$$Z_{1j}(z) = A_j \cos[\xi_{1j} z] \quad (18)$$

$$Z_{2j}(z) = \left[(\cos(\xi_{1j} l_1) - R\kappa_1\xi_{1j}\sin(\xi_{1j} l_1))\cos(\xi_{2j}(z - l_1)) - \frac{k_1\xi_{1j}}{k_2\xi_{2j}}\sin(\xi_{1j} l_1)\sin(\xi_{2j}(z - l_1))\right] A_j \quad (19)$$

where j indexes the eigenvalues, ε_j. To determine the A_j, I use the initial condition defined by the heat source applied at $t = 0$. First, I write the expression for T_i with the more explicit eigenfunction expansion as,

$$T_i(x, z, t) = \left[1 + e^{-p^2 D_i t}\cos(px)\right] \sum_{j=1}^{\infty} Z_{ij}(z) e^{-\varepsilon_j t}, \quad (20)$$

where i still indexes the layers, and j indexes the eigenvalues. Applying the initial condition,

$$T_i(x, z, 0) = Q_i(x, z, 0)$$

$$[1 + \cos(px)] \sum_{j=1}^{\infty} Z_{ij}(z) = I_0[1 + \cos(px)] E_i(z)$$

$$\sum_{j=1}^{\infty} Z_{ij}(z) = I_0 E_i(z).$$

Now, doing a "Fourier's Trick" integral on both sides,

$$\int_{d_{i-1}}^{d_i} \left[\sum_{j=1}^{\infty} Z_{ij}(z)\right] Z_{im}^A(z) dz = \int_{d_{i-1}}^{d_i} \left[I_0 E_i(z)\right] Z_{im}^A(z) dz, \quad (21)$$

where $Z_{ij}^A(z)$ is defined by the relationship

$$Z_{ij}(z) = A_j Z_{ij}^A(z). \quad (22)$$

Pulling the sum outside the integral, I obtain

$$\begin{aligned}\int_{d_{i-1}}^{d_i} I_0 E_i(z) Z_{im}^A(z) dz &= \sum_{j=1}^{\infty} \int_{d_{i-1}}^{d_i} Z_{ij}(z) Z_{im}^A(z) dz \\ &= \sum_{j=1}^{\infty} A_j \int_{d_{i-1}}^{d_i} Z_{ij}^A(z) Z_{im}^A(z) dz \\ &= A_m \int_{d_{i-1}}^{d_i} Z_{im}^A(z)^2 dz,\end{aligned} \tag{23}$$

where the final step used the fact that the integral on the right-hand side of Eqn. 23 is zero unless $j = m$. Relabeling $m \rightarrow j$, I finally obtain

$$A_j = \left[\int_{d_{i-1}}^{d_i} Z_{ij}^A(z)^2 dz\right]^{-1} \int_{d_{i-1}}^{d_i} I_0 E_i(z) Z_{ij}^A(z) dz. \tag{24}$$

Defining

$$N_{ij} \equiv \left[\int_{d_{i-1}}^{d_i} Z_{ij}^A(z)^2 dz\right]^{-1} \tag{25}$$

$$F_{ij} \equiv \int_{d_{i-1}}^{d_i} I_0 E_i(z) Z_{ij}^A(z) dz, \tag{26}$$

I obtain the final expression for the temperature field,

$$T_i(x, z, t) = \left[1 + e^{-p^2 D_i t} \cos(px)\right] \sum_{j=1}^{\infty} N_{ij} F_{ij} Z_{ij}^A(z) e^{-\varepsilon_j t}. \tag{27}$$

Assuming linear thermal expansion, the surface displacement measured by our EUV probe is

$$U(x, t) = \sum_{i=1}^{2} \int_{d_{i-1}}^{d_i} a_i T_i(x, z, t) dz, \tag{28}$$

where a_i is the linear thermal expansion coefficient of each layer. To obtain a change in diffraction signal to fit to our data, I numerically diffract an ideal Gaussian beam from this surface using Fresnel propagation, as described in Chapter 2. Note that in general, the coupled thermoelastic equations should be solved, but this equation may be sufficient when acoustic waves are not important.

Using this approach, I calculate theoretical change in diffraction efficiency signals to fit to our experimental data. I calculate signals for a sweep of film thermal conductivities and interpolate between calculated signal curves to fit the best effective thermal conductivity to the data using least squares. The

other film material properties are defined as inputs to the calculation depending on the material system under consideration.

5.3.2 Thermal Transport in Novel Nanosystems

We successfully measured two novel nanosystems using EUV-probed optical TG, both of which are promising thermoelectric materials, as described in Chapter 1. The first sample is a 2D hybrid nanoparticle array, fabricated by the Hihath group at UC Davis. Arrays like these have been shown to have very low thermal conductivities, below 0.5W/mK, which is promising for a high thermoelectric figure of merit, ZT [147]. Our arrays consist of one to four layers of oleylamine-coated, 10nm-diameter gold nanoparticles in a hexagonal close packed (HCP) arrangement. The oleylamine molecules inter-digitate, such that the molecule length (1.5nm) is also the inter-particle spacing, as described in [131]. Part of the value of these systems is that the ligands can be exchanged for more electrically conductive molecules, further enhancing ZT. The arrays are assembled as single monolayers, which are then stamp transferred onto substrates, in our case BK7 glass and a silicon wafer. We characterized both monolayers and four-layer assemblies on the two substrates. See Fig. 5.9 for an example of these nanoparticle arrays.

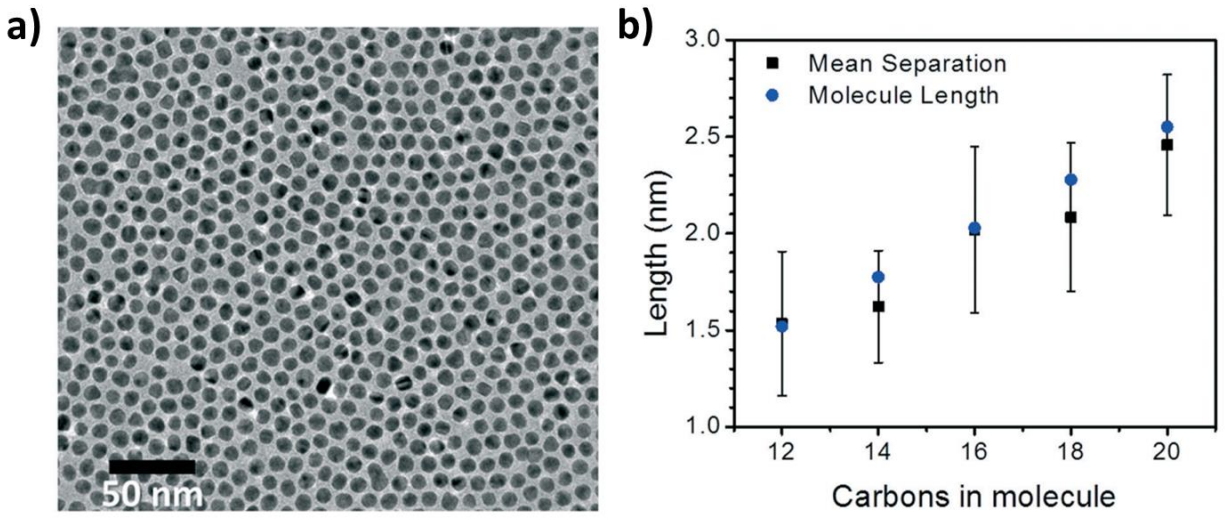

Figure 5.9: Nanoparticle molecular hybrid arrays. a) TEM image of a ligand coated gold nanoparticle array with 2D HCP order. b) Comparison of average nanoparticle separation (black squares) versus molecular ligand length (blue circles) when exchanging a variety of different length organic molecules onto the nanoparticle surfaces. The good agreement between the two lengths indicates the ligands strongly interdigitate. For our measurements, the nanoparticles are coated in oleylamine, which should result in a nanoparticle spacing of 1.5nm. Figure from [131].

The second material we characterize is a gold nanomesh, consisting of periodic holes in an HCP arrangement in a thin gold film. We measure three different nanomeshes on a BK7 substrate, with hole diameters and periods of 758nm/919nm, 1245nm/1500nm, and 2105nm/2560nm, respectively. Each gold film is 13nm thick and is prepared as described in [137]. Unlike the nanoparticle arrays, the nanomeshes have a large enough period to diffract our probe within the numerical aperture of our camera. Fig. 5.10 shows both an example of nanomeshes, and the 2D EUV diffraction that we measure. The hexagonal symmetry of our diffraction indicates the nanomesh is ordered on the scale of at least 50-100μm. When scanning the beam across the sample, we observe regions where two, slightly rotated hexagonal diffraction patterns are visible. This indicates the presence of grains and grain boundaries in the array of nanomesh holes.

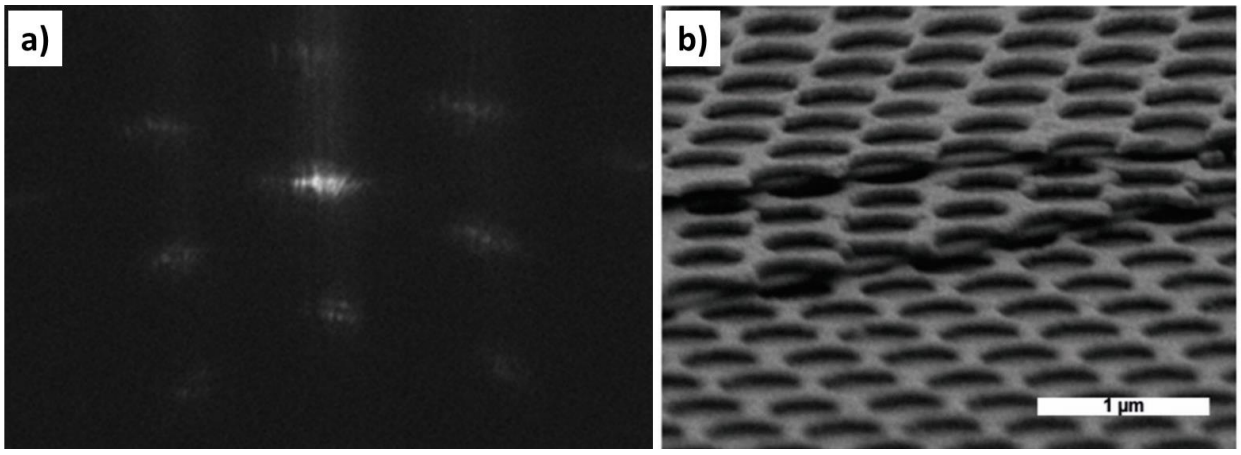

Figure 5.10: Example of nanomesh geometry and diffraction. a) Experimentally measured EUV diffraction from a 2560nm period gold nanomesh on BK7 glass. Note the six-fold symmetry expected for the HCP order of the nanomesh. b) Example of nanomesh geometry, taken from [137]. Pictured is an SEM image of a stack of nanomeshes. Our samples consist of a single gold nanomesh, 13nm thick, on a BK7 glass substrate.

To fit the conductivity of these materials using the approach described in Section 5.3.1, we must input effective densities, specific heats, thermal expansion coefficients, and optical absorption coefficients for the film materials. I use a volume-weighted average for density, expansion coefficient, and absorption coefficient, where the ratios of gold to vacuum to oleylamine (in the case of the nanoparticle arrays) are determined by geometry, and the constituent values are assumed to be bulk. For the heat capacity, a mass-weighted average must be used, so density and volume ratios are both used, according to

$$c_{p,avg} = \frac{f_{Au}\rho_{Au}c_{p,Au} + f_{Ol}\rho_{Ol}c_{p,Ol} + f_{Vc}\rho_{Vc}c_{p,Vc}}{\rho_{avg}}, \quad (29)$$

where f_i is the volume fraction of each constituent, and ρ_{avg} is the volume-weighted-average density of the material. To calculate the volume ratios from geometry, I approximate both the nanomeshes and each nanoparticle array layer as having ideal HCP order. For the 4 layer nanoparticle arrays, however, the order in the stacking direction is not controlled. Thus, I fit the data using two different cross plane orders to capture the bounds of maximum and minimum packing. For maximum packing, I assume 3D HCP order of the four layers, while for minimum packing I assume each nanoparticle in a given layer is stacked directly above a nanoparticle in the layer below. The volume ratios of the different constituent materials in the nanoparticle arrays and nanomeshes is given in Table 5.1. Table 5.2 lists the bulk material properties used.

Sample	Fraction gold	Fraction oleylamine	Fraction vacuum	Height (nm)
1 layer NP array	35.17%	37.64%	27.19%	13
4 layer NP array (HCP)	44.588%	43.436%	11.976%	42.88
4 layer NP array (stack)	38.50%	39.99%	21.51%	47.5
919nm nanomesh	38.303%	-	61.697%	13
1500nm nanomesh	37.524%	-	62.476%	13
2560nm nanomesh	38.683%	-	61.317%	13

Table 5.1: Volume fraction of constituent elements in nanoparticle arrays and nanomeshes. Each ligand-coated nanoparticle in the 2D array (top three rows) has a full diameter of 13nm. However, the ligands interdigitate by 1.5nm, resuling in the volume fractions shown. For the four layer samples, the order is not controlled in the cross-plane direction, so two limiting cases are considered. Minimum volume of vacuum is achieved by a full 3D HCP order (FCC used in calculation) in the bulk of the layer. Maximum volume of vacuum is achieved by stacking the nanoparticles in each layer directly on top of one another. Note that the height of each sample is also listed, as the assumption chosen for the cross-plane order changes what the total height is. Fractions for the nanomeshes are calculated assuming perfect HCP order in-plane.

Property	Gold	Oleylamine	BK7 glass	Silicon
κ [W/mK]	(in effective fit)	(in effective fit)	1.2 [63]*	149 [62]
ρ [kg/m^3]	19300 [148]	813 [149]	2650 [70]*	2330 [62]
c_p [J/kgK]	129 [148]	2349 [150]	750 [70]*	710 [61]
Thermal expansion [1/K]	14.2×10^{-6} [151]	2.87×10^{-4} [152]*	0.54×10^{-6} [65]*	3×10^{-6} [69]
Absorption coeff. [1/m]	7.562×10^{7} [153]	(neglected)	0.1482 [154]	98820 [155]

Table 5.2: Bulk material properties used in eigenfunction calculations. Thermal conductivities of gold and oleylamine in the samples are not input, as the effective conductivity is the fitting parameter used. The specific heat for oleylamine is a calculated value, based on the group additivity approach. I have neglected the optical absorption coefficient of oleylamine in the eigenfunction calculations as the absorption is very high for gold, and small percent changes to this value do not affect the resulting signal. Note the (*) marks properties of SiO_2 used as approximations for BK7 borosilicate glass, and octadecane used as an approximation for oleylamine.

To fit the data collected on the nanoparticle arrays, we first had to exclude all the measurements where the sample was burned by our pump beam, as shown in Fig. 5.11. Because the pump fluence used is large due to the low signal from these systems, and because the material is easy to burn, it is vital to check every measurement for permanent change or damage that could skew results. To do this, I calculate the change in the un-pumped diffraction pattern from the beginning of a measurement to the end of a measurement, and then I compare that result to the change in diffraction upon pumping at the beginning of a measurement. The pump-dependent change shows where the diffracted orders from TG excitation are. Any change in the unpumped diffraction over the course of the measurement at those camera pixels indicates that some permanent change has taken place at that spatial frequency, i.e. the TG pattern has been burned into the sample. An example of this process is given in Fig. 5.12(a). While measurements that burned the sample are unsuitable to learn about the repeatable dynamics of these materials, subsequent characterization of the burns allows for confirmation of the TG period. By analyzing the Fourier transforms of optical microscope images of burned regions, as shown in Fig. 5.12(b), I confirm that the TG periods achieved are 2.48±0.02μm and 3.18±0.02μm. These values are extremely close to the nominal 2.5μm and 3.2μm phase masks used to generate TG, indicating good alignment of the 4f imaging system.

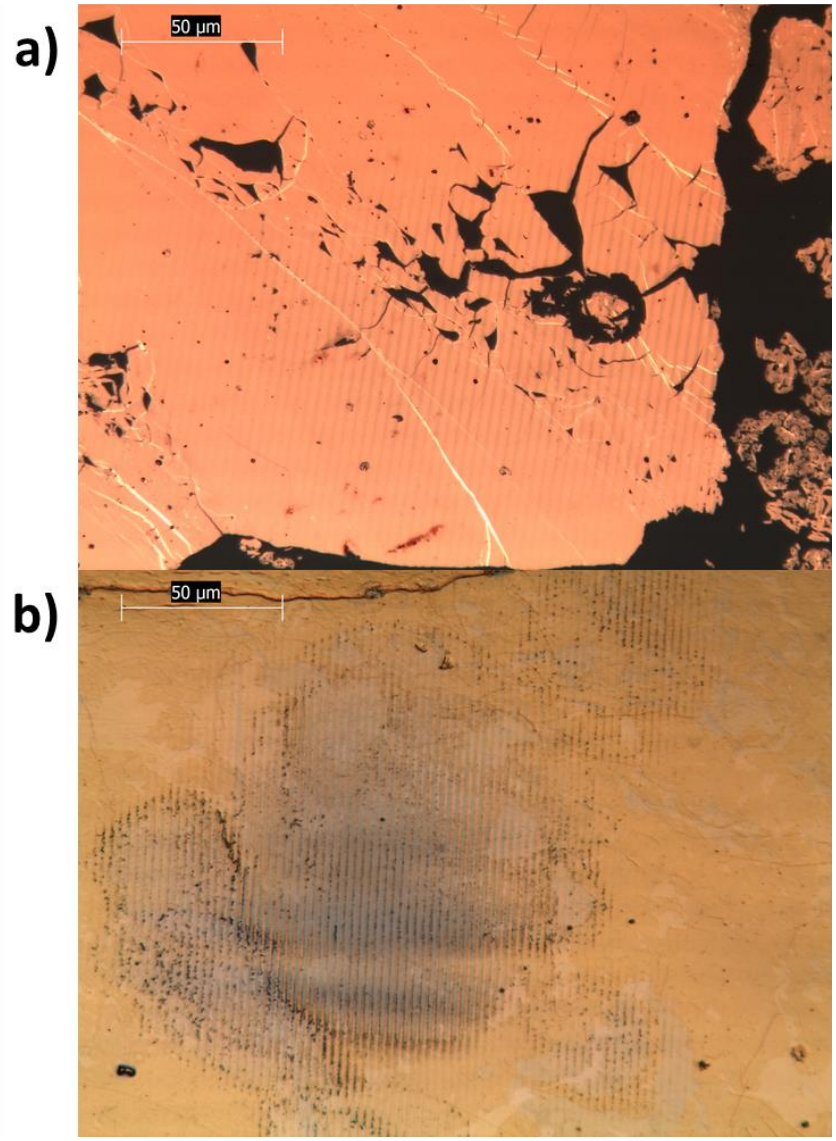

Figure 5.11: Optical microscope images of burned-in TG patterns. a) One layer of nanoparticle molecular array on a BK7 substrate. Defects, gaps, and edges are visible in this image, as well as faint periodic lines. These lines have a period that matches the expected period the TG excitation. b) Four layers of nanoparticle molecular array on a silicon substrate. At the most intense area of the burn, the dark silicon substrate is visible. Note the sample area is otherwise uniform. The goal is always to measure in uniform sample regions like (b), rather than in defect-heavy regions like (a), but this is not perfectly enforced.

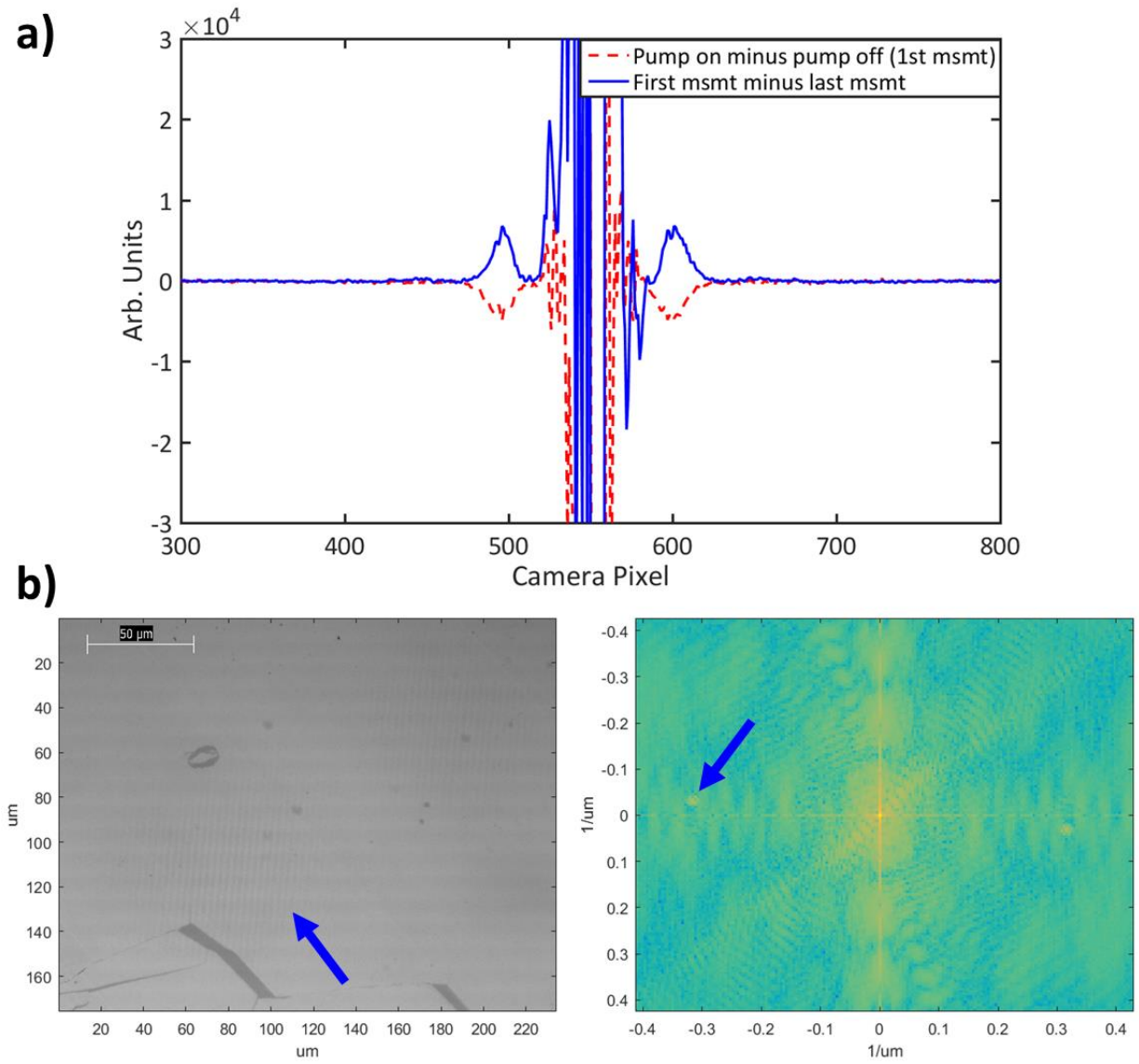

Figure 5.12: Identification of sample burning and subsequent calculation of TG period. a) Each scan of our experiment consists of several sweeps through the time window, which are averaged together. The difference between the pumped and unpumped diffraction patterns for the first sweep (red dotted line) shows the appearance of TG diffracted orders. The difference between unpumped diffraction patterns between the first sweep and the last sweep (blue line) indicates whether permanent change has taken place. Note the random changes in the DC order come from mode fluctuations and/or carbon deposition, not necessarily just burning. Data shown here is for 3.2µm TG on a hole-free region of the 919nm nanomesh (uniform gold film). b) After taking optical microscope images of burned-in gratings (left), I Fourier transform the image to find the spatial frequency of the periodic grating (right). The blue arrows indicate the burned-in grating area and the resulting peak in the Fourier transform. Data shown is for 3.2µm TG on one layer of nanoparticle molecular array with a silicon substrate.

After I exclude the damaging measurements, I average together all traces for a given substrate, layer thickness, and TG period configuration. I obtain fits for the effective thermal conductivity of each of

these average traces, as shown in Table 5.3 and Fig. 5.13. The best fit thermal conductivities are in the same range from 0.1-0.5W/mK, as obtained by thermoreflectance measurements on similar, thicker stacks of arrays in [147]. This is a reduction of three orders of magnitude from the thermal conductivity of bulk gold. The best fit thermal conductivity in each of our configurations varies only slightly, indicating this is indeed the effective thermal conductivity of the nanoparticle arrays. Note that one exception is the sample of four layers on BK7 glass, which has a notably lower thermal conductivity than the others. Due to the agreement between the other fits, I attribute this discrepancy to sample deviations. Similar to Fig. 5.11(a), the sample of four layers on BK7 has several cracks, gaps, and other large scale defects. Because each measurement location was not tightly controlled, it is possible that the only remaining measurements after excluding burning correspond to locations with large defects, resulting in a spuriously slow decay.

Sample	**Effective κ [W/mK]**
1 layer, 3.2μm TG, Si	0.27±0.01
1 layer, 3.2μm TG, BK7	0.27±0.02
4 layers, 3.2μm TG, BK7	0.37±0.03
4 layers, 2.5μm TG, Si	0.36±0.02
4 layers, 2.5μm TG, BK7	0.13±0.01

Table 5.3 Best fit conductivities for nanoparticle molecular arrays. These are the five samples that have useable data on them. Note that not all combinations of 1 vs 4 layers, 2.5μm vs 3.2μm periods, and silicon vs BK7 substrates have useable data, after excluding burning measurements. The error bars on the effective thermal conductivity are preliminary and reflect only variance in model substrate thickness and 4-layer cross-plane order. The error bars will be larger once all sources of uncertainty are accounted for.

The next step is to verify the numerical model fits by also fitting the data using the FEA approach described in Chapter 3. There are a number of assumptions in the numerical model derivation that need to be confirmed as valid, most notably the uncoupled treatment of temperature and strain. Once the model is confirmed, it may be applied to analyze the data taken on the gold nanomesh samples as well.

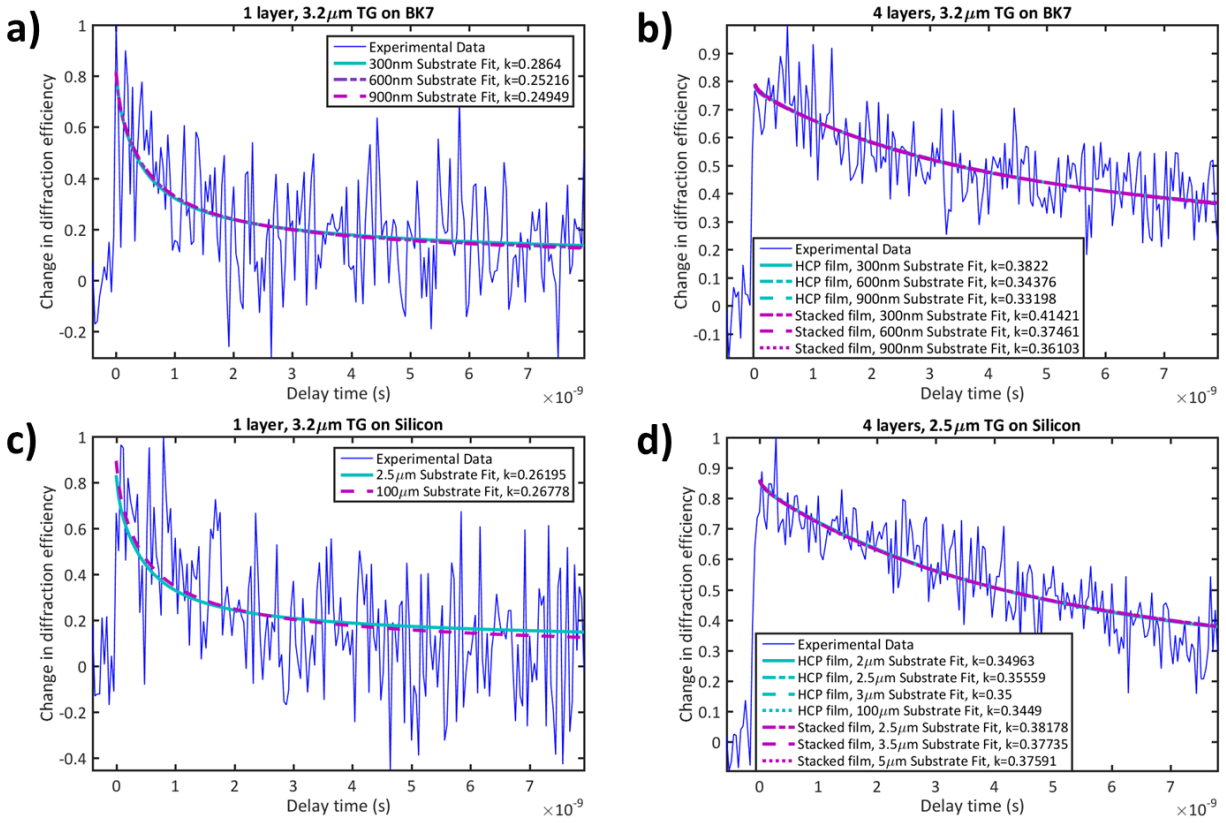

Figure 5.13: Best fits for the nanoparticle molecular arrays. Experimental data traces (dark blue lines) are obtained by averaging together all non-burning measurements for a given layer number, TG period, and substrate combination. In the numerical model, the substrate thickness is specified. The full experimental thicknesses of ~1mm for BK7 and ~400μm for silicon, however, are not required for the transport that happens within our experimental time window. Additionally, using too thick of a substrate, sampled properly, becomes computationally expensive. The above fits show the results for a variety of substrate thicknesses, once the substrate is thick enough to avoid finite-thickness effects. The results indicate our best fits are not spuriously dominated by model substrate thickness. For the four-layer samples, the light blue curves correspond to HCP cross-plane order, while the purple curves correspond to nanoparticle-over-nanoparticle stacking cross-plane order.

5.4 Extreme Ultraviolet Transient Gratings

Transient gratings achieved by the interference of two EUV beams has long been a goal for nanosystem metrology. The approach is truly non-contact and non-destructive—EUV TG excitations reach deep nanoscale lengths and ultrafast times without the limits or unintended influence of nanostructured transducers. It is furthermore a very general approach to studying surface excitations, as all materials strongly absorb EUV. In addition to the thermal and elastic characterizations described above, the EUV TG geometry is suitable for super-resolution imaging via structured illumination microscopy [156, 157],

nanoscale spin gratings by interfering crossed polarization beams [158], and even nonlinear optics in the EUV wavelength range [159]. To achieve the full utility of EUV TG at the deep nanoscale, however, there are some fundamental challenges that must be overcome.

Transient gratings generated by EUV can be tuned from micron scale periods at low crossing angles, to nanoscale periods at very large crossing angles. This is defined by the familiar transient grating relationship

$$\Lambda = \frac{\lambda}{2\sin\theta}, \tag{30}$$

where Λ is the grating period, λ is the wavelength of the excitation beams, and θ is the half crossing angle. Eqn. 30 shows that reaching a TG period that matches the wavelength of the EUV beam used requires a half crossing angle of 30°. This is a substantial angle to reach, given the requirement of designing EUV optical systems with no refractive elements, and with high losses at each reflective element. This is the first challenge in reaching the deep nanoscale with EUV TG – achieving large crossing angles with sufficient EUV flux at the sample.

The next challenge in reaching deep nanoscale TG periods is in exciting measurable dynamics in the sample itself. Materials reflect EUV more when approaching a glancing angle of incidence. This limits the energy that is absorbed by the sample, once going to very large crossing angles. The ultrafast nature of the EUV beams also makes it difficult to excite a measurable number of TG periods. The EUV bursts generated during HHG lie within an ~10fs envelope, and free electron laser (FEL) sources can reach femtosecond scale pulse durations as well. This means that pulse front tilt severely reduces the interaction region between the two TG arms at high crossing angle, as shown in Fig. 5.14. While pulse front tilt is mitigated at visible wavelengths through a 4f imaging system [44], the lack of refractive optics in the EUV eliminates the same solution. It remains an open question how to design an EUV optical system with optimized pulse front tilt to produce interference across the full width of the pump arms.

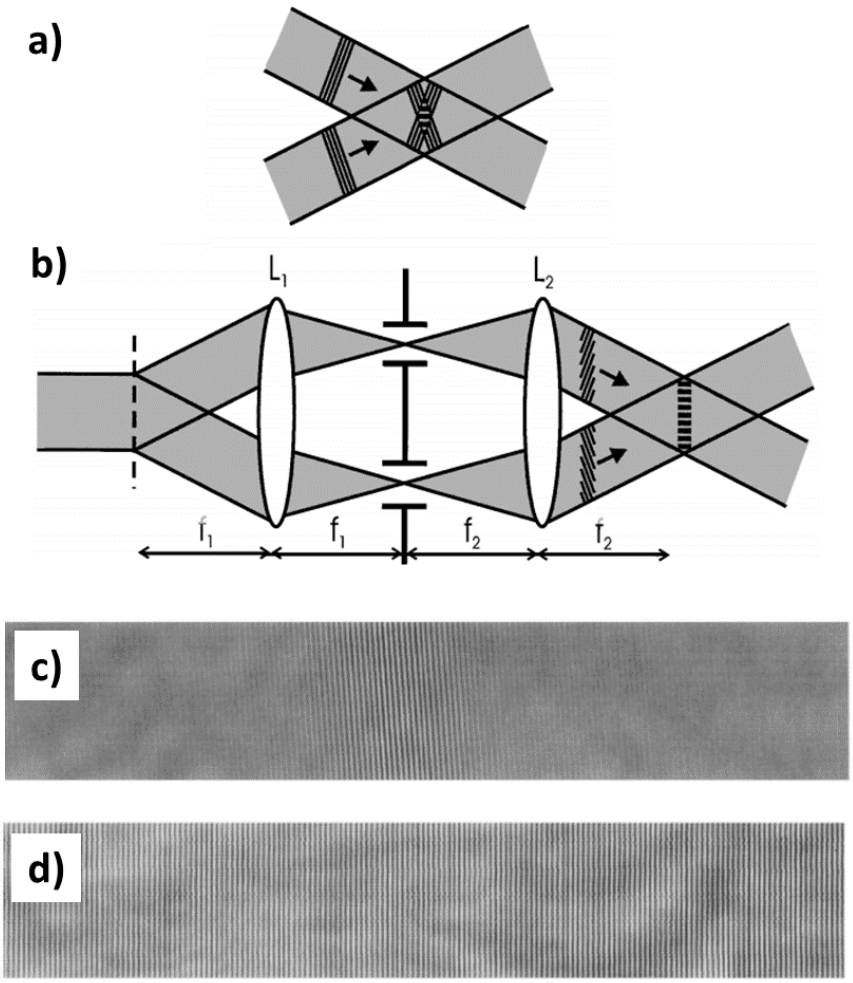

Figure 5.14: Pulse front tilt and the 4f optical TG setup. a) Ultrafast lasers produce very narrow pulses in the longitudinal direction (short temporal duration). When crossing two such pulses at large angles, this severely reduces the region where the two pulses can interfere to produce a TG pattern. b) A 4f imaging system with a transmission phase mask to generate the two TG beams produces a favorable pulse front tilt to achieve interference across the full width of the crossing beams at the sample plane. Panels (c) and (d) are charge coupled device (CCD) images of crossing two near infrared 30fs pulses in the (a) and (b) geometries, respectively. Images taken from [44].

Though these challenges are fundamental, we have already demonstrated EUV TG at the seeded FEL, FERMI, at Elettra, near Trieste, Italy. In the following section, I will present optical measurements of thermal and acoustic dynamics launched by EUV TG, obtained in collaboration with the Nelson group at MIT and the team at FERMI. I will further present FERMI's first demonstration of EUV TG down to 28nm period, probed by a third EUV beam. I will close this section with a description of the work so far to implement EUV TG on a tabletop, using HHG beams at JILA. To reduce the complexity of the experiment,

and to optimize one component at a time, both the experiments at FERMI and the designs at JILA have begun with an optical probe, and correspondingly large EUV TG periods.

5.4.1 EUV TG with an Optical Probe

The first work I collaborated on with FERMI used the mini-TIMER setup in the DiProI end station. In this experiment, the beam from the FEL is slowly focused, then split in two by a half mirror. Two other flat mirrors then recombine the two beams at shallow crossing angles to launch thermal and acoustic dynamics at large enough EUV TG periods to be probed optically. Fig. 5.15 shows the setup used. In the present work, we generate EUV TG with 12.7nm FEL radiation, with 70fs pulse duration, 3μJ total pulse energy, 50Hz repetition rate, and a 100μm diameter spot size on the sample. The full crossing angle is 2.62°, producing a 277nm period TG pattern. This period is smaller than the visible TG periods commonly used, but it is still large enough to be probed by an optically-generated 400nm wavelength probe.

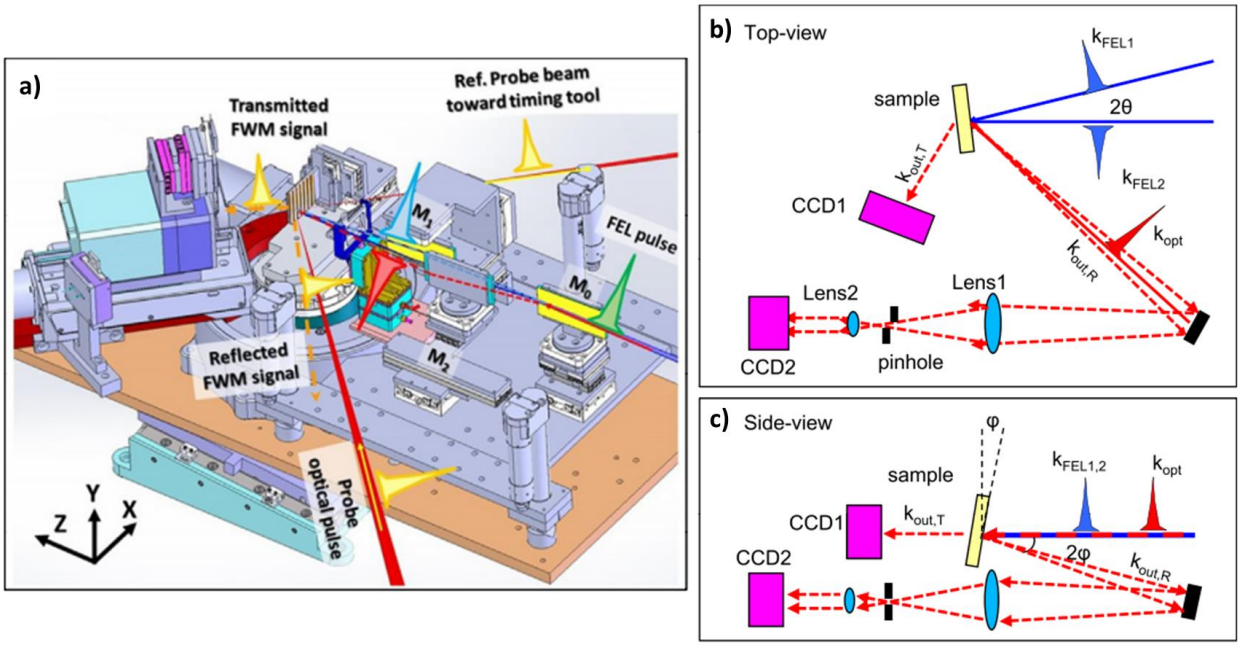

Figure 5.15: The mini-TIMER setup for optically-probed EUV TG. a) Model of the experimental setup and beam paths. The two TG arms are split from the FEL beam by clipping half of the beam at the edge of a sharp half mirror. The two arms are then recombined in a parallelogram geometry, with their relative timing adjustable by the M_2 mirror position. b) Top view of the beam paths. The probe beam is incident at the Bragg condition, producing both a transmitted and reflected first diffracted order. The reflected, or back-diffracted, beam is refocused to a separate camera from the transmitted diffracted beam, allowing simultaneous signal measurement. c) Side view of the beam paths. The sample is tilted downward by a small angle, φ, allowing the reflected diffraction beam to be collected by a mirror just below the incident optical probe. Figures from [160].

To probe the EUV transient gratings, we use the second harmonic of the FEL seed laser. It has 400nm wavelength, 100fs pulse duration, and good timing stability with the FEL radiation. The probe was delayed by up to 600ps after the pump via a mechanical delay stage, defining the maximum time window for this experiment. Because we are probing with visible wavelengths, we simultaneously measure signals both in reflection and transmission geometries, for transparent samples. We probe at the Bragg condition, meaning that the reflected diffracted order is collinear and counterpropagating to the incident probe beam. To separate it for measurement, we slightly tilt the sample downward, as shown in Fig. 5.15(c). This angles the reflected beam below the incident probe beam, where it is collected by an additional optical system. Measurement of this reflected signal is vital when characterizing opaque samples.

We measured a variety of samples during this experiment. First, we measured thick, transparent samples, where we characterized acoustic waves both on the surface (Rayleigh waves) and in the bulk (longitudinal waves) of the sample. These samples included single-crystal diamond, BK7 glass, and the scintillator $Bi_4Ge_3O_{12}$. We then measured thermal transport in the same diamond sample, a 349nm silicon membrane, and a bulk silicon germanium sample (6% Ge). For the SiGe measurement, the sample was opaque to 400nm light, meaning that only the reflected signal could be used.

The signal obtained by the optical probe is proportional to the refractive index modulation squared. This must be taken into account to understand the dynamics observed. Consider the simplified equation

$$I = \left[A_e e^{-t/\tau_e} + A_{th} e^{-t/\tau_{th}} + A_L \cos(\omega_L t) + A_R \cos(\omega_R t)\right]^2, \tag{31}$$

where the A_i refer to the amplitudes of the electronic, thermal, longitudinal wave, and Rayleigh wave signals, in order, and I is the measured intensity of the diffracted beam. When the square is carried out, the direct terms will appear to have half the decay times, τ, and double the frequencies, ω, while the cross terms will have the intrinsic values of the sample. The thermal-acoustic cross terms will be single-frequency oscillations on top of a thermal decay. The acoustic-acoustic cross terms, however, will produce beat frequencies in the measured signal. Each of these terms has a different starting amplitude and decay time, meaning that they will be dominant at different points in the measured total signal. In general, the electronic

decay will dominate at the earliest times, followed by the thermal decay and acoustic waves. If the thermal signal decays before the acoustic waves, then there is an apparent "frequency doubling" as the thermal-acoustic cross terms die out.

With this simple model in mind, we can now discuss the results of the optically-probed EUV TG measurements. First, I present the acoustic results. For diamond, both the electronic and thermal signals decay within the first 50ps, leaving just the frequency-doubled and beat frequency acoustic signals, as shown in Fig. 5.16. Acoustic wave velocities calculated from the measured frequencies are close to the literature values for diamond [23]. For BK7, we compare the reflection signal to the transmission signal, as shown in Fig. 5.17. Because of the low thermal conductivity of BK7, the thermal signal persists for the full experimental time window, and the measured frequencies are those of the intrinsic Rayleigh and bulk longitudinal waves. In reflection, the Rayleigh wave signal is stronger, as it is confined to the surface. We also observe a second longitudinal frequency that is back diffracted from the bulk of the sample. This diffraction can be phase matched and observed because of the very short penetration depth of the EUV pump, which produces a broad spatial frequency distribution in the depth-direction. See [23] for more details. Measured frequencies for BK7 also agree with expectations from literature. Finally, in $Bi_4Ge_3O_{12}$, we directly excite a 2.8THz optical phonon with the EUV TG beyond just the Rayleigh and longitudinal waves, as shown in Fig. 5.18. This optical phonon mode has previously been observed, though with a slightly lower frequency.

In addition to demonstrating acoustic characterizations, the mini-TIMER experiment demonstrates that thermal characterizations are indeed possible using EUV TG. Though limited to shallow crossing angles by the visible probe, the 277nm period achieved is sufficient to launch non-diffusive thermal transport in silicon and diamond. Both of these materials have long phonon mean free paths at room temperature, as discussed in Chapter 3. Though work is ongoing to analyze the thermal measurements, preliminary results show quasiballistic thermal transport in silicon, as expected at this TG period, and nearly fully ballistic transport in diamond. Together, all of these results show that EUV TG is a versatile and powerful metrology tool. All that is needed to go to the deep nanoscale is the addition of an EUV probe.

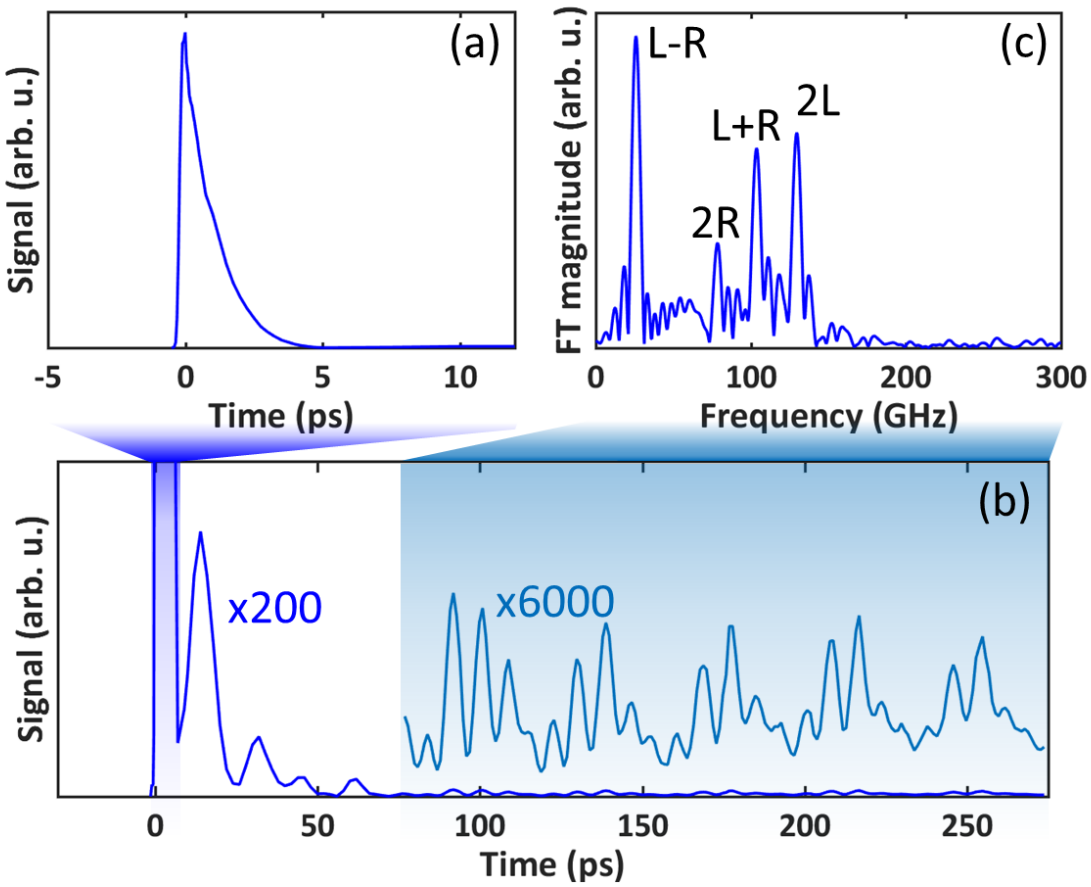

Figure 5.16: Optically probed EUV TG signal on single crystal diamond. As is common for optical probes, the first few picoseconds are dominated by the hot electron signal (a). Afterward, thermal and acoustic dynamics are visible, as shown in the composite trace in (b). This signal is amplified 200x to make it comparable to the electronic signal in (a). The inset shows the long timescale acoustic dynamics amplified by 6000x compared to (a). These inset data are then Fourier transformed in (c) to show the doubled and beat frequencies of the Rayleigh (R) and bulk longitudinal (L) waves. All data presented are obtained in transmission geometry. Figure from [23].

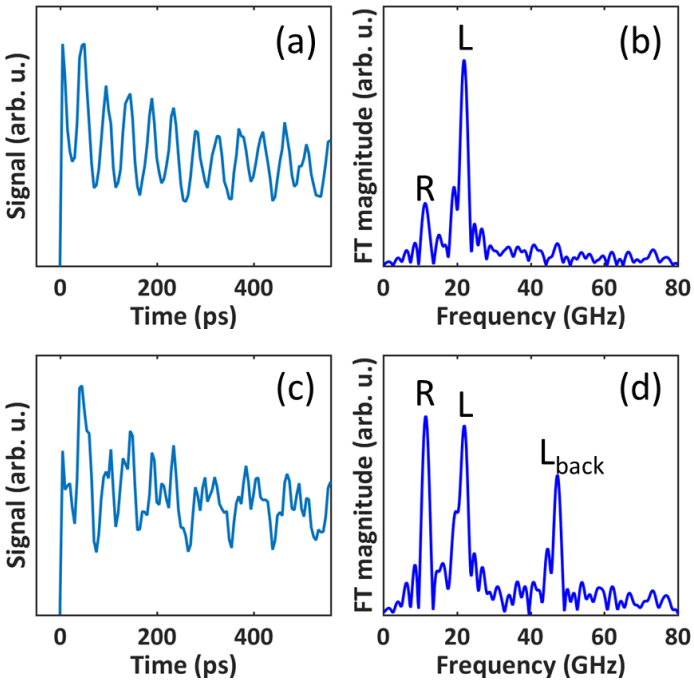

Figure 5.17: Optically probed EUV TG signal on BK7 glass. Panels (a) and (b) show the experimental signal and its Fourier transform, respectively, for the transmitted diffracted beam. Panels (c) and (d) show the signal and Fourier transform, respectively, for the reflected diffracted beam. The additional longitudinal frequency in reflection mode comes from a back diffracted beam that is phase matched in the bulk. Figure from [23].

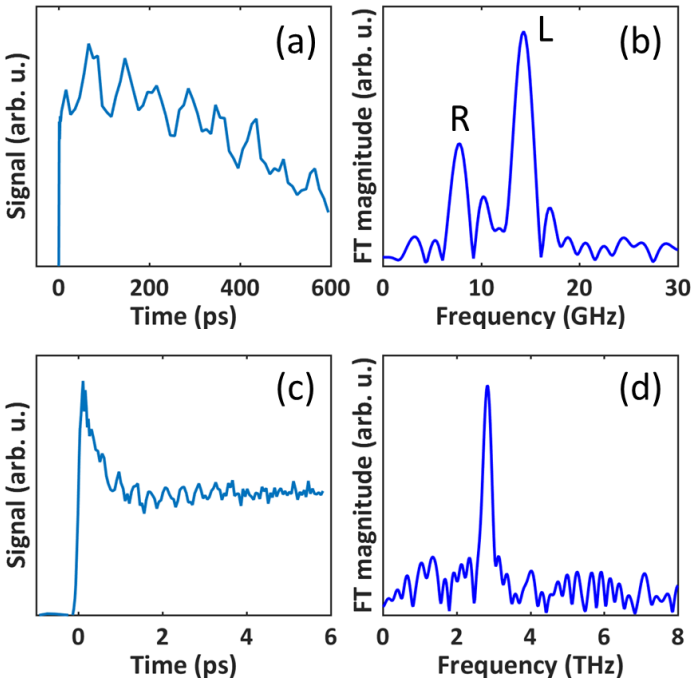

Figure 5.18: Optically probed EUV TG signal on $Bi_4Ge_3O_{12}$. a) Long timescale data show the Rayleigh and bulk longitudinal wave frequencies of $Bi_4Ge_3O_{12}$. The Fourier transform of these data are shown in (b). c) At short timescales, a 2.8THz optical phonon is observed, as seen in the Fourier transform (d). Figure from [23].

5.4.2 EUV TG with an EUV Probe

After the successful demonstration of optically probing EUV TG at mini-TIMER, we returned to FERMI, along with members of the Keith Nelson and Gang Chen groups from MIT, to attempt an all-EUV experiment at the TIMER end station, where both the pump and probe are FEL radiation. In this setup, the EUV beam, which contains multiple harmonics, is first split between pump and probe arms using a half mirror, as for mini-TIMER. The half that serves as probe is delayed via a mechanical stage, using multilayer mirrors that select a single EUV wavelength to serve as probe. The half that serves as pump is split once again by a half mirror, and then filtered to the desired pump wavelength by thin solid state filters. Each of the three beams is focused onto the sample using a separate toroidal mirror. A schematic of the TIMER setup is given in Fig. 5.19. To change TG period, the pump toroids are removed, allowing the beams to propagate closer to the sample, where shorter object distance toroids are set up to recombine the beams at a larger crossing angle. The TG period is further tuned by changing which FEL harmonic is used as the pump wavelength. For this work, the full crossing angle is maintained at 27.6°, while the pump wavelength is changed from 53.4nm to 39.9nm, to 13.3nm. This produces the record TG periods 110nm, 85nm, and 28nm, respectively.

Excited dynamics are measured in a transmission geometry, requiring that the samples be very thin, as the EUV probe will be strongly absorbed by any material. Probe wavelengths are chosen to be 17.8nm, 13.3nm, and 13.3nm, respectively for each pump wavelength. The probe is incident at 4.5°, achieving the Bragg condition for the first two geometries. The smallest TG period is not probed at the Bragg condition, but the grating is sufficiently thin that appreciable signal is still obtained. The FERMI team successfully measured thermal and acoustic dynamics in thin Si_3N_4 and Si membranes, marking the first demonstration of all-EUV TG with three distinct EUV beams. The work we did during our collaboration with FERMI contributed to obtaining this result a short time later.

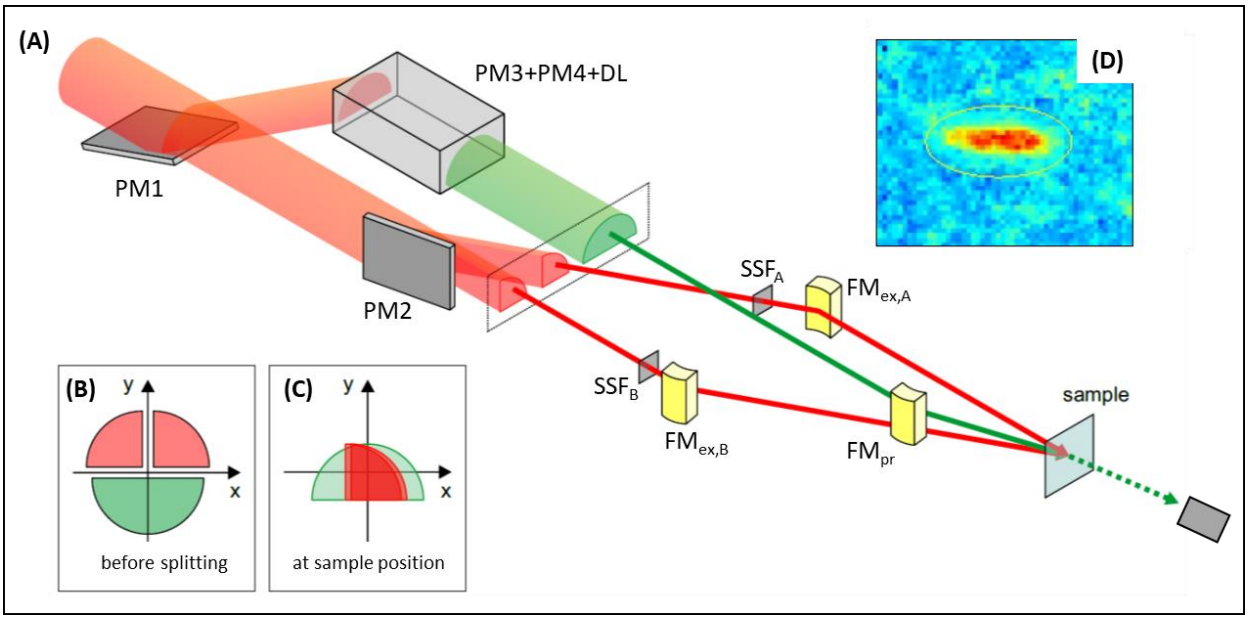

Figure 5.19: Schematic of the TIMER experiment with EUV-probed EUV TG. A) Schematic of the splitting, delay, filter, and focusing optics. Additional toroidal mirrors for larger crossing angle TG are not shown. B) The FEL beam is split with half going to the probe, and the remaining two quarters being split into the two pump beams. The lossy EUV mirrors in the delay line reduce the probe intensity to be below that of the pumps. C) The three beams are recombined on the sample. The delay optics filter the probe to the desired wavelength, while separate solid state filters select the pump wavelength. D) Focusing after splitting achieves a better mode at the sample, as indicated by the signal beam measured on the CCD camera. Note the signal is "background free" as the diffracted beam is not colinear with any other beam. Figure from [24].

The signals obtained on Si_3N_4 and Si are shown in Figs. 5.20 and 5.21, respectively. These signals contain both thermal decays, and acoustic oscillations. On Si_3N_4, the calculated acoustic wave velocities and thermal diffusivities agree with literature values [24]. This indicates that the TG excitation is behaving as expected, even in the EUV regime, and it also indicates that Si_3N_4 membranes exhibit diffusive thermal transport even down to 28nm periods. For silicon, however, there is strong non-diffusive thermal transport, as expected for a long mean free path material. The observed decay is much slower than the diffusive prediction, as shown in Fig. 5.21. Note that for both samples the earliest times are not dominated by the electronic response present in optically-probed measurements. As expected from our work using EUV to probe optically excited metals, the probe is largely insensitive to hot electron dynamics, as long as the EUV energy is tuned away from core-level resonances. The signal is instead dominated by the lattice response, e.g. thermal expansion and acoustic waves.

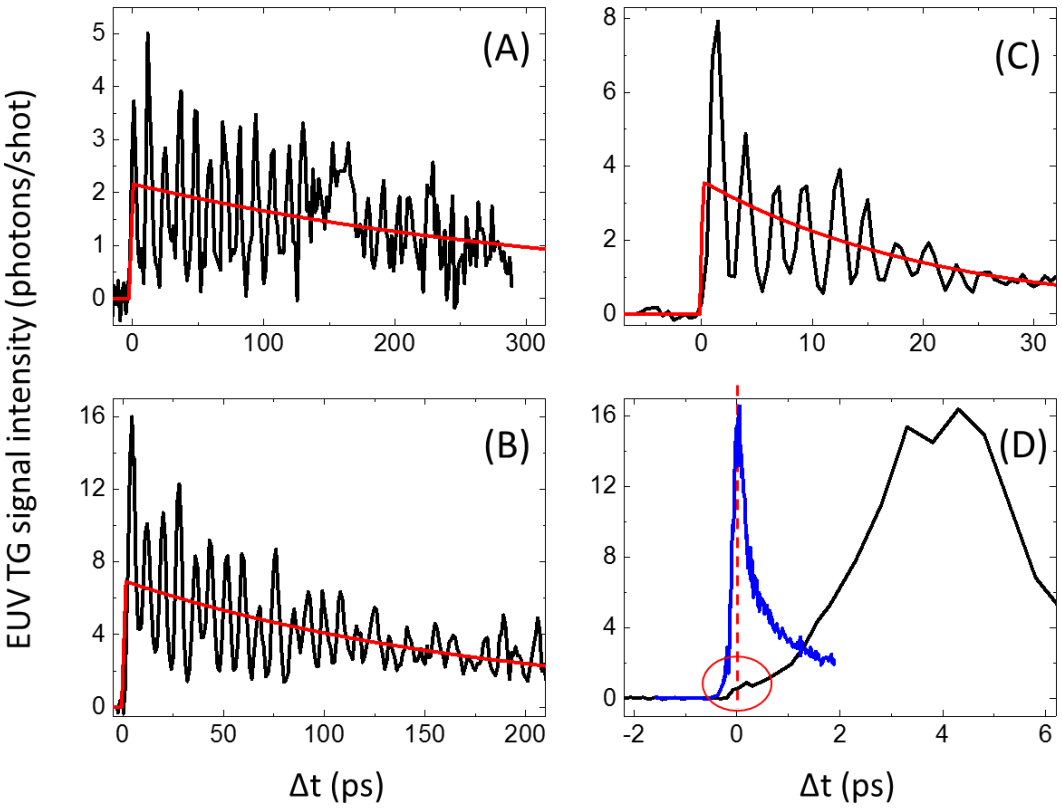

Figure 5.20: EUV TG signal on a Si_3N_4 membrane. TG periods are 110nm, 85nm, and 28nm in panels (A), (B), and (C), respectively. Panel (D) compares the short timescale signal from the 85nm TG to optically-probed 280nm EUV TG on a thicker Si_3N_4 membrane. The optically-probed signal (in blue) has been scaled down to match the EUV signal. The small bump circled in red is the electronic response measured by the EUV probe. Red lines are exponential fits thermal signals. Figure from [24].

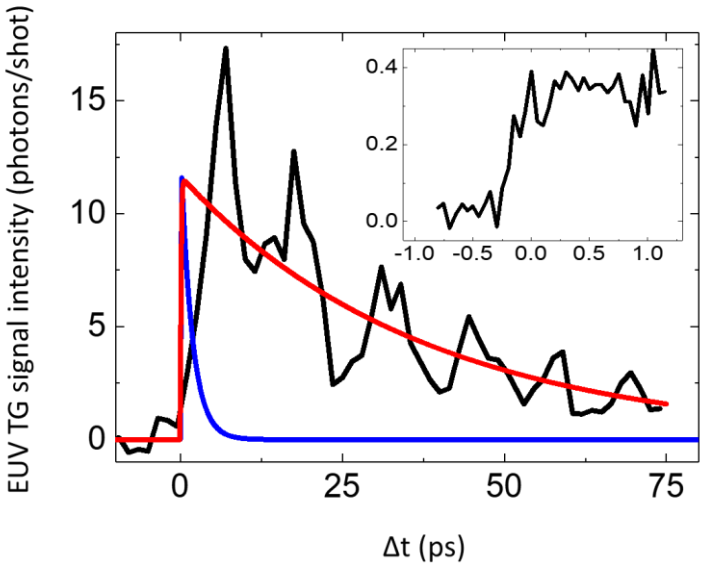

Figure 5.21: EUV TG signal on a Si membrane. Data (black) follow a much slower thermal decay (fit in red) than the diffusive prediction (blue) at 110nm TG period. Inset: there is no dominant electronic signal at early times. Figure from [24].

5.4.3 EUV TG on a Tabletop

Shortly before getting the opportunity to collaborate with the FERMI team, we began designing an EUV TG experiment using HHG beams at JILA. We considered many approaches to producing an EUV transient grating using the unique properties of HHG. The ideas ranged from recombining the distinct beams from non-collinear HHG in a gas jet [161], to doing all of the beam steering in the visible, and finally generating EUV with a separate waveguide for each TG arm. However, the final design we chose, to optimize both stability and flux, is to split the EUV beam with a half mirror, similar to the design used by mini-TIMER. This design can be rather compact and monolithic, and it limits the number of optical elements, which are always lossy in the EUV wavelength range. This approach also allows for spatial and temporal overlap to be found by adjusting the final flat mirrors in situ. Fig. 5.22 shows a schematic of our experimental design. While our design shares many similarities with the FEL experiments, it is worth noting one difference that takes advantage of our HHG sources. We push the delay line on the probe from the EUV to the optical portion of the beam path. This allows us to reduce the losses encountered at FERMI in the EUV delay line.

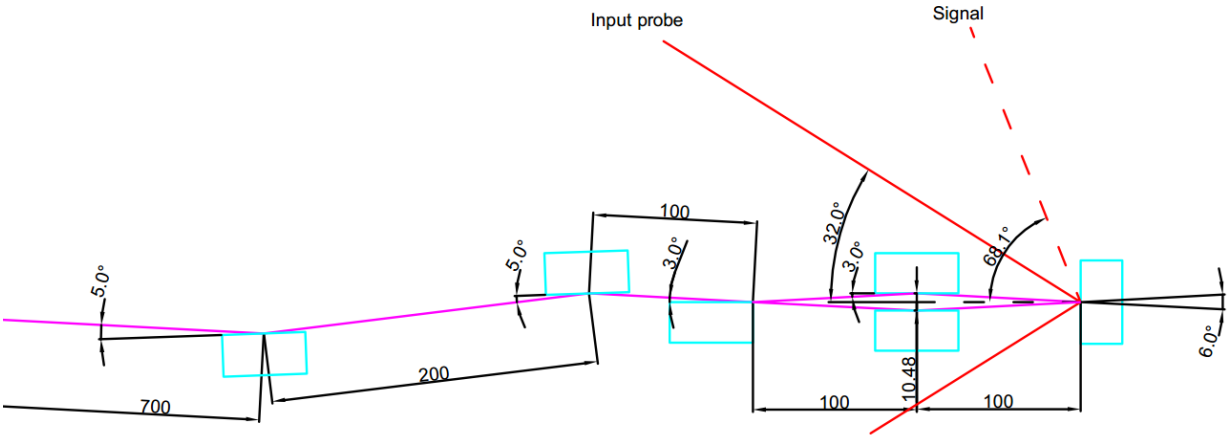

Figure 5.22: Design for initial demonstration of EUV TG at JILA. We will follow a focus-then-split design to generate EUV TG. The blue rectangles represent a silicon rejector mirror, a 3:1 toroidal mirror, the half mirror, the two recombining mirrors, and finally the sample. The 3:1 toroid should compensate for the slope error that expands the focal spot by ~3x for standard toroidal mirrors. Using a 150μm fiber, this should result in a 30μm diameter pump spot on the sample. The probe will first be 780nm wavelength for optical probing, and it will then be up-converted to 30nm by HHG for all-EUV TG. Note the probe here is not at the Bragg condition, so the reflected signal beam is not colinear with the input probe. The Bragg condition here is 46.8°. Probing at the Bragg angle would require only one access port to both input the probe and output the signal beam. Distances are listed in mm. The full 700mm to the fiber is not shown.

To develop EUV TG capabilities, we will first use shallow crossing angles and a visible probe. This allows us to simplify the problem and troubleshoot the TG setup without the added complexity of an HHG probe. Conveniently, once the system is working with an optical probe, we can add a fiber to the existing probe line, turn up the power, and generate an HHG probe with relatively small changes to the setup. One difference between the two probes, however, is that the Bragg angle would be very different between 780nm and 30nm wavelengths, given the same grating being probed.

The Bragg condition is a phase matching angle where the strongest diffracted signal will be obtained. This phase matching can be understood by matching the wavevectors of the probe and signal beams to the wavevector of the TG, as shown in Fig. 5.23(b). Note, however, that this condition is only required when the grating is optically thick. For a thin grating, the Bragg requirement is relaxed, and several diffracted orders may be observed at any incident angle [29], as shown in Fig. 5.23(a). Due to the high absorption of EUV photons in materials, EUV TG should always be relatively thin, allowing for non-Bragg probing. There is still a reduction in the diffracted beam intensity when not meeting the Bragg condition, however, given by the factor

$$\alpha = \mathrm{sinc}^2\left(\Delta k \frac{L}{2}\right), \tag{32}$$

where L is the grating thickness, determined by either the EUV penetration depth, or the sample thickness, whichever is smaller. Δk is the longitudinal wavevector mismatch between the probe and signal beams, given by

$$\Delta k = k_{probe}\left(\cos\theta_{signal} - \cos\theta_{probe}\right), \tag{33}$$

where k_{probe} is the magnitude of the probe wavevector, θ_{probe} is the incident angle of the probe (measured from the sample normal), and the output angle of the diffracted signal is defined by

$$\theta_{signal} = \arcsin\left(\frac{\lambda_{probe}}{\Lambda} - \sin\theta_{probe}\right), \tag{34}$$

where λ_{probe} is the wavelength of the probe beam, and Λ is the TG grating period [24, 159]. Though non-Bragg probing is possible for a thin grating, the losses can still be substantial, as shown in Table 5.4. This is a significant concern for EUV TG using HHG, where photon flux is the main constraint.

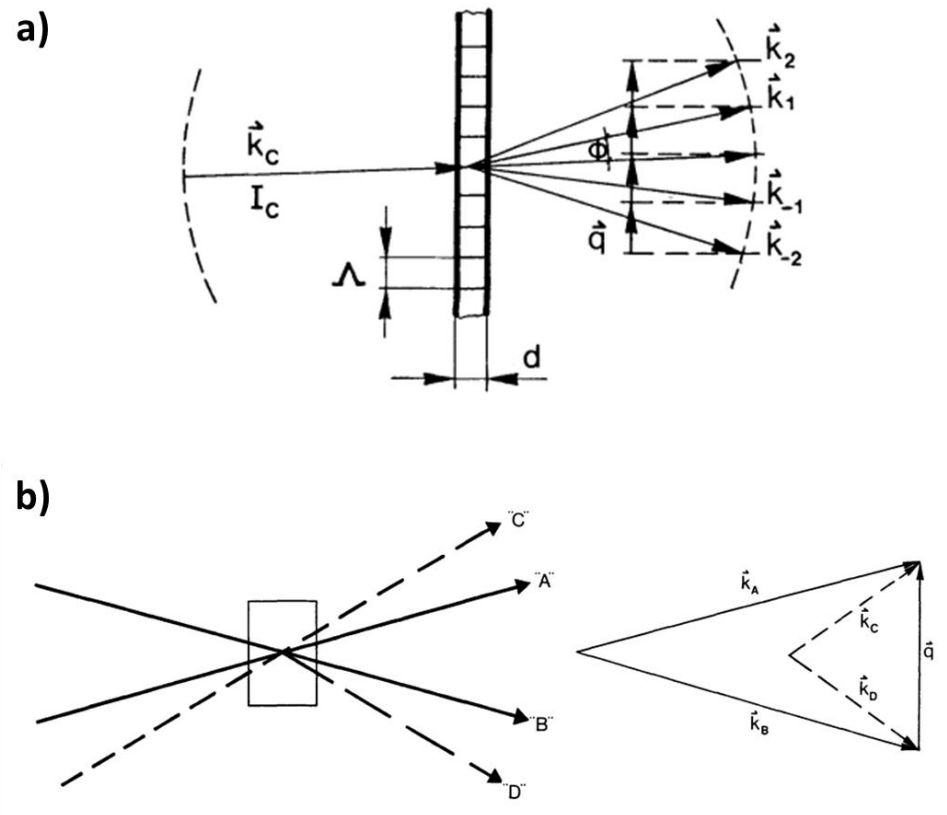

Figure 5.23: Thin and thick grating diffraction conditions. a) For thin gratings, the probe may be set to any angle, and several diffracted orders will be produced. b) For thick gratings, the incident probe beam, "C", must meet the Bragg condition to phase match the diffracted beam, "D", and emit it from the sample with appreciable intensity. Right: the phase matching condition is met by matching the probe and diffracted beams' wavevectors to the TG wavevector, $\vec{q}$, which is itself determined by the two pump wavevectors "A" and "B". Figures from [29].

Grating thickness	$\boldsymbol{\theta_{probe} = \theta_{pump}}$	$\boldsymbol{\theta_{probe} = \theta_{pump} + 1°}$	$\boldsymbol{\theta_{probe} = \theta_{pump} - 1°}$
L=10nm	99%	99%	99%
L=20nm	97%	97%	96%
L=50nm	83%	85%	81%
L=100nm	46%	52%	41%

Table 5.4 Example signal strength reductions for non-Bragg probing. In this example, I assume a 30nm EUV beam is probing a 56nm period TG pattern, generated by crossing two 56nm beams at 60° full crossing angle. The probe is incident very close to the incident pump angle, which would be the case for steering the probe to the same recombining mirrors as the pump (to avoid geometric constraints). Though most of the signal is preserved for a 10nm thick grating, the diffracted intensity is reduced by half for a 100nm thick grating. Reductions in signal strength for other configurations may be calculated by Eqns. 32-34.

The main challenge to implementing EUV TG on a tabletop is generating enough flux to excite the sample. Whereas the FEL has more than enough flux to burn the sample with EUV [162], HHG in general produces much lower flux. Thus, it is essential to test the maximum HHG flux achievable, in a configuration suitable for TG excitation, before construction of the experiment can begin.

To obtain a high-flux, single-frequency source for EUV TG, we test "blue-driven" harmonics. As described in [163], high harmonics driven by the second harmonic of the Ti:sapphire laser (390nm wavelength, blue-UV regime) are more widely separated in frequency space because each photon being added is of a higher energy. This makes the harmonic comb easier to separate into single frequencies suitable for the generation of a pure TG pattern. When driving high harmonics in krypton, the cutoff energy for the high harmonic process lands at about the 9^{th} harmonic, and the absorption of a thin aluminum filter lands at about the 5^{th} harmonic. This leaves nearly single-frequency HHG at the 7^{th} harmonic, 56nm wavelength, without the need for additional filtering by multilayer mirrors, which can be lossy. Moreover, HHG driven by UV pulses can have enhanced brightness and efficiency from enhanced single-atom yield, and phase matching of multiply ionized atoms [164]. However, second harmonic generation, for instance in a thin BBO crystal, is at best only 40% efficient. This more than doubles the energy required from the Ti:sapphire amplifier, even before high harmonics are generated. The 2mJ laser system described in Chapter 2 is insufficient for this high-flux, single harmonic HHG approach, especially once a second HHG beam is required to be generated for the probe. Instead, we collaborate with another project team within our group that has a higher-powered driving laser and do flux tests with them. Their laser system produces 8-10mJ of Ti:sapphire light at a 1kHz repetition rate. Using a 400nm wavelength driving beam, a 150μm inner diameter fiber, a silicon rejector mirror (to help filter the driving laser), an aluminum filter, and a toroidal mirror, we measure a per-pulse fluence of 13.7μJ/cm^2, with a 72μm diameter spot at the focus. This is very promising, as the mini-TIMER experiment only needed 2μJ/cm^2 (with a 100μm diameter spot) to make thermal and acoustic EUV TG measurements [23]. This lower-energy regime of HHG is known to have higher flux, comparable to synchrotron radiation [165], which is another reason we will start at 56nm wavelength rather than 30nm wavelength. Note, however, that the 13.7μJ/cm^2 quoted above is measured

for HHG in argon, which could have different spectral content. We must measure the spectrum of this HHG beam to ensure it is still single-frequency for EUV TG.

Single frequency beams are required to generate a purely sinusoidal TG pattern. Even relatively small intensities of other wavelengths from neighboring harmonics will create beat frequencies that modulate the TG pattern. See Fig. 5.24 for an example. Because our measurement is primarily sensitive to the phase grating defined by thermal expansion, the multiple sine waves of the multiple interfering harmonics will be added in phase to define the diffraction grating. Adding in phase is equivalent to multiplying complex exponentials together. According to the rules of Fourier transforms, these terms are then convolved to define the peaks in diffraction space. Thus, the presence of low-intensity additional wavelengths in the pump arms will produce "side bands" around both the DC beam and the diffracted orders of a pure, single-frequency TG diffraction pattern. This is shown in Fig. 5.24. This would complicate the analysis of the measured data, though perhaps with appropriate modelling it would allow us to measure dynamics at multiple spatial frequencies simultaneously by selecting different diffracted orders.

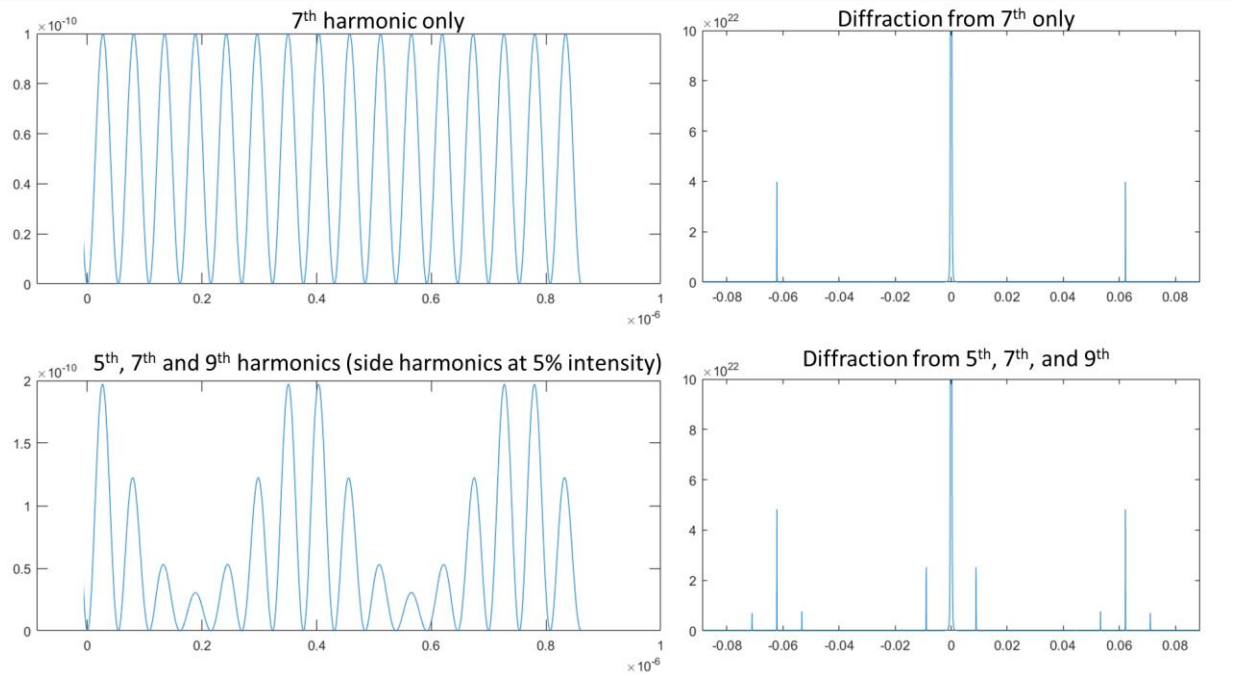

Figure 5.24: Calculated TG patterns and diffraction for single- and multi-frequency beams. The imperfect filtering of the HHG comb to a single wavelength leads to beat frequencies in the TG pattern generated. This effect is significant even for relatively low (5%) intensities of undesired harmonics. When diffracting from the phase grating produced by thermal expansion, side-bands are observed from the convolution of each sine wave from each interfering harmonic.

Now that we have a promising flux measurement, and a plan for single-frequency excitation, we are simply waiting for components to arrive to start building the EUV TG setup. In the meantime, however, we have been designing an optimization procedure for the experiment. First, to optimize the mode and flux of the HHG beam, it must be directed to a CCD camera. For the optically-probed initial demonstration, there is no need for an EUV-sensitive CCD camera to measure the diffracted signal, so we may place our camera directly behind the sample. Then, we simply move the splitting mirror and sample out of the way, so the full beam is visible on the CCD. We may then insert the splitting mirror until half of the beam is clipped, and the other TG arm may also be directed to the CCD. As long as the crossing angle is sufficiently shallow, and the CCD sufficiently close to the sample, both beams should be simultaneously observable. Even with only the first TG arm visible on the camera, we will still be able to observe the point when half of the beam has been clipped by the splitting mirror. For the all-EUV TG experiment, the probe and pump HHG beams may be directed by sample rotation to a flange-mounted CCD camera placed in a reflection measurement geometry. This would require either a highly reflective sample, or a suitably reflective surface to be mounted on the sample holder, near the sample of interest.

To achieve spatial and temporal overlap, we have a number of tools at our disposal. Phosphorous and cerium YAG scintillators both fluoresce upon EUV irradiation, allowing the use of simple visible cameras to spatially overlap the beams using the final flat mirrors. Phosphorous is particularly useful as it may be painted on the corner of a sample to ensure the overlap plane matches the sample plane precisely. At high crossing angles, even micron scale differences between planes can rapidly take the sample out of the interference region of the beams. We will also have adjustability of the sample in the z-direction (along the bisector of the TG arms) to ensure the interference and sample planes match. To overlap the two TG arms and the probe temporally, we can get close by the careful measurement of optical path lengths, and/or the use of a fast oscilloscope. EUV radiation can generate electrons in the exposed core of an SMA cable, which produces a measurable signal on an oscilloscope. The two TG arms may then be coarsely synchronized by moving one of the mirrors to change the separation between the mirrors, and adjusting the mirror angles as needed. This is similar to what is described in [160, 162]. Once the TG arms are roughly

overlapped in time, they will be more precisely overlapped by using EUV-induced change in optical reflectivity. When pumped by EUV radiation, the intensity of reflected or scattered optical light is transiently changed [162]. Using this effect, each TG arm may be separately synchronized to the optical probe, which in turn synchronizes the two TG arms to one another as well. During our experiment using TIMER at FERMI, we found that CoFeB has a particularly strong optical reflectivity signal. We have three samples of CoFeB films at JILA now, to aid in finding temporal overlap using this method. As described in Chapter 2, the HHG pulses consist of attosecond bursts under a 10fs envelope. Trying to align these bursts would greatly increase the difficulty in finding temporal overlap between the two pump arms, and it would make them more susceptible to jitter than if only the 10fs envelopes needed to be synchronized. As no one has produced EUV TG using HHG, it is not known how much of a concern this would be. According to [164], UV driven harmonics have shorter attosecond bursts due to reduced intrinsic chirp, indicating the individual bursts may have to be synchronized. However, even occasional overlap due to jitter would still produce signal, just requiring more pulses to be averaged over in the measurement.

The initial demonstration of EUV TG at JILA using a visible probe will be designed for a single crossing angle. We can vary the angle somewhat in situ by increasing the recombining mirror separation and translating the sample, but large changes would require a large displacement of the mirrors, and likely a repositioning of the camera. However, it is still possible, even at a fixed angle, to produce different TG periods by changing from 56nm wavelength harmonics to 30nm, and finally to 13nm. The flux constraints become more dire at shorter wavelengths, as the HHG efficiency is reduced and additional filtering would be needed to select a single frequency, so we will likely try all-EUV TG before changing HHG wavelengths.

For all-EUV TG, we will add additional mirrors on translation stages to allow for in situ tuning of the TG period, and to reach very large crossing angles, as shown in Fig. 5.25. By translating the final two additional recombining mirrors along the arcs of two ellipses whose foci are at the first pair of recombining mirrors and the sample, respectively, the total path length of each arm will be preserved, maintaining temporal overlap, while still tuning the TG crossing angle. This can be achieved by placing the two final mirrors on programmable x-y stages. Though this design adds optical elements, generally sources of loss

in the EUV, it also makes each reflection more glancing, which increases reflectivity. These two effects cancel each other out at 56nm and 30nm wavelengths, producing a similar final flux at the sample. At 13nm, the four-mirror design actually transmits a greater flux as the reflectivity is more angle-dependent. Note that this design has a very short working distance, making it difficult to probe the TG pattern. This constraint can be overcome by probing slightly out of plane, or by reflecting the probe off of the same recombining mirrors to impinge on the sample at a similar angle to one of the pump arms. For a 30nm probe wavelength, the resulting diffracted beam is emitted nearly normal to the sample surface, which may then be collected by an in-vacuum photodiode. This arrangement does, however, depart from the Bragg condition, with resulting signal strength losses shown in Table 5.4. In the end, however, these are engineering constraints that can be addressed with more insight once we have done the initial demonstration of EUV TG with an optical probe. The flux numbers are promising that we can match mini-TIMER, where EUV TG has already been demonstrated, and the outlook is good for demonstrating tabletop EUV TG metrology using HHG.

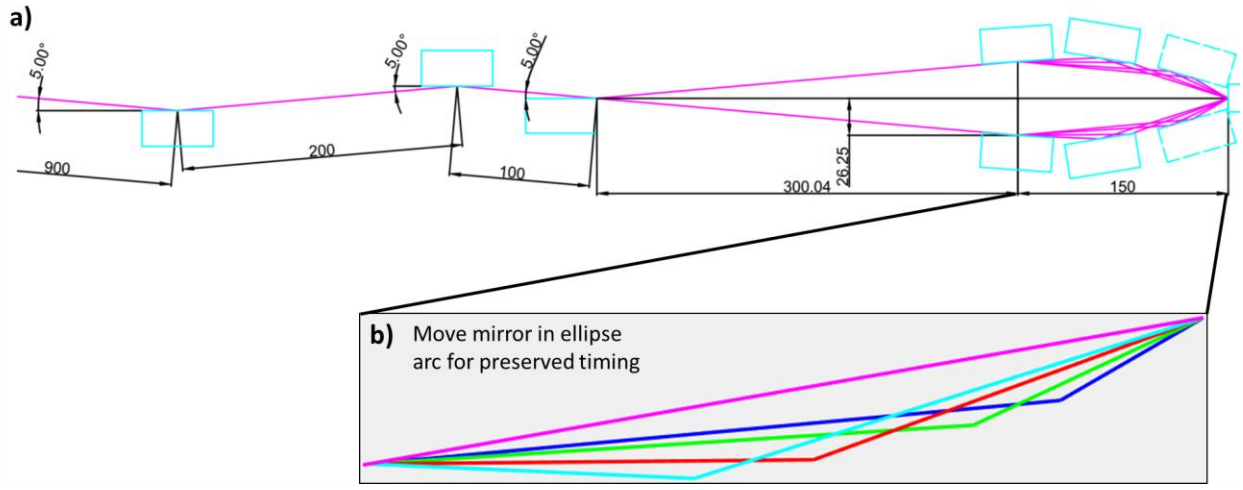

Figure 5.25: Schematic of four-mirror design for all-EUV TG at JILA. a) The design is similar to that shown in Fig. 5.22, but with the addition of two more recombining mirrors. Also shown are two dotted mirrors that represent an alternative position for these new mirrors as they are moveable to change the TG crossing angle. Note the path lengths have also been scaled up compared to Fig. 5.22 to counteract the reduction in working distance caused by the additional mirrors. b) By using x-y translation and rotation stages, the final two mirrors may be moved along the arcs of two ellipses whose foci are at the first recombining mirrors and the sample. This preserves the path length, and thus the temporal overlap.

5.5 Conclusions and Future Work

In this chapter, I have presented works that extend our established EUV metrology technique to more complex samples. First, I presented thermal and acoustic characterizations of silicon metalattices, a 3D hierarchical material promising for thermoelectrics. I then presented the reinstitution of optical TG pumping capabilities in our lab for the characterization of novel samples that preclude transducer fabrication. I used this capability to measure ultra-low thermal conductivity in nanoparticle molecular arrays and gold nanomeshes. Finally, I presented work using EUV transient gratings to directly excite dynamics in the deep nanoscale without the need for separate nanostructure fabrication. The first results were obtained in collaboration with the FERMI free electron laser in Italy, and work is underway to demonstrate EUV TG on a tabletop at JILA.

The future work will primarily consist of the full development of a robust EUV TG metrology technique using HHG beams. This will allow for nanoscale characterization of a general set of novel samples, such as metamaterials, magnetic systems, and even liquids. The TG geometry moreover enables the extension of powerful visible techniques into the EUV regime, such as super-resolution imaging and four wave mixing. Now that the EUV TG approach has been proven at the FERMI FEL, and we have achieved comparable fluxes using HHG, all that remains is to build the experiment on a tabletop.

Chapter 6

Conclusions and Future Work

In this thesis, I have used coherent, ultrafast EUV beams to measure how nanoscale thermal and elastic properties deviate from bulk predictions. As our technique is one of the few that accesses the deep nanoscale at its intrinsic timescales, the results we have obtained are critically important to inform both functional nanosystems design, and theoretical and computational approaches to nanosystem modeling. To measure a more general set of samples and move towards in-situ metrology, I have additionally extended our EUV measurements to a fully non-contact modality using transient gratings (TG). The main conclusions of this thesis are as follows:

- Heat no longer travels diffusively when the relevant length scales of heat transfer are comparable to the mean free paths (MFP) of the heat carriers. Instead, some of the heat carriers travel ballistically across the relevant length scales and deposit their heat non-locally, producing a thermal conductivity much lower than what Fourier's law of heat conduction would predict. For silicon and other semiconductors, the MFP's of heat-carrying phonons reach from nanometers to several microns—sizes extremely relevant to nanoelectronics, where heat management is of major concern. We have found that bringing such quasiballistic heat sources closer together, so that their spacing is also comparable to the phonon MFP's, counteracts the quasiballistic effect and produces faster thermal transport, closer to the diffusive prediction. By separately tuning the size and spacing of laser-heated nanostructures on a silicon substrate, I have mapped the transitions between the diffusive, the quasiballistic, and the collectively

diffusive regimes of thermal transport. I have also performed a control study on fused silica glass, where no non-diffusive behavior is expected or observed.

- Acoustic waves are an excellent tool to characterize the elastic properties of materials. Our EUV probe allows us to measure surface acoustic waves far below the diffraction limit of visible light. By confining acoustic waves to nanoscale dimensions using nanoline transducers, I have successfully characterized the full elastic tensor of ultrathin films, down to 11nm thickness. In my first study, we found that hydrogenation, which lowers a film's dielectric constant for nanoelectronics applications, causes a divergence towards incompressible behavior, once the hydrogenation has broken a critical number of bonds. In my second study, we found that two different materials, with two different levels of hydrogenation, exhibited different thickness dependence of their elastic properties. For highly-hydrogenated SiOC:H, we observed no thickness dependence down to 11nm thickness, while for less-hydrogenated SiC:H we observed evidence of thickness-dependent softening at 5nm thickness. We hypothesize that the under-coordinated atoms at a film's free surface have less of a softening effect once hydrogenation has already terminated many network bonds in the bulk of the film.
- To go beyond bulk substrates and 1D-confined thin films, I have worked to extend our technique to general samples, including those with 3D complex structures. First, we used nanoline transducers to characterize the thermal and elastic properties of silicon metalattices, formed by infiltrating silicon into the interstitial regions between self-assembled silica nanospheres. We found that these metalattices had very low thermal conductivity, but predictable elastic properties according to continuum mechanics. Next, I used optical TG to characterize the effective thermal conductivity of 2D nanoparticle-molecular arrays, without disrupting the system with nanoline transducers. We found the thermal conductivity of these arrays was extremely low, which is potentially useful for thermoelectric applications. Finally, I collaborated with the FERMI free electron laser to directly excite nanoscale thermal and elastic dynamics using EUV transient gratings. We demonstrated this technique on a number

of transparent and opaque materials, and our work later contributed to the first demonstration of all-EUV TG measurements by the FERMI team. By both pumping and probing samples with EUV beams, this technique directly accesses deep nanoscale dynamics without the need for transducers, and with the promise of compatibility with any sample that has a flat surface.

The next step for our experiment is to build an EUV TG setup here at JILA, using HHG beams. So far, we have designed our approach, conducted flux tests, and gathered most of our equipment. It is very promising to have a first demonstration of tabletop EUV TG within a few months' time. This will greatly broaden the number of samples we can measure with our nanometrology technique and remove the complexity and time it takes to perform nanofabrication prior to our measurements. Additionally, the EUV TG geometry enables other techniques, such as super-resolution imaging using structured illumination microscopy, and nonlinear four wave mixing.

In addition to the new EUV TG setup, there is still much opportunity for study using our established nanograting-based technique. We already have samples of long MFP materials with nanostructure sizes that reach into the fully ballistic transport regime. At these scales, the ultrafast dynamics we measure can be dominated by highly non-equilibrium transport, which depends greatly on the specific excitation pathways accessed in the material. By using laser-heated nanostructures, our established grating-based technique uses a fundamentally different mechanism for depositing energy in the substrate, compared to direct excitation by EUV TG. Comparing the two excitation approaches on the same substrate, at the same grating periods, would be a new way to study ultrafast couplings and light-matter interactions in the EUV regime. HHG sources would be particularly well-suited for these studies, given their exquisite time resolution. Similarly, by changing between optical and EUV probing of our measurements, we can cleanly distinguish between ultrafast phonon and electron dynamics—non-resonant EUV probes are almost exclusively sensitive to the former, while optical probes are dominated by the latter at early times. A study such as this would enable the precise study of electron-phonon coupling in metal nitrides and other optically-excitable materials.

Both the nanograting and transient grating techniques are complementary to our dynamic imaging technique, which accesses local nanostructure information. The former techniques rapidly characterize the

overall material properties of a sample, while the latter technique informs what is happening near a single nanostructure. All of these approaches will be needed to characterize advanced, hierarchical nanosystems that have critical dynamics at sizes from the single nanometer, up to microns.

Given the ability of our nanograting-based technique to study technologically relevant materials, and the promising ability of TG to measure even more novel samples, coherent EUV nanometrology based on HHG sources is well-positioned to continue informing the next generation of materials development.

Bibliography

[1] L. R. Hirsch, R. J. Stafford, J. A. Bankson, S. R. Sershen, B. Rivera, R. E. Price, J. D. Hazle, N. J. Halas, and J. L. West, "Nanoshell-mediated near-infrared thermal therapy of tumors under magnetic resonance guidance," Proc. Natl. Acad. Sci. U. S. A. **100**(23), 13549–13554 (2003).

[2] K. Riehemann, S. W. Schneider, T. A. Luger, B. Godin, M. Ferrari, and H. Fuchs, "Nanomedicine—Challenge and Perspectives," Angew. Chem. Int. Ed. **48**(5), 872–897 (2009).

[3] G. Mie, "Contributions to the Optics of Turbid Media, Especially Colloidal Metal Solutions," Ann. Physik **25**(3), 377–445 (1908).

[4] S. Link and M. A. El-Sayed, "Size and Temperature Dependence of the Plasmon Absorption of Colloidal Gold Nanoparticles," J. Phys. Chem. B **103**(21), 4212–4217 (1999).

[5] I. Freestone, N. Meeks, M. Sax, and C. Higgitt, "The Lycurgus Cup — A Roman nanotechnology," Gold Bull. **40**(4), 270–277 (2007).

[6] M. M. Waldrop, "More than Moore," Nature **530**(7589), 144 (2016).

[7] G. Chen, "Nonlocal and Nonequilibrium Heat Conduction in the Vicinity of Nanoparticles," J. Heat Transfer **118**(3), 539–545 (1996).

[8] Y. K. Koh and D. G. Cahill, "Frequency dependence of the thermal conductivity of semiconductor alloys," Phys. Rev. B **76**(7), 075207 (2007).

[9] M. E. Siemens, Q. Li, R. Yang, K. A. Nelson, E. H. Anderson, M. M. Murnane, and H. C. Kapteyn, "Quasi-ballistic thermal transport from nanoscale interfaces observed using ultrafast coherent soft X-ray beams," Nat. Mater. **9**(1), 26–30 (2010).

[10] A. J. Minnich, J. A. Johnson, A. J. Schmidt, K. Esfarjani, M. S. Dresselhaus, K. A. Nelson, and G. Chen, "Thermal Conductivity Spectroscopy Technique to Measure Phonon Mean Free Paths," Phys. Rev. Lett. **107**(9), 095901 (2011).

[11] K. Esfarjani, G. Chen, and H. T. Stokes, "Heat transport in silicon from first-principles calculations," Phys. Rev. B **84**(8), 085204 (2011).

[12] D. Shamiryan, T. Abell, F. Iacopi, and K. Maex, "Low-k dielectric materials," Mater. Today **7**(1), 34–39 (2004).

[13] L. G. Zhou and H. Huang, "Are surfaces elastically softer or stiffer?," Appl. Phys. Lett. **84**(11), 1940–1942 (2004).

[14] N. Nakamura, H. Ogi, T. Yasui, M. Fujii, and M. Hirao, "Mechanism of Elastic Softening Behavior in a Superlattice," Phys. Rev. Lett. **99**(3), 035502 (2007).

[15] M. Sigalas and E. N. Economou, "Band structure of elastic waves in two dimensional systems," Solid State Commun. **86**(3), 141–143 (1993).

[16] M. S. Kushwaha, P. Halevi, L. Dobrzynski, and B. Djafari-Rouhani, "Acoustic band structure of periodic elastic composites," Phys. Rev. Lett. **71**(13), 2022–2025 (1993).

[17] R. Liontas and J. R. Greer, "3D nano-architected metallic glass: Size effect suppresses catastrophic failure," Acta Mater. **133**, 393–407 (2017).

[18] B. L. Davis and M. I. Hussein, "Nanophononic Metamaterial: Thermal Conductivity Reduction by Local Resonance," Phys. Rev. Lett. **112**(5), 055505 (2014).

[19] M. Martín-González, O. Caballero-Calero, and P. Díaz-Chao, "Nanoengineering thermoelectrics for 21st century: Energy harvesting and other trends in the field," Renew. Sust. Energ. Rev. **24**, 288–305 (2013).

[20] K. M. Hoogeboom-Pot, J. N. Hernandez-Charpak, X. Gu, T. D. Frazer, E. H. Anderson, W. Chao, R. W. Falcone, R. Yang, M. M. Murnane, H. C. Kapteyn, and D. Nardi, "A new regime of nanoscale thermal transport: Collective diffusion increases dissipation efficiency," Proc. Natl. Acad. Sci. U. S. A. **112**(16), 201503449 (2015).

[21] T. D. Frazer, J. L. Knobloch, K. M. Hoogeboom-Pot, D. Nardi, W. Chao, R. W. Falcone, M. M. Murnane, H. C. Kapteyn, and J. N. Hernandez-Charpak, "Engineering Nanoscale Thermal Transport: Size- and Spacing-Dependent Cooling of Nanostructures," Phys. Rev. Appl. **11**(2), 024042 (2019).

[22] J. N. Hernandez-Charpak, K. M. Hoogeboom-Pot, Q. Li, T. D. Frazer, J. L. Knobloch, M. Tripp, S. W. King, E. H. Anderson, W. Chao, M. M. Murnane, H. C. Kapteyn, and D. Nardi, "Full Characterization of the Mechanical Properties of 11–50 nm Ultrathin Films: Influence of Network Connectivity on the Poisson's Ratio," Nano Lett. **17**(4), 2178–2183 (2017).

[23] A. A. Maznev, F. Bencivenga, A. Cannizzo, F. Capotondi, R. Cucini, R. A. Duncan, T. Feurer, T. D. Frazer, L. Foglia, H.-M. Frey, H. Kapteyn, J. Knobloch, G. Knopp, C. Masciovecchio, R. Mincigrucci, G. Monaco, M. Murnane, I. Nikolov, E. Pedersoli, A. Simoncig, A. Vega-Flick, and K. A. Nelson, "Generation of coherent phonons by coherent extreme ultraviolet radiation in a transient grating experiment," Appl. Phys. Lett. **113**(22), 221905 (2018).

[24] F. Bencivenga, R. Mincigrucci, F. Capotondi, L. Foglia, D. Naumenko, A. A. Maznev, E. Pedersoli, A. Simoncig, F. Caporaletti, V. Chiloyan, R. Cucini, F. Dallari, R. A. Duncan, T. D. Frazer, G. Gaio, A. Gessini, L. Giannessi, S. Huberman, H. Kapteyn, J. Knobloch, G. Kurdi, N. Mahne, M. Manfredda, A. Martinelli, M. Murnane, E. Principi, L. Raimondi, S. Spampinati, C. Spezzani, M. Trovò, M. Zangrando, G. Chen, G. Monaco, K. A. Nelson, and C. Masciovecchio, "Nanoscale transient gratings excited and probed by extreme ultraviolet femtosecond pulses," Sci. Adv. (Submitted).

[25] R. I. Tobey, E. H. Gershgoren, M. E. Siemens, M. M. Murnane, H. C. Kapteyn, T. Feurer, and K. A. Nelson, "Nanoscale photothermal and photoacoustic transients probed with extreme ultraviolet radiation," Appl. Phys. Lett. **85**(4), 564–566 (2004).

[26] D. H. Peregrine, G. Shoker, and A. Symon, "The bifurcation of liquid bridges," J. Fluid Mech. **212**, 25–39 (1990).

[27] J. A. Rogers, A. A. Maznev, M. J. Banet, and K. A. Nelson, "Optical Generation and Characterization of Acoustic Waves in Thin Films: Fundamentals and Applications," Annu. Rev. Mater. Sci. **30**(1), 117–157 (2000).

[28] G. Cachier, "Optical excitation of high-amplitude surface waves," Appl. Phys. Lett. **17**(10), 419–421 (1970).

[29] H. J. Eichler, P. Günter, and D. W. Pohl, *Laser-Induced Dynamic Gratings.* New York, NY: Springer-Verlag Berlin Heidelberg (1986).

[30] C. Thomsen, H. T. Grahn, H. J. Maris, and J. Tauc, "Surface generation and detection of phonons by picosecond light pulses," Phys. Rev. B **34**(6), 4129–4138 (1986).

[31] A. Neubrand and P. Hess, "Laser generation and detection of surface acoustic waves: Elastic properties of surface layers," J. Appl. Phys. **71**(1), 227–238 (1992).

[32] K. M. Hoogeboom-Pot, E. Turgut, J. N. Hernandez-Charpak, J. M. Shaw, H. C. Kapteyn, M. M. Murnane, and D. Nardi, "Nondestructive Measurement of the Evolution of Layer-Specific Mechanical Properties in Sub-10 nm Bilayer Films," Nano Lett. **16**(8), 4773–4778 (2016).

[33] J. L. Krause, K. J. Schafer, and K. C. Kulander, "High-order harmonic generation from atoms and ions in the high intensity regime," Phys. Rev. Lett. **68**(24), 3535–3538 (1992).

[34] T. Popmintchev, M.-C. Chen, P. Arpin, M. M. Murnane, and H. C. Kapteyn, "The attosecond nonlinear optics of bright coherent X-ray generation," Nat. Photonics **4**(12), 822–832 (2010).

[35] M. Lewenstein, Ph. Balcou, M. Yu. Ivanov, A. L'Huillier, and P. B. Corkum, "Theory of high-harmonic generation by low-frequency laser fields," Phys. Rev. A **49**(3), 2117–2132 (1994).

[36] A. Rundquist, C. G. Durfee, Z. Chang, C. Herne, S. Backus, M. M. Murnane, and H. C. Kapteyn, "Phase-Matched Generation of Coherent Soft X-rays," Science **280**(5368), 1412–1415 (1998).

[37] K. J. Schafer, B. Yang, L. F. DiMauro, and K. C. Kulander, "Above threshold ionization beyond the high harmonic cutoff," Phys. Rev. Lett. **70**(11), 1599–1602 (1993).

[38] P. B. Corkum, "Plasma perspective on strong field multiphoton ionization," Phys. Rev. Lett. **71**(13), 1994–1997 (1993).

[39] M.-C. Chen, C. Mancuso, C. Hernández-García, F. Dollar, B. Galloway, D. Popmintchev, P.-C. Huang, B. Walker, L. Plaja, A. A. Jaroń-Becker, A. Becker, M. M. Murnane, H. C. Kapteyn, and T. Popmintchev, "Generation of bright isolated attosecond soft X-ray pulses driven by multicycle midinfrared lasers," Proc. Natl. Acad. Sci. U. S. A. **111**(23), E2361–E2367 (2014).

[40] J. Chen, E. Louis, C. J. Lee, H. Wormeester, R. Kunze, H. Schmidt, D. Schneider, R. Moors, W. van Schaik, M. Lubomska, and F. Bijkerk, "Detection and characterization of carbon contamination on EUV multilayer mirrors," Opt. Express **17**(19), 16969–16979 (2009).

[41] R. I. Tobey, M. E. Siemens, O. Cohen, M. M. Murnane, H. C. Kapteyn, and K. A. Nelson, "Ultrafast extreme ultraviolet holography: dynamic monitoring of surface deformation," Opt. Lett. **32**(3), 286–288 (2007).

[42] Q. Li, K. Hoogeboom-Pot, D. Nardi, M. M. Murnane, H. C. Kapteyn, M. E. Siemens, E. H. Anderson, O. Hellwig, E. Dobisz, B. Gurney, R. Yang, and K. A. Nelson, "Generation and control of ultrashort-

wavelength two-dimensional surface acoustic waves at nanoscale interfaces," Phys. Rev. B **85**(19), 195431 (2012).

[43] A. R. Duggal and K. A. Nelson, "Picosecond–microsecond structural relaxation dynamics in polypropylene glycol: Impulsive stimulated light-scattering experiments," J. Chem. Phys. **94**(12), 7677–7688 (1991).

[44] A. A. Maznev, T. F. Crimmins, and K. A. Nelson, "How to make femtosecond pulses overlap," Opt. Lett. **23**(17), 1378–1380 (1998).

[45] R. I. Tobey, M. E. Siemens, M. M. Murnane, H. C. Kapteyn, D. H. Torchinsky, and K. A. Nelson, "Transient grating measurement of surface acoustic waves in thin metal films with extreme ultraviolet radiation," Appl. Phys. Lett. **89**(9), 091108 (2006).

[46] Z. Qin and J. C. Bischof, "Thermophysical and biological responses of gold nanoparticle laser heating," Chem. Soc. Rev. **41**(3), 1191–1217 (2012).

[47] Y. Lan, A. J. Minnich, G. Chen, and Z. Ren, "Enhancement of Thermoelectric Figure-of-Merit by a Bulk Nanostructuring Approach," Adv. Funct. Mater. **20**(3), 357–376 (2010).

[48] P. Pichanusakorn and P. Bandaru, "Nanostructured thermoelectrics," Mater. Sci. Eng. R Rep. **67**(2), 19–63 (2010).

[49] M. Maldovan, "Sound and heat revolutions in phononics," Nature **503**(7475), 209–217 (2013).

[50] H. Honarvar, L. Yang, and M. I. Hussein, "Thermal transport size effects in silicon membranes featuring nanopillars as local resonators," Appl. Phys. Lett. **108**(26), 263101 (2016).

[51] J. A. Johnson, A. A. Maznev, J. Cuffe, J. K. Eliason, A. J. Minnich, T. Kehoe, C. M. S. Torres, G. Chen, and K. A. Nelson, "Direct Measurement of Room-Temperature Nondiffusive Thermal Transport Over Micron Distances in a Silicon Membrane," Phys. Rev. Lett. **110**(2), 025901 (2013).

[52] J. Cuffe, J. K. Eliason, A. A. Maznev, K. C. Collins, J. A. Johnson, A. Shchepetov, M. Prunnila, J. Ahopelto, C. M. Sotomayor Torres, G. Chen, and K. A. Nelson, "Reconstructing phonon mean-free-path contributions to thermal conductivity using nanoscale membranes," Phys. Rev. B **91**(24), 245423 (2015).

[53] K. T. Regner, D. P. Sellan, Z. Su, C. H. Amon, A. J. H. McGaughey, and J. A. Malen, "Broadband phonon mean free path contributions to thermal conductivity measured using frequency domain thermoreflectance," Nat. Commun. **4**, 1640 (2013).

[54] T. Oyake, M. Sakata, and J. Shiomi, "Nanoscale thermal conductivity spectroscopy by using gold nano-islands heat absorbers," Appl. Phys. Lett. **106**(7), 073102 (2015).

[55] Y. Hu, L. Zeng, A. J. Minnich, M. S. Dresselhaus, and G. Chen, "Spectral mapping of thermal conductivity through nanoscale ballistic transport," Nat. Nanotechnol. **10**(8), 701–706 (2015).

[56] L. Zeng, K. C. Collins, Y. Hu, M. N. Luckyanova, A. A. Maznev, S. Huberman, V. Chiloyan, J. Zhou, X. Huang, K. A. Nelson, and G. Chen, "Measuring Phonon Mean Free Path Distributions by Probing Quasiballistic Phonon Transport in Grating Nanostructures," Sci. Rep. **5**, 17131 (2015).

[57] F. Yang and C. Dames, "Mean free path spectra as a tool to understand thermal conductivity in bulk and nanostructures," Phys. Rev. B **87**(3), 035437 (2013).

[58] I. Horcas, R. Fernández, J. M. Gómez-Rodríguez, J. Colchero, J. Gómez-Herrero, and A. M. Baro, "WSXM: A software for scanning probe microscopy and a tool for nanotechnology," Rev. Sci. Instrum. **78**(1), 013705 (2007).

[59] F. Banfi, F. Pressacco, B. Revaz, C. Giannetti, D. Nardi, G. Ferrini, and F. Parmigiani, "Ab initio thermodynamics calculation of all-optical time-resolved calorimetry of nanosize systems: Evidence of nanosecond decoupling of electron and phonon temperatures," Phys. Rev. B **81**(15), 155426 (2010).

[60] COMSOL, Inc. (2013) COMSOL Multiphysics, Version 4.3b (COMSOL, Inc., Burlington, MA).

[61] P. D. Desai, "Thermodynamic Properties of Iron and Silicon", J. Phys. Chem. Ref. Data **15**(3), 967–983 (1986).

[62] J. A. Dean and N. A. Lange, *Lange's Handbook of Chemistry*, 15. ed, New York, NY: McGraw-Hill (1999).

[63] Y. S. Touloukian, *Thermophysical Properties of Matter: Vol 2. Thermal Conductivity – Nonmetallic Solids.* New York, NY: Plenum Publishing Corporation (1970).

[64] D. Nardi, M. Travagliati, M. E. Siemens, Q. Li, M. M. Murnane, H. C. Kapteyn, G. Ferrini, F. Parmigiani, and F. Banfi, "Probing Thermomechanics at the Nanoscale: Impulsively Excited Pseudosurface Acoustic Waves in Hypersonic Phononic Crystals," Nano Lett. **11**(10), 4126–4133 (2011).

[65] M. J. Weber, *Handbook of Optical Materials: Vol 3. Optical Materials, Part 1*. Boca Raton, FL: CRC Press, LLC (2003).

[66] J. Zacharias, "The Temperature Dependence of Young's Modulus for Nickel," Phys. Rev. **44**(2), 116–122 (1933).

[67] J. J. Wortman and R. A. Evans, "Young's Modulus, Shear Modulus, and Poisson's Ratio in Silicon and Germanium," J. Appl. Phys. **36**(1), 153–156 (1965).

[68] T. G. Kollie, "Measurement of the thermal-expansion coefficient of nickel from 300 to 1000 K and determination of the power-law constants near the Curie temperature," Phys. Rev. B **16**(11), 4872–4881 (1977).

[69] Y. Okada and Y. Tokumaru, "Precise determination of lattice parameter and thermal expansion coefficient of silicon between 300 and 1500 K," J. Appl. Phys. **56**(2), 314–320 (1984).

[70] Y. S. Touloukian, *Thermophysical Properties of High Temperature Solid Materials: Vol. 4. Oxides and their solutions and mixtures.* New York, NY: The Macmillan Company (1967).

[71] A. A. Maznev, J. A. Johnson, and K. A. Nelson, "Onset of nondiffusive phonon transport in transient thermal grating decay," Phys. Rev. B **84**(19), 195206 (2011).

[72] R. Cheaito, J. T. Gaskins, M. E. Caplan, B. F. Donovan, B. M. Foley, A. Giri, J. C. Duda, C. J. Szwejkowski, C. Constantin, H. J. Brown-Shaklee, J. F. Ihlefeld, and P. E. Hopkins, "Thermal boundary conductance accumulation and interfacial phonon transmission: Measurements and theory," Phys. Rev. B **91**(3), 035432 (2015).

[73] P. B. Allen and J. L. Feldman, "Thermal conductivity of disordered harmonic solids," Phys. Rev. B **48**(17), 12581–12588 (1993).

[74] C. Hua and A. J. Minnich, "Heat dissipation in the quasiballistic regime studied using the Boltzmann equation in the spatial frequency domain," Phys. Rev. B **97**(1), 014307 (2018).

[75] P. Torres, A. Torelló, J. Bafaluy, J. Camacho, X. Cartoixà, and F. X. Alvarez, "First principles kinetic-collective thermal conductivity of semiconductors," Phys. Rev. B **95**(16), 165407 (2017).

[76] A. Ziabari, P. Torres, B. Vermeersch, Y. Xuan, X. Cartoixà, A. Torelló, J.-H. Bahk, Y. R. Koh, M. Parsa, P. D. Ye, F. X. Alvarez, and A. Shakouri, "Full-field thermal imaging of quasiballistic crosstalk reduction in nanoscale devices," Nat. Commun. **9**(1), 255 (2018).

[77] B. Vermeersch and N. Mingo, "Quasiballistic heat removal from small sources studied from first principles," Phys. Rev. B **97**(4), 045205 (2018).

[78] P. Torres, A. Ziabari, A. Torelló, J. Bafaluy, J. Camacho, X. Cartoixà, A. Shakouri, and F. X. Alvarez, "Emergence of hydrodynamic heat transport in semiconductors at the nanoscale," Phys. Rev. Mater. **2**(7), 076001 (2018).

[79] A. Beardo, M. Calvo-Schwarzwälder, J. Camacho, T. G. Myers, P. Torres, L. Sendra, F. X. Alvarez, and J. Bafaluy, "Hydrodynamic Heat Transport in Compact and Holey Silicon Thin Films," Phys. Rev. Appl. **11**(3), 034003 (2019).

[80] N. K. Ravichandran and A. J. Minnich, "Coherent and incoherent thermal transport in nanomeshes," Phys. Rev. B **89**(20), 205432 (2014).

[81] J. Lee, W. Lee, G. Wehmeyer, S. Dhuey, D. L. Olynick, S. Cabrini, C. Dames, J. J. Urban, and P. Yang, "Investigation of phonon coherence and backscattering using silicon nanomeshes," Nat. Commun. **8**, 14054 (2017).

[82] S. W. King, J. Bielefeld, G. Xu, W. A. Lanford, Y. Matsuda, R. H. Dauskardt, N. Kim, D. Hondongwa, L. Olasov, B. Daly, G. Stan, M. Liu, D. Dutta, and D. Gidley, "Influence of network bond percolation on the thermal, mechanical, electrical and optical properties of high and low-k a-SiC:H thin films," J. Non-Cryst. Solids **379**, 67–79 (2013).

[83] C. A. Yuan, O. van der Sluis, G. Q. Zhang, L. J. Ernst, W. D. van Driel, R. B. R. van Silfhout, and B. J. Thijsse, "Chemical–mechanical relationship of amorphous/porous low-dielectric film materials," Comput. Mater. Sci. **42**(4), 606–613 (2008).

[84] H. Li, J. M. Knaup, E. Kaxiras, and J. J. Vlassak, "Stiffening of organosilicate glasses by organic cross-linking," Acta Mater. **59**(1), 44–52 (2011).

[85] R. J. Wang, C. Y. Wang, and Y. T. Feng, "Effective geometric size and bond-loss effect in nanoelasticity of GaN nanowires," Int. J. Mech. Sci. **130**, 267–273 (2017).

[86] H. Ogi, M. Fujii, N. Nakamura, T. Yasui, and M. Hirao, "Stiffened Ultrathin Pt Films Confirmed by Acoustic-Phonon Resonances," Phys. Rev. Lett. **98**(19), 195503 (2007).

[87] P. Villain, P. Goudeau, P.-O. Renault, and K. F. Badawi, "Size effect on intragranular elastic constants in thin tungsten films," Appl. Phys. Lett. **81**(23), 4365–4367 (2002).

[88] N. Nakamura, A. Uranishi, M. Wakita, H. Ogi, M. Hirao, and M. Nishiyama, "Elastic stiffness of L10 FePt thin film studied by picosecond ultrasonics," Appl. Phys. Lett. **98**(10), 101911 (2011).

[89] M. G. Beghi, A. C. Ferrari, C. E. Bottani, A. Libassi, B. K. Tanner, K. B. K. Teo, and J. Robertson, "Elastic constants and structural properties of nanometre-thick diamond-like carbon films," Diam. Relat. Mater. **11**(3), 1062–1067 (2002).

[90] M. G. Beghi, C. S. Casari, A. Li Bassi, C. E. Bottani, A. C. Ferrari, J. Robertson, and P. Milani, "Acoustic phonon propagation and elastic properties of nano-sized carbon films investigated by Brillouin light scattering," Thin Solid Films **420–421**, 300–305 (2002).

[91] C. S. Ewing, S. Bhavsar, G. Veser, J. J. McCarthy, and J. K. Johnson, "Accurate Amorphous Silica Surface Models from First-Principles Thermodynamics of Surface Dehydroxylation," Langmuir **30**(18), 5133–5141 (2014).

[92] J. Weissenrieder, S. Kaya, J.-L. Lu, H.-J. Gao, S. Shaikhutdinov, H.-J. Freund, M. Sierka, T. K. Todorova, and J. Sauer, "Atomic Structure of a Thin Silica Film on a Mo(112) Substrate: A Two-Dimensional Network of SiO2 Tetrahedra," Phys. Rev. Lett. **95**(7), 076103 (2005).

[93] C. Lee, X. Wei, J. W. Kysar, and J. Hone, "Measurement of the Elastic Properties and Intrinsic Strength of Monolayer Graphene," Science **321**(5887), 385–388 (2008).

[94] D. C. Hurley, V. K. Tewary, and A. J. Richards, "Thin-film elastic-property measurements with laser-ultrasonic SAW spectrometry," Thin Solid Films **398–399**, 326–330 (2001).

[95] X. Li, T. Ono, Y. Wang, and M. Esashi, "Ultrathin single-crystalline-silicon cantilever resonators: Fabrication technology and significant specimen size effect on Young's modulus," Appl. Phys. Lett. **83**(15), 3081–3083 (2003).

[96] A. I. Fedorchenko, A.-B. Wang, and H. H. Cheng, "Thickness dependence of nanofilm elastic modulus," Appl. Phys. Lett. **94**(15), 152111 (2009).

[97] C. M. Stafford, B. D. Vogt, C. Harrison, D. Julthongpiput, and R. Huang, "Elastic Moduli of Ultrathin Amorphous Polymer Films," Macromolecules **39**(15), 5095–5099 (2006).

[98] C. Q. Sun, "Size dependence of nanostructures: Impact of bond order deficiency," Prog. Solid State Chem. **35**(1), 1–159 (2007).

[99] P.-O. Renault, E. Le Bourhis, P. Villain, P. Goudeau, K. F. Badawi, and D. Faurie, "Measurement of the elastic constants of textured anisotropic thin films from x-ray diffraction data," Appl. Phys. Lett. **83**(3), 473–475 (2003).

[100] H. Ogi, M. Fujii, N. Nakamura, T. Shagawa, and M. Hirao, "Resonance acoustic-phonon spectroscopy for studying elasticity of ultrathin films," Appl. Phys. Lett. **90**(19), 191906 (2007).

[101] J. Luo, J. Wang, E. Bitzek, J. Y. Huang, H. Zheng, L. Tong, Q. Yang, J. Li, and S. X. Mao, "Size-Dependent Brittle-to-Ductile Transition in Silica Glass Nanofibers," Nano Lett. **16**(1), 105–113 (2016).

[102] R. E. Miller and V. B. Shenoy, "Size-dependent elastic properties of nanosized structural elements," Nanotechnology **11**(3), 139–147 (2000).

[103] R. Dingreville, J. Qu, and Mohammed Cherkaoui, "Surface free energy and its effect on the elastic behavior of nano-sized particles, wires and films," J. Mech. Phys. Solids **53**(8), 1827–1854 (2005).

[104] K. Geng, F. Yang, and E. A. Grulke, "Nanoindentation of submicron polymeric coating systems," Mater. Sci. Eng. A **479**(1), 157–163 (2008).

[105] J. Hay and B. Crawford, "Measuring substrate-independent modulus of thin films," J. Mater. Res. **26**(6), 727–738 (2011).

[106] B. Gong, Q. Chen, and D. Wang, "Molecular dynamics study on size-dependent elastic properties of silicon nanoplates," Mater. Lett. **67**(1), 165–168 (2012).

[107] C. M. Flannery, T. Wittkowski, K. Jung, B. Hillebrands, and M. R. Baklanov, "Critical properties of nanoporous low dielectric constant films revealed by Brillouin light scattering and surface acoustic wave spectroscopy," Appl. Phys. Lett. **80**(24), 4594–4596 (2002).

[108] P. A. Mante, J. F. Robillard, and A. Devos, "Complete thin film mechanical characterization using picosecond ultrasonics and nanostructured transducers: experimental demonstration on SiO2," Appl. Phys. Lett. **93**(7), 071909 (2008).

[109] M. Colletta, W. Gachuhi, S. A. Gartenstein, M. M. James, E. A. Szwed, B. C. Daly, W. Cui, and G. A. Antonelli, "Picosecond ultrasonic study of surface acoustic waves on periodically patterned layered nanostructures," Ultrasonics **87**, 126–132 (2018).

[110] S. W. King, M. M. Paquette, J. W. Otto, A. N. Caruso, J. Brockman, J. Bielefeld, M. French, M. Kuhn, and B. French, "Valence and conduction band offsets at amorphous hexagonal boron nitride interfaces with silicon network dielectrics," Appl. Phys. Lett. **104**(10), 102901 (2014).

[111] A. Giri, S. W. King, W. A. Lanford, A. B. Mei, D. Merrill, L. Li, R. Oviedo, J. Richards, D. H. Olson, J. L. Braun, J. T. Gaskins, F. Deangelis, A. Henry, and P. E. Hopkins, "Interfacial Defect Vibrations Enhance Thermal Transport in Amorphous Multilayers with Ultrahigh Thermal Boundary Conductance," Adv. Mater. **30**(44), 1804097 (2018).

[112] T. Denneulin, D. Cooper, J.-M. Hartmann, and J.-L. Rouviere, "The addition of strain in uniaxially strained transistors by both SiN contact etch stop layers and recessed SiGe sources and drains," J. Appl. Phy. **112**(9), 094314 (2012).

[113] L. Bluestein, "A linear filtering approach to the computation of discrete Fourier transform," IEEE Trans. Audio Electroacoust. **18**(4), 451–455 (1970).

[114] A. A. Maznev, "Band gaps and Brekhovskikh attenuation of laser-generated surface acoustic waves in a patterned thin film structure on silicon," Phys. Rev. B **78**(15), 155323 (2008).

[115] H. T. Grahn, H. J. Maris, J. Tauc, and B. Abeles, "Time-resolved study of vibrations of a-Ge:H/a-Si:H multilayers," Phys. Rev. B **38**(9), 6066–6074 (1988).

[116] C. Rossignol, B. Perrin, B. Bonello, P. Djemia, P. Moch, and H. Hurdequint, "Elastic properties of ultrathin permalloy/alumina multilayer films using picosecond ultrasonics and Brillouin light scattering," Phys. Rev. B **70**(9), 094102 (2004).

[117] J. L. Arlein, S. E. M. Palaich, B. C. Daly, P. Subramonium, and G. A. Antonelli, "Optical pump-probe measurements of sound velocity and thermal conductivity of hydrogenated amorphous carbon films," J. Appl. Phys. **104**(3), 033508 (2008).

[118] B. A. Auld, *Acoustic Fields and Waves in Solids*, 2nd ed. (Krieger Publishing Company, Inc., 1990), **1**.

[119] T. Atanackovic and A. Guran, *Theory of Elasticity for Scientists and Engineers* (Birkhauser Boston, 2000).

[120] L. D. Landau and E. M. Lifshitz, *Theory of Elasticity*, 2nd ed., Course of Theoretical Physics No. 7 (Pergamon Press Ltd., 1970).

[121] D. Nardi, F. Banfi, C. Giannetti, B. Revaz, G. Ferrini, and F. Parmigiani, "Pseudosurface acoustic waves in hypersonic surface phononic crystals," Phys. Rev. B **80**(10), 104119 (2009).

[122] J. C. Phillips and M. F. Thorpe, "Constraint theory, vector percolation and glass formation," Solid State Commun. **53**(8), 699–702 (1985).

[123] J. C. Mauro, "Topological constraint theory of glass," Am. Ceram. Soc. Bull. **90**(4), 31–37 (2011).

[124] J. Zizka, S. King, A. Every, and R. Sooryakumar, "Acoustic Phonons and Mechanical Properties of Ultra-Thin Porous Low-k Films: A Surface Brillouin Scattering Study," J. Electron. Mater. **47**(7), 3942–3950 (2018).

[125] M. A. Shandiz, "Effective coordination number model for the size dependency of physical properties of nanocrystals," J. Phys. Condens. Matter **20**(32), 325237 (2008).

[126] J. Zizka, S. King, A. G. Every, and R. Sooryakumar, "Mechanical properties of low- and high-k dielectric thin films: A surface Brillouin light scattering study," J. Appl. Phys. **119**(14), 144102 (2016).

[127] R. M. Karl, G. F. Mancini, J. L. Knobloch, T. D. Frazer, J. N. Hernandez-Charpak, B. Abad, D. F. Gardner, E. R. Shanblatt, M. Tanksalvala, C. L. Porter, C. S. Bevis, D. E. Adams, H. C. Kapteyn, and M. M. Murnane, "Full-field imaging of thermal and acoustic dynamics in an individual nanostructure using tabletop high harmonic beams," Sci. Adv. **4**(10), eaau4295 (2018).

[128] A. D. Sinelnik, M. V. Rybin, S. Y. Lukashenko, M. F. Limonov, and K. B. Samusev, "Optical properties of honeycomb photonic structures," Phys. Rev. A **95**(6), 063837 (2017).

[129] L. R. Meza, G. P. Phlipot, C. M. Portela, A. Maggi, L. C. Montemayor, A. Comella, D. M. Kochmann, and J. R. Greer, "Reexamining the mechanical property space of three-dimensional lattice architectures," Acta Mater. **140**, 424–432 (2017).

[130] M. A. Boles, M. Engel, and D. V. Talapin, "Self-Assembly of Colloidal Nanocrystals: From Intricate Structures to Functional Materials," Chem. Rev. **116**(18), 11220–11289 (2016).

[131] C. E. McCold, Q. Fu, S. Hihath, J.-M. Han, Y. Halfon, R. Faller, K. van Benthem, L. Zang, and J. Hihath, "Ligand exchange based molecular doping in 2D hybrid molecule-nanoparticle arrays: length determines exchange efficiency and conductance," Mol. Syst. Des. Eng. **2**(4), 440–448 (2017).

[132] W. R. Lenart and M. J. A. Hore, "Structure–property relationships of polymer-grafted nanospheres for designing advanced nanocomposites," Nano-Struct. Nano-Objects **16**, 428–440 (2018).

[133] J. He, X.-M. Lin, H. Chan, L. Vuković, P. Král, and H. M. Jaeger, "Diffusion and Filtration Properties of Self-Assembled Gold Nanocrystal Membranes," Nano Lett. **11**(6), 2430–2435 (2011).

[134] F. J. Ibañez and F. P. Zamborini, "Chemiresistive Sensing with Chemically Modified Metal and Alloy Nanoparticles," Small **8**(2), 174–202 (2012).

[135] E. Alonso-Redondo, M. Schmitt, Z. Urbach, C. M. Hui, R. Sainidou, P. Rembert, K. Matyjaszewski, M. R. Bockstaller, and G. Fytas, "A new class of tunable hypersonic phononic crystals based on polymer-tethered colloids," Nat. Commun. **6**, 8309 (2015).

[136] S. J. van der Molen, J. Liao, T. Kudernac, J. S. Agustsson, L. Bernard, M. Calame, B. J. van Wees, B. L. Feringa, and C. Schönenberger, "Light-Controlled Conductance Switching of Ordered Metal−Molecule−Metal Devices," Nano Lett. **9**(1), 76–80 (2009).

[137] C. Stelling and M. Retsch, "Nanomeshes at Liquid Interfaces: From Free-Standing Hole Arrays toward Metal–Insulator–Metal Architectures," Adv. Mater. Interfaces **5**(10), 1800154 (2018).

[138] G. F. Mancini, R. M. Karl, E. R. Shanblatt, C. S. Bevis, D. F. Gardner, M. D. Tanksalvala, J. L. Russell, D. E. Adams, H. C. Kapteyn, J. V. Badding, T. E. Mallouk, and M. M. Murnane, "Colloidal crystal order and structure revealed by tabletop extreme ultraviolet scattering and coherent diffractive imaging," Opt. Express **26**(9), 11393–11406 (2018).

[139] J. E. Han and V. H. Crespi, "Abrupt Topological Transitions in the Hysteresis Curves of Ferromagnetic Metalattices," Phys. Rev. Lett. **89**(19), 197203 (2002).

[140] Y. Liu, S. Kempinger, R. He, T. D. Day, P. Moradifar, S.-Y. Yu, J. L. Russell, V. M. Torres, P. Xu, T. E. Mallouk, S. E. Mohney, N. Alem, N. Samarth, and J. V. Badding, "Confined Chemical Fluid Deposition of Ferromagnetic Metalattices," Nano Lett. **18**(1), 546–552 (2018).

[141] J. Ma, B. R. Parajuli, M. G. Ghossoub, A. Mihi, J. Sadhu, P. V. Braun, and S. Sinha, "Coherent Phonon-Grain Boundary Scattering in Silicon Inverse Opals," Nano Lett. **13**(2), 618–624 (2013).

[142] M. T. Barako, A. Sood, C. Zhang, J. Wang, T. Kodama, M. Asheghi, X. Zheng, P. V. Braun, and K. E. Goodson, "Quasi-ballistic Electronic Thermal Conduction in Metal Inverse Opals," Nano Lett. **16**(4), 2754–2761 (2016).

[143] L. Yang, N. Yang, and B. Li, "Extreme Low Thermal Conductivity in Nanoscale 3D Si Phononic Crystal with Spherical Pores," Nano Lett. **14**(4), 1734–1738 (2014).

[144] O. W. Käding, H. Skurk, A. A. Maznev, and E. Matthias, "Transient thermal gratings at surfaces for thermal characterization of bulk materials and thin films," Appl. Phys. A **61**(3), 253–261 (1995).

[145] H. Ju, S. Zhang, Z. Li, X. Shui, and P. Kuo, "Size-dependent thermal diffusivity of multilayered thin films deposited on substrates characterized by transient grating technique," Appl. Phys. Lett. **94**(3), 031902 (2009).

[146] R. M. Slayton, K. A. Nelson, and A. A. Maznev, "Transient grating measurements of film thickness in multilayer metal films," J. Appl. Phys. **90**(9), 4392–4402 (2001).

[147] W.-L. Ong, S. M. Rupich, D. V. Talapin, A. J. H. McGaughey, and J. A. Malen, "Surface chemistry mediates thermal transport in three-dimensional nanocrystal arrays," Nat. Mater. **12**(5), 410–415 (2013).

[148] Y. S. Touloukian, *Thermophysical Properties of High Temperature Solid Materials: Vol. 1. Elements*. New York, NY: The Macmillan Company (1967).

[149] Oleylamine, ≥98% (primary amine), Sigma-Aldrich. Accessed April 4, 2019.

[150] X. Yin, J. Wu, P. Li, M. Shi, and H. Yang, "Self-Heating Approach to the Fast Production of Uniform Metal Nanostructures," ChemNanoMat **2**(1), 37–41 (2016).

[151] Y.S. Touloukian, *Thermophysical Properties of Matter: Vol 12. Thermal Expansion – Metallic Elements and Alloys*. New York, NY: Plenum Publishing Corporation (1975).

[152] R. A. Orwoll and P. J. Flory, "Equation- of-state parameters for normal alkanes. Correlation with chain length," J. Am. Chem. Soc. **89**(26), 6814–6822 (1967).

[153] R. L. Olmon, B. Slovick, T. W. Johnson, D. Shelton, S.-H. Oh, G. D. Boreman, and M. B. Raschke, "Optical dielectric function of gold," Phys. Rev. B **86**(23), 235147 (2012).

[154] Optical Glass Data Sheet, Schott, 2017. Accessed via refractiveindex.info April 4, 2019.

[155] C. Schinke, P. Christian Peest, J. Schmidt, R. Brendel, K. Bothe, M. R. Vogt, I. Kröger, S. Winter, A. Schirmacher, S. Lim, H. T. Nguyen, and D. MacDonald, "Uncertainty analysis for the coefficient of band-to-band absorption of crystalline silicon," AIP Adv. **5**(6), 067168 (2015).

[156] M. G. L. Gustafsson, L. Shao, P. M. Carlton, C. J. R. Wang, I. N. Golubovskaya, W. Z. Cande, D. A. Agard, and J. W. Sedat, "Three-Dimensional Resolution Doubling in Wide-Field Fluorescence Microscopy by Structured Illumination," Biophys. J. **94**(12), 4957–4970 (2008).

[157] E. S. Massaro, A. H. Hill, and E. M. Grumstrup, "Super-Resolution Structured Pump–Probe Microscopy," ACS Photonics **3**(4), 501–506 (2016).

[158] A. R. Cameron, P. Riblet, and A. Miller, "Spin Gratings and the Measurement of Electron Drift Mobility in Multiple Quantum Well Semiconductors," Phys. Rev. Lett. **76**(25), 4793–4796 (1996).

[159] L. Foglia, F. Capotondi, R. Mincigrucci, D. Naumenko, E. Pedersoli, A. Simoncig, G. Kurdi, A. Calvi, M. Manfredda, L. Raimondi, N. Mahne, M. Zangrando, C. Masciovecchio, and F. Bencivenga, "First Evidence of Purely Extreme-Ultraviolet Four-Wave Mixing," Phys. Rev. Lett. **120**(26), 263901 (2018).

[160] R. Mincigrucci, L. Foglia, D. Naumenko, E. Pedersoli, A. Simoncig, R. Cucini, A. Gessini, M. Kiskinova, G. Kurdi, N. Mahne, M. Manfredda, I. P. Nikolov, E. Principi, L. Raimondi, M. Zangrando, C. Masciovecchio, F. Capotondi, and F. Bencivenga, "Advances in instrumentation for FEL-based four-wave-mixing experiments," Nucl. Instrum. Methods Phys. Res. A **907**, 132–148 (2018).

[161] D. D. Hickstein, F. J. Dollar, P. Grychtol, J. L. Ellis, R. Knut, C. Hernández-García, D. Zusin, C. Gentry, J. M. Shaw, T. Fan, K. M. Dorney, A. Becker, A. Jaroń-Becker, H. C. Kapteyn, M. M. Murnane, and C. G. Durfee, "Non-collinear generation of angularly isolated circularly polarized high harmonics," Nat. Photonics **9**(11), 743–750 (2015).

[162] R. Mincigrucci, F. Bencivenga, E. Principi, F. Capotondi, L. Foglia, D. Naumenko, A. Simoncig, S. Dal Zilio, A. Gessini, G. Kurdi, N. Mahne, M. Manfredda, A. Matruglio, I. Nikolov, E. Pedersoli, L. Raimondi, R. Sergo, M. Zangrando, and C. Masciovecchio, "Timing methodologies and studies at the FERMI free-electron laser," J. Synchrotron Rad. **25**, 44–51 (2018).

[163] S. Eich, A. Stange, A. V. Carr, J. Urbancic, T. Popmintchev, M. Wiesenmayer, K. Jansen, A. Ruffing, S. Jakobs, T. Rohwer, S. Hellmann, C. Chen, P. Matyba, L. Kipp, K. Rossnagel, M. Bauer, M. M. Murnane, H. C. Kapteyn, S. Mathias, and M. Aeschlimann, "Time- and angle-resolved photoemission spectroscopy with optimized high-harmonic pulses using frequency-doubled Ti:Sapphire lasers," J. Electron Spectros. Relat. Phenomena **195**, 231–236 (2014).

[164] D. Popmintchev, C. Hernández-García, F. Dollar, C. Mancuso, J. A. Pérez-Hernández, M.-C. Chen, A. Hankla, X. Gao, B. Shim, A. L. Gaeta, M. Tarazkar, D. A. Romanov, R. J. Levis, J. A. Gaffney, M. Foord, S. B. Libby, A. Jaron-Becker, A. Becker, L. Plaja, M. M. Murnane, H. C. Kapteyn, and T. Popmintchev, "Ultraviolet surprise: Efficient soft x-ray high-harmonic generation in multiply ionized plasmas," Science **350**(6265), 1225–1231 (2015).

[165] H. Wang, Y. Xu, S. Ulonska, J. S. Robinson, P. Ranitovic, and R. A. Kaindl, "Bright high-repetition-rate source of narrowband extreme-ultraviolet harmonics beyond 22 eV," Nat. Commun. **6**, 7459 (2015).

Appendix

COMSOL Finite Element Analysis

Throughout the work of this thesis, I have relied on the commercial software COMSOL to analyze both thermal and elastic measurements of nanoscale systems. COMSOL uses the finite element method to solve differential equations that model physical systems, a process known as finite element analysis (FEA). While the differential equations used assume classical, continuum mechanics, this approach has great power and utility in that it can model our real experimental geometries, and it does not require prohibitive amounts of computing power. For the thermal transport problem, the use of an effective Fourier model means that the bulk diffusion equation may be directly implemented in COMSOL, as long as either conductivity or resistivity is adjusted to account for nanoscale effects. For the elastic properties problem, we have observed good agreement between COMSOL and diffraction measurements, indicating that continuum mechanics remains a reasonable approximation for acoustic propagation, even at deep nanoscale sizes. In the following appendix, I will discuss in more detail the COMSOL modelling performed for each of these measurements.

A.1 Finite Element Analysis

To solve partial differential equations, the finite element method first discretizes a system into a series of points. These are the discrete locations where variables such as temperature and displacement are calculated as a function of time. These points together make a mesh that may be explicitly defined or, more commonly, “grown” from the defined boundaries according to established algorithms and user inputs. Generally, a higher density mesh is needed in locations with more confined dimensions. For our nanoline systems, the mesh must be high density at the nanoline-substrate interface, and it can grow to a much larger

spacing between mesh points as it extends into the depth of the substrate. Fig. A.1 gives examples of standard meshes used in our analysis.

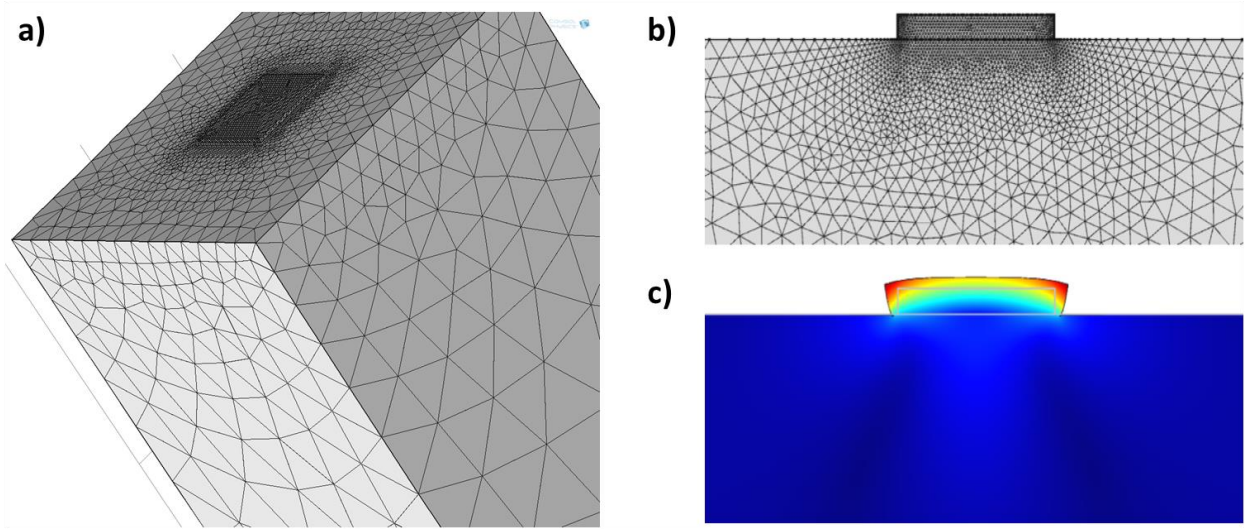

Figure A.1: Finite element analysis meshes. These meshes are grown using one of COMSOL's built-in algorithms, which is based off of a triangular lattice. a) 3D simulation cell used for 2D nanocubes. b) 2D simulation cell used for 1D nanolines. c) Calculated displacements on mesh in (b) after thermal expansion. Displacements are represented both by moving the point positions in cartesian space and by color. Displacements are exaggerated for visualization in (c). Panels (b) and (c) taken from [20].

One important practical aspect of FEA is that an improper mesh can give inaccurate results or inhibit the convergence of the calculation. As an example, if the mesh point spacing is similarly sized to the acoustic wavelength being studied, the wave can unphysically diffract or disperse due to the mesh itself and produce dynamics not present in the experiment. It is thus important to give great care to the mesh generation when using FEA to interpret experimental results. We confirm there is no spurious mesh-dependence in our calculations by changing the number of mesh points, rerunning the simulation, and verifying there is no change in our results.

Similar to requiring proper sampling in space with an appropriate mesh, FEA requires a small enough step size in time to properly sample the dynamics that are occurring. If too large of a time step is used, the simulation will not be properly constrained, and it will produce unrealistic values or in the worst cases diverge. As mentioned in Chapter 3, the fastest dynamic we simulate in COMSOL is electron-phonon coupling according to the two-temperature model. For these simulations, the step size must start at 2fs until the ultrafast transients have decayed. For both time step size and number of mesh points used, there is a

trade-off between accuracy and computational time. The more steps and mesh points used, the longer it takes for a simulation to finish. Generally, we try to use the fewest time steps and mesh points we can, without losing accuracy.

A.2 Thermal modelling and fitting

To analyze our thermal experiments, we first model a single unit cell of the periodic grating, as presented in [20], and described below. As all of the COMSOL-based thermal analysis presented in this thesis uses nanolines, I will limit discussion here to the 2D cross section case (approximates nanolines as infinite), as shown in Fig. A.1(b). The sides of the simulation cell use periodic boundary conditions to capture the dynamics of an infinite nanograting. This is a reasonable approximation as we probe the center of our gratings. The nanoline-substrate interface has continuous displacements (no-slip condition), but discontinuous temperature due to the thermal boundary resistivity. The top surface has unconstrained displacement, but the heat flux is set to zero as losses due to radiation are minimal, and convection is not a concern for our in-vacuum experiments. The substrate is modeled as several microns thick – enough so that no heat will reach the bottom boundary within the simulated time window. The bottom surface has both zero displacement and heat flux. We solve for the temperature, T, and displacement, **u**, at every point as a function of time using the coupled thermoelastic equations,

$$\nabla \cdot \left(\mathrm{c} : \nabla(\mathrm{u} - \alpha\Delta\mathrm{T})\right) = \rho \frac{\partial^2 \mathrm{u}}{\partial \mathrm{t}^2},$$

$$\rho c_p \frac{\partial T}{\partial t} + \rho c_p u \cdot \nabla T = \nabla \cdot (\kappa \nabla T) + Q,$$

where **c** is the elastic tensor, α is the linear thermal expansion coefficient, ρ is the density, c_p is the specific heat capacity, κ is the thermal conductivity, and Q is the heat source (absorbed laser pulse in our case). The effective resistivity, r_{eff}, at the nanoline-substrate interface is introduced using the relationship

$$n \cdot (\kappa \nabla T) = -\frac{\Delta T}{r_{eff}},$$

where **n** is the unit vector normal to the surface, and ΔT is the temperature discontinuity across the interface introduced by the boundary resistivity.

Using this approach for each COMSOL calculation, we perform a suit of simulations to fit each grating geometry (linewidth and period). We first calculate the surface displacement for a variety of effective resistivities, with all other parameters held constant. We then numerically diffract from each simulated surface displacement, using the Fresnel approximation. Building change in diffraction signals in the same way as for experimental measurements, we obtain a single change in diffraction efficiency signal versus time for each COMSOL simulation. This is shown for a single grating on silicon in Fig. A.2.

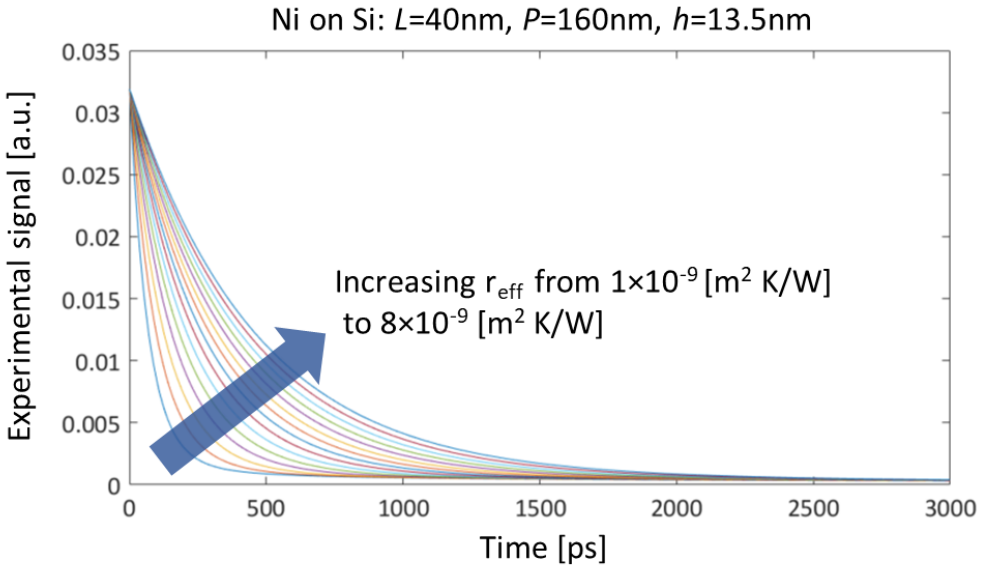

Figure A.2: Sweep of effective resistivity simulations for a nickel grating on silicon. As the effective resistivity is increased, the thermal decay slows down, as expected. A separate set of simulations is performed for each grating geometry on each sample being investigated. Note that these diffraction signals are calculated under the quasistatic approximation, which removes acoustic oscillations.

When performing thermal simulations, we use the quasistatic approximation rather than calculating the full elastic dynamics of the system. This retains the necessary information for thermal analysis but greatly reduces computation times. The quasistatic approximation discards the second derivatives of displacement in the thermoelastic equations, meaning that acoustic waves are eliminated from the calculated displacements, but the thermal expansion is still properly influenced by the elastic tensor of the

material. As shown in Fig. A.3, the quasistatic diffraction signal goes through the average of the acoustic dynamics, enabling least squares fitting of the quasistatic signals to experimental signals.

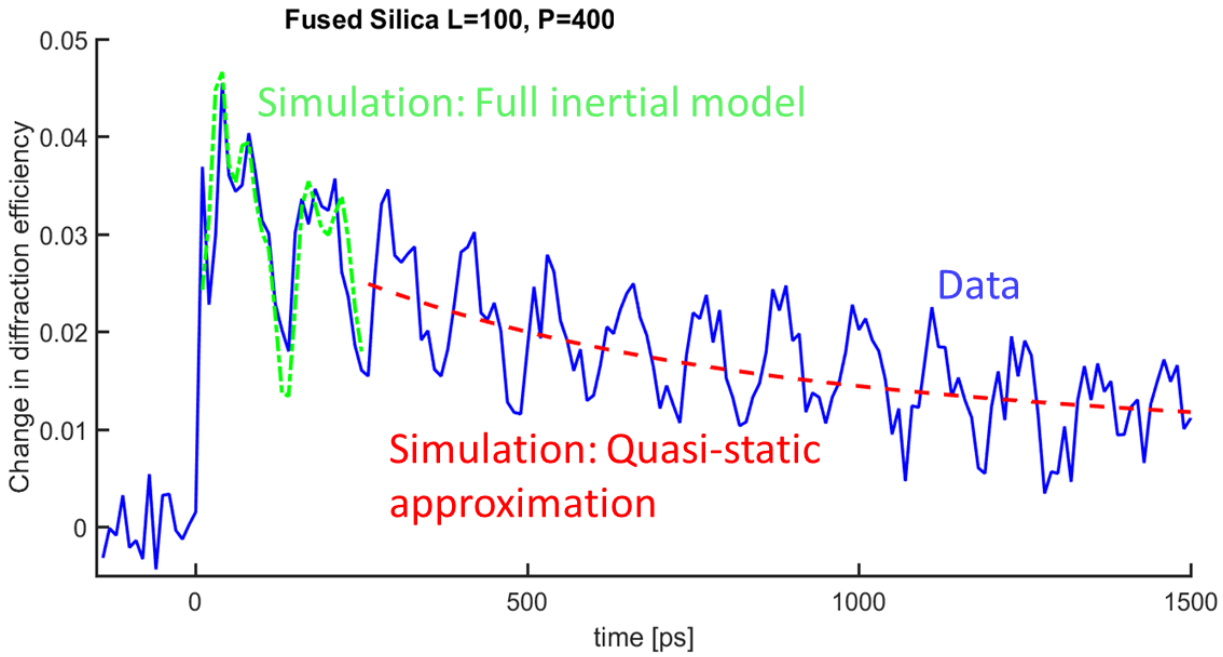

Figure A.3: Comparison of full inertial and quasistatic simulations. The blue line is measured data for a 100nm linewidth, 400nm period nickel nanograting on a fused silica substrate. The green dotted line is a full inertial COMSOL calculation that includes all acoustic dynamics in this system. The red dashed line is a quasistatic calculation for this system, which passes through the moving average of the acoustic waves. note that the full inertial model is calculated at a very fine time step, but it is down-sampled here to provide a better comparison with the measured data.

After calculating a series of diffraction signals as a function of r_{eff}, we must find the value of r_{eff} that produces the best fit curve for our measured data. For improved resolution in our fit, we require some form of continuous interpolation between the series of simulated curves, such as those shown in Fig. A.2. For the work presented in this thesis, we do this by first fitting a double exponential to each simulated curve. We then look at how each of the four parameters (amplitude and time constant for both exponentials) change from one resistivity to the next, and fit a polynomial to each parameter as a function of resistivity. This produces a final analytical function that closely approximates our simulated curves, but allows for continuous tuning of resistivity between the simulated bounds. Mathematically then, the function we fit to our experimental data trace is

$$f(t) = a(r)e^{-t/b(r)} + c(r)e^{-t/d(r)},$$

where the parameters $a(r)$, $b(r)$, $c(r)$, and $d(r)$ are polynomial fits to how the double exponential parameters change as a function of resistivity. Because the polynomial and double exponential fits are simply used to analytically reproduce our COMSOL-calculated signals, we do not ascribe any physical meaning to these parameters. The polynomial fits to the double exponential parameters are usually of degree three, as that is sufficient to reproduce our COMSOL results, though some simulations require a fourth order polynomial for the polynomial fit to reliably reproduce COMSOL results.

In addition to fitting the effective resistivity, we include three other fit parameters that aid in the registration of the simulated curve to the experimental data. These parameters are horizontal offset, vertical offset, and normalization, as shown in Fig. A.4. Of course, unconstrained offsets and normalizations can give spurious and non-unique fits, so we limit these parameters according to the experimental data trace itself. The horizontal offset is limited to sweep the points along the rise in signal from time 0 to the peak of thermal expansion. This range is chosen because the appropriate start point lies somewhere within this range for the quasistatic curve that excludes inertial effects at early times. The vertical offset is bound by the noise level before time 0, which can obscure where the real zero signal line lies. The normalization is the most difficult parameter to bound because the inertial effects excluded by the quasistatic approximation can cause significant changes in signal amplitude at early times. The most reliable method for setting the range of normalization is thus to compare the initial heights of full inertial and quasistatic simulations of the same grating geometry. As the full inertial simulation captures all the acoustic dynamics present in the experiment, this relative height bounds the relative height between the quasistatic simulation and the experimental data.

Once all of these bounds are determined, we perform a least squares fit to the data for each combination of r_{eff}, horizontal offset, vertical offset, and normalization. The combination that has the lowest residual error is then taken to be the best fit. In most cases, there is a clear minimum in the residual that is not at the edges of the simulated parameter space, indicating a true fit. In some cases, we do have to limit the offsets or normalization at the edge of their allowed values, according to the physical constraints listed above. For r_{eff}, however, we always ensure the best fit lies somewhere in the middle of the calculated range

so that the best fit value is not artificially limited by the scope of our calculated range. This process is repeated for each independent measurement on a given grating, with the final quoted value and uncertainty of r_{eff} for that geometry being the average and standard deviation, respectively, of each best fit.

A.3 Acoustic wave modelling for elastic properties

To extract the elastic properties of ultrathin films using our experimentally measured surface acoustic waves (SAW), we follow the procedure described in [22] and outlined in Chapter 4. This process fully accounts for the mass loading of the nanostructures, which depresses the SAW velocities compared to the values that can be derived for a pure film-on-substrate sample without any nanostructures. Similar to the thermal simulations, our procedure minimizes the amount of full inertial calculations needed, as they are the most computationally expensive. The quasistatic approximation is not an option in this case, since it removes all acoustic waves. Instead, we leverage the power of eigenfrequency analysis in COMSOL, which only requires the static geometry of the nanoline – thin film – substrate unit cell. In this analysis, COMSOL solves for the eigenfrequencies, *f*, of the static structure using the equation

$$\rho(f2\pi)^2 u - \nabla \cdot \sigma = F_V,$$

where ρ is the density, $\mathbf{u}$ is the displacement, σ is the stress, and $\mathbf{F_V}$ is the load on the material. These calculations proceed very fast, and give all of the supported eigenfrequencies of the structure, within a specified frequency range. The surface acoustic waves we measure must match one of these frequencies.

To determine which of these eigenmodes are excited in our experiment, we now turn to the full inertial COMSOL simulations. Using the same thermoelastic equations described in the previous section, we calculate the complete dynamics of the system from laser heating to maximum thermal expansion. This only requires a simulation time window of ~100-200ps, which is well below the ~8ns time window required to reproduce the full experimental measurement. Once we have calculated the point of maximum thermal expansion, we have the excitation that launches all the acoustic waves we observe. Thus, we can project the maximum displacement field onto the basis of eigenmodes we previously calculated to determine which eigenfrequency corresponds to our measured SAW frequency. As shown in Fig. A.4, the projected

amplitude of the maximum displacement field, decomposed onto the eigenmode basis, will reach a maximum at the eigenfrequency corresponding to the excited SAW frequency. This provides a ready identification of the calculated SAW frequency that can be directly compared to the measured SAW frequency, without having to simulate a full inertial signal that is fit to the raw data.

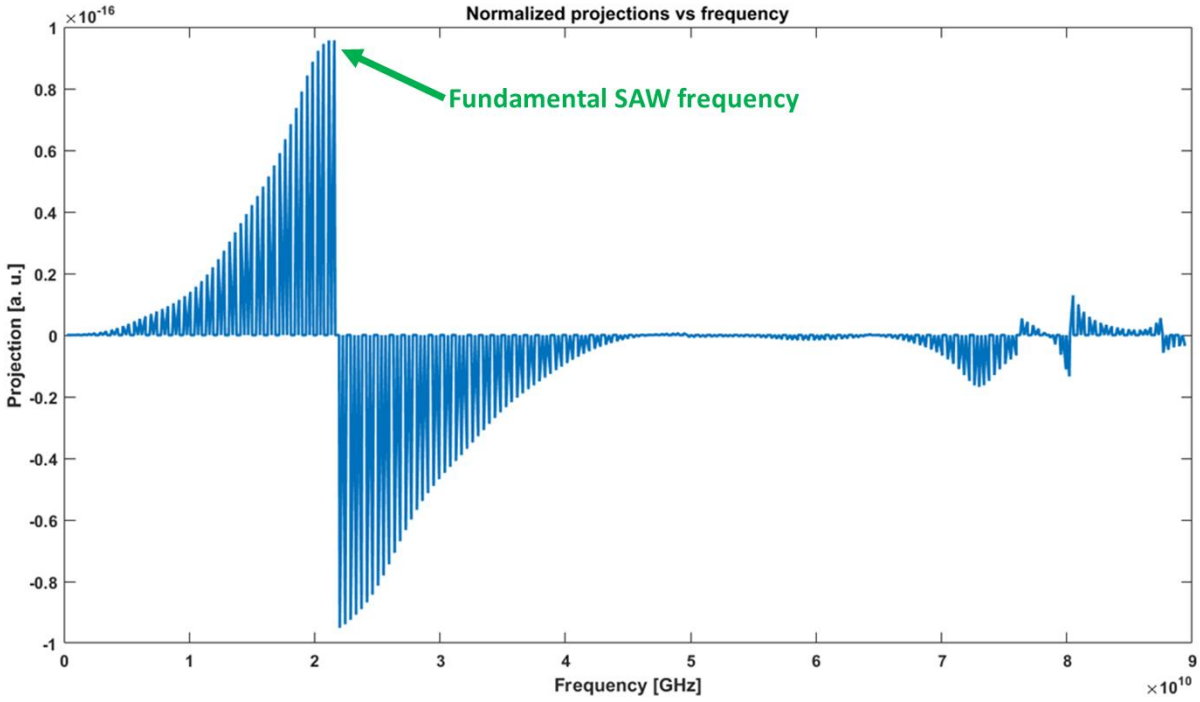

Figure A.4: Determination of SAW frequency using eigenfrequency analysis. When the maximum displacement field is projected onto the basis of eigenmodes for the nanostructure-film-substrate system, each eigenfrequency has a different weight contributing to the maximum displacement field. As the laser-heated nanoline grating predominantly excites the fundamental SAW, the large amplitude projection corresponds to this wave. Note that flips in sign are just a 180 degree phase shift when adding that mode to form the total displacement field, and this does not always line up with the maximum projected amplitude.

We tune the elastic properties of the film-substrate system until the calculated SAW frequency matches the measured SAW frequency. As described in Chapter 4, we first simulate a large grating, where the SAW has a long penetration depth and travels mostly in the substrate. The wave speed is thus primarily sensitive to the substrate elastic properties, and we tune the elastic constants of the substrate a small percentage from their nominal values to fit the measured SAW frequency. This accounts for manufacturing imperfections and film-induced strain in the substrate. Next, we simulate a small grating where the wave is fully confined to the film. By tuning the Young's Modulus of the film in COMSOL, we match the calculated and measured SAW velocities, and thus extract the elastic constants of the film accounting for mass loading.